Atmospheric neutrino oscillation analysis with solar terms in Super-Kamiokande

Yumiko Takenaga

February 15, 2008

Abstract

The atmospheric neutrino data have been well explained in the two-flavor $\nu_\mu \leftrightarrow \nu_\tau$ oscillation scheme and the Δm^2_{23} and $\sin^2 2\theta_{23}$ parameters have been measured. No evidence of the atmospheric ν_e oscillation has been observed and the mixing angle θ_{13} is consistent with zero by the results of θ_{13} search experiments. On the other hand, thanks to the precise measurements by solar neutrino observations and the KamLAND experiment, the LMA-MSW solution of the solar neutrino problem is established and the mixing angle θ_{12} and mass difference Δm^2_{12} have been measured accurately.

If these 1-2 parameters are considered into the atmospheric neutrino oscillation analysis, the oscillation of low energy atmospheric ν_e might be observed even in case of zero-θ_{13}. The effect of the ν_e oscillation induced by the 1-2 parameters depends on the octant of θ_{23} ($\theta_{23} > 45^\circ$ or $\theta_{23} < 45^\circ$). Therefore the atmospheric neutrino oscillation analysis including the 1-2 parameters has a possibility to determine the octant of θ_{23} for the non-maximal $\sin^2 2\theta_{23}$. This information cannot be obtained by the standard $\nu_\mu \leftrightarrow \nu_\tau$ two-flavor oscillation analysis because the oscillation probability in that framework depends on $\sin^2 2\theta_{23}$, not on $\sin^2 \theta_{23}$.

We have observed large number of atmospheric neutrino events in Super-Kamiokande. In this thesis, the atmospheric neutrino data from the Super-Kamiokande-I (1996-2001) and Super-Kamiokande-II (2003-2005) are summarized and used in the oscillation analysis. The analysis has been done in the two schemes, pure two-flavor $\nu_\mu \leftrightarrow \nu_\tau$ analysis and three-flavor analysis with the 2-3 and 1-2 parameters. There is no significant discrepancy of θ_{23} from 45°, though the effect of the 1-2 parameters is seen in the χ^2 distribution. The stronger constraint on $\sin^2 \theta_{23}$ has been observed in the analysis with the 1-2 parameters. The 1σ arrowed region for $\sin^2 \theta_{23}$ is $0.43 < \sin^2 \theta_{23} < 0.58$, which is equivalent to $\sin^2 2\theta_{23} > 0.973$.

Acknowledgments

First of all, I would like to express my great gratitude to Prof. Takaaki Kajita for giving me the opportunity of studying atmospheric neutrino. I have learned a lot of things under his excellent guidance. This thesis would never exist without his invaluable support.

I would like to be appreciative to Prof. Yoichiro Suzuki, the spokesperson of the Super-Kamiokande experiment. He encouraged me in many cases.

I further owe my sincere thanks to Prof. M.Shiozawa and K.Okumura. They were willing to give me many valuable advice and support since I entered graduate school.

I would be grateful to all the members of the atmospheric neutrino analysis group, especially Prof. K.Kaneyuki, Prof. Y.Itow, Prof. S.Moriyama, Prof. Y.Hayato, M.Miura, Y.Obayashi, J.Kameda, C.Saji, S.Nakayama, M.Ishitsuka, I.Higuchi, G.Mitsuka, H.Nishino, C.Ishihara, S.Hazama, E.Kearns, H.W.Sobel, C.K.Jung, R.J.Wilkes, J.G.Learned, C.W.Walter, K.Scholberg, A.Habig, S.Mine, N.Tanimoto, J.L.Raaf, S.Desai, W.Wang, J.S.Jang, H.K.Seo, T.Kato, R.Terri, R.Wendell, C.Regis, F.Dufour, E.Thrane, M.Litos, and C.Simon.

I would like to extend my gratitude to ICRR staffs and members, Prof. M.Nakahata, Prof. Y.Takeuchi, Y.Koshio, K.Abe, A.Takeda, H.Sekiya, S.Yamada, H.Ogawa, K.Kobayashi, H.Watanabe, A.Minamino, T.Iida, M.Ikeda, K.Ueshima, K.Ueno, and Y.Nakajima.

The analysis in this thesis has also relied on the hard work by all members of Super-Kamiokande. This thesis is greatly indebted to them. I gratefully acknowledge the cooperation of Kamioka Mining and Smelting Company.

I would like to thank all the people who supported and encouraged me during my time in graduate school.

Contents

Chapter 1

Introduction

1.1 Neutrino Oscillation

In the Standard Model of elementary particles, neutrinos are regarded as exactly massless particles [1, 2, 3]. However, there is no fundamental reason to forbid the finite masses of neutrinos. Neutrino oscillation is proposed by Maki, Nakagawa and Sakata in 1962 as a consequence of the finite masses of neutrinos [4].

If neutrinos have finite masses, their flavor eigenstates can be written as the superpositions of the mass eigenstates as follows :

$$|\nu_\alpha\rangle = \sum_{i=1}^{3} U_{\alpha i}|\nu_i\rangle, \tag{1.1}$$

where $|\nu_\alpha\rangle$ represents the flavor eigenstates ν_e, ν_μ and ν_τ and $|\nu_i\rangle$ represents the mass eigenstates ν_1, ν_2 and ν_3. $U_{\alpha i}$ is a 3×3 unitary mixing matrix known as the MNS matrix. The mixing matrix U can be written as a product of three rotation matrices using the mixing angle θ_{12}, θ_{23} and θ_{13} for each flavor and a CP-violating phase δ as follows :

$$\mathrm{U} = \begin{pmatrix} 1 & 0 & 0 \\ 0 & c_{23} & s_{23} \\ 0 & -s_{23} & c_{23} \end{pmatrix} \begin{pmatrix} c_{13} & 0 & s_{13}e^{-i\delta} \\ 0 & 1 & 0 \\ -s_{13}e^{i\delta} & 0 & c_{13} \end{pmatrix} \begin{pmatrix} c_{12} & s_{12} & 0 \\ -s_{12} & c_{12} & 0 \\ 0 & 0 & 1 \end{pmatrix}, \tag{1.2}$$

where $c_{ij} \equiv \cos\theta_{ij}$, $s_{ij} \equiv \sin\theta_{ij}$. The time evolution of the flavor eigenstates is represented as :

$$|\nu_\alpha(t)\rangle = \sum_i U_{\alpha i} \exp(-iE_i t)|\nu_i(t=0)\rangle \tag{1.3}$$

$$= \sum_i \sum_{\alpha'} U_{\alpha i} U^*_{\alpha' i} \exp(-iE_i t)|\nu'_\alpha(t=0)\rangle, \tag{1.4}$$

where E_i is an eigenvalue of the mass eigenstate $|\nu_i\rangle$. Therefore the probability for flavor

eigenstate ν_α at t=0 to change the state ν_β at time t, is calculated as :

$$\begin{aligned} P(\nu_\alpha \to \nu_\beta) &= |\langle \nu_\beta(t)|\nu_\alpha(0)\rangle|^2 && (1.5)\\ &= \left|\sum_i U_{\beta i}U^*_{\alpha i}\exp(-iE_i t)\right|^2 && (1.6)\\ &= \sum_i |U_{\alpha i}U_{\beta i}|^2 + \sum_{i\neq j} U_{\alpha i}U^*_{\beta i}U^*_{\alpha j}U_{\beta j}\exp(-i(E_i-E_j)t). && (1.7)\end{aligned}$$

Thus, due to the flavor mixing of massive neutrinos, the flavor transition phenomenon, neutrino oscillation could occur.

In the two-flavor mixing case, the mixing matrix U is simplified as follows :

$$\mathrm{U} = \begin{pmatrix} \cos\theta & \sin\theta \\ -\sin\theta & \cos\theta \end{pmatrix}. \tag{1.8}$$

The transition probability for $\nu_\alpha \to \nu_\beta$ (Equation (1.7)) is expressed in much simpler form :

$$P_(\nu_\alpha \to \nu_\beta) = \sin^2 2\theta \sin^2\left(\frac{(E_i-E_j)t}{2}\right). \tag{1.9}$$

If neutrinos have finite masses, the following approximation can be used :

$$\begin{aligned} E_i - E_j &= \sqrt{m_i^2+p_i^2} - \sqrt{m_j^2+p_j^2} \\ &\simeq \left(p+\frac{m_i^2}{2p}\right) - \left(p+\frac{m_j^2}{2p}\right) \\ &\simeq \frac{\Delta m^2_{ij}}{2E}, && (1.10)\end{aligned}$$

where $\Delta m^2_{ij} \equiv m_i^2 - m_j^2$ is the mass-squared difference of neutrino mass eigenstates. Finally using the neutrino flight length L_ν and the neutrino energy E_ν, the survival probability of ν_α in the two-flavor mixing case is written as follows :

$$\begin{aligned} P(\nu_\alpha \to \nu_\alpha) &= 1 - \sin^2 2\theta \sin^2\left(\frac{\Delta m^2_{ij} L_\nu}{4E_\nu}\right) && (1.11)\\ &= 1 - \sin^2 2\theta \sin^2\left(\frac{1.27\Delta m^2_{ij}(\mathrm{eV}^2) L_\nu(\mathrm{km})}{E_\nu(\mathrm{GeV})}\right) && (1.12)\\ &= 1 - \sin^2 2\theta \sin^2\left(\pi\frac{L_\nu}{l}\right), && (1.13)\end{aligned}$$

where $l \equiv 4\pi E/\Delta m^2_{ij}$ is the oscillation length. The oscillation probability is characterized by the mixing angle θ, the mass squared difference Δm^2_{ij}, the neutrino flight length L_ν and the neutrino energy E_ν. The oscillation amplitude is maximum when $L_\nu[\mathrm{km}]/\mathrm{E}_\nu[\mathrm{GeV}] = \pi/2.53 \cdot \Delta m^2_{ij}[\mathrm{eV}^2]$.

1.2 Neutrino Oscillation Experiments

There are a lot of experiments which have observed neutrino oscillations and measured oscillation parameters, such as the mass-squared difference and the mixing angle. In this section, the current status of our knowledge of neutrino oscillations is summarized.

1.2.1 Solar Neutrino and Reactor Neutrino Observations

Electron neutrinos are produced by nuclear reactions in the Sun. Since the energy range of the solar neutrinos is from several hundred keV to 15 MeV and the distance between the Sun and the Earth is $\sim 10^8$ km, the observation of ν_e disappearance is sensitive to Δm^2 down to $\sim 10^{-11}\,\mathrm{eV}^2$. Homestake [5] experiment is the oldest solar neutrino experiment, which used the interaction $\nu_e + {}^{37}\mathrm{Cl} \rightarrow \mathrm{e}^- + {}^{37}\mathrm{Ar}$. The produced Ar atoms were counted by a chemical technique. Kamiokande [6] experiment used electrons in H_2O molecules for targets of elastic scattering $\nu_l + \mathrm{e}^- \rightarrow \nu_l + \mathrm{e}^-$ (l=e, μ, τ). SAGE [7] and GALLEX [8] experiments used $\nu_e + {}^{71}\mathrm{Ga} \rightarrow \mathrm{e}^- + {}^{71}\mathrm{Ge}$ interaction and the produced Ge atoms were counted by a chemical technique. Super-Kamiokande [9] is a successor of Kamiokande experiment. SNO experiment [10] started in 1999, which uses the Cherenkov detector filled with heavy water D_2O. They measures the flux of ν_e via $\nu_e + \mathrm{D} \rightarrow \mathrm{e}^- + \mathrm{p} + \mathrm{p}$, as well as the total neutrino flux via $\nu_x + \mathrm{D} \rightarrow \nu_x + \mathrm{p} + \mathrm{n}$.

All the results except for the neutral current interaction measurement at the SNO observed the significant deficit in the solar neutrino flux compared with the standard solar model [11]. Combining the results of SNO and SK, the LMA-MSW solution of the solar neutrino problem was indicated [12]. The result was confirmed by the KamLAND experiment, which is a liquid scintillator detector and searches for $\overline{\nu}_e$ oscillations. $\overline{\nu}_e$'s generated at distant power reactors are detected by the interaction $\overline{\nu}_e + \mathrm{p} \rightarrow e^+ + \mathrm{n}$, where the prompt signal from the positron and the delayed coincidence of characteristic gammas from neutron capture allow an efficient reduction of backgrounds. The $\overline{\nu}_e$ flux at the detector site is dominated by a number of reactors at an average distance of ~ 180 km. Since the energy of the produced $\overline{\nu}_e$s is around 3 MeV, the experiment is sensitive to Δm^2 down to several $10^{-6}\,\mathrm{eV}^2$. The combined analysis of the solar neutrino data and the KamLAND data leads to the oscillation parameters [13]:

$$\begin{aligned} &7.3 \times 10^{-5} < \Delta m^2_{12} < 8.1 \times 10^{-5} eV^2, \\ &0.28 < \sin^2\theta_{12} < 0.37 \quad (2\sigma). \end{aligned} \tag{1.14}$$

1.2.2 Atmospheric Neutrino and Accelerator Neutrino Observations

Atmospheric neutrinos are produced by the decays of pions and kaons which are generated when primary cosmic rays interact with the nuclei in the Earth's atmosphere :

$$\begin{aligned} \pi^+ &\rightarrow \mu^+ + \nu_\mu \\ &\quad \hookrightarrow e^+ + \nu_e + \overline{\nu}_\mu, \end{aligned} \tag{1.15}$$

$$\begin{aligned} \pi^- &\rightarrow \mu^- + \overline{\nu}_\mu \\ &\quad \hookrightarrow e^- + \overline{\nu}_e + \nu_\mu, \end{aligned} \tag{1.16}$$

The energy spectrum of the atmospheric neutrinos peaks around 40 MeV and extends to the energy range above TeV. The neutrino flight length ranges from about 15 km for neutrinos produced above the detector to 13000 km for neutrinos produced on the opposite side of the

Earth. Since typical atmospheric neutrino experiments have enough event statistics for neutrino energies above several hundred MeV, the observation of atmospheric neutrinos is sensitive to Δm^2 down to $10^{-4} eV^2$. The predicted total flux of atmospheric neutrinos has $\sim 20\,\%$ uncertainty which mostly comes from the uncertainties on cross sections of hadronic interactions and on fluxes of primary cosmic ray components [14]. However, the flavor ratio $(\nu_\mu + \overline{\nu}_\mu)/(\nu_e + \overline{\nu}_e)$ is predicted with only $3\,\%$ uncertainty. This ratio has been measured by several underground experiments and reported in terms of a double ratio R$\equiv (N_\mu/N_e)_{Data}/(N_\mu/N_e)_{MC}$, where N_μ (N_e) is the number of muon (electron) events produced by charged current interactions.

The double ratio R obtained by underground Cherenkov detectors, Kamiokande [15, 16] and IMB [17, 18] and an iron calorimeter detector Soudan 2 [19] was significantly lower than 1. In 1998, Super-Kamiokande reported that the zenith angle distributions of muon neutrino events were asymmetric and concluded that their measurement results gave an evidence for neutrino oscillation [20]. MACRO [21] and Super-Kamiokande [22] have studied about upward-going muons produced by energetic ν_μ charged current neutrino interactions in the rock surrounding the detector and their data are consistent with the two-flavor neutrino oscillation $\nu_\mu \leftrightarrow \nu_\tau$. Super-Kamiokande also reported the observation of an oscillation signature with L/E dependence [26], which is well described by the hypothesis that ν_μ oscillates to ν_τ with a probability of the nearly maximal mixing.

Long-baseline experiments using the muon neutrino beam produced by accelerators, such as K2K [23] and MINOS [24] also confirmed the atmospheric neutrino oscillation by measuring the spectral distortion and the decreasing ν_μ flux during the travel. In the two-flavor mixing framework, the neutrino oscillation parameters are constrained to be :

$$\begin{aligned} & 1.9 \times 10^{-3} < \Delta m^2_{23} < 3.1 \times 10^{-3} eV^2, \\ & 0.92 < \sin^2 2\theta_{23} \end{aligned} \tag{1.17}$$

at $90\,\%$ C.L.. Figure 1.1 shows $90\,\%$ confidence level allowed parameter regions of the several experiments.

1.2.3 Constraint on the Mixing Angle θ_{13}

The atmospheric neutrino data have also been used to constrain θ_{13} in the three-flavor mixing framework with the one mass scale dominance approximation ($|m^2_2 - m^2_1| \ll |m^2_3 - m^2_2| \sim |m^2_3 - m^2_1|$). In this framework, oscillations of atmospheric ν_es are expressed by :

$$\mathrm{P}(\nu_e \to \nu_e) = 1 - \sin^2 2\theta_{13} \sin^2(\frac{1.27\Delta m^2 L}{E}), \tag{1.18}$$

$$\begin{aligned} \mathrm{P}(\nu_\mu \to \nu_e) &= \mathrm{P}(\nu_e \to \nu_\mu) \\ &= \sin^2\theta_{23} \sin^2 2\theta_{13} \sin^2(\frac{1.27\Delta m^2 L}{E}), \end{aligned} \tag{1.19}$$

So far, no evidence for the atmospheric ν_e oscillation has been observed and the mixing angle θ_{13} is consistent with zero as a result of the oscillation analysis using the atmospheric neutrino data. Non-zero θ_{13} has also been searched for by reactor neutrino experiments or accelerator neutrino experiments and their results are also consistent with zero-θ_{13}. The current upper limit on θ_{13} comes from the CHOOZ experiment [27]:

$$\sin^2 2\theta_{13} < 0.15 \tag{1.20}$$

at $90\,\%$ C.L.(assuming $\Delta m^2_{23} = 2.5 \times 10^{-3}\,\mathrm{eV}^2$).

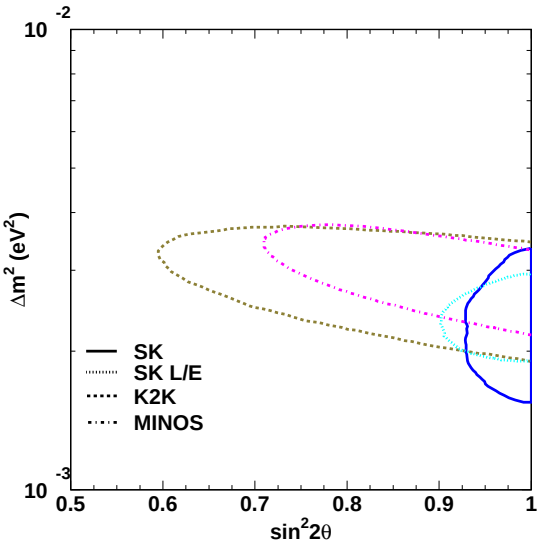

Figure 1.1: 90 % confidence level allowed regions of oscillation parameters for $\nu_\mu \leftrightarrow \nu_\tau$ oscillation. The horizontal axis shows $\sin^2 2\theta$ and the vertical axis shows Δm^2. The results are taken from Super-Kamiokande[25] (solid line), SK L/E [26] (dotted line), K2K experiment [23] (dashed line) and MINOS experiment[24] (dash-dotted line).

1.3 Sub-dominant Oscillation Effects driven by the Solar Terms

As described in the previous section, no evidence for the atmospheric ν_e oscillation induced by non-zero θ_{13} has been found. However, if the LMA-MSW oscillation parameters are taken into account, the oscillation of low energy atmospheric ν_es is expected to appear even in the case of θ_{13}=0.

If the transition probability from ν_e to ν_x ($x = \mu$ or τ) in matter driven by Δm^2_{12} is denoted by P_2, the oscillation probabilities of ν_e and ν_μ are expressed as [28, 29]:

$$\begin{aligned}
\mathrm{P}(\nu_e \to \nu_e) &= 1 - P_2, && (1.21)\\
\mathrm{P}(\nu_e \to \nu_\mu) &= \mathrm{P}(\nu_\mu \to \nu_e) = c^2_{23} P_2, && (1.22)\\
\mathrm{P}(\nu_\mu \to \nu_\mu) &= 1 - c^4_{23} P_2 - 2 s^2_{23} c^2_{23} \left(1 - \sqrt{1 - P_2}\cos\phi\right), && (1.23)\\
\phi &\sim \left(\Delta m^2_{31} + s^2_{12}\Delta m^2_{21}\right)\frac{L}{2E_\nu}. && (1.24)
\end{aligned}$$

Using these oscillation probabilities, the oscillated atmospheric electron and muon neutrino fluxes are expressed by :

$$\begin{aligned}
F^{osc}_e &= F^0_e \cdot \mathrm{P}(\nu_e \to \nu_e) + F^0_\mu \cdot \mathrm{P}(\nu_\mu \to \nu_e)\\
&= F^0_e \left(1 + P_2(r c^2_{23} - 1)\right), && (1.25)\\
F^{osc}_\mu &= F^0_e \cdot \mathrm{P}(\nu_e \to \nu_\mu) + F^0_\mu \cdot \mathrm{P}(\nu_\mu \to \nu_\mu)\\
&= F^0_\mu \left(1 - \frac{c^2_{23}}{r}(r c^2_{23} - 1) P_2 - \frac{1}{2}\sin^2 2\theta_{23}(1 - \sqrt{1 - P_2}\cos\phi)\right), && (1.26)
\end{aligned}$$

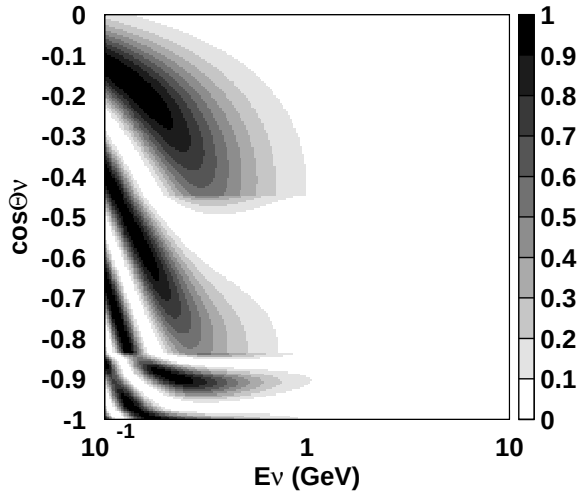

Figure 1.2: The calculated ν_e transition probability P_2 for atmospheric neutrinos with an energy E_ν (horizontal axis) and a direction of $\cos\Theta_\nu$ (vertical axis). The 1-2 oscillation parameters are assumed to be $\Delta m^2_{12} = 7.9 \times 10^{-5} eV^2$ and $\sin^2\theta_{12} = 0.31$. The Earth's matter effect is taken into account.

where F^0_e and F^0_μ are the atmospheric neutrino fluxes without oscillations. r is the ratio of the original muon and electron neutrino fluxes F^0_μ/F^0_e, which is ~ 2 for neutrinos in the low energy region.

Figure 1.2 shows the calculated P_2 for atmospheric neutrinos with an energy E_ν and a direction Θ_ν assuming $\Delta m^2_{12} = 7.9 \times 10^{-5} eV^2$ and $\sin^2\theta_{12} = 0.31$. Since the oscillation effect is larger in the lower energy region as shown in Figure 1.2, the Sub-GeV atmospheric neutrino events play an important role to observe the sub-dominant oscillation effect.

The atmospheric electron neutrino flux decreases by P_2, on the other hand, it increases by the muon neutrino oscillation (Equation (1.22)). As a result, the atmospheric electron neutrino flux changes by the effect of oscillations driven by the 1-2 parameters and the size of the oscillation effect depends on $\cos^2\theta_{23}$ as seen in Equation (1.25). Equation (1.25) can be rewritten as follows :

$$\frac{F^{osc}_e}{F^0_e} - 1 = P_2(r\cos^2\theta_{23} - 1). \tag{1.27}$$

Since the flavor ratio r is approximately 2 in the Sub-GeV neutrino energy region, in the case of $\cos^2\theta_{23} = 0.5$ (i.e. $\sin^2\theta_{23} = 0.5$, $\theta_{23} = 45°$), the increasing effect and the decreasing effect on the electron neutrino flux are expected to be canceled out. If $\cos^2\theta_{23} > 0.5$ (i.e. $\sin^2\theta_{23} < 0.5$, $\theta_{23} < 45°$), an excess of the Sub-GeV e-like sample is expected. If $\cos^2\theta_{23} < 0.5$ (i.e. $\sin^2\theta_{23} > 0.5$, $\theta_{23} > 45°$), the Sub-GeV e-like sample is expected to be reduced.

Therefore the atmospheric neutrino experiments have a possibility to determine the octant of θ_{23} for the non-maximal $\sin^2\theta_{23}$ using the effect due to the solar neutrino oscillation parameters. The information on the octant of θ_{23} cannot be obtained by the standard $\nu_\mu \leftrightarrow \nu_\tau$ two-flavor oscillation analysis because the oscillation probability depends on $\sin^2 2\theta_{23}$, not on $\sin^2\theta_{23}$ in that framework.

In this thesis, the precise oscillation analysis of the Super-Kamiokande atmospheric neutrino data considering the sub-dominant oscillation effect induced by the 1-2 parameters is described.

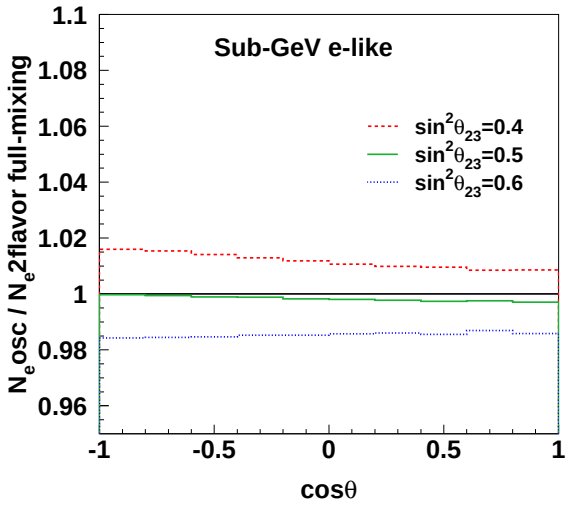

Figure 1.3: Zenith angle dependence of the ratio of the number of FC Sub-GeV single-ring e-like events including sub-dominant oscillations due to the 1-2 oscillations (N_e^{osc}) and with pure $\nu_\mu \leftrightarrow \nu_\tau$ two-flavor full-mixing oscillations ($N_e^{2flavorfull-mixing}$). For calculation of N_e^{osc}, $\Delta m^2_{12} = 7.9 \times 10^{-5} eV^2$, $\sin^2\theta_{12} = 0.31$, $\Delta m^2_{23} = 2.5 \times 10^{-3} eV^2$ and three different values of $\sin^2\theta_{23}$, $\sin^2\theta_{23} = 0.4$ (dashed line), 0.5 (solid line) and 0.6 (dotted line), are assumed. For calculation of $N_e^{2flavorfull-mixing}$, $\Delta m^2_{23} = 2.5 \times 10^{-3} eV^2$ and $\sin^2\theta_{23} = 0.5$ are assumed.

Figure 1.3 shows the zenith angle dependence of relative effect due to 1-2 oscillations on the number of FC Sub-GeV single-ring e-like events for different values of $\sin^2\theta_{23}$. Here "Sub-GeV" is defined to be less than 1.33 GeV in visible energy in a water Cherenkov detector. The 1-2 oscillation parameters are assumed as $\Delta m^2_{12} = 7.9 \times 10^{-5} eV^2$ and $\sin^2\theta_{12} = 0.31$. In the figure, the number of e-like events with sub-dominant 1-2 oscillations (N_e^{osc}) is normalized by the number of e-like events with pure $\nu_\mu \leftrightarrow \nu_\tau$ two-flavor full-mixing oscillations ($N_e^{2flavorfull-mixing}$). For $\sin^2\theta_{23} = 0.4$ (dashed line) and 0.6 (dotted line), the sub-dominant 1-2 oscillation effect appears as a $\sim$2 % excess and deficit of Sub-GeV e-like events, respectively. The sub-dominant 1-2 oscillation effect is expected to be larger in the lower energy region (see Figure 1.2).

Figure 1.4 shows the corresponding plot for Sub-GeV single-ring μ-like events. The sub-dominant 1-2 oscillation effect for the μ-like sample is smaller in size and opposite. This is understood from Equations (1.25) and (1.26).

However, due to the large uncertainty in the absolute neutrino flux ($\sim$20 %), it should not be possible to extract the 1-2 oscillation effect by comparing the total number of e-like (or μ-like) events of the data and Monte Carlo. On the other hand, we notice that the $(\nu_\mu + \overline{\nu}_\mu)/(\nu_e + \overline{\nu}_e)$ flux ratio is accurately predicted ($\sim$3 %). Furthermore, the sub-dominant 1-2 oscillation effect is opposite for e-like and μ-like as seen in Figures 1.3 and 1.4 . Therefore, by taking the μ-like/e-like ratio, one might be able to observe the 1-2 oscillation effect.

Figure 1.5 shows the zenith angle dependence of the ratio between the number of FC Sub-GeV single-ring μ-like events and the number of FC Sub-GeV single-ring e-like events. For upward-going events, the difference on the μ/e ratio between the $\sin^2\theta_{23} = 0.4$ and $\sin^2\theta_{23} = 0.6$ cases reaches about 5 %, which is comparable to the size of the estimated systematic error on the μ/e ratio measurement.

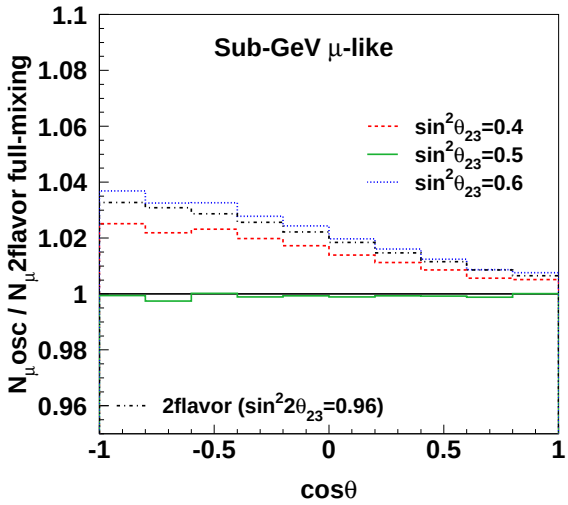

Figure 1.4: Zenith angle dependence of the ratio of the number of FC Sub-GeV single-ring e-like events including sub-dominant oscillations due to the 1-2 oscillations (N_μ^{osc}) and with pure $\nu_\mu \leftrightarrow \nu_\tau$ two-flavor full-mixing oscillations ($N_\mu^{2flavorfull-mixing}$). For the dash-dotted line, the numerator is the number of μ-like events in the case of pure $\nu_\mu \leftrightarrow \nu_\tau$ two-flavor oscillations with $\sin^2 2\theta_{23} = 0.96$, which corresponds to $\sin^2\theta_{23} = 0.4$ or $\sin^2\theta_{23} = 0.6$. The other line definitions are same as Figure 1.3.

Figure 1.5 suggests that the observation of the 1-2 oscillation effect might be possible, if we control the N_μ/N_e ratio accurately. Therefore, in this thesis, we discuss the systematic error in the $(\nu_\mu + \overline{\nu}_\mu)/(\nu_e + \overline{\nu}_e)$ flux ratio carefully.

Experimentally, the fraction of charged-current quasi-elastic (CCQE) events in the standard Sub-GeV single-ring e-like (μ-like) sample in Super-Kamiokande is about 71 % (74 %). The remaining events are due to charged-current non-quasi-elastic (CC non-QE) events and neutral-current (NC) events. However, the understanding of the details of the cross-section and the kinematics are rather poor. Therefore, in this thesis, we try to improve the purity of the events by eliminating CC non-QE and NC events by several methods. Figure 1.6 compares the sensitivity of this experiment based on the standard Super-K event samples [25] and the special event samples which the CC non-QE and NC events are reduced. It is clear that the sensitivity in the octant of θ_{23} due to the 1-2 oscillation effect is improved by this work.

In this thesis, details of the improvements in the analysis of the 1-2 oscillation effect together with the related systematic errors are described. Finally the results from this work using the Super-K-I and II data are described.

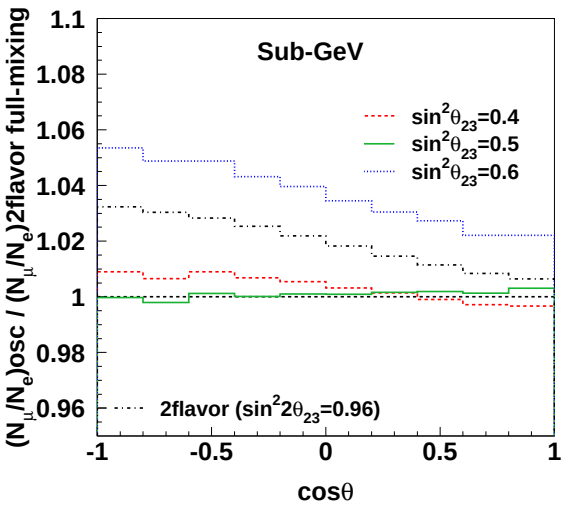

Figure 1.5: Zenith angle dependence of the N_μ/N_e ratio for FC Sub-GeV single-ring events including sub-dominant oscillations due to the 1-2 oscillations normalized by the N_μ/N_e with pure $\nu_\mu \leftrightarrow \nu_\tau$ two-flavor full-mixing oscillations. The line definitions are same as Figure 1.4.

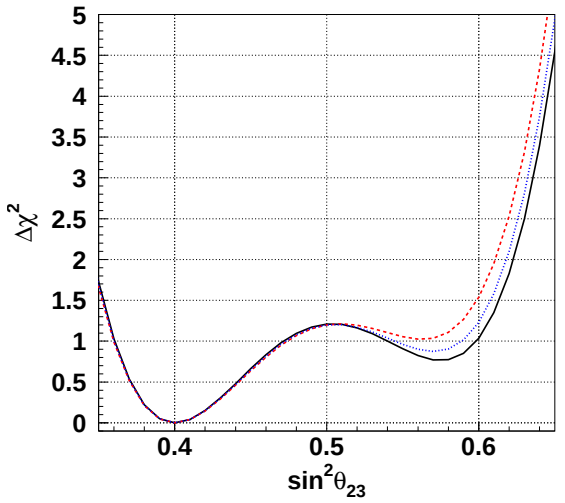

Figure 1.6: χ^2-χ^2_{min} distribution as a function of $\sin^2\theta_{23}$ using the oscillated Monte Carlo events of a 6 year exposure with the true oscillation parameters of $\theta_{13} = 0$, $\sin^2\theta_{12} = 0.32$, $\Delta m^2_{12} = 7.8\times10^{-5}$ eV^2, $\Delta m^2_{23} = 2.5\times10^{-3}$ eV^2 and $\sin^2\theta_{23} = 0.4$. Details of the definition of χ^2 will be described in Section 7.2. The solid line shows the sensitivity based on the standard Super-K event samples, the dotted (blue) line based on the event samples which are reduced the CC non-QE and NC interactions to half and the dashed (red) line based on the event samples where all the CC non-QE and NC interactions are eliminated.

Chapter 2

The Super-Kamiokande Detector

Super-Kamiokande is a cylindrical 50 kt water Cherenkov detector located at Kamioka Observatory in Gifu Prefecture, Japan. The geographic coordinates of the site are 36°25'N and 137°18'E, and the altitude above sea level is 370 m. The detector lies in a zinc mine under the peak of Mt.Ikenoyama, where the mean rock overburden is $\sim$ 1000 m (2700 m water equivalent). This overburden serves as a shield against cosmic ray muon background. The cosmic ray muon flux at the Super-Kamiokande site is reduced by 5 orders of magnitude compared to that on the surface of the earth.

The main scientific purposes of the Super-Kamiokande experiment are the searches for nucleon decays and the studies of various types of neutrinos: atmospheric neutrinos, solar neutrinos, and the neutrinos from supernovae and the other astrophysical sources. The Super-Kamiokande detector is also used as a target of the artificial neutrino beam in long-baseline neutrino oscillation experiments. The Super-Kamiokande experiment started taking data in April, 1996 and continued the observation for five years within the running period referred to SK-I till the detector maintenance in July, 2001. During refilling water after the maintenance, an accident occurred in November, 2001 in which more than a half of the PMTs were destroyed. The Super-Kamiokande detector was rebuilt after the accident with the half of the original PMT density in the inner detector and resumed observation from October, 2002, which is referred to the SK-II running period. The SK-II continued the physics measurement for three years and finished in October 2005 for the reconstruction work to put the PMT density back to the SK-I level. The Super-Kamiokande detector has restarted observation in June, 2006.

In this thesis, the data observed in the SK-I (1996-2001) and the SK-II running periods (2002-2005) are used.

2.1 Cherenkov Radiation

The Super-Kamiokande detector observes relativistic charged particles in water by detecting the emitted Cherenkov light. The Cherenkov photons are radiated when the velocity of a charged particle exceeds the light velocity in the medium :

$$v \geq \frac{c}{n}, \tag{2.1}$$

where v is the velocity of the charged particle, n is the refractive index of the medium and c is the light velocity in vacuum [30]. The momentum threshold of Cherenkov radiation is determined

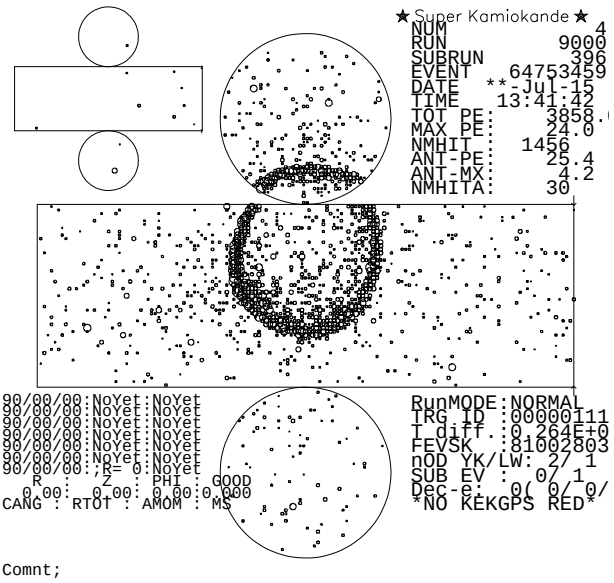

Figure 2.1: A typical observed neutrino event in Super-Kamiokande. The size of small circles in the unrolled cylinder represents the amount of Cherenkov photons detected in each photomultiplier tube. The Cherenkov ring image is clearly visible.

by the refractive index of the medium and the mass of the particle. Since the refractive index of water is about 1.34, the momentum thresholds of Cherenkov radiation for electrons, muons and charged pions are 0.57, 118 and 156 MeV/c, respectively.

Cherenkov light is emitted on a cone with a characteristic half opening angle θ_C along the direction of the particle. The opening angle, called Cherenkov angle, is determined as follows :

$$\cos\theta_C = \frac{1}{n\beta}, \tag{2.2}$$

where $\beta = v/c$. For the particle with $\beta \simeq 1$ in water, the Cherenkov angle is about 42°.

The number of photons emitted by Cherenkov radiation is given as a function of the wavelength λ as follows :

$$\frac{d^2N}{dxd\lambda} = \frac{2\pi\alpha}{\lambda^2}\left(1 - \frac{1}{n^2\beta^2}\right), \tag{2.3}$$

where x is the path length of the charged particle and α is the fine structure constant. About 340 photons/cm are emitted between the wavelength of 300 nm to 600 nm, which is the sensitive wavelength region of the PMTs used in the Super-Kamiokande detector.

Particles emitting Cherenkov light project ring images on the wall inside the detector. Super-Kamiokande detects the Cherenkov photons by the PMTs arranged on the wall and the Cherenkov rings can be recognized. Figure 2.1 shows a visual display of a typical neutrino event in the Super-Kamiokande detector.

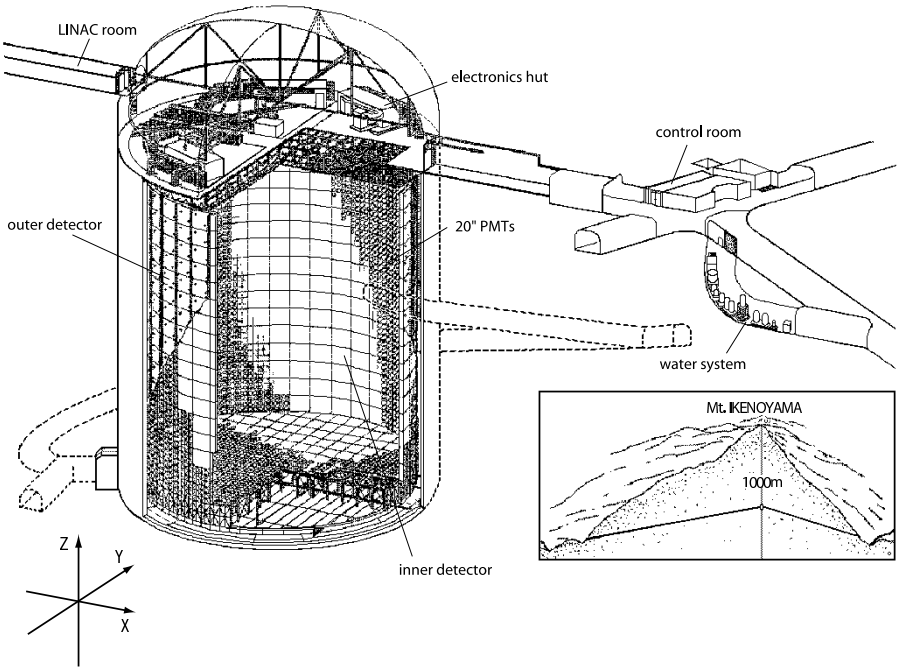

Figure 2.2: Super-Kamiokande detector and its location.

2.2 Detector

2.2.1 Water Tank

A schematic view of the detector is shown in Figure 2.2. The whole size of the water tank is 41.4 m in the hight and 39.3 m in the diameter, in which 50 kt highly pure water is filled. The water tank is optically separated into two concentric cylindrical regions by a PMT support structure and a pair of opaque sheets as shown in Figure 2.3.

The inner region, this part of the detector is referred to the inner detector (ID), contains 32 kt water with the size of 36.2 m in the hight and 33.8 m in the diameter. 11,146 inward-facing 20-inch PMTs are attached to the supporting frame uniformly at intervals of 70 cm for SK-I. The effective photocathode coverage of the ID is about 40 %, and the rest of the surface is covered with black polyethylene terephthalate sheet, called "black sheet". For SK-II, 5,182 20-inch PMTs are attached at one intervals to the supporting frame and the photocathode coverage of the ID is about 20 %.

The outer region completely surrounds the ID with the thickness of 2.05 m on top and bottom and 2.2 m along the barrel wall. This region, called the outer detector (OD), is monitored by 1,885 outward-facing 8-inch PMTs attached to the outer side of the supporting frame. To improve the light collection efficiency, each PMT in the OD is attached to a 60 cm $\times$ 60 cm wavelength shifting plate, and the walls are covered with reflective material called "tyvek sheet". The OD is used to veto entering cosmic ray muons and to tag the outgoing charged particles. Furthermore, the 2 m thickness water layer itself serves as a shield to attenuate gamma ray and neutron fluxes from the rock.

The inner and outer volumes are separated by a 55 cm thick dead region. This region is not

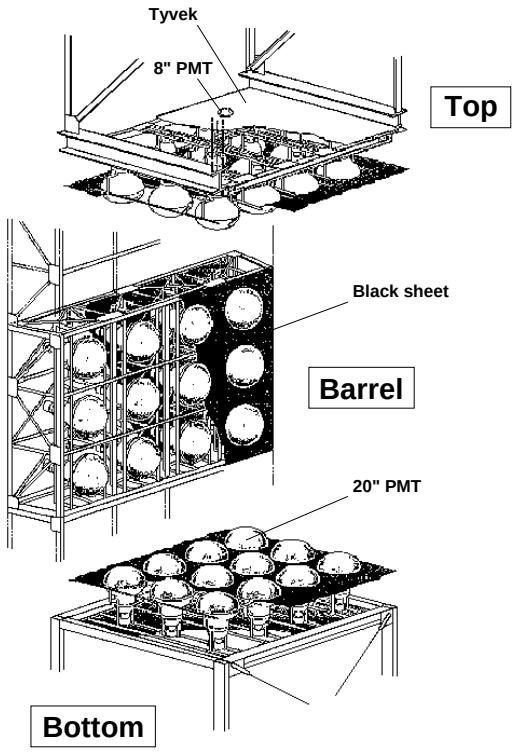

Figure 2.3: Supporting frame of PMTs.

instrumented with any PMT. Stainless steel frames and signal and HV cables of the ID and OD PMTs are contained in this dead region.

2.2.2 Inner detector photomultiplier tube

The photomultiplier tubes used in the ID, product name Hamamatsu R3600, have photocathode with a diameter of 50 cm (20 inch). This 20 inch PMT was originally developed by Hamamatsu Photonics K.K. in cooperation with the Kamiokande collaborators [31]. Later, the dynode structure and the bleeder circuit were modified for Super-Kamiokande to improve timing response and photon collection efficiency [32]. A schematic view of the PMT is shown in Figure 2.4 and the specifications are summarized in Table 2.1.

The photocathode of the PMT is coated by bialkali (Sb-K-Cs) owing to the high spectral sensitivity to Cherenkov light and the low thermionic emission. The quantum efficiency of the PMT together with the Cherenkov spectrum is shown in Figure 2.5, in which the peak is 22 % at 360-400 nm (Figure 2.6). The dynode structure and the bleeder circuit are optimized to achieve high collection efficiency, fast timing response and good energy resolution. The averaged value of the collection efficiency at the first dynode is 70 %, which is uniform within a difference of ± 7 % everywhere on the photocathode. The gain of the ID PMTs is 10^7 at a supply high voltage from 1500 V to 2000 V. Figure 2.7 shows the charge distribution for the single photoelectron signal in which a clear 1 p.e. peak can be seen. The transit time spread of the single photoelectron signal is about 2.2 nsec. The average dark noise rate at the 0.25 p.e.s threshold used in Super-Kamiokande is about 3 kHz.

The magnetic field over 100 mG affects photoelectron trajectories in the PMT and makes the timing resolution worse, while geomagnetic field at the detector site is about 450 mG. To compensate for the magnetic field, 26 sets of horizontal and vertical Helmholtz coils are arranged around the tank. As the result, the magnetic field inside the detector is reduced to about 50 mG.

On November 12th, 2001 while refilling the SK tank after completing the upgrade work, one ID PMT on the bottom of the tank imploded, which triggered a cascade of implosions. About 60 % of the ID and OD PMTs were destroyed. To avoid a chain reaction of implosion, all of the inner PMTs are instrumented with acrylic covers in SK-II. A clear 12 mm thick UV-transparent acrylic dome is put over the photo-cathode area of each PMT and the side of the PMT is protected by the fiberglass shield with holes, which let water flow into the case freely as shown in Figure 2.8. Figure 2.9 shows the transparency of the acrylic cover for photons with normal incidence in water, which is mode than 96 % above 350 nm of wavelength and the effect of the PMT case is small. 11,146 and 5,182 PMTs are used in SK-I and SK-II, respectively.

2.2.3 Outer detector photomultiplier tube

1,885 8-inch PMTs, Hamamatsu R1408, are used in the OD. For SK-I, the OD PMTs were reused from the IMB experiment [33] after finishing that experiment. The photocathode of the OD PMT is fitted with 60 cm $\times$ 60 cm $\times$ 1.3 cm wavelength shifter plate. The wavelength shifter increases the light collection efficiency by 60 %. The timing resolution at single photoelectron is about 13 nsec without the wavelength shifter and about 15 nsec with the plate. However, since the OD is used as a veto counter, rather than a particle traceker, The extra photons are of importande while the poor timing resolution is of little consequence.

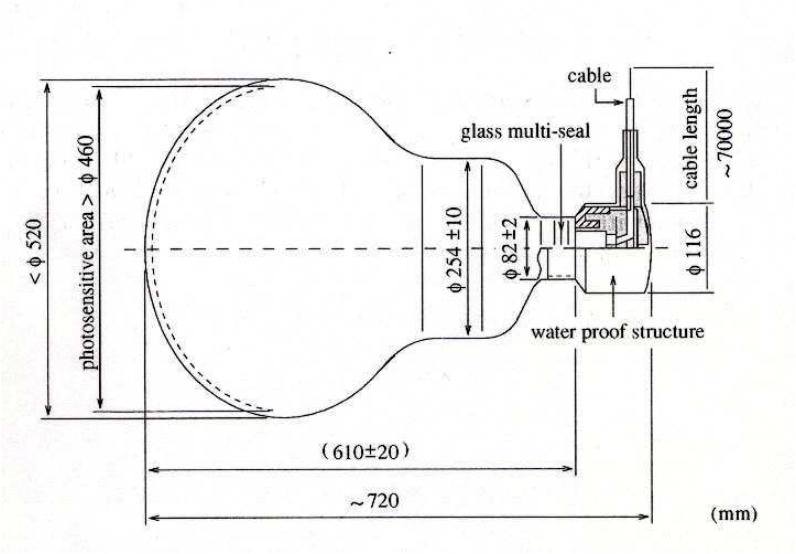

Figure 2.4: A schematic view of a 20-inch PMT.

Shape	Hemispherical
Photocathode area	50 cm diameter
Window material	Pyrex glass ($4 \sim 5$ mm)
Photocathode material	Bialkali (Sb-K-Cs)
Quantum efficiency	22 % at $\lambda = 390$ nm
Dynodes	11 stage Venetian blind type
Gain	10^7 at ~ 2000 V
Dark current	200 nA at 10^7 gain
Dark pulse rate	3 kHz at 10^7 gain
Cathode non-uniformity	< 10 %
Anode non-uniformity	< 40 %
Transit time	90 nsec at 10^7 gain
Transit time spread	2.2 nsec ($1\,\sigma$) for 1 p.e. equivalent signals
Weight	13 kg
Pressure tolerance	6 kg/cm^2 water proof

Table 2.1: Specifications of 20-inch PMT.

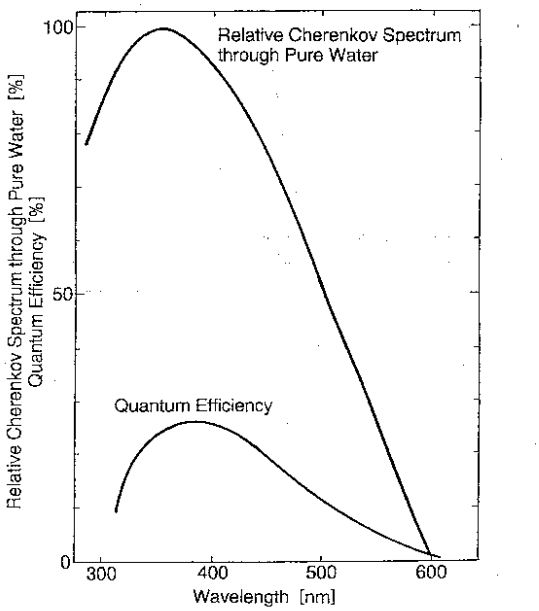

Figure 2.5: The spectrum shape of Cherenkov light through pure water and the quantum efficiency of 20-inch PMT as a function of wavelength.

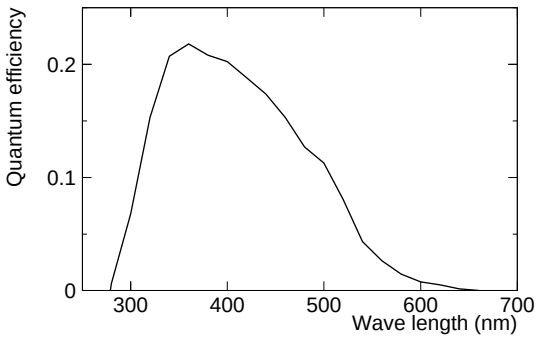

Figure 2.6: the quantum efficiency of ID 20-inch PMT as a function of wavelength.

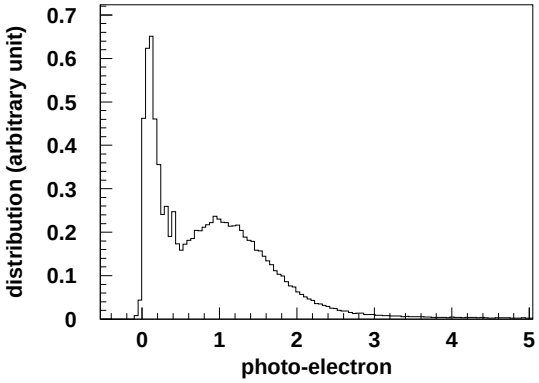

Figure 2.7: Single photoelectron distribution of a typical 20-inch PMT.

Figure 2.8: PMT case attached to the inner PMT after SK-II experiment

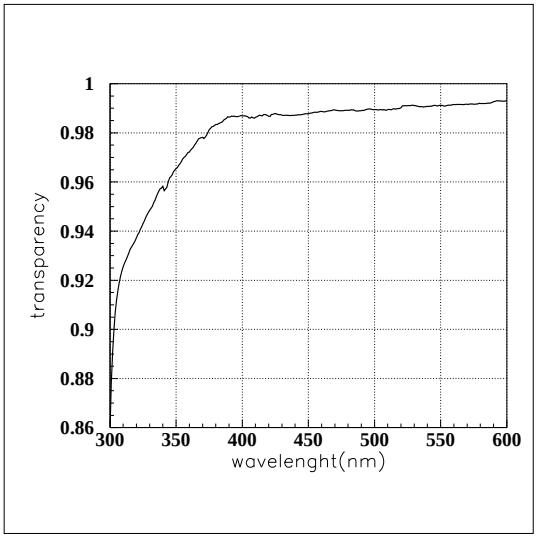

Figure 2.9: The transparancy of the acylic case as a function of wavelength

2.3 Water Purification System

The water for the Super-Kamiokande experiment is produced from abundant spring water in the mine. The water in the tank is continuously circulated through the water purification system to keep the high attenuation length. It is also an important purpose of this system to remove the radioactive materials, especially radon (Rn), which is a background source for the solar neutrino observation in the MeV energy range. The water is constantly circulated through the purification system with flow rate of about 35 ton/hour. The outline of the system is shown in Figure 2.10. The system consists of the following components.

- 1 μm mesh filter — removes dust and small particles which reduce the water transparency.
- Heat exchanger — cools water to suppress the growth of bacteria. The water temperature in the detector is kept at 14 °C.
- Cartridge polisher — eliminates ions which also reduce water transparency.
- Ultra-Violet sterilizer — kills bacteria.
- Radon-reduced air dissolving tank — dissolves radon-reduced air into the water to increase radon removal efficiency at the vacuum degasifier stage which follows.
- Reverse osmosis filter — removes particulates.
- Vacuum degasifier — removes dissolved gases in water, such as the oxygen and radon.
- Ultra filter — removes minute particles of the order of 10 nm.
- Membrane degasifier — removes radon dissolved in water.

The typical number of particles larger than 0.2 μm is reduced to 6 particles/cc and the light attenuation length is achiedved to be $\sim$100 m after purification. The resistivity of the water entering the purification system from the detector is about 11 MΩ·cm. After the purification, the water has an average resistivity of 18.20 MΩ·cm, approching the chemical limit.

2.4 Radon Hut and Air Purification System

It is also essential to have clean air in the detector and the experimental area to minimize the radon level in the detector water. The radon concentration of the mine air in the access tunnel to the experimental site has a strong seasonal variation of 2,000 $\sim$ 3,000 Bq/m^3 during summer and 100 $\sim$ 300 Bq/m^3 during winter as shown in Figure 2.11. This is caused by the seasonal variation of the air flow inside the mine.

Fresh air from outside the mine is continuously pumped into the SK dome area at the rate of 10 m^3/minute through an air duct along the 1.8 km Atotsu access tunnel to the SK experimental area. As a result, the typical radon concentration in the SK dome air is 20 $\sim$ 30 mBq/m^3.

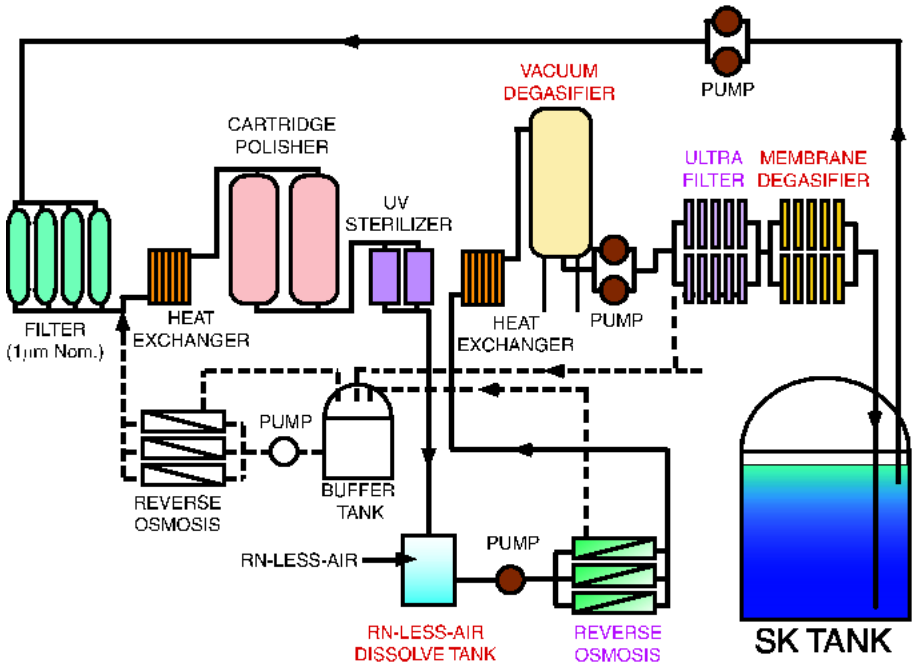

Figure 2.10: The water purification system for Super-Kamiokande.

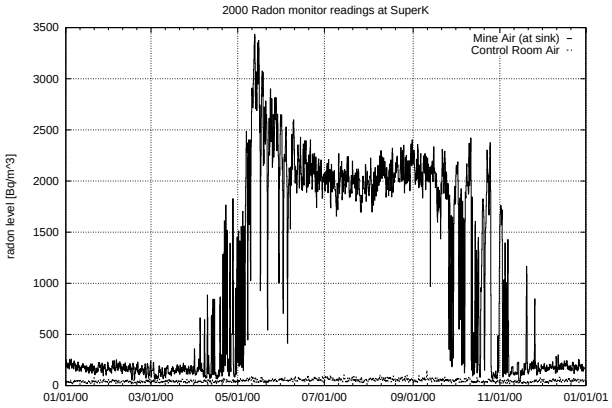

Figure 2.11: The upper histogram (solid curve) shows the measured radon concentration levels in the mine air [34]. The lower histogram (dashed curve) shows the corresponding radon levels in the SK dome.

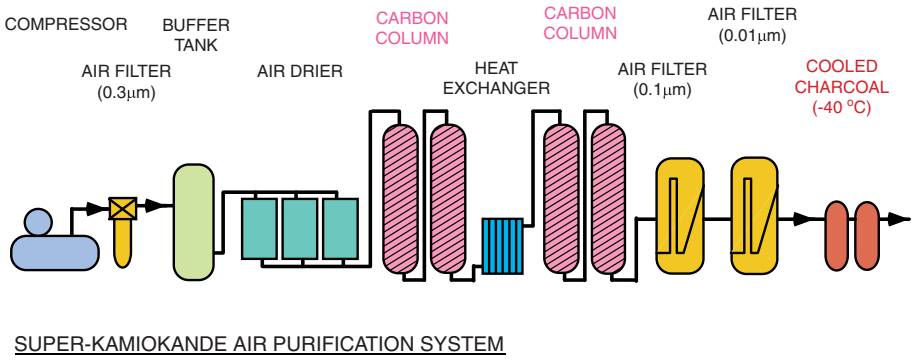

Figure 2.12: A schematic view of the radon-reducing air system.

Furthermore, to keep the radon level inside the detector absolute minimum, radon-free air is produced by the air purification system in the mine and is continuously pumped into the space above the water surface inside the tank at a positive pressure to prevent radon in the SK dorm air from entering the detector and dissolving into the purified water [35]. A schematic view of the air purification system is shown in Figure 2.12. The radon concentration of the radon-free air is less than $3\,\mathrm{mBq/m^3}$. The air purification system consists of compressors, a buffer tank, driers, and the filters. The air flow rate is about $18\,\mathrm{m^3/hour}$. The process of the air purification system is described as follows:

- **Compressor:**
  Compresses air to $7 \sim 8.5$ atmospheric pressure.
- **Air Filter:**
  Removes dusts in sizes of $\sim 0.3\,\mu$m.
- **Buffer Tank:**
  Stores the air.
- **Air Drier:**
  Dries the air and removes CO_2 gas to improve the radon removal capability in Carbon Columns.
- **Carbon Columns:**
  Removes radon gas using activated charcoal.
- **Air Filter:**
  Further Removes small dust and particles of $\sim 0.01\,\mu$m.
- **Cooled Charcoal Columns:**
  Further removes the remaining radon gas with the charcoal cooled down to –40°C.

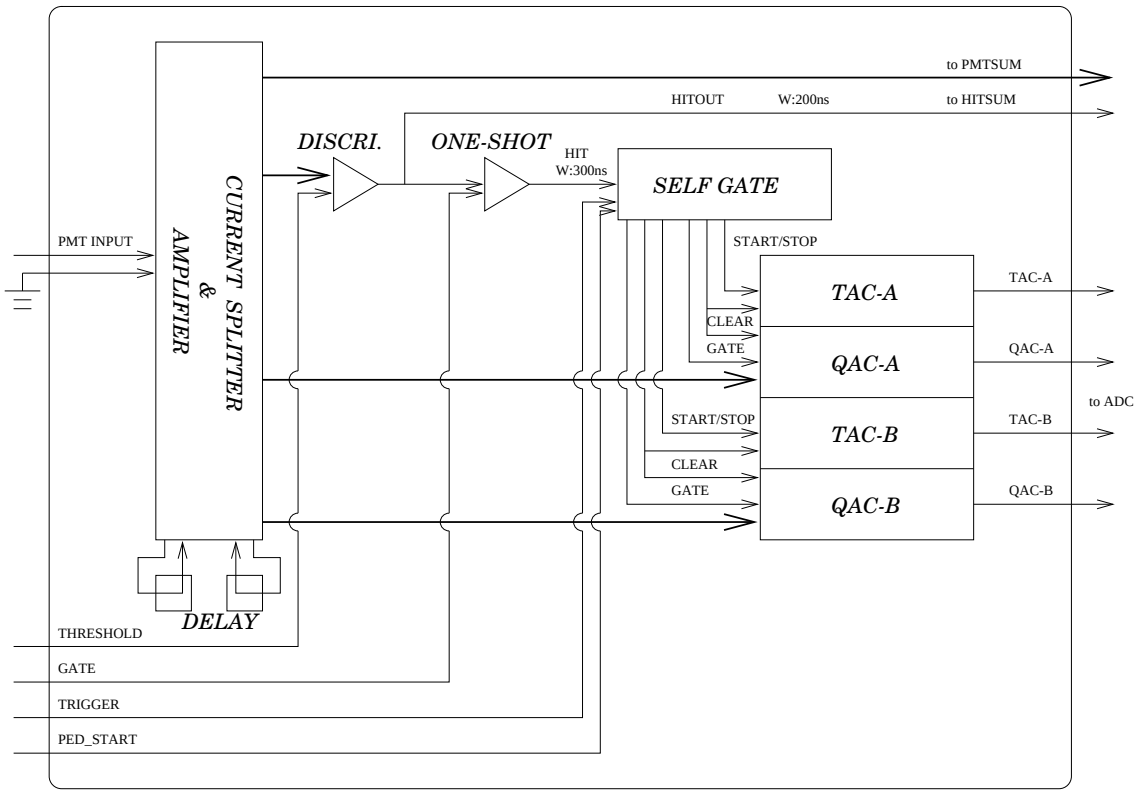

Figure 2.13: A block diagram of analog input part of ATM.

2.5 Electronics and Data Acquisition System

2.5.1 Inner detector electronics and data acquisition

ID PMT signals are processed by custom built electronics modules called ATM (Analog-Timing-Module) of the TKO standard (TRISTAN KEK Online) [36, 37]. The ATM module records the integrated charge and the arrival timing information of each PMT signal.

Figure 2.13 shows the block diagram of the analog input part of the ATM module. Each PMT input channel of ATM has two switching pairs of QAC (Charge to Analog Converter) and TAC (Time to Analog Converter) to minimize the electronics dead time in the data taking for two successive events, such as a muon followed by its decay electron. Each PMT signal sent to ATM is amplified 100 times, and then divided into four signals. One of them is sent to the discriminator. When the pulse height of the PMT signal exceeds the threshold level, which is set to 0.25 p.e.s , a 400 nsec gate signal for QAC and a start signal for TAC are generated. At the same time, rectangular signal called HITSUM(200 ns width and 15 mV pulse hight) is sent to a global trigger module. Other two branches of the splitted PMT signal are fed to QAC. If a global trigger is issued, a stop signal is sent to TAC and the information in QAC and TAC is digitized by ADC. The digitized charge and timing information is stored in internal FIFO memory in ATM. If a global trigger is not issued within 1.3 μsec, all the information in QAC and TAC is cleared. ATM has 450 pC dynamic range with a resolution of 0.2 pC, and 1.3 μsec

dynamic range with a resolution of 0.4 nsec. The remaining one signal becomes an output signal of ATM called PMTSUM.

Figure 2.14 shows a schematic view of the ID data acquisition system. Signals from 12 PMTs are fed to an ATM board to be processed. There are in total 946 ATM boards installed in 48 TKO crates. The digitized data in ATM FIFO memory are sent to VME memory modules called SMP (Super Memory Partner) every 16 events. 48 SMP are installed in 8 VME crates, and one SMP module handles the data of 20 ATMs. The data in SMP memories are read out by 8 slave computers and sent to the online host computer.

2.5.2 Outer detector electronics and data acquisition

Figure 2.15 shows a schematic view of the OD data acquisition system [38]. The paddle cards distribute high voltage from the main frame to the OD PMTs. A coaxial cable is used to supply the high voltage to an OD PMT and to send a signal from the PMT. These cards also pick off the PMT signals through a high voltage capacitor. Signals from the OD PMTs are sent to QTC (Charge to Time Converter) modules. A QTC module converts the PMT signal to a rectangular pulse whose width is proportional to the input charge. At the same time, a rectangular HITSUM signal is generated by QTC and sent to a global trigger module. The threshold of QTC modules is set to 0.25 p.e.. If a global trigger is received, the leading edge and the width of the rectangular pulse are converted to the timing and charge information by a LeCroy 1877 multi-hit TDC module. TDC module can record up to 8 QTC pulses with a resolution of 0.5 nsec. The dynamic range is set to 16 μsec which starts from 10 μsec before the global trigger timing. The digitized data stored in TDC are read by a slave computer through VME memory module called DPM (Dual Port Memory) and then sent to the online host computer.

2.5.3 Trigger

Figure 2.16 shows a overview of the ID trigger scheme. An ATM module generates a rectangular HITSUM signal with 15 mV in pulse height and 200 nsec in width if an ID PMT signal exceeds the threshold. These signals are analog-summed over all PMTs to generate an ID-HITSUM signal. The pulse height of the ID-HITSUM signal is proportional to the number of hit PMTs within 200 nsec time window. There are three types of trigger signals derived from the ID-HITSUM signal. In SK-I, the high energy (HE) trigger is generated when the pulse hight of ID-HITSUM signal exceeds a threshold of -340 mV, which corresponds to 31 hits within a 200 nsec time window. The threshold for the low energy (LE) trigger is set to -320 mV, which corresponds to 29 hits. This is equivalent to a signal expected from a 5.7 MeV electron assuming 50 % of trigger efficiency . The trigger rates for HE and LE triggers are ~ 5 Hz and ~ 11 Hz, respectively. The super low energy (SLE) trigger was implemented in May 1997 in order to lower the solar neutrino analysis threshold. The threshold is set to 4.6 MeV equivalent. The SLE triggered events are not used in atmospheric neutrino analysis. In SK-II, the same trigger scheme with the different thresholds is used. The threshold energies for the SK-II HE and LE triggers are 10 MeV and 8 MeV, respectively.

The OD trigger is generated by a similar procedure. When an OD PMT signal exceeds a threshold, a QTC module generates a rectangular pulse with 20 mV in height and 200 nsec in width. These signals are also analog summed up to generate an OD-HITSUM signal. The threshold for the OD trigger is set to 19 hits within a 200 nsec time window.

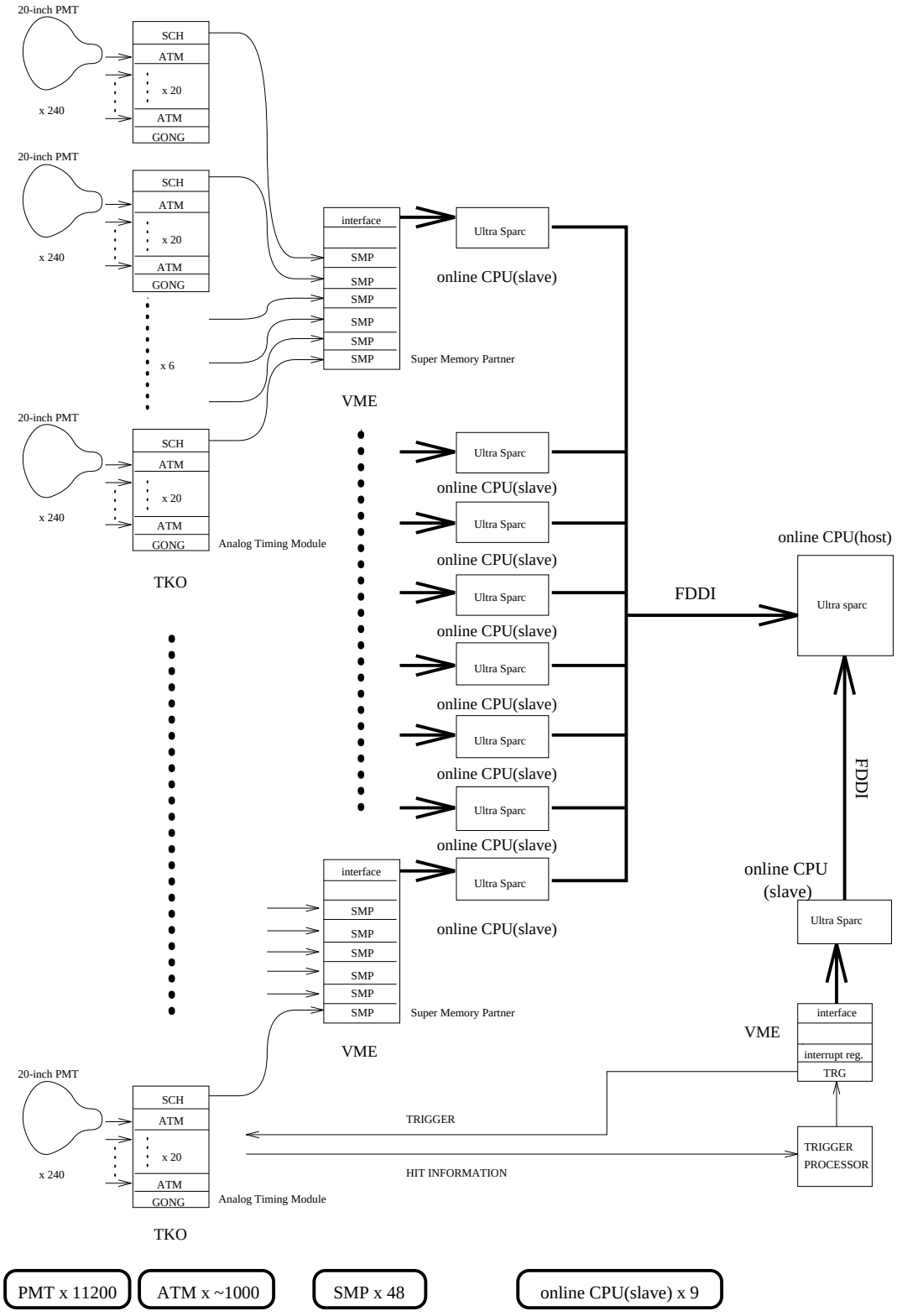

Figure 2.14: A schematic view of the inner detector data acquisition system.

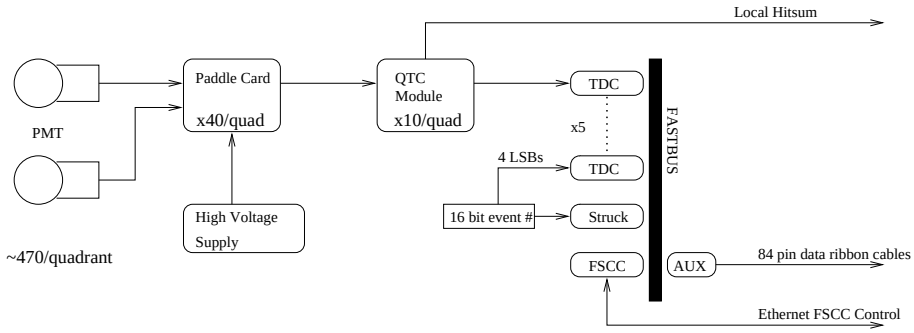

Figure 2.15: A schematic view of the outer detector data acquisition system.

These four types of trigger signals (HE, LE, SLE and OD) are fed to a hardware trigger module called TRG. The TRG module generates a global trigger signal when any one of the trigger signals is issued.

2.6 Calibration

2.6.1 Relative Gain Calibration

The high voltage value of each PMT is set to provide approximately uniform gain for all PMTs in the detector. The uniformity of the PMT gain is necessary to determine the momentum without systematic difference depending on its vertex position or direction.

Figure 2.17 shows a schematic view of the relative gain calibration system. Light generated by a Xe lamp is passed through an ultraviolet (UV) filter and neutral density (ND) filter and then split into four. One is injected into a scintillator ball via an optical fiber. The others are used to monitor the intensity of the Xe light and to make a calibration trigger. The scintillator ball is made of acrylic resin mixed with BBOT wavelength shifter and MgO powder diffuser. BBOT wavelength shifter absorbs UV light and emits light with a peak at 440 nm, which is a typical wavelength of Cherenkov light.

The high voltage value of each PMT is adjusted to give the same gain with the others. The relative gain G_i of the i-th PMT is obtained by :

$$G_i = \frac{Q_i}{Q_0 f(\theta)} \cdot l_i^2 \cdot \exp\left(\frac{l_i}{L}\right) \tag{2.4}$$

where Q_i is the charge detected by the i-th PMT, l_i is the distance from the light source to the PMT, $f(\theta)$ is the PMT acceptance as a function of the photon incidence angle θ, L is the attenuation length and Q_0 is the normalization factor. This measurement is performed for several positions of the scintillator ball, changing the voltage.

Figure 2.18 shows the relative gain distribution of all the PMTs after adjusting high voltage values. The relative gain spread is about 7 %. The remaining gain difference is corrected in software.

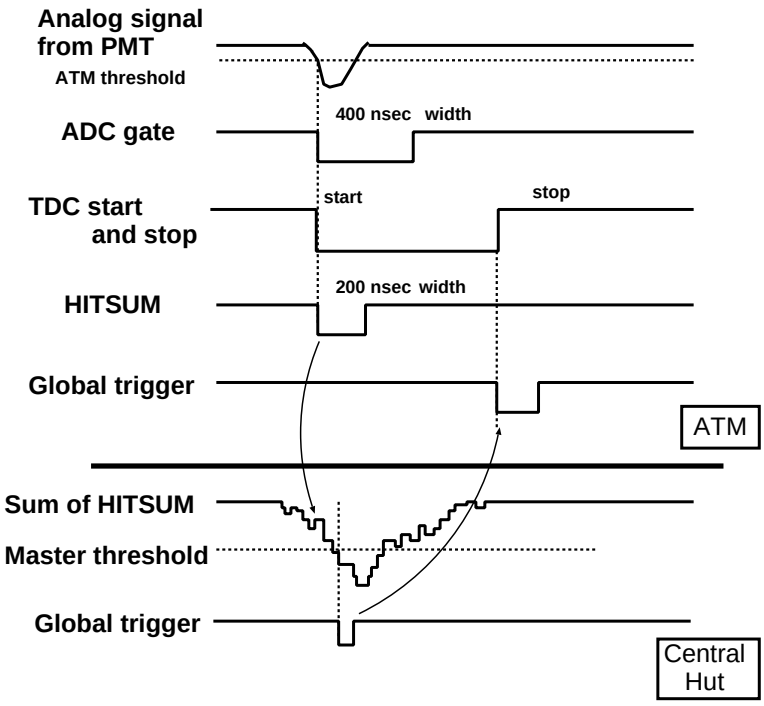

Figure 2.16: An overview of the ID trigger scheme.

2.6.2 Absolute Gain Calibration

The absolute gain calibration is necessary to convert the charge detected by each PMT in pico Coulomb (pC) into the number of photoelectrons. The absolute gain is determined using the charge distribution of single photoelectron signals.

The low energy gamma ray generated from neutron capture on Nickel nucleus is used as a calibration source to measure the single photoelectron distributions. The schematic view of the Nickel calibration source is shown in Figure 2.19. Neutrons produced by spontaneous fission of ^{252}Cf are captured on surrounding Ni wires in polyethylene vessel, and low energy ($6 \sim 9$ MeV) gamma rays are generated simultaneously. The number of hit PMT is about $50 \sim 80$ in total, so that the number of p.e. detected by each PMT is at most one. The charge distribution of a typical PMT is also shown in Figure 2.19. The sharp peak near zero is caused by electrons that are emitted from the photocathode but miss the first dynode, and the peak around 2 pC corresponds to that of single photoelectrons. The mean value 2.055 pC is used as a constant to convert the PMT charge from pico Coulomb to the number of p.e.s .

2.6.3 Relative Timing Calibration

The relative timing calibration is important for the vertex position reconstruction. The timing response of the PMT depends on not only the length of the signal cable but also the detected charge because of the slewing effect of discriminator. The large signal tends to exceed the threshold earlier than the small one.

Figure 2.20 shows the schematic view of the relative timing calibration system. N_2 laser gen-

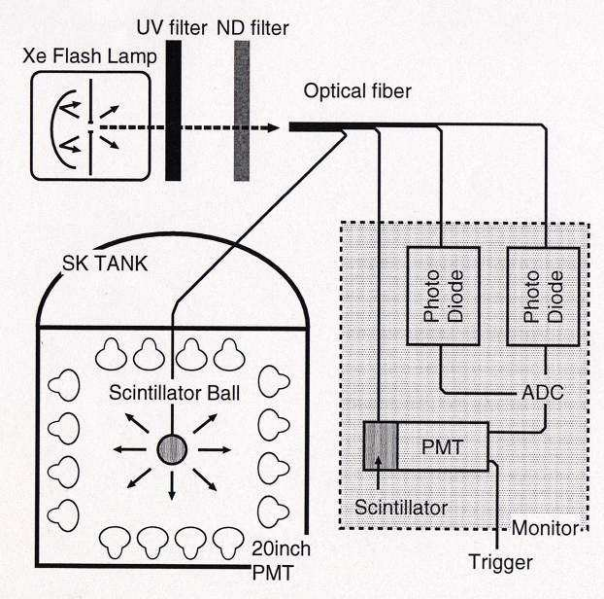

Figure 2.17: A schematic view of the relative gain measurement system using a Xe lamp.

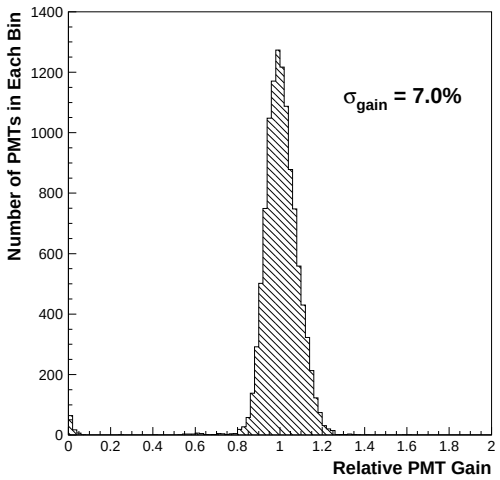

Figure 2.18: The relative gain distribution of all the ID PMTs, measured in 1996.

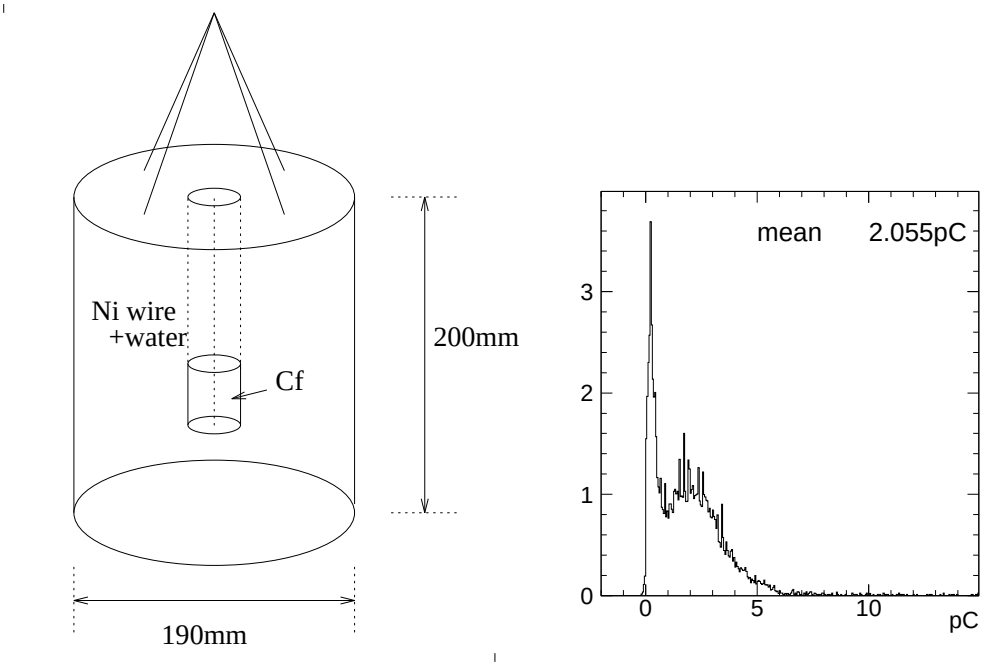

Figure 2.19: Schematic view of an Nickel calibration source (left) and charge distribution of a typical ID PMT (right).

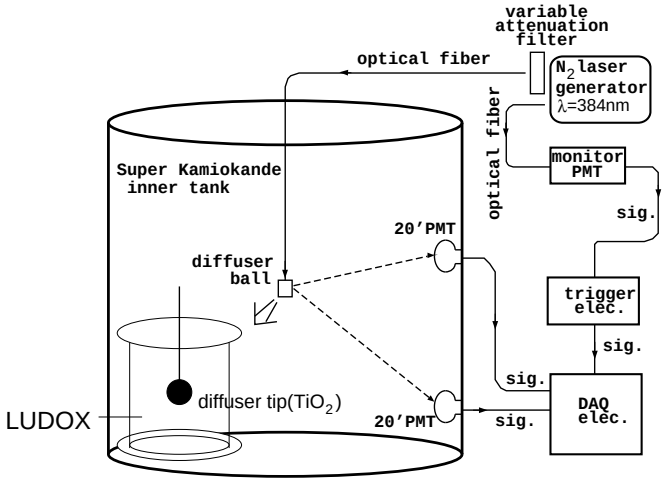

Figure 2.20: A schematic view of the timing measurement system using a laser.

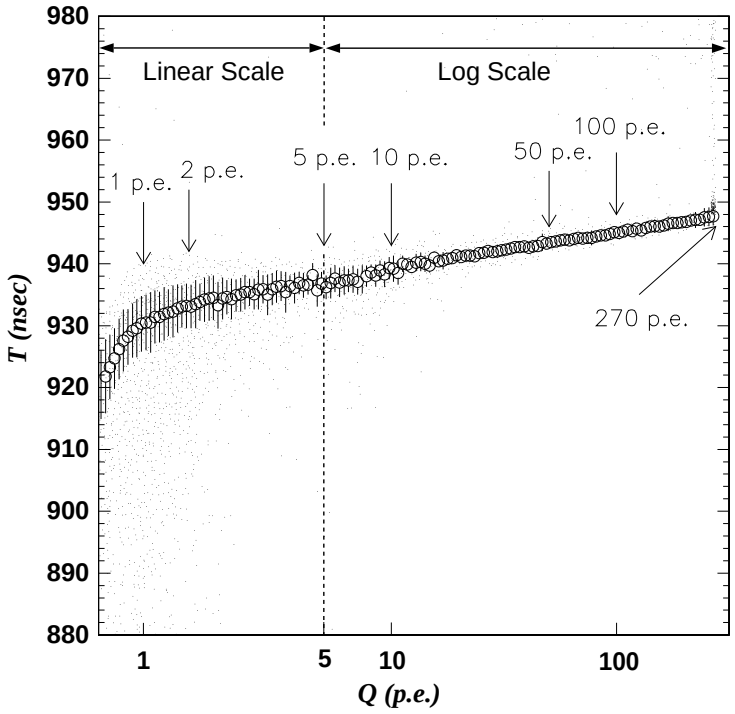

Figure 2.21: TQ-map, a measured two-dimensional plot of timing vs. charge distribution.

erator emits intense light with 337 nm wavelength within a time width of 3 nsec. The wavelength of the laser light is converted to 384 nm by a dye laser module. The PMT is most sensitive to this wavelength. Then the light is split into two. One is injected into a diffuser ball in the ID via an optical fiber and the other is used to monitor the light intensity. The schematic view of the diffuser ball is also shown in Figure 2.20. The laser light injected to the diffuser ball is first diffused by a TiO_2 diffuser tip at the center and then further diffused by the surrounding LUDOX silica gel made of 20 nm glass fragments. The PMT timing response is measured with various light intensity from 1 p.e. to a few hundreds of p.e. using an adjustable attenuation filter. The results are shown as a scatter plot of the timing and the charge called TQ-map in Figure 2.21. Each dot represents one measurement, and the open circles are the average timing with respect to charge for a PMT.The TQ-map is made for all ID PMTs and used to correct the timing information.

2.6.4 Water Transparency Measurement

Water transparency is the length scale of the optical attenuation in water, which represents the combined effect of absorption and scattering on the intensity of the light. Water transparency in Super-Kamiokande is measured using N_2 laser beam injected into the detector. The wavelength dependence of the attenuation length can be measured by changing the dye of the laser. The absorption and scattering coefficients are separately measured by this method. Further, the water transparency is independently measured using Cherenkov light from cosmic ray muons. The time variation of the water transparency can be monitored by this method without

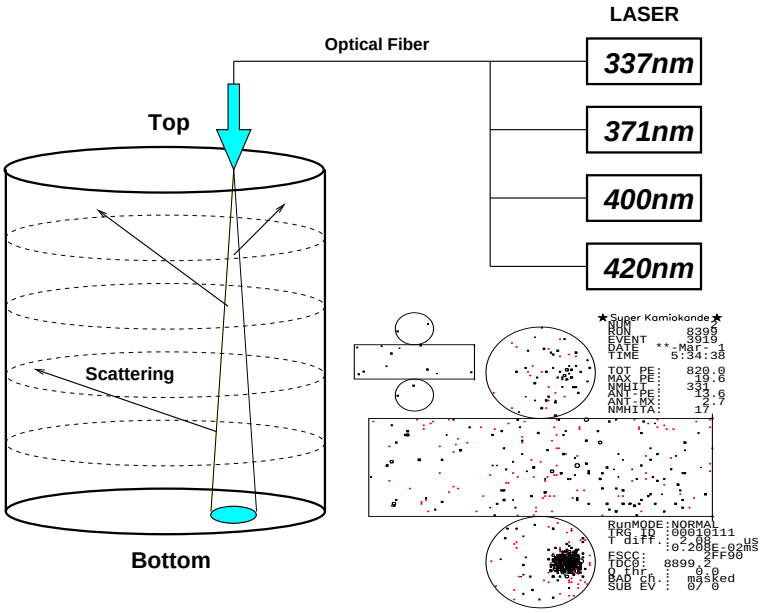

Figure 2.22: A schematic view of the scattering and absorption parameter measurement using laser systems, and a typical laser event.

disturbing the normal data taking.

Light scattering measurement using a laser

The light attenuation length in water can be described as $L = (\alpha_{abs} + \alpha_{scat})^{-1}$, where α_{abs} and α_{scat} are the absorption coefficient and scattering coefficient, respectively. The absorption and scattering coefficients are separately measured using a N_2 laser [39]. Figure 2.22 shows a schematic view of the measurement system. Each laser, wavelength of 337, 371, 400 and 420 nm, fires every 6 seconds during normal data taking. The light from the laser is injected into the ID via an optical fiber toward the bottom of the tank. A typical event by the laser light is also shown in Figure 2.22. The PMT hits clustered at the bottom of the tank are due to the direct (unscattered) photons.

In the analysis, the detector is separated into 6 regions, top and 5 in barrel, as shown in Figure 2.22. The total charge of bottom PMTs is used for the normalization of the light intensity. Figure 2.23 shows the PMT hit timing distributions in each region for data and Monte Carlo simulation. These PMT hits on the top and barrel wall are due to the photons scattered in water, or the photons reflected by surfaces of bottom PMTs or black sheets. The first peaks and slopes are characterised by the absorption and scattering coefficients and the second peaks around 1100 nsec are due to the photons reflected by the PMTs or black sheets. For the Monte Carlo simulation, the absorption and scattering coefficients are adjusted so that the PMT hit time distributions are in agreement with data. The attenuation length in water is calculated using the measured absorption and scattering coefficients.

The attenuation coefficients (L^{-1}) obtained by this method are plotted in Figure 2.24 with a star symbol. The lines shows a model used in the Monte Carlo simulation, which are determined

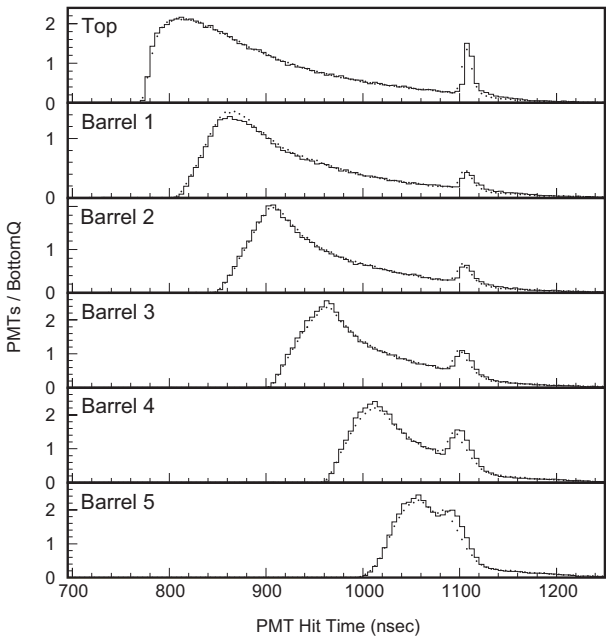

Figure 2.23: PMT hit time distributions of 337 nm-laser events in each detector region for the data (dots) and the Monte Carlo events which is tuned by the scattering and absorption parameters (histograms).

by fitting the measurements from this method.

Measurement using cosmic ray muons

Water transparency is also measured by using Cherenkov light from cosmic ray muons passing through the detector. Since the energy deposit of such a energetic muon is almost constant (about 2 MeV/cm), cosmic ray muons can be used as a calibration source.

Only vertical downward muons are selected for this measurement. The muon track is reconstructed by connecting the entrance and the exit points in the ID. Under the assumption that the light detected by each PMT is not scattered, the detected charge (photoelectrons) is expressed by :

$$Q = Q_0 \cdot \frac{f(\theta)}{l} \cdot \exp\left(-\frac{l}{L}\right) \tag{2.5}$$

where Q_0 is a constant, $f(\theta)$ is the PMT acceptance, l is the photon path length and L is the attenuation length. Figure 2.25 shows $\log(Q \cdot l / f(\theta))$ as a function l in a typical run. The attenuation length is estimated to be 95 m for this data set.

Since the cosmic ray muons are measured during the normal data taking, continuous check of the water transparency is possible by this method. Figure 2.26 shows the time variation of the attenuation length. This time variation is corrected in event reconstruction processes.

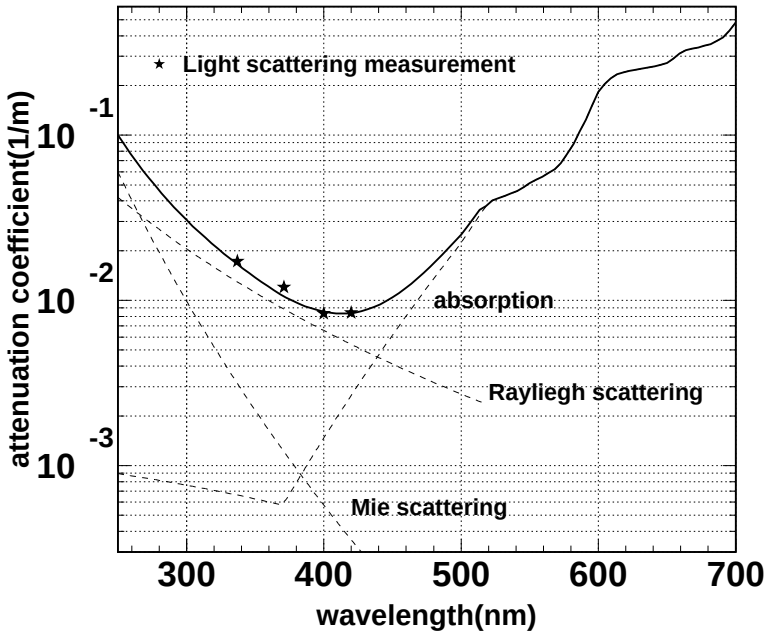

Figure 2.24: Wavelength dependence of attenuation coefficients ($L^{-1}_{\rm atten}$) obtained by the light scattering measurement (points) together with a model in the detector simulation (lines, see Section 3.5).

2.6.5 Absolute Energy Calibration

The momentum of a particle is determined by the charge information of PMTs. Since the systematic uncertainty in the absolute energy scale affects the atmospheric neutrino analysis, it is essential to understand the absolute energy scale as accurte as possible . Four kind of methods are employed in momentum range from a few ten MeV/c to about 10 GeV/c by using independent calibration sources: decay electrons from stopping muons, π^0 events, low and high energy stopping muons.

Decay electrons

Many electron events produced by the decay of cosmic ray muons are observed in Super-Kamiokande. These electrons have the well known energy spectrum extending up to $\sim$53 MeV and are used to determine the absolute energy scale by comparing the energy spectrum between the observed data and the Monte Carlo simulation. Decay electrons are selected by the following criteria :

1. The time interval from a stopping muon event is 1.5 μsec to 8.0 μsec.
2. The number of hit PMT in a 50 nsec time window is larger than 60(30) for SK-I (SK-II).
3. The goodness of the vertex fit is greater than 0.5 .
4. The vertex position is reconstructed more than 2 m away from the ID wall.

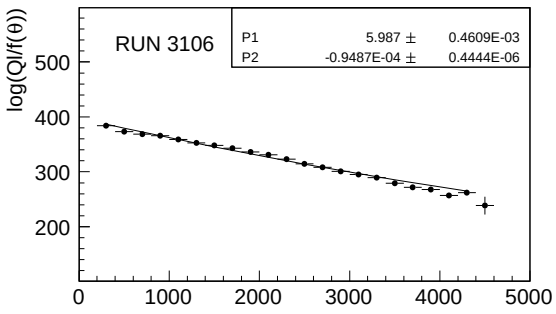

Figure 2.25: Effective observed charge ($\log(Ql/f(\theta))$) for through-going muons as a function of the photon path length (l) where Q is the detected charge and $f(\theta)$ is the PMT acceptance.

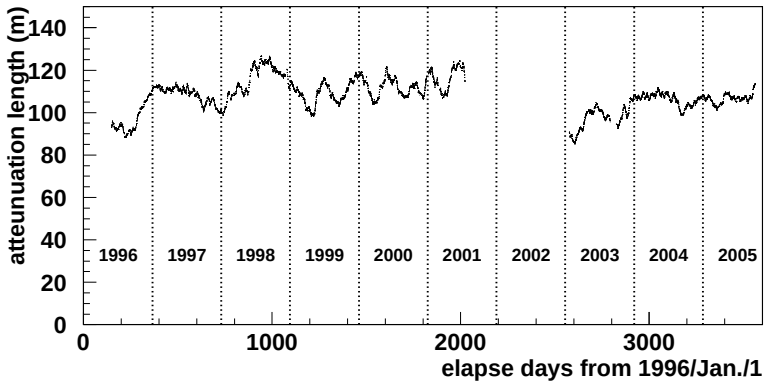

Figure 2.26: Time variation of water attenuation length.

Criterion (2) rejects $\sim$6 MeV gammma rays from μ^- capture on the nucleon. Figure 2.27 shows the momentum spectra of decay electrons compared with the prediction from the Monte Carlo simulation. In the Monte Carlo, measured μ^+/μ^- ratio of 1.37 [40] is used and the effect of μ^- capture by oxygen nuclei is also considered. The mean values of data agree with the Monte Carlo prediction within 0.4 %(2.4 %) for SK-I (SK-II).

Neutrino induced π^0 events

The π^0 events produced in the interactions of the atmospheric neutrino are used for the energy scale calibration in the several hundred MeV energy range. Since a π^0 decays immedeately into two γ-rays, the invariant mass of π^0 is obtained by the reconstructed momentum of two γ-rays, $P_{\gamma 1}$ and $P_{\gamma 2}$, and the opening angle θ as follows :

$$M_{\pi^0} = \sqrt{2P_{\gamma 1}P_{\gamma 2}(1-\cos\theta)} \tag{2.6}$$

The π^0 events are selected from the atmospheric neutrino sample (see Chapter 6) by the following criteria :

1. Two Cherenkov rings are recognized and both of them are identified as electron-like.

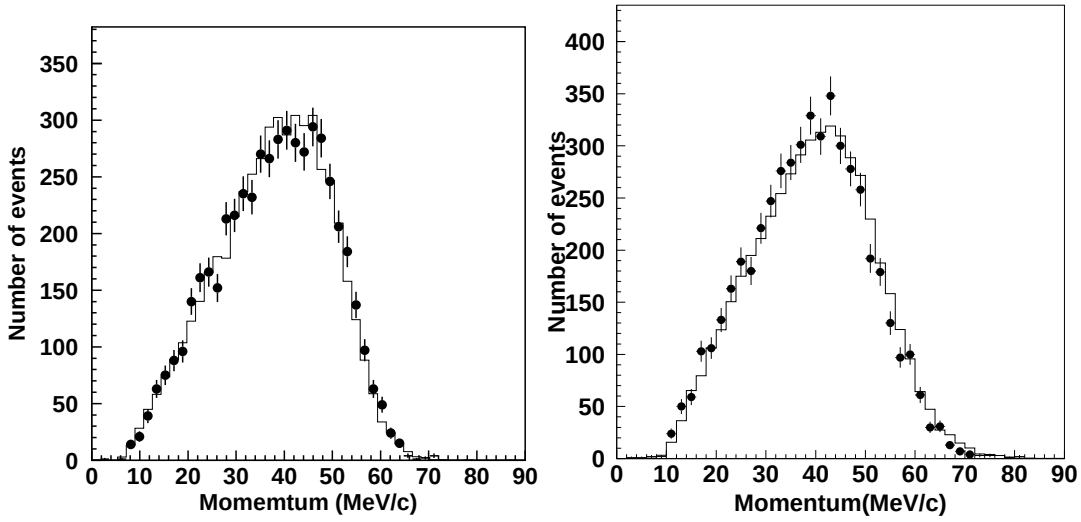

Figure 2.27: The momentum distribution of decay electrons of the data (dot) and the Monte Carlo (line) for SK-I (left) and SK-II (right).

2. Electrons from muon decay is not detected.

3. The vertex position is reconstructed more than 2 m away from the ID wall.

Criterion (2) rejects the contamination of $\pi^+\pi^0$ or $\mu^\pm\pi^0$ events. Figure 2.28 shows the invariant mass distribution of π^0 events, which is compared with the prediction from the Monte Carlo simulation. A peak from π^0 is clearly observed at around 135 MeV/c^2. The peak position of the data is 1.6 %(1.4 %) higher than that of the Monte Carlo simulation for SK-I (SK-II).

Low energy stopping muons

The Cherenkov angle of charged particles is expressed as a function of the momentum :

$$\cos\theta_C = \frac{1}{n\beta} = \frac{1}{n}\sqrt{1+\frac{m^2}{p^2}} \tag{2.7}$$

where θ_C, n, β, m and p are the Cherenkov angle, the refraction index of water, v/c, mass and momentum. Since the Cherenkov angle has a large dependence on the momentum for low energy stopping muons (< 400 MeV/c), the momentum can be estimated by measuring the Cherenkov angle. The momentum estimated from the detected charge ($P_{p.e.}$) is used to check the systematic uncertainty of the momentum determination by comparing it with the momentum derived from the Cherenkov angle (P_θ). On the other hand, this method is not useful for electrons or high energy muons because the Cherenkov angle approaches a limit when the momentum is high compared to its mass. Low momentum stopping muon events are selected for this study by the following criteria :

1. The total number of p.e.s in the ID is less than 1500 p.e.s for SK-I (750 for SK-II)

2. One cluster of hit PMTs in the outer detector.

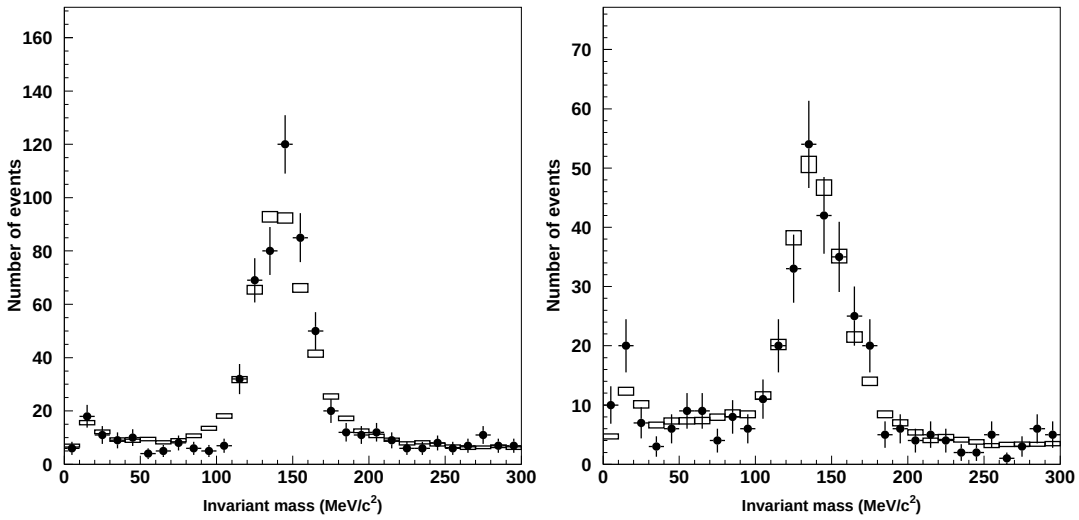

Figure 2.28: Invariant mass distribution of neutrino induced π^0 events of the observed data (dot) and the atmospheric neutrino Monte Carlo events (boxes) for SK-I (left) and SK-II (right). The peak position is fitted by a Gaussian distribution.

3. The entrance point is on the top wall.
4. The direction is downward ($\cos\theta > 0.9$).
5. One decay electron event is detected.

Criterion (1) corresponds to the approximate muon momentum of $< 380\,\mathrm{MeV/c}$. Criterion (2) requires an entrance point of a muon in the OD and criterion (3) and (4) select the muon events which are straight downgoing.

Figure 2.29 shows the scattered plots of the reconstructed Cherenkov opening angle and the momentum $\mathrm{P}_{p.e.}$ for the data and the Monte Carlo simulation. The momentum dependence of the Cherenkov opening angle is seen in both figures. The energy scale of the data is compared with that of the Monte Carlo simulation by comparing the ratios of $\mathrm{P}_{p.e.}/\mathrm{P}_\theta$. Figure 2.30 shows the averaged $\mathrm{P}_{p.e.}/\mathrm{P}_\theta$ for the data and the Monte Carlo simulation and the MC/data ratio as a function of the expected momentum P_θ. They agree within 1.5 % for SK-I and 2.3 % for SK-II.

High energy stopping muons

The momentum for high energy stopping muons can be estimated from its track length because the range of the muon track is well understood and approximately proportional to the momentum. Since the measurement of the range can be independent of the measurement of the momentum that is based on the observed photoelectrons, the estimated momentum from its range is used for checking the energy scale from $1\,\mathrm{GeV}/c$ up to $10\,\mathrm{GeV}/c$. Stopping muon events are selected by the following criteria :

1. The entrance point is on the top wall.
2. The direction is downward ($\cos\theta > 0.94$).

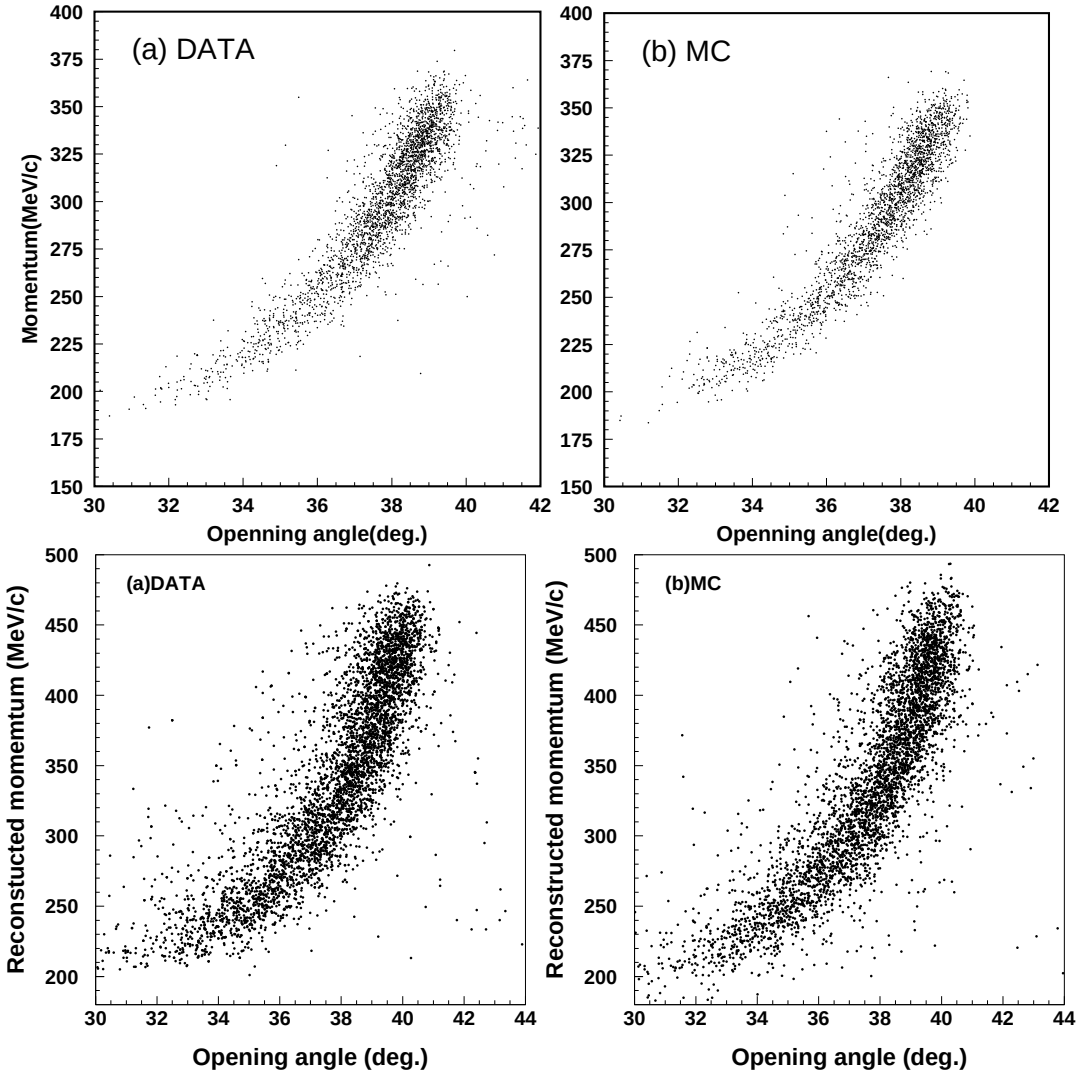

Figure 2.29: Scatter plot of the reconstructed Cherenkov opening angle and the reconstructed momentum $P_{p.e.}$ for (a) the data and (b) the Monte Carlo simulation. The momentum dependence of the Cherenkov opening angle is seen in both figures. The top two panels show for SK-I and the bottom two panels show for SK-II.

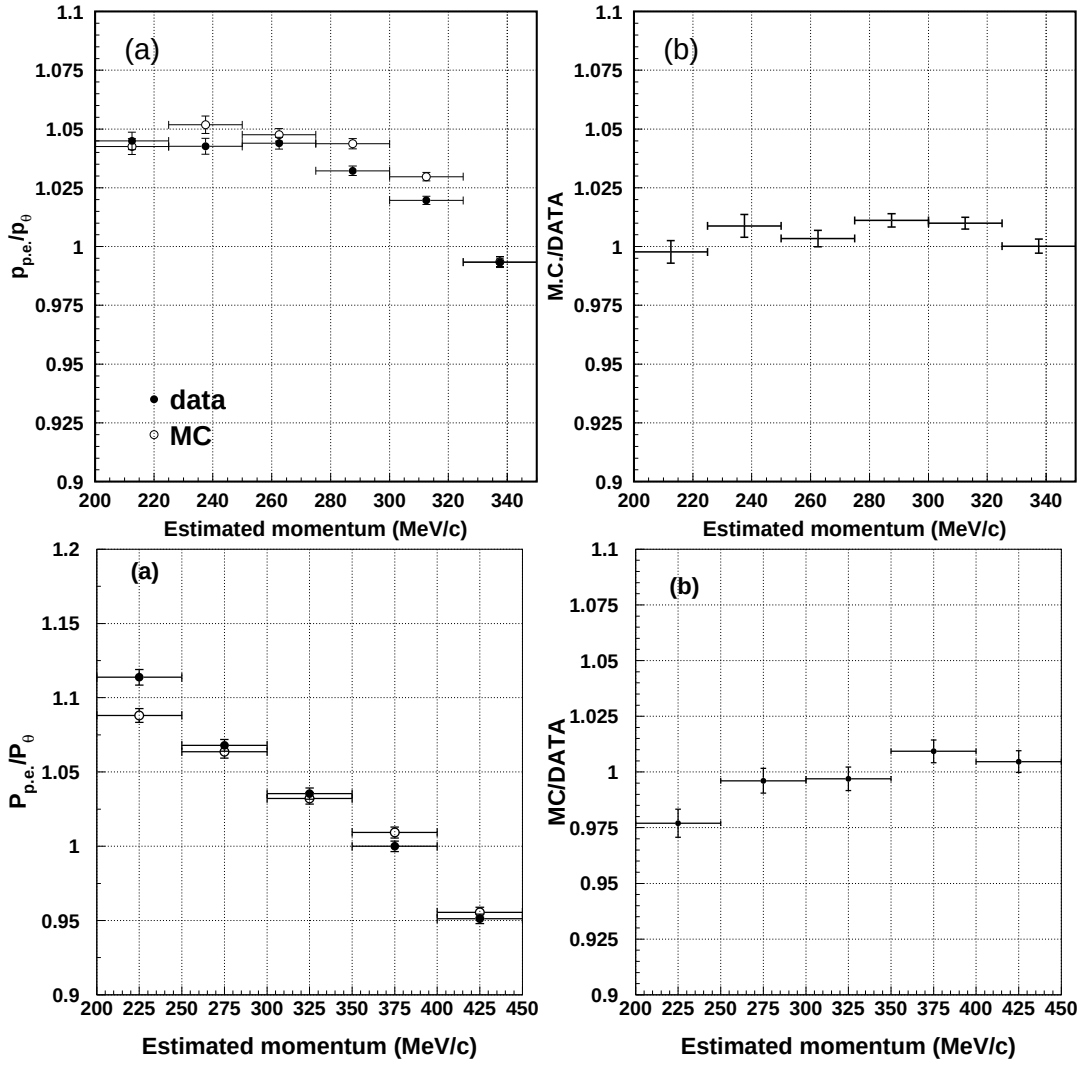

Figure 2.30: Figure (a) shows the averaged ratio of the momentum derived from the charge to that from the opening angle ($P_{p.e.}/P_\theta$) as a function of the momentum P_θ for the data (black points) and the Monte Carlo events (white points), and figure (b) shows the ratio of the data to the Monte Carlo events. The top two panels show for SK-I and the bottom two panels show for SK-II.

3. One decay electron event is detected.

4. The reconstructed range of muon track is greater than 7 m.

The range of the muon is determined by the entrance position of the stopping muon and the vertex position of the subsequent decay electron. Figure 2.31 shows the averaged value of the ratio momentum/range as a function of the range for the data and the Monte Carlo simulation. The momentum loss per cm is about 2.3 MeV/c. The comparison of the momentum/range between the data and the Monte Carlo simulation is also shown in Figure 2.31. Although the momentum dependence is seen, the deviations from unity are less than 2 %(1 %) for SK-I (SK-II).

Time variation of energy scale

The stability of the energy scale is also monitored by the stopping muons and the decay electrons. Figure 2.32 shows the time variation of the averaged momentum/range of stopping muons and the reconstructed momentum of the decay electrons as a function of elapse days from April 1st, 1996. The RMS of the energy scale variation is 0.8 %(0.9 %) for SK-I (SK-II).

Uniformity of Energy Scale

The uniformity of the detector is measered using the decay electrons from the cosmic ray muons. They are good calibration sources to check the detector uniformity, because the vertex is distributed uniformly in the fiducial volume and the momentum distribution is almost uniform in all directions. To take into account the muon polarization, only electrons whose direction is perpendicular to the parent muon direction are used. This condition is -0.25$<\cos\Theta_{e\leftrightarrow\mu}<0.25$, where $\cos\Theta_{e\leftrightarrow\mu}$ is the opening angle between the electron and muon directions. Figure 2.33 shows the averaged momentum of decay electrons for the Monte Carlo events normalized by that for data as a function of the zenith angle of the electrons. From this figure, the detector gain is uniform within $\pm$0.6 % for SK-I and SK-II.

Summary of the absolute energy calibration

Figure 2.34 shows the summary of the absolute energy calibration. The absolute energy scale is checked by various methods over a wide energy range. The uncertainty of the energy scale is estimated to be less than 1.8 % and 2.4% for the momentum range from a few ten MeV/c to about 10 GeV/c for SK-I and SK-II, respectively. Combined with the RMS of the time variation of the energy scale, 2.0 % (2.5 %) is adopted to the systematic error for SK-I (SK-II).

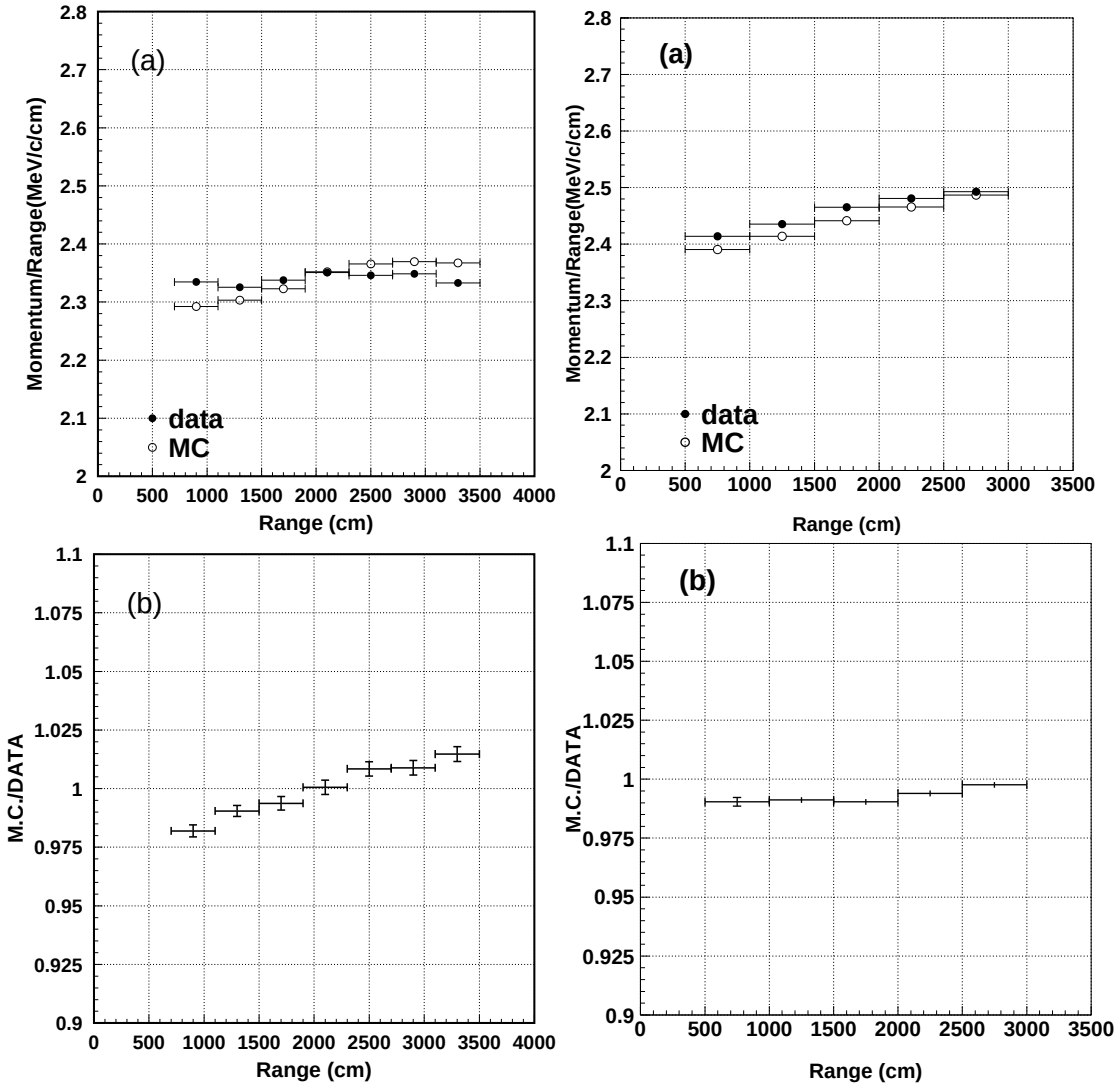

Figure 2.31: Figure (a) shows the range v.s. averaged momentum/range of stopping muon events for the data (black points) and the Monte Carlo events (open circles), and figure (b) shows the ratio of the Monte Carlo events to the data for SK-I (left) and SK-II (right).

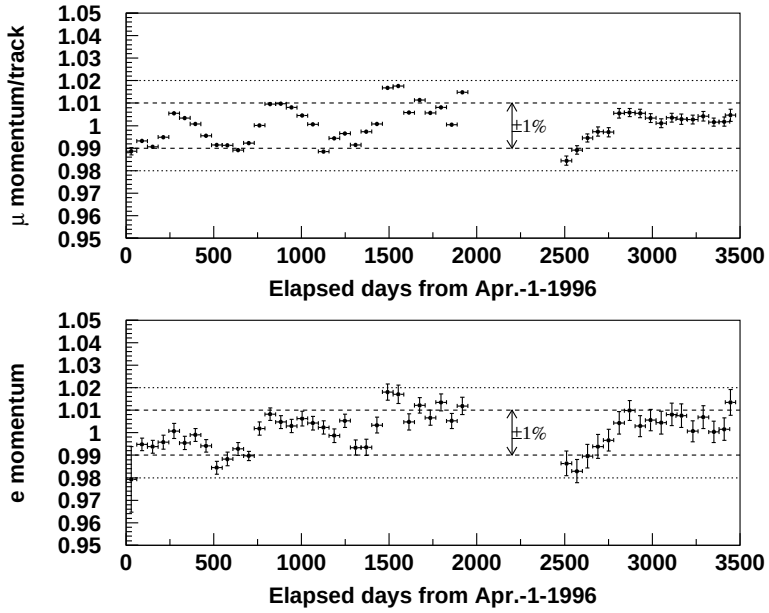

Figure 2.32: The time variation of the averaged momentum/range of stopping muons (upper) and the reconstructed momentum of the decay electrons (bottom) as a function of elapsedays from April 1st, 1996.

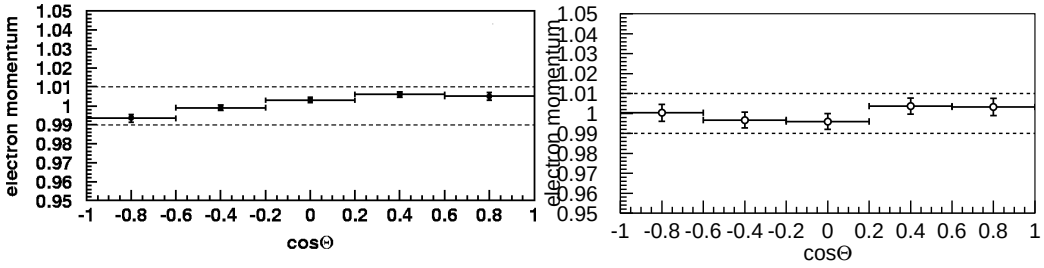

Figure 2.33: The uniformity of the detector gain as a function of zenith angle for SK-I (left) and SK-II (right). The vertical axes in the two figures are the averaged momentum of decay electron events.

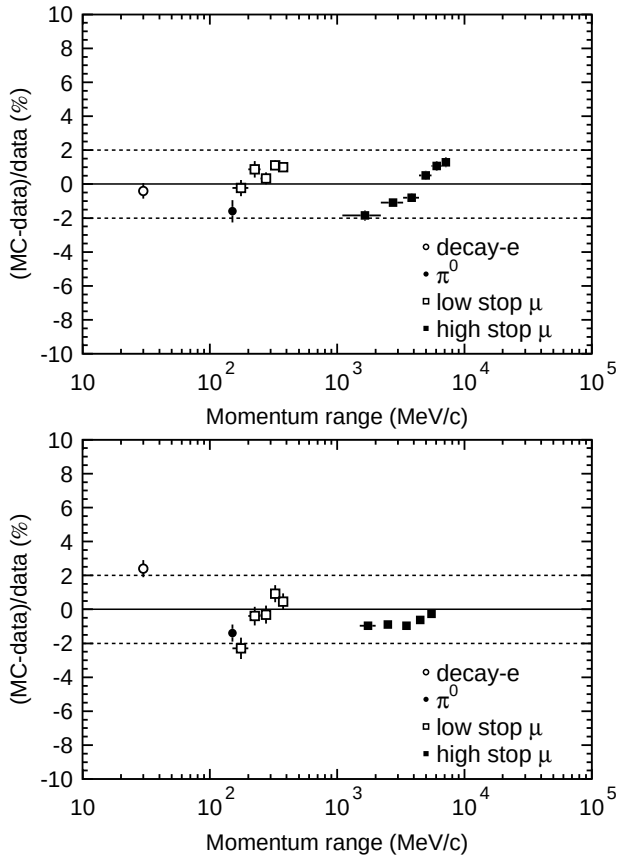

Figure 2.34: The summary of the absolute energy scale calibration for SK-I (top) and SK-II (bottom). The horizontal axis shows the momentum range of each source and the vertical axis shows the deviation of the data from the Monte Carlo predictions.

Chapter 3

Simulation

3.1 Overview

Expectation of atmospheric neutrino events in Super-Kamikande is calculated by a Monte Carlo simulation. The Monte Carlo simulation consists of four components : atmospheric neutrino flux, neutrino interactions, particle tracking in the detector and the detector hardware simulation.

3.2 Atmospheric Neutrino Flux

There have been several atmospheric neutrino flux models calculated by M.Honda *et al.* [14] (Honda flux), G.Battistoni *et al.* [41] (Fluka flux) and G.Barr *et al.* [42] (Bartol flux). In our Monte Carlo simulation program, the Honda flux is adopted and two other flux calculations are used to estimate the systematic uncertainties in the flux calculation. The primary cosmic ray flux model as an input of the flux calculation is determined based on the experimental measurements. Current status of the measurements of cosmic ray proton flux is shown in Figure 3.1 with the model used in the Honda flux calculation. The primary cosmic ray spectrum has been precisely measured by BESS and AMS experiments up to 100 GeV [43, 44]. The cosmic ray flux changes depending on the turbulence of the solar wind, which is higher when the solar activities are high (solar maximum) than when the solar activities are low (solar minimum). The difference of the cosmic ray flux at solar maximum and solar minimum is more than a factor of two for 1 GeV cosmic rays, while it decrease to $\sim 10\,\%$ for 10 GeV. The effect of geomagnetic field is represented as rigidity (= momentum/charge) cutoff. The geomagnetic field works as a shield, by which cosmic ray with lower momentum than the cutoff cannot arrive at the Earth. Cosmic ray flux above 100 GeV, which are responsible for ≥ 10 GeV neutrinos, is not affected by the solar activity nor the geomagnetic field.

Primary cosmic ray protons and nuclei interact with air nuclei, and secondary particles, mostly pions and some kaons, are generated in the atmosphere. The US Standard Atmosphere model [55] is employed for the density structure of the atmosphere and the structure gives the zenith angle dependence of the atmospheric neutrinos.

For the hadronic interactions of the cosmic rays with air nuclei, the two theoretical models, NUCRIN [56] for the primary cosmic ray energies < 5 GeV and DPMJET-III [57] for > 5 GeV. Through the interactions, mostly pions and some kaons are generated. Then they decay into

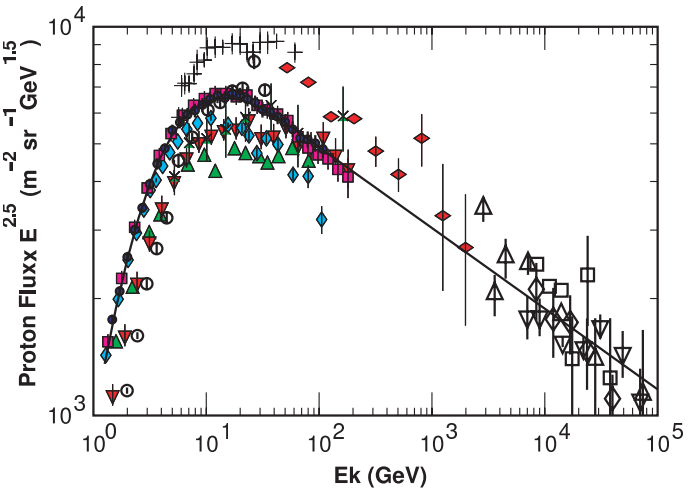

Figure 3.1: Measurements of primary cosmic ray proton flux and the model used in Honda flux calculation. The data are taken from Webber [45] (crosses), LEAP [46] (upward triangles), MASS1 [47] (open circles), CAPRICE [48] (vertical diamonds), IMAX [49] (downward triangles), BESS98 [43] (circles), AMS [44] (squares), Ryan [50] (horizontal diamonds), JACEE [51] (downward open triangles), Ivanenko [52] (upward open triangles), Kawamura [53] (open squares) and Runjob [54] (open diamonds).

muons and neutrinos. The flux of the secondary cosmic ray muons have been measured by several experiments such as BESS [58]. The hadronic interaction model used in the Honda flux calculation agree with the measurement in the 1∼10 GeV muon energy range as shown in Figure 3.2.

The calculated energy spectrum of atmospheric neutrinos at the Super-Kamiokande site for the Honda flux, Fluka flux and Bartol flux is shown in Figure 3.3, in which the flux of $\nu_e+\overline{\nu}_e$ to $\nu_\mu+\overline{\nu}_\mu$ is averaged over all of the direction. The flavor ratio is about two up to a few GeV energy regions, but it becomes larger than two as the neutrino energy increases because more cosmic ray muons reach the ground before decaying. The systematic uncertainty in absolute flux is estimated to be about 20 % due to the uncertainty of the absolute primary cosmic ray flux and the uncertainties in the cosmic ray interaction, while the uncertainty in the flavor ratio is smaller than 3 %. The systematic error in the flavor ratio is one of the dominant errors to observe the 1-2 oscillation effect.

Figure 3.4 shows the calculated flux ratios of $\nu_e/\overline{\nu}_e$ and $\nu_\mu/\overline{\nu}_\mu$. The calculations agree to about 5 % for both below 10 GeV, while above 10 GeV the disagreement is larger as a function of the neutrino energy to 10 % and 25 % at 100 GeV for ν_e and ν_μ, respectively.

Figure 3.5 shows the zenith angle distributions of the atmospheric neutrino flux, where cosθ = -1 refers to upward-going neutrinos and cosθ = 1 refers to downward-going neutrinos. The enhancement of the Sub-GeV flux near horizon is due to the 3 dimensional nature of the earth geometry and the poor angular correlation between the primary cosmic ray and the neutrino directions. Details of the horizontal enhancement in discussed in [61]. The enhancement of the Multi-GeV flux toward the horizontal directions is due to the larger decay volume of the cosmic ray muons. The cosmic ray muons coming in the horizontal direction travel for a longer distance

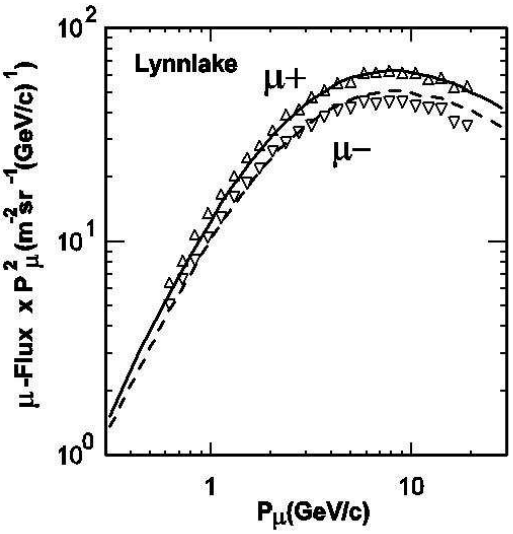

Figure 3.2: Secondary cosmic ray muon flux at Lynnlake observed by the BESS experiment [58] (points) and the prediction from the Honda flux calculation [60] (lines).

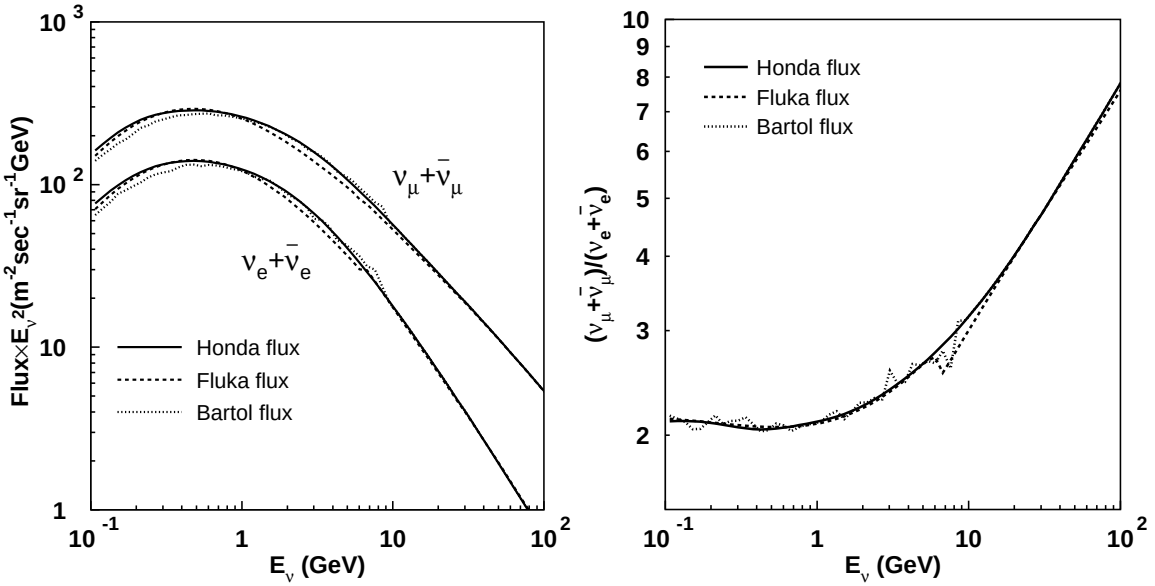

Figure 3.3: Predictions of the direction averaged atmospheric neutrino flux and the flavor ratio. Solid lines show the Honda flux, dashed lines show the Fluka flux and dotted lines show the Bartol flux.

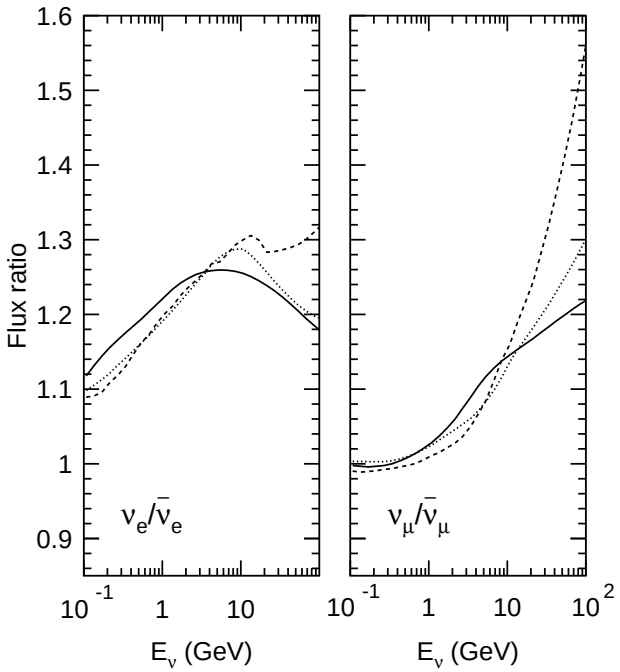

Figure 3.4: The calculated flux ratios of $\nu_e/\overline{\nu}_e$ and $\nu_\mu/\overline{\nu}_\mu$ as a function of the neutrino energy for the Honda flux (solid line), the Bartol flux (dashed line), and the Fluka flux (dotted line).

than those in the vertical direction and have a higher probability to decay into neutrinos. For lower energy netrinos, the flux shows up-down asymmetry. This is caused by the geomagnetic field. The promary cosmic rays of the lower energy neutrinos are deflected by the rigidity cutoff. This up-down asymmetry for low energy neutrinos largely washed out due to the poor angular correlation between neutrinos and leptons.

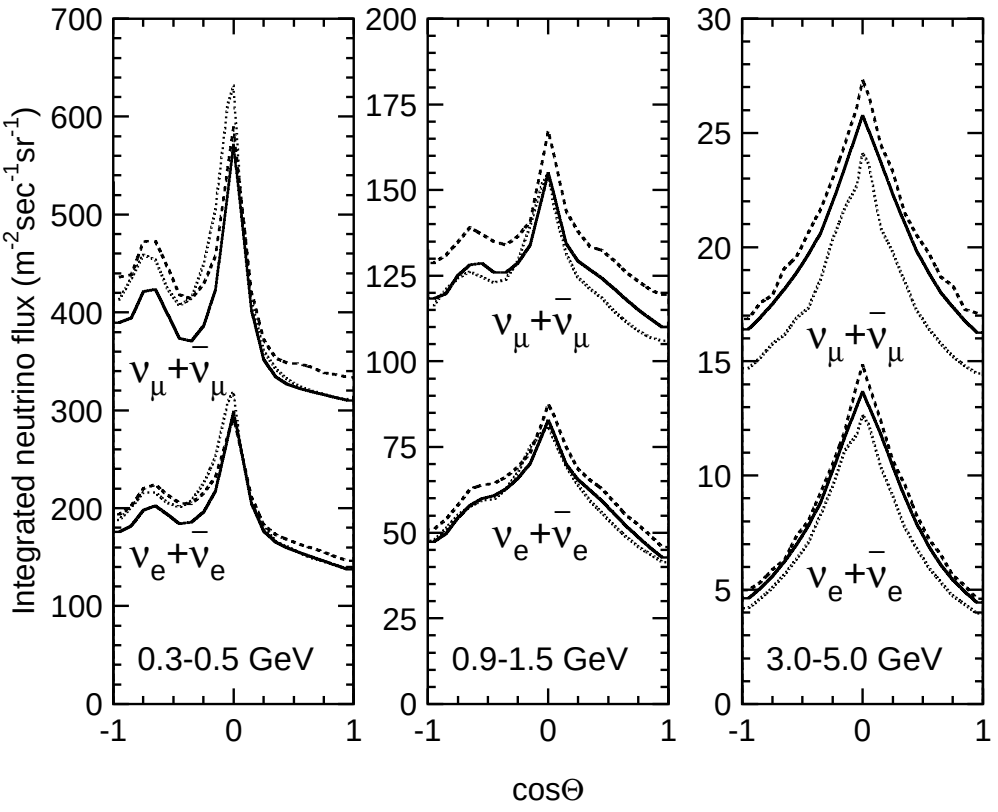

Figure 3.5: The atmospheric neutrino flux as a function of zenith angle for the Honda flux (solid line), the Bartol flux (dashed line), and the Fluka flux (dotted line). Zenith angle $\cos\Theta = -1(+1)$ indicates upward-going (downward-going).

3.3 Neutrino Interaction

Atmospheric neutrinos interact with nucleons and electrons in water. The neutrino interactions are treated using NEUT program library [62] in our Monte Carlo simulation. This library was first developed to study atmospheric neutrinos as a background of nucleon decay analysis in the Kamiokande experiment, and then it was inherited to the Super-Kamiokande experiment with various modifications. In the NEUT code, the following charged current (CC) and neutral current (NC) interactions are considered :

CC/NC (quasi-)elastic scattering	$\nu + N \rightarrow\ l + N'$
CC/NC single meson production	$\nu + N \rightarrow\ l + N' + meson$
CC/NC deep inelastic interaction	$\nu + N \rightarrow\ l + N' + hadrons$
CC/NC coherent pion production	$\nu +\ ^{16}\mathrm{O} \rightarrow\ l +\ ^{16}\mathrm{O} + \pi$

where N and N' are nucleons (proton or neutron) and l is a lepton.

Since the cross-section of neutrino-electron elastic scattering is about 10^3 times smaller than that of the neutrino-nucleon interactions at a neutrino energy of $\sim$1 GeV, this interaction mode is neglected in our simulation.

3.3.1 Elastic and Quasi-Elastic Scattering

The differential cross-section of the charged current quasi-elastic scattering for free protons (i.e. hydrogen atom in water) is given by [63, 64] :

$$\frac{d\sigma^{\nu(\bar{\nu})}}{dq^2} = \frac{M^2 G_F^2 \cos^2\theta_c}{8\pi E_\nu^2}\left[A(q^2) \mp B(q^2)\frac{s-u}{M^2} + C(q^2)\frac{(s-u)^2}{M^4}\right] \tag{3.1}$$

where E_ν is the neutrino energy, M is the mass of the target nucleon, G is the Fermi coupling constant, θ_c is the Cabbibo angle, q is the four-momentum transfered of the lepton, and s and u are Mandelstam variables [63]. The factors A, B and C are :

$$\begin{aligned} A(q^2) &= \frac{m^2-q^2}{4M^2}\left[\left(4-\frac{q^2}{M^2}\right)|F_A|^2 - \left(4+\frac{q^2}{M^2}\right)|F_V^1|^2\right. \\ &\quad - \frac{q^2}{M^2}|\xi F_V^2|^2\left(1+\frac{q^2}{4M^2}\right) - \frac{4q^2 F_V^1 \xi F_V^2}{M^2} \\ &\quad \left. - \frac{m^2}{M^2}\left((F_V^1+\xi F_V^2)^2 + |F_A|^2\right)\right] \end{aligned} \tag{3.2}$$

$$B(q^2) = \frac{q^2}{M^2}\left(F_A(F_V^1+\xi F_V^2)\right) \tag{3.3}$$

$$C(q^2) = \frac{1}{4}\left(|F_A|^2 + |F_V^1|^2 - \frac{q^2}{4M^2}|\xi F_V^2|^2\right) \tag{3.4}$$

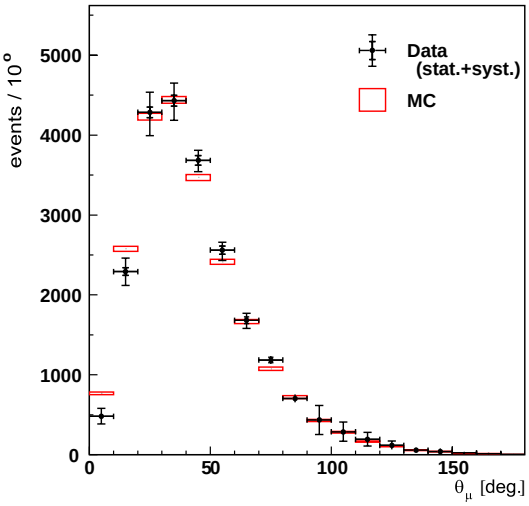

Figure 3.6: The scattering angle distribution by neutrino interactions off the H_2O target from the K2K experiment (dot) [65] together with our Monte Carlo events (histgram).

where m is the lepton mass, $\xi \equiv \mu_p - \mu_n = 3.71$. The vector form factors, $F_V^1(q^2)$ and $F_V^2(q^2)$, and the axial vector form factor, $F_A(q^2)$ are determined experimentally and are given by :

$$F_V^1(q^2) = \left(1 - \frac{q^2}{4M^2}\right)^{-1} \left[G_E(q^2) - \frac{q^2}{4M^2} G_M(q^2)\right] \tag{3.5}$$

$$\xi F_V^2(q^2) = \left(1 - \frac{q^2}{4M^2}\right)^{-1} \left[G_E(q^2) - G_M(q^2)\right] \tag{3.6}$$

$$F_A(q^2) = -1.23 \left(1 - \frac{q^2}{M_A^2}\right)^{-2} \tag{3.7}$$

$$G_E(q^2) = (1+\xi)^{-1} G_M(q^2) = \left(1 - \frac{q^2}{M_V^2}\right)^{-2} \tag{3.8}$$

where G_E and G_M are the electric and magnetic form factor, the vector mass M_V is set to be 0.84 GeV and the axial vector mass M_A is set to be 1.11 GeV from experimental data [65], which is common parameter for single meson production model.

For larger M_A values, interactions with higher Q^2 values (and therefore larger scattering angles) are enhanced. The M_A value is tuned using the K2K near detector data. The uncertainty of the value is estimated to be 10 % comparing the K2K data with our Monte Carlo. Figure 3.6 shows the K2K 1 kton water Cherenkov data on the scattering angle for single-ring events [65] together with our Monte Carlo events. The scattering angle agrees well between the data and Monte Carlo overall, although the suppression of events at small angle is being studied by several groups[66].

For scattering off nucleons in ^{16}O, the Fermi motion of the nucleons and Pauli exclusion principle must be considered [67]. Since nucleons are fermions, the outgoing momentum of the nucleons in the interactions is required to be greater than the Fermi surface momentum to allow quasi-elastic scattering to occur. In NEUT, the Fermi surface momentum is set to be 225 MeV/c.

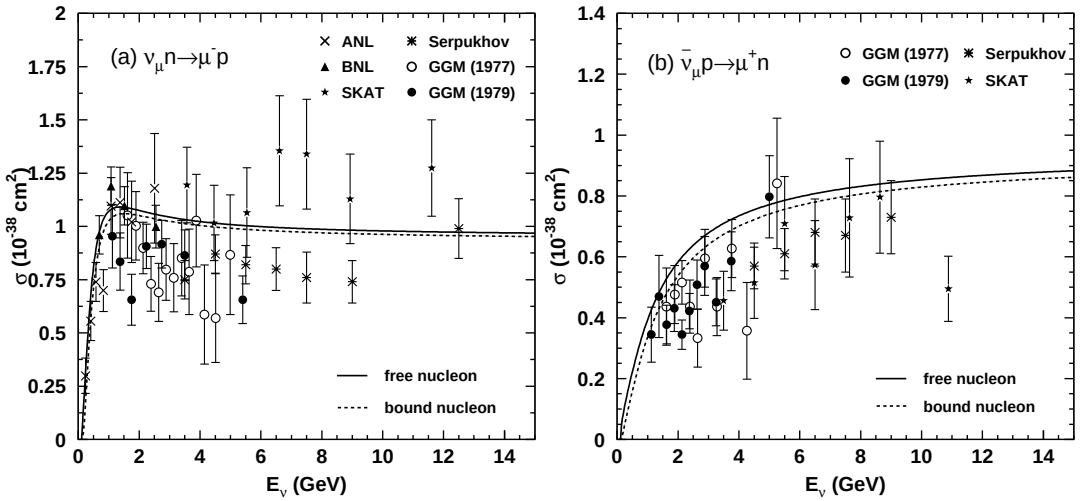

Figure 3.7: cross-sections of (a) ν_μ and (b) $\overline{\nu}_\mu$ with the experimental data from ANL [70], Gargamelle [71, 72], BNL [73], Serpukhov [74] and SKAT [75].

The cross-section for neutral current elastic scattering are estimated from the following relations [68, 69] :

$$\begin{aligned}
\sigma(\nu p \to \nu p) &= 0.153 \times \sigma(\nu n \to e^- p) && (3.9)\\
\sigma(\bar{\nu} p \to \bar{\nu} p) &= 0.218 \times \sigma(\bar{\nu} p \to e^+ n) && (3.10)\\
\sigma(\nu n \to \nu n) &= 1.5 \times \sigma(\nu p \to \nu p) && (3.11)\\
\sigma(\bar{\nu} n \to \bar{\nu} n) &= 1.0 \times \sigma(\bar{\nu} p \to \bar{\nu} p) && (3.12)
\end{aligned}$$

Figure 3.7 shows the cross-section of the quasi-elastic scattering for the experimental data and the calculation by NEUT. Figure 3.8 shows the calculated cross-sections with free nucleon and bound nucleon in oxygen nuclei in the low energy region.

The systematic uncertainty of the CCQE cross-sections with bound nucleons is estimated from the difference between the model of Nieves *et al.* [125] and that of Smith and Monitz [67]. The uncertainties in the $\overline{\nu}_\mu + \overline{\nu}_e$ to $\nu_\mu + \nu_e$ ratio and the $\nu_\mu + \overline{\nu}_\mu$ to $\nu_e + \overline{\nu}_e$ ratio are also taken into account (see Section 7.3). The systematic errors in M_A and in the CCQE cross-sections are important to observe the 1-2 sub-dominant oscillation effect.

3.3.2 Single Meson Production

The resonant single meson production of π, K, and η is simulated based on the model of Rein & Sehgal [76]. This method assumes an intermediate baryon resonance :

$$\begin{aligned}
\nu + N &\to l + N^* \\
N^* &\to N' + \text{meson}
\end{aligned} \qquad (3.13)$$

where N and N' are nucleons and N^* is a baryon resonance. The differential cross-section of single-meson production is a product of the amplitude of each resonance production and the

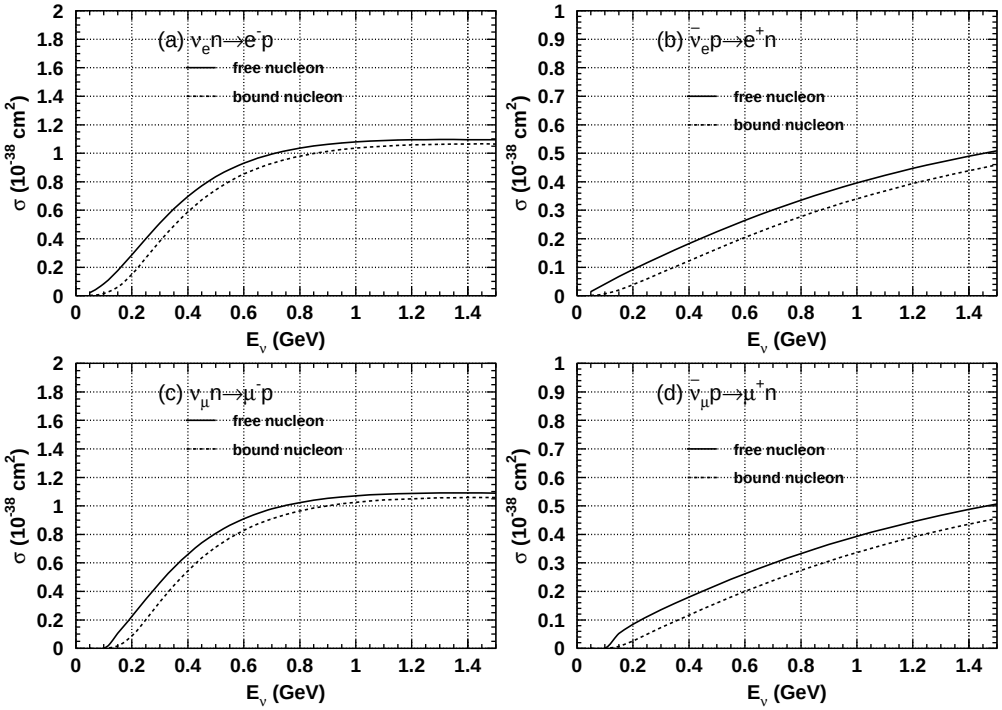

Figure 3.8: cross-sections of quasi-elastic scattering in the low energy region for (a) ν_e, (b) $\overline{\nu}_e$, (c) ν_μ and (d) $\overline{\nu}_\mu$. The solid lines show the cross-sections for free nucleon and the dashed lines show that for bound nucleon.

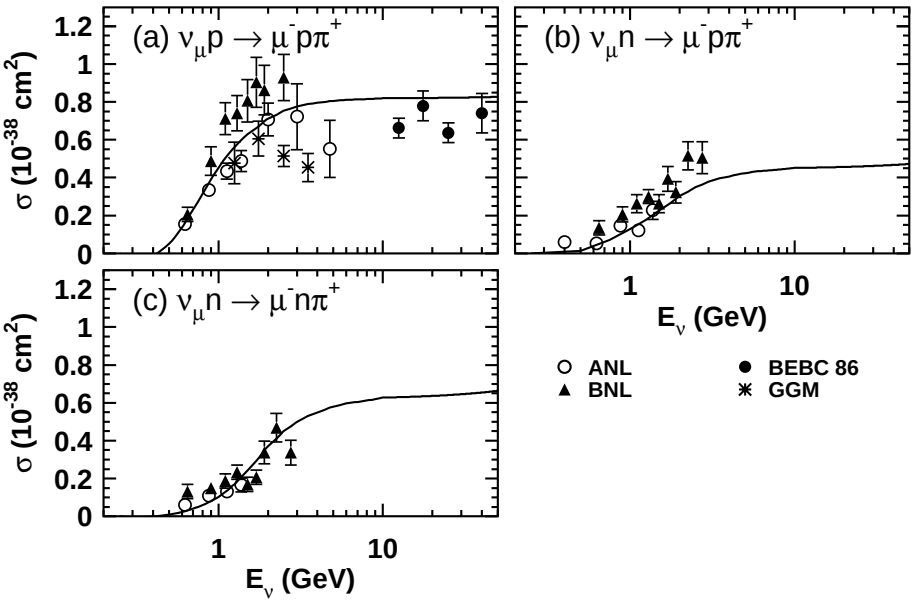

Figure 3.9: Cross-sections for charged current single pion productions of ν_μ. (a) $\nu_\mu p \to \mu^- p \pi^+$, (b) $\nu_\mu n \to \mu^- p \pi^0$, (c) $\nu_\mu n \to \mu^- n \pi^+$. Solid lines show our calculations. Experimental data are from ANL [80], BNL [81], BEBC [82] and Gargamelle [84].

probability of the baryon resonance decay to this meson. For negligible decay width of a baryon resonance (N^*), the differential cross-section is :

$$\frac{d^2\sigma}{dq^2 dE_\nu} = \frac{1}{32\pi M E_\nu^2} \cdot \frac{1}{2} \sum_{j,spin} \left| T(\nu N \to l N_j^*) \right|^2 \delta(W^2 - M_j^2) \tag{3.14}$$

where M is the mass of the target nucleon, E_ν is neutrino energy, W is the invariant mass of the hadronic system (or the mass of the intermediate baryon resonance), M_j is the mass of the baryon resonance (N_j^*), and $T(\nu N \to l N^*)$ is the amplitude of resonance production, which is calculated using the FKR (Feynman-Kislinger-Ravndal) model [77]. The invariant mass, W, is restricted to be less than $2\,\mathrm{GeV/c^2}$. For W larger than $2\,\mathrm{GeV}$, the interactions are simulated as deep-inelastic scattering as described in Section 3.3.3. The differential cross-section for the resonance with finite decay width Γ can be derived by replacing the δ-function with a Breit-Wignar factor :

$$\delta(W^2 - M_j^2) \quad \to \quad \frac{1}{2\pi} \cdot \frac{\Gamma}{(W - M_j)^2 + \Gamma^2/4} \tag{3.15}$$

For a single-meson production, the axial vector mass M_A is also set to be $1.11\,\mathrm{GeV}$ experimentally [65]. Total of 18 resonances are simulated in our simulation. The Pauli blocking effect in the decay of the baryon resonance is considered by requiring the momentum of the nucleon to be greater than the Fermi surface momentum. Pion-less decay of Δ resonance in ^{16}O nuclei, where about 20 % of the events don't have a pion in the decay, is also simulated [79]. Figures 3.9, 3.10 and 3.11 show the cross-sections of charged current and neutral current resonant single-meson productions for our calculations and the experimental data.

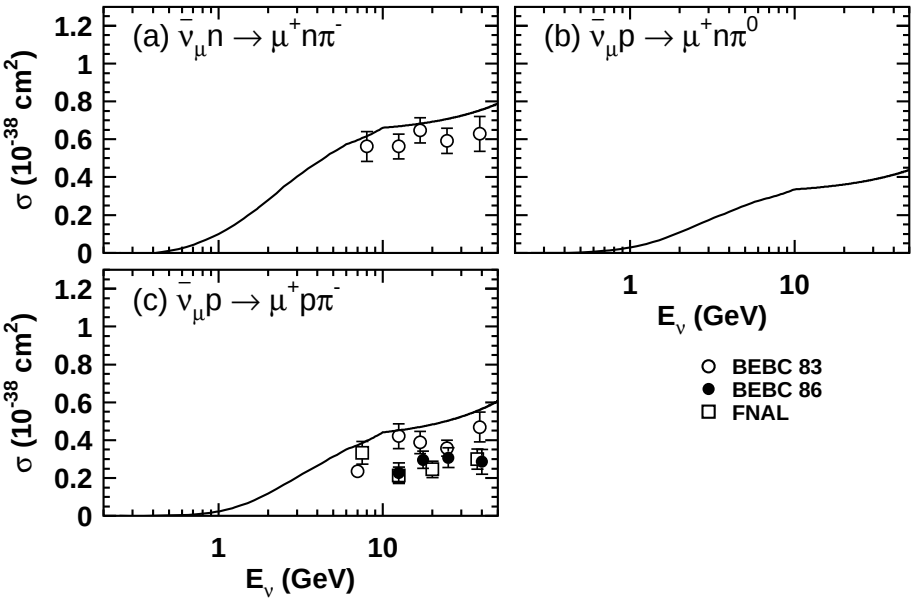

Figure 3.10: Cross-sections for charged current single pion productions of $\overline{\nu}_\mu$. (a) $\overline{\nu}_\mu n \to \mu^+ n\pi^-$, (b) $\overline{\nu}_\mu p \to \mu^+ n\pi^0$, (c) $\overline{\nu}_\mu p \to \mu^+ p\pi^-$. Solid lines show the result of our calculations. Experimental data are from BEBC [85, 82] and FNAL [86].

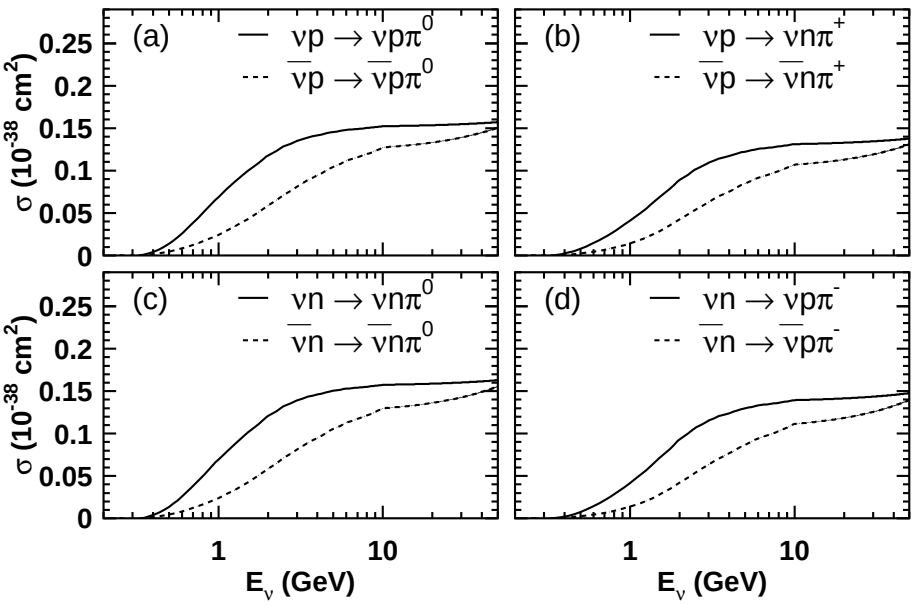

Figure 3.11: Cross-sections for neutral current single pion productions of ν_μ and $\overline{\nu}_\mu$. Solid(dashed) lines show the result of our calculations for $\nu_\mu(\overline{\nu}_\mu)$ interactions.

The uncertainty in total cross-sections for single pion productions is estimated from the different between the FKR model [77] and the model calculation based on [78] to be 20 %. The uncertainty in the single pion production cross-section for each π^+, π^0 and π^- production is also estimated from the model difference to be 20 %.

3.3.3 Deep Inelastic Scattering

The cross-section of charged current deep inelastic scattering is calculated by integrating the following equation in the range of the invariant mass $W > 1.3\,\mathrm{GeV}/c$ [126] :

$$\begin{aligned}
\frac{d^2\sigma^{\nu,\bar{\nu}}}{dxdy} &= \frac{G_F^2 M_N E_\nu}{\pi}\left((1-y+\frac{y^2}{2}+C_1)F_2(x,q^2) \pm y(1-\frac{y}{2}+C_2)xF_3(x,q^2)\right) \\
C_1 &= \frac{yM_l^2}{4M_N E_\nu x} - \frac{xyM_N}{2E_\nu} - \frac{m_l^2}{4E_\nu^2} - \frac{m_l^2}{2M_N E_\nu x} \\
C_2 &= -\frac{m_l^2}{4M_N E_\nu x}
\end{aligned} \tag{3.16}$$

where $x = -q^2/(2M(E_\nu - E_l))$ and $y = (E_\nu - E_l)/E_\nu$ are Bjorken scaling parameters, M_N is the nucleon mass, m_l is the outgoing lepton mass, E_ν and E_l are the energy of incoming neutrino and outgoing lepton in the laboratory frame, respectively. The nucleon structure functions F_2 and xF_3 are taken from GRV94 [88].

In our simulation, the cross-section of deep inelastic scattering induced by neutral current are assumed to have the following relations which are estimated from experimental results [89, 90] :

$$\frac{\sigma(\nu N \to \nu X)}{\sigma(\nu N \to \mu^- X)} = \begin{cases} 0.26 & (\ E_\nu < 3\,\mathrm{GeV}\ ) \\ 0.26 + 0.04\,(E_\nu/3 - 1) & (\ 3\,\mathrm{GeV} \le E_\nu < 6\,\mathrm{GeV}\ ) \\ 0.30 & (\ E_\nu \ge 6\,\mathrm{GeV}\ ) \end{cases} \tag{3.17}$$

$$\frac{\sigma(\bar{\nu} N \to \bar{\nu} X)}{\sigma(\bar{\nu} N \to \mu^+ X)} = \begin{cases} 0.39 & (\ E_\nu < 3\,\mathrm{GeV}\ ) \\ 0.39 - 0.02\,(E_\nu/3 - 1) & (\ 3\,\mathrm{GeV} \le E_\nu < 6\,\mathrm{GeV}\ ) \\ 0.37 & (\ E_\nu \ge 6\,\mathrm{GeV}\ ) \end{cases} \tag{3.18}$$

The kinematics of the hadronic system is simulated by two different methods according to the range of invariant mass. In the region of $1.3\,\mathrm{GeV}/c^2 < W < 2.0\,\mathrm{GeV}/c^2$, only pions are considered as outgoing mesons. The mean multiplicity of pions is estimated from the result of Fermilab 15-foot hydrogen bubble chamber experiment [91] :

$$\langle n_\pi \rangle = 0.09 + 1.83 \ln(W^2) \tag{3.19}$$

The number of pions in each event is determined by using KNO (Koba-Nielsen-Olsen) scaling. Since the range of W overlaps with that in single pion production, $n_\pi \ge 2$ is required in this W region. The forward-backward asymmetry of pion multiplicity in the hadronic center of mass system is included using the results from BEBC experiment [92] :

$$\frac{n_\pi^F}{n_\pi^B} = \frac{0.35 + 0.41 \ln(W^2)}{0.5 + 0.09 \ln(W^2)} \tag{3.20}$$

In the region of $W > 2.0\,\mathrm{GeV}/c^2$, the kinematics of the hadronic system are calculated by using JETSET/GRV94 package [93]. This package treats not only π but also K, η, ρ and so on.

For neutrino energy above a few ten GeV, the cross-section calculation agrees with the experimental measurement within 5 %, but in the lower energy region, the uncertainty is large. The difference between the model calculation based on [126] and A. Bodek and U. K. Yang [127] are considered as a systematic error. The difference in these two models depends on the square of 4-momentum transfer q^2 and is quite large in a few GeV energy region.

3.3.4 Coherent Pion Production

The coherent pion production is a neutrino interaction with a oxygen nucleus, which remains intact, and one pion with the same charge as the incoming weak current is produced. Since very little momentum is transferred to the oxygen nucleus, the angular distributions of the outgoing leptons and pions are peaked in the forward direction. The formalism developed by Rein and Sehgal [94] is used to simulate the interactions, and the differential cross-section is given by :

$$\begin{aligned} \frac{d^3\sigma}{dQ^2dydt} &= \beta \times \frac{G_F^2 M}{2\pi^2} f_\pi^2 A^2 E_\nu (1-y) \frac{1}{16\pi} (\sigma_{total}^{\pi N})^2 \\ &\quad \times (1+r^2)(\frac{M_A^2}{M_A^2+Q^2})^2 e^{-b|t|} F_{abs} \qquad (3.21) \\ r &= Re(f_{\pi N}(0))/Im(f_{\pi N}(0)) \qquad (3.22) \end{aligned}$$

where β is the axial vector couping constant and is 1 (2) for neutral current (charged current) interactions, G_F is the weak coupling constant, M is the nucleon mass, f_π is pion decay constant and is $0.93\,m_\pi$, A is the atomic number ($=16$ for oxygen), E_ν is the neutrino energy, y is the lepton fractional energy loss, $\sigma_{total}^{\pi N}$ is the averaged pion-nucleon cross-section, b is in the order of the nucleus transverse dimensions and is $80\,\mathrm{GeV}^{-2}$, M_A is the axial-vector mass, Q^2 is the square of the four–momentum transfer of the lepton, and t is the square of the four-momentum transfer to the nucleus, F_{abs} is a factor to account for the absorption of pions in the nucleus. $f_{\pi N}(0))$ in r is the πN scattering amplitude. However, the K2K experiment set an upper limit on the cross-section of coherent CC pion production [96]. The upper limit was significantly lower than the predicted cross-section by Rein and Sehgal. Therefore some modification is necessary to the Monte Carlo coherent pion production cross-sections. The calculated cross-sections of the coherent pion production for the CC and NC interactions by Kartavtsev and Paschos [95], agree better with the several experimental data than that of Rein and Sehgal as shown in Figure 3.12. In this thesis, events due to coherent pion production are re-weighted by the cross-section ratio, $\sigma_{\mathrm{KartavtsevandPaschos}}(\mathrm{E}_\nu)/\sigma_{\mathrm{ReinandSehgal}}(\mathrm{E}_\nu)$. Namely, we use the cross-section by Kartavtsev and Paschos in this thesis. The difference between the experimental data and the model proposed by Kartavtsev and Paschos is taken into account as a systematic uncertainty of 100 %.

3.3.5 Nuclear Effects

It is also important to simulate the secondary interactions of mesons produced in neutrino interactions with nucleons inside the ^{16}O nuclei. All of the mesons produced within the ^{16}O nuclei are tracked from their production points until they exit or are absorbed in the nuclei. This is done for π, K and η by using a cascade model in our simulation. The interactions of pions

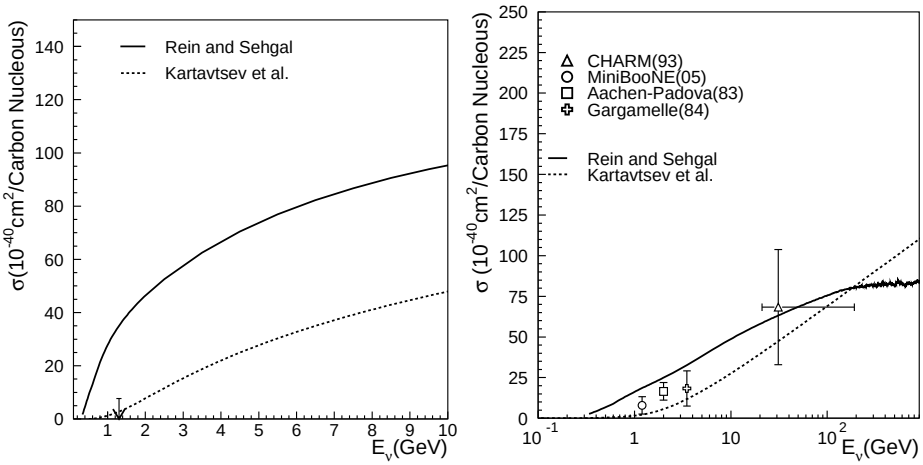

Figure 3.12: The cross-sections of coherent pion productions off the carbon nucleus for CC interaction(left) and NC interaction(right) by two models with the experimental data. The solid lines are calculation by Rein and Sehgal, while the dashed lines are by Kartavtsev and Paschos. On the left figure, the arrow shows the experimental upper limit by K2K [96] and on the right figure, experimental data are from CHARM [97], MiniBooNE [98], Aachen-Padove [99] and Gargamelle [100].

are especially important since the cross-section for pion productions are large for $E_\nu > 1\,\mathrm{GeV}$, and the pion-nucleon interaction cross-section is also large. The pion interactions in ^{16}O nuclei considered in our simulation are : inelastic scattering, charge exchange, and absorption. First, the initial pion production point in the nucleus, where neutrino-nucleon interactions occur, is determined by the Wood-Saxon density distribution [101] :

$$\rho(r) = \frac{Z}{A}\rho_0 \frac{1}{1+\exp(\frac{r-c}{a})} \tag{3.23}$$

where ρ_0 is the average density of the nucleus, a and c are the density parameters, Z is the atomic number, and A is the mass number. For ^{16}O nucleus : $\rho_0 = 0.48\,m_\pi^3$, $a = 0.41\,\mathrm{fm}$, $c = 2.69\,\mathrm{fm}$, $Z = 8$ and $A = 16$. The pion interaction is determined from the calculated mean-free path for each interactions, which is modeled by L. Salcedo *et al.* [102]. The mean-free path of pions depends on their momenta and positions in the nucleus. In the interactions, the Fermi motion of the nucleus and the Pauli blocking are considered, and the outgoing nucleon must have the energy above the Fermi surface momentum defined by :

$$p_F(r) = \left(\frac{3}{2}\pi^2\rho(r)\right)^{\frac{1}{3}}. \tag{3.24}$$

The angular and momentum distributions of the outgoing pions are determined by using the results of a phase shift analysis from π - N scattering experiments [103]. The pion interaction simulation is tested using the experimental data for the following three interactions : π - ^{12}C scattering, π - ^{16}O scattering, and pion photo-production ($\gamma + ^{12}\mathrm{C} \to \pi^- + X$) [104, 105] as shown in Figure 3.13. For kaons, the elastic scattering and charge exchange interactions are considered

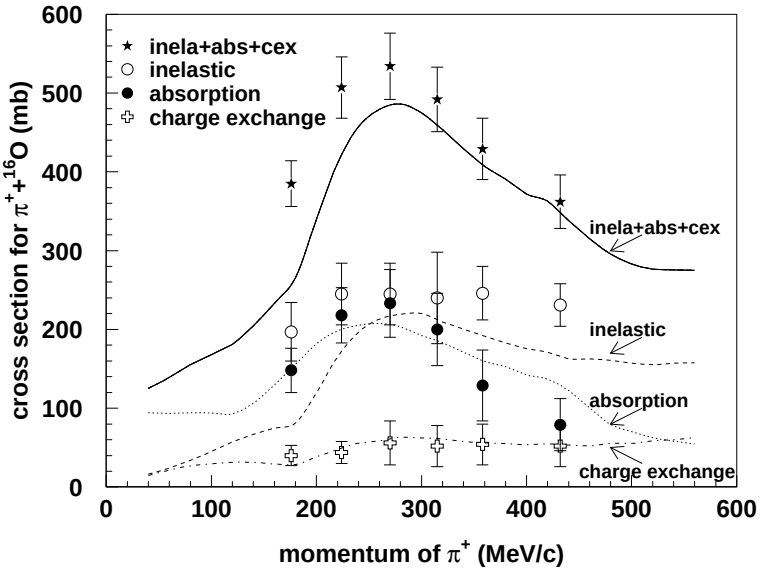

Figure 3.13: The cross-sections of π^+-^{16}O scattering as a function of π^+ momentum. The lines are the cross-sections calculated by our simulation for each interaction mode, and the experimental data points are taking from [105].

using the results from the cross-sections measured by the $K^{\pm}$-N scattering experiments [106, 107, 108]. For η mesons, the absorption ($\eta N \to N^* \to \pi(\pi)N$) is considered [109]. These pions are tracked as described above.

In our simulation, the nucleon re-scattering inside the oxygen nucleus is also considered using the cascade model, which is similar to that for the pion simulation. With the cross-sections obtained from nucleon-nucleon scattering experiments [110], the interactions of elastic scattering and resonance production processes for nucleon propergating through the ^{16}O nucleus are simulated in NEUT [111]. The pions from delta decay are traced by the method described above.

3.4 Upward-Going Muon

The prediction of upward-going muon signals is also calculated by Monte Carlo method using the identical tools to that for the vertex contained events. The energy range and the target volume are extended for upward-going muons. The energy range of the atmospheric flux is extended up to 100 TeV, which is calculated by M.Honda *et al.* [14] up to 7 TeV, and by L.V.Volkova [112] above that. The target volume of neutrino interactions is extended to the rock around the detector. The composition of the rock is set to be SiO_2 with the density 2.7 g/cm^3. Neutrino interactions occur in the water of the OD are also considered. The output of the Monte Carlo simulation are passed through the same reduction and event reconstruction process as that for the observed data.

γ	(e^+, e^-) pair production
	Compton scattering
	Photoelectric effect
$e^\pm$	Multiple scattering
	Ionization and δ-rays production
	Bremsstrahlung
	Annihilation of positron
	Generation of Cherenkov radiation
$\mu^\pm$	Decay in flight
	Multiple scattering
	Ionization and δ-rays production
	Bremsstrahlung
	Direct (e^+, e^-) pair production
	Nuclear interaction
	Generation of Cherenkov radiation
Hadrons	Decay in flight
	Multiple scattering
	Ionization and δ-rays production
	Hadronic interactions
	Generation of Cherenkov radiation

Table 3.1: List of the processes considered in simulator.

3.5 Detector Simulation

The produced particles in neutrino interactions are fed into a detector simulation code, which simulates the tracks of particles, the generation and propagation of Cherenkov photons in water, and the PMT response and the readout electronics.

The detector simulation has been developed based on GEANT package [113]. Table 3.1 lists various processes which are considered in our simulation program. The hadronic interactions in water are simulated using CALOR package [114]. This package is known to reproduce the pion interactions well including low energy region ($\sim 1\,\mathrm{GeV}/c$). For still lower energy region ($p_\pi \leq 500\,\mathrm{MeV}/c$), a custom program [115] based on experimental data from $\pi - {}^{16}\mathrm{O}$ scattering [116] and $\pi - p$ scattering [117] is used in our simulation code.

The uncertainty in the hadron simulation is estimated by comparing the model used in our detector simulation, CALOR [114], and the FLUKA model. The uncertainty affects the contamination of NC interactions in single-ring μ-like, i.e. hadrons (mostly pions) in NC interactions are identified as μ-like events. The difference from the FLUKA model is assumed to be a systematic error.

Chapter 4

Data Reduction

4.1 Overview

The Super-Kamiokande detector collects about 10^6 events per day (except for the super low energy triggered events) and most of the events are cosmic ray muons and low energy background from radioactivities such as radon decay. The efficient event selection is required to select neutrino events from a large quantity of data.

The atmospheric neutrino events observed in Super-Kamiokande are classified into the following four categories; fully contained (FC), partially contained (PC), upward stopping muons and upward through-going muons as shown in Figure 4.1. For FC and PC events, the vertices of neutrino interactions are required to be within a fiducial volume, 2 m from the ID wall. If the tracks of entire particles are contained inside the ID, the event is classified into FC. If one of the particles exits the ID and deposits energy in the OD, the event is classified into PC. The upward-going muons are produced by the atmospheric muon neutrinos via charged-current interactions in the rock surrounding the detector. Since the downward-going neutrino-induced muons cannot be distinguished from the cosmic ray muons, only muons traveling in the upward-going direction are selected. The upward going stopping muons enter from outside the detector and stop inside the ID, while the upward through-going muons enter the detector and exit the ID.

The neutrino energy range for each event class are, ~ 1 GeV for FC, ~ 10 GeV for PC, ~ 10 GeV for upward stopping muons, and ~ 100 GeV for upward through-going muons. Figure 4.2 shows the expected number of neutrino events in each category as a function of neutrino energy.

A data sample for each event class goes through a different reduction process. To separate FC and PC events, the number of hit PMTs in the OD hit cluster (NHITAC, see Section 4.3.2) is used, where hit cluster means the spatial cluster of neighboring hit PMTs. Figure 4.3 shows the NHITAC distribution for both FC and PC final samples in the fiducial volume. FC and PC events are clearly separated at NHITAC = 10 (16) for SK-I (SK-II). Since the reflective sheet covered on the OD wall is exchanged to a new one improving the reflectivity in SK-II, the number of the OD hits is increased and the cut criterion is tuned. The systematic uncertainties for FC/PC separation are estimated to be 0.9 % for SK-I and 0.5 % for SK-II by comparing the NHITAC distributions for the data and the Monte Carlo events.

The reduction processes are basically automated and are the same for SK-I and SK-II except for some of the event selection criteria because of the difference in the number of the ID PMTs.

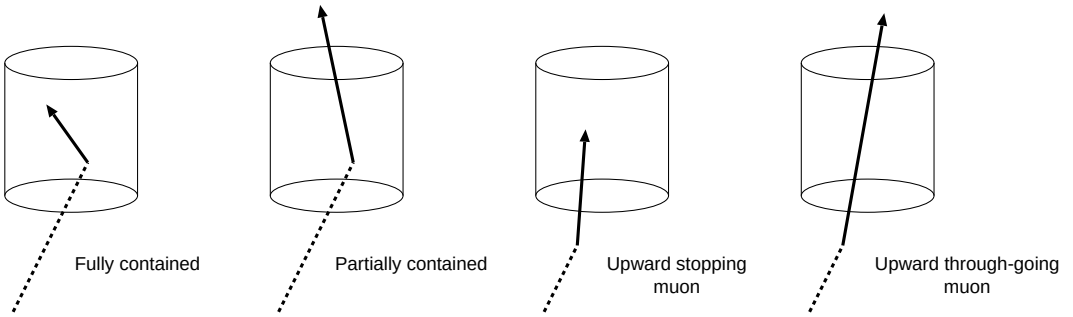

Figure 4.1: Categories of atmospheric neutrino events in Super-Kamiokande. Dashed lines show trajectories of primary neutrinos, and solid arrows show those of secondary charged particles.

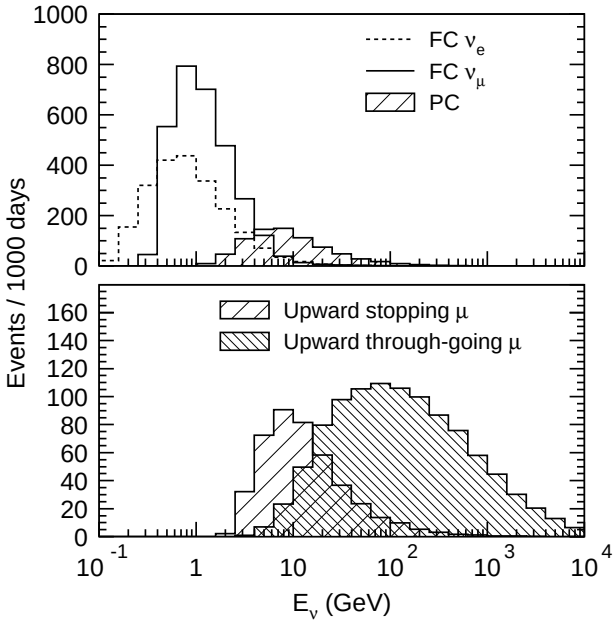

Figure 4.2: The expected parent neutrino energy distribution for each event class.

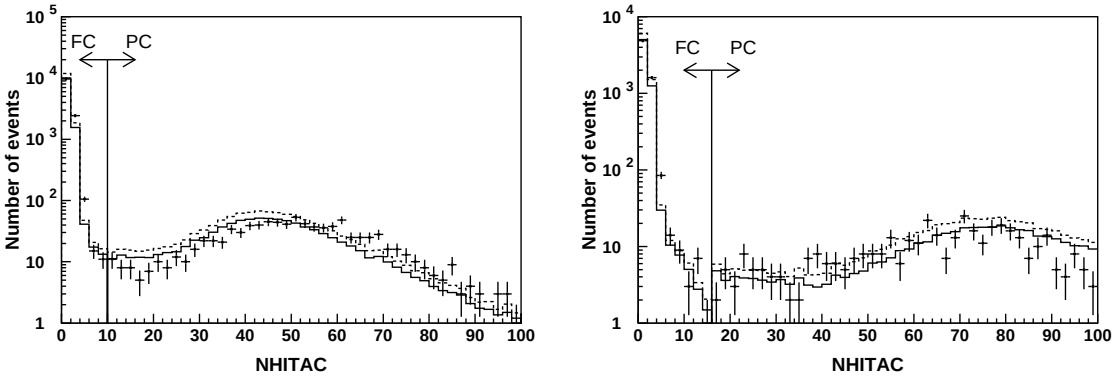

Figure 4.3: NHITAC distributions for FC and PC final samples for SK-I (left) and SK-II (right). The points show the observed data, and histograms show the atmospheric neutrino Monte Carlo events assuming no oscillation (dashed lines) and $\nu_\mu \leftrightarrow \nu_\tau$ 2-flavor oscillation with $(\sin^2 2\theta,\, \Delta m^2) = (1.00,\, 2.5 \times 10^{-3}\,\mathrm{eV}^2)$ (solid lines).

In this section the procedures of the data reduction for FC, PC and upward-going muon events are described.

4.2 Reduction for Fully Contained Sample

There are five steps in FC reduction process. The main background sources are cosmic ray muons, low energy events from radio isotopes and electrical noise events.

4.2.1 First Reduction

The selection criteria of the FC 1st reduction are the following :

(1) PE_{300} should be ≥ 200 p.e.s (100 for SK-II).
PE_{300} is the maximum number of total p.e.s observed by the ID PMTs in a sliding 300 nsec time window.

and

(2) NHITA_{800} should be ≤ 50 or OD trigger is off.
NHITA_{800} is the number of hit OD PMTs in a fixed 800 nsec time window from -400 nsec to $+400$ nsec before and after the trigger timing.

and

(3) TDIFF should be $> 100\,\mu$sec
TDIFF is a time interval to the previous event.

Criterion (1) rejects the low energy background events from radio isotopes. Figure 4.4 shows the PE_{300} distributions for the raw data and the FC final events. The 200 p.e.s (100 p.e.s for SK-II) corresponds to 22 MeV/c of electron momentum. Since the events which have visible energy below 30 MeV are not used in the analysis, this cut is safe. Criterion (2) removes the

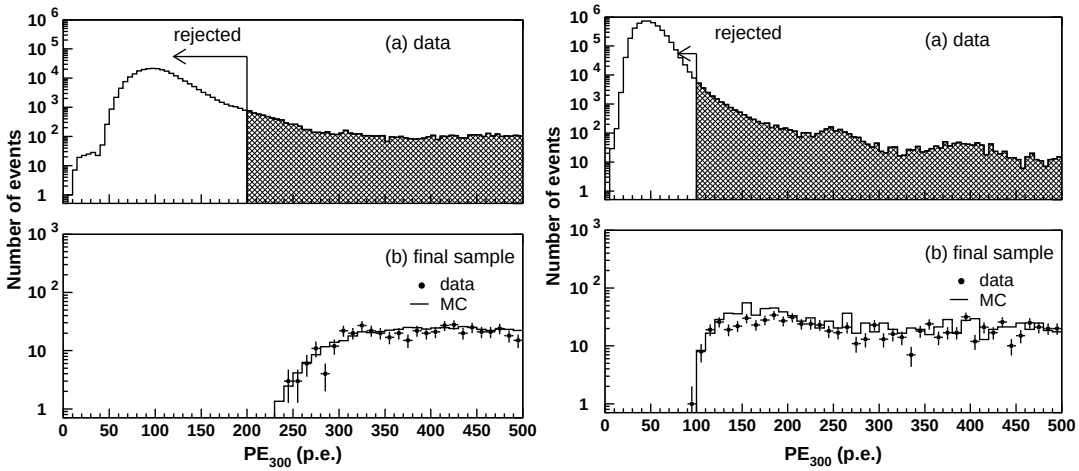

Figure 4.4: PE_{300} distribution for (a) the raw data and (b) the final FC data and atmospheric neutrino Monte Carlo events (no oscillation) in FC final samples for SK-I (left) and SK-II (right). The number of the Monte Carlo events in (b) is normalized to that of the data. The selection criterion is shown by arrows.

cosmic ray muon events. Figure 4.5 shows the $NHITA_{800}$ distributions for the raw data, FC atmospheric neutrino Monte Carlo events and the FC final events. Criterion (3) removes the electron events from the decay of the cosmic ray muons stopped in the ID. The events within 30 μsec after the selected events by the above criteria are selected to keep the decay electrons. These events are attached to the fully contained event candidates as sub-events and not counted as a primary atmospheric neutrino event. These cuts reduce the data size from 10^6 events/day to 3000 (2200) events/day for SK-I (SK-II).

4.2.2 Second Reduction

In the second reduction, the low energy events and cosmic ray muons are rejected. The selection criteria of the FC 2nd reduction are the following :

(1) $NHITA_{800}$ should be ≤ 25 if $PE_{tot} < 100{,}000$ p.e.s (50,000 for SK-II) or OD trigger is off.

and

(2) PE_{max}/PE_{300} should be < 0.5.
PE_{max} is the maximum number of p.e.s observed by an ID PMT.

Criterion (1) is to reject cosmic ray muons by tighter threshold than the 1st reduction as shown in Figure 4.5 by solid lines. The second cut removes the low energy events and electrical noise events, which have one larger hit signal from a single PMT. Figure 4.6 shows the PE_{max}/PE_{300} distributions for the data after the 1st reduction, FC atmospheric neutrino Monte Carlo events and the FC final events. A PMT sometimes flashes because of a discharge around the dynode structure. The flashing PMT tends to record a very large charge. The flasher

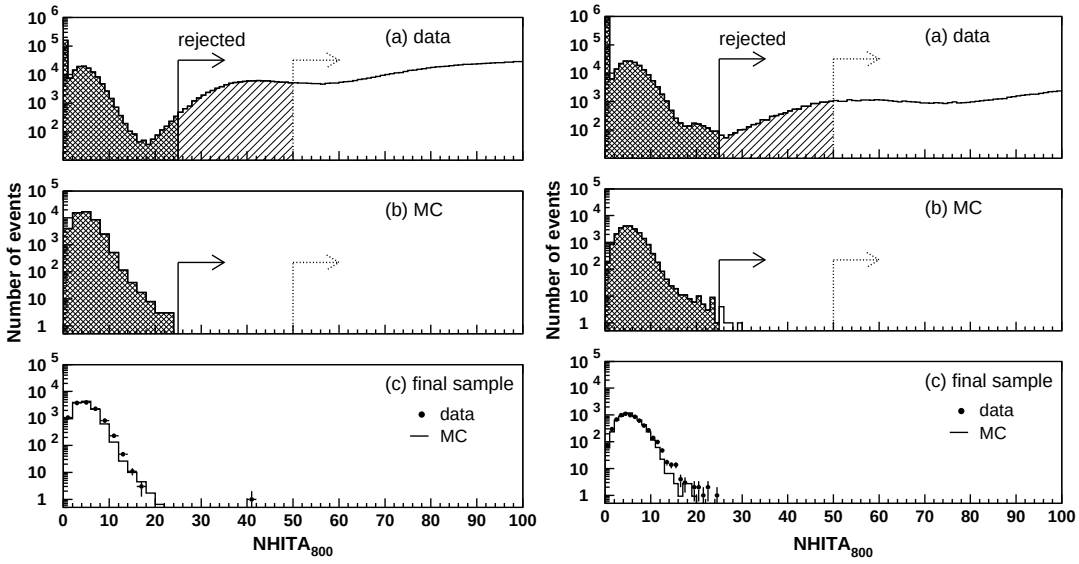

Figure 4.5: NHITA_{800} distributions for (a) the raw data, (b) fully contained atmospheric neutrino Monte Carlo events whose vertex position is more than 2 m away from the ID wall and (c) final samples of the data and the Monte Carlo events for SK-I (left) and SK-II (right). The number of the Monte Carlo events in (c) is normalized to that of the data. The arrows written by dotted (solid) lines show the selection criteria in the FC 1st (2nd) reduction.

events due to such a noisy PMT are rejected further in the next step. The event rate is 200 (280) events/day for SK-I (SK-II) after the FC 2nd reduction.

4.2.3 Third Reduction

After the 1st and 2nd reduction steps, remaining background events are mostly noise events and cosmic ray muons which have a small number of OD hits.

Through-going muon cut

The through-going muons are very energetic and deposit a lot of charge in the ID. To eliminate these events, a special through-going muon fitter is applied if the number of p.e.s in any single PMT is larger than 230 p.e.s. This fitter selects the entrance point, which is the point of the earliest hit PMT with some neighboring hit PMTs and the exit point, which is defined the center of the saturated ID PMTs. Then, if the goodness of the fit is greater than 0.75, and the number of hit OD PMTs around the reconstruted muon entrance or exit point is more than 9, the events are rejected as through-going muons. In SK-II, the condition to apply a special through-going muon fitter is modified to additionally require that number of hit ID PMTs exceeds 1000. The rejection criteria are summarized :

(1) $\mathrm{PE}_{\mathrm{max}} > 230$ p.e.s (and NHIT > 1000 for SK-II)

and

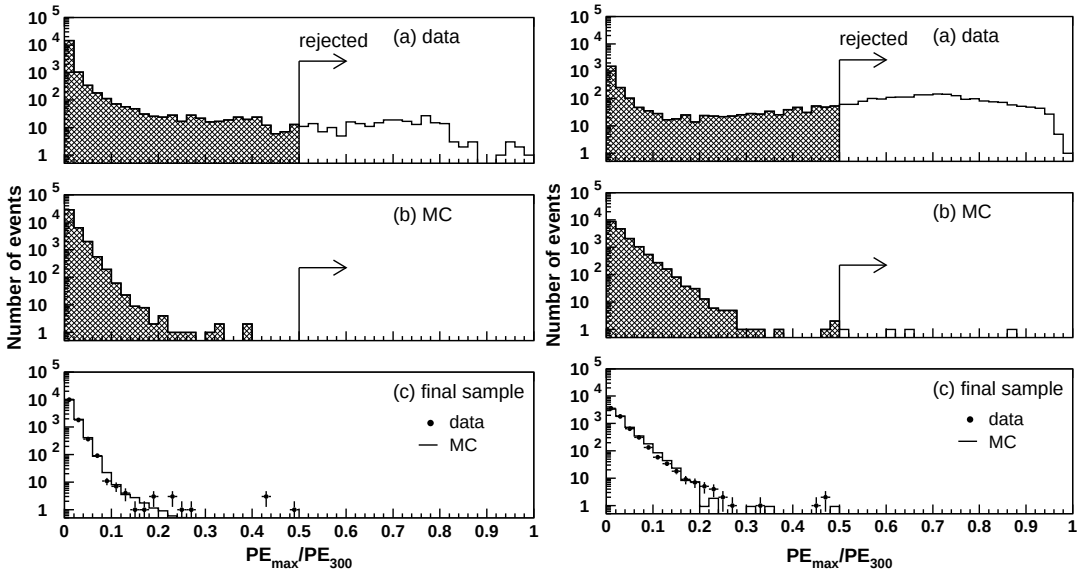

Figure 4.6: PE_{max}/PE_{300} distribution for (a) the data after the FC 1st reduction, (b) fully contained atmospheric neutrino Monte Carlo events and (c) final samples of the data and the the Monte Carlo events for SK-I (left) and SK-II (right). The number of the Monte Carlo events in (c) is normalized to that of the data. The selection criteria are shown by arrows.

(2) goodness of through-going muon fit > 0.75

and

(3) $\mathrm{NHITA_{in}} \geq 10$ or $\mathrm{NHITA_{out}} \geq 10$
$\mathrm{NHITA_{in}}$ ($\mathrm{NHITA_{out}}$) is the number of hit OD PMTs located within 8 m from the entrance (exit) point in a fixed 800 nsec time window.

The goodness of through-going muon fit is defined as :

$$goodness \quad = \quad \frac{1}{\sum_i \frac{1}{\sigma_i^2}} \times \sum_i \frac{1}{\sigma_i^2} \exp\left(-\frac{(t_i - T_i)^2}{2(1.5 \times \sigma_i)^2}\right) \tag{4.1}$$

where t_i and σ_i are the observed hit time of the i-th PMT and its resolution, and T_i is the hit time expected from the entering time of muon and its track. Figure 4.7 and 4.8 show the number of hit OD PMTs near the entrance and the exit points for the data after the 2nd reduction, the FC atmospheric neutrino Monte Carlo events and the FC final events satisfying the above criteria (1) and (2).

Stopping muon cut

To eliminate stopping muons, a stopping muon fitter is applied, which finds the entrance point in the similar way as through-going muon fit. The events satisfying the following criteria are classified as stopping muons and removed :

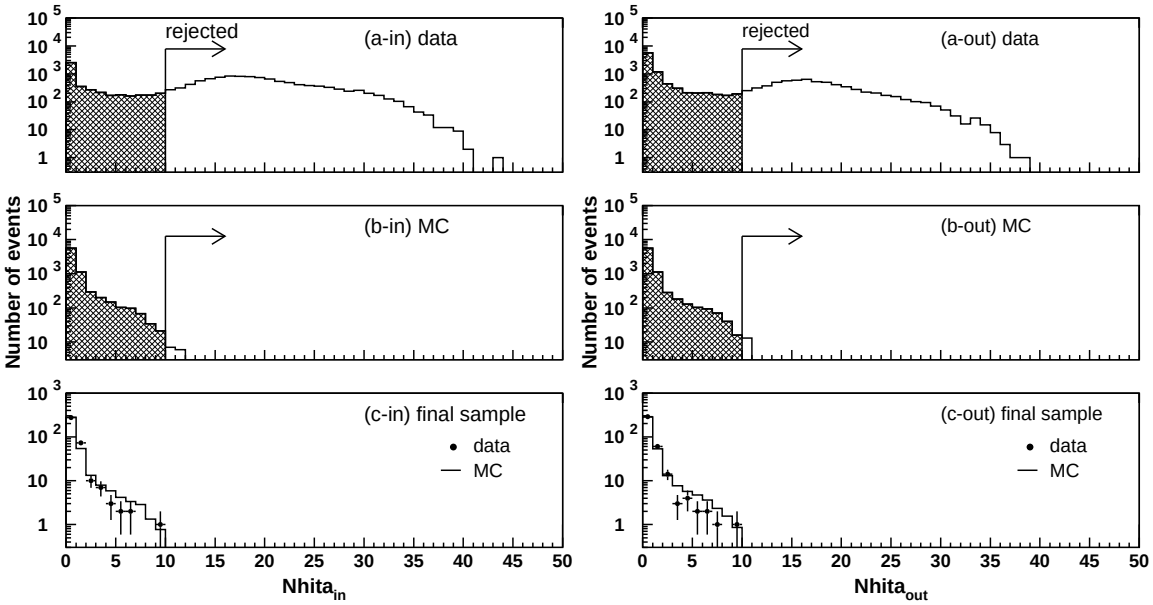

Figure 4.7: Number of hit OD PMTs within 8 m of the entrance point (left) of muons and within 8 m of the exit position (right) for (a) the data after FC 2nd reduction, (b) fully contained atmospheric neutrino Monte Carlo events and (c) final samples for SK-I. The number of the Monte Carlo events in (c) is normalized to that of the data. The selection criteria are shown by arrows.

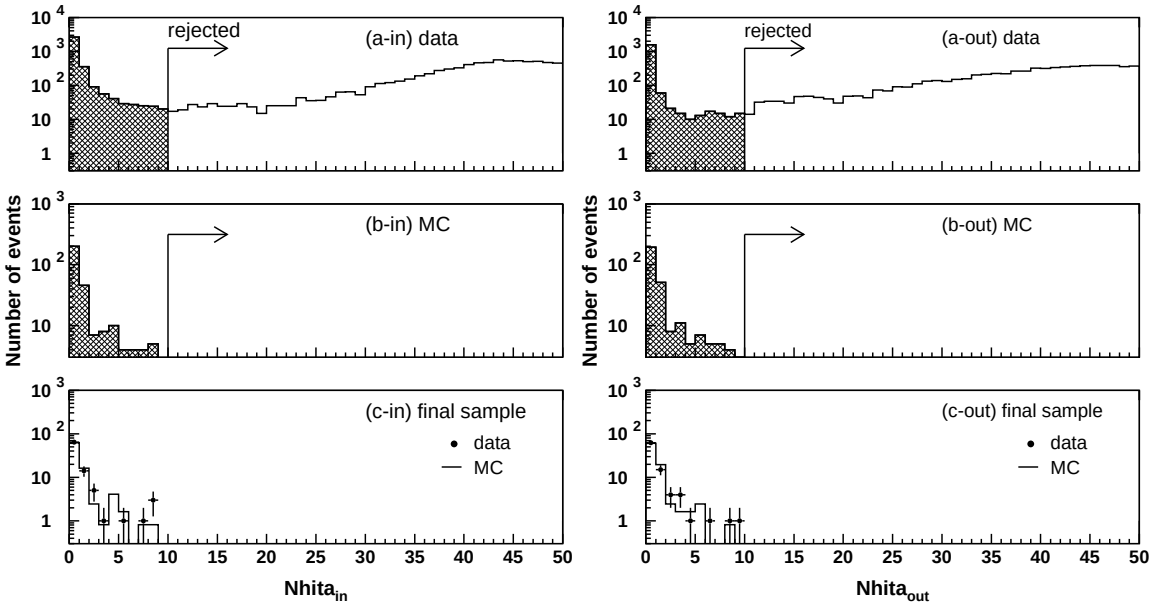

Figure 4.8: Number of hit OD PMTs within 8 m of the entrance point (left) of muons and within 8 m of the exit position (right) for (a) the data after FC 2nd reduction, (b) fully contained atmospheric neutrino Monte Carlo events and (c) final samples for SK-II. The number of the Monte Carlo events in (c) is normalized to that of the data. The selection criteria are shown by arrows.

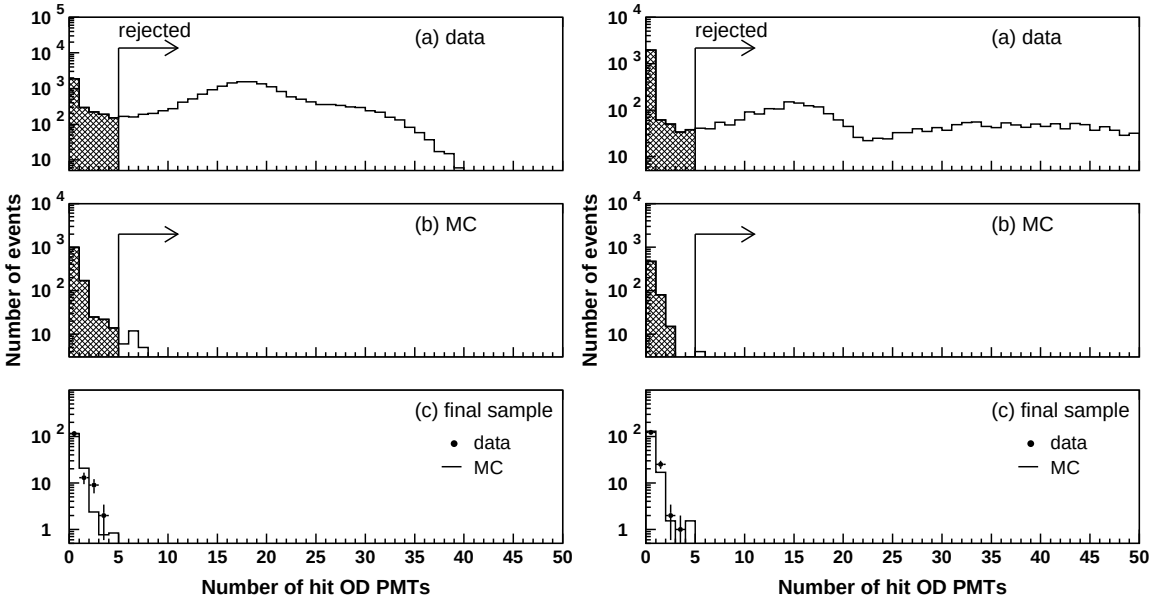

Figure 4.9: Number of hit OD PMTs near the entrance point of muons for (a) the data after FC 2nd reduction, (b) fully contained atmospheric neutrino Monte Carlo events and (c) final samples satisfying a condition, goodness > 0.5 for SK-I (left) and SK-II (right). The number of the Monte Carlo events in (c) is normalized to that of the data. The selection criteria are shown by arrows.

(1) $\mathrm{NHITA_{in}} \geq 10$
or
$\mathrm{NHITA_{in}} \geq 5$ if goodness of stopping muon fit > 0.5
$\mathrm{NHITA_{in}}$ is the number of hit OD PMTs located within 8 m from the entrance point in a fixed 800 nsec time window.

The direction of muon is reconstructed to maximize the total number of p.e.s inside the cone with a half opening angle 42°. The goodness definition is same as that of through-going muon fit. Figure 4.9 shows $\mathrm{NHITA_{in}}$ distributions for the data after the 2nd reduction, the FC atmospheric neutrino Monte Carlo events and the FC final events satisfying the condition, goodness > 0.5.

Cable hole muons

On top of the detector tank, there are twelve cable holes to take signal and HV supply cables out. Four holes out of twelve are directly above the ID and block the OD. Cosmic ray muons going through these holes would not leave any OD signal and could be detected as contained neutrino events. To eliminate this mis-identification possibility, a set of veto counters (2 m $\times$ 2.5 m plastic scintillation counters) were installed in April, 1997 (see Figure 4.10). The rejection criteria for cable hole muons are :

(1) One veto counter hit

and

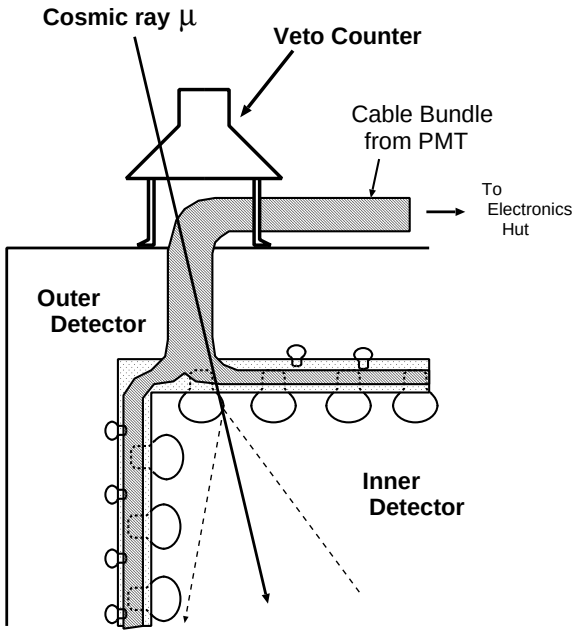

Figure 4.10: A schematic view of a cable-hole muon and a veto counter.

(2) $L_{veto} < 4\,m$
L_{veto} is the distance from the cable hole to the the reconstructed vertex.

Figure 4.11 shows the reconstructed vertex distribution for the FC 1-ring μ-like events before and after the installation of veto counters. Cable hole muons are well eliminated by veto counters as shown in this figure.

Flasher event cut

Flasher events usually have a broad hit timing distribution compared with that of the neutrino events. The cut criteria to eliminate these flasher events for SK-I are :

(1) $NMIN_{100} \geq 14$
or
$NMIN_{100} \geq 10$ if the number of hit ID PMTs < 800
$NMIN_{100}$ is the minimum number of hit ID PMTs in a sliding 100 nsec time window from +300 nsec to +800 nsec after the trigger.

For SK-II, the cut criteria are :

(1) $NMIN_{100} \geq 20$

Figure 4.12 shows the timing distribution of (i) a typical flashing PMT event and (ii) a typical FC neutrino event and the time window for $NMIN_{100}$ is shown by arrows.

Figure 4.13 and 4.14 shows $NMIN_{100}$ distributions for the data after the 2nd reduction, the FC atmospheric neutrino Monte Carlo events and the FC final events.

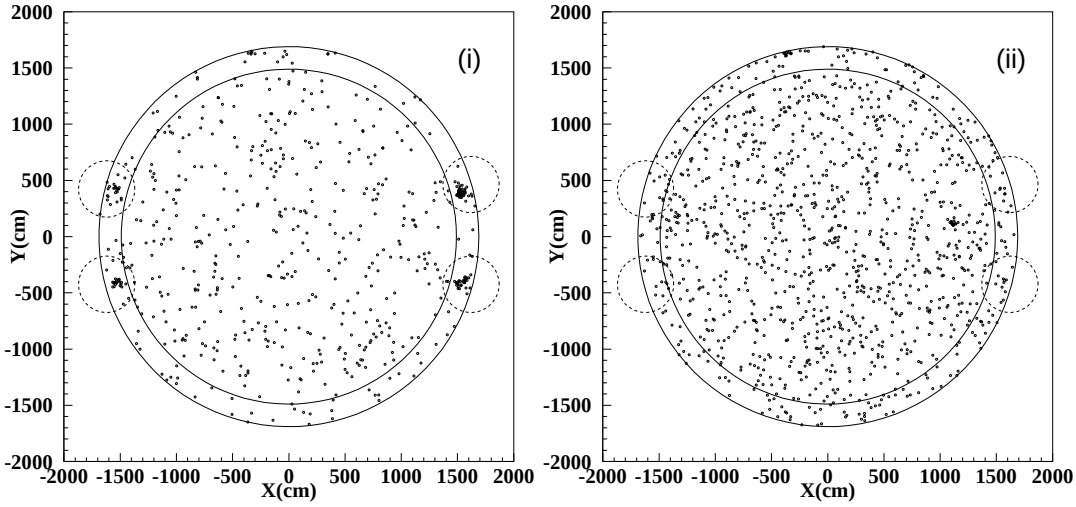

Figure 4.11: Reconstructed vertex distribution for the fully contained 1-ring μ-like events (i) before the installation of the veto counters and (ii) after installation. The outer solid circle shows the ID wall and the inner solid circle shows the fiducial volume (2 m from the wall). Small dashed circles indicate the positions of the veto counters. Four clusters are clearly seen around cable holes for data without veto counters, while no cluster is visible for data after the installation.

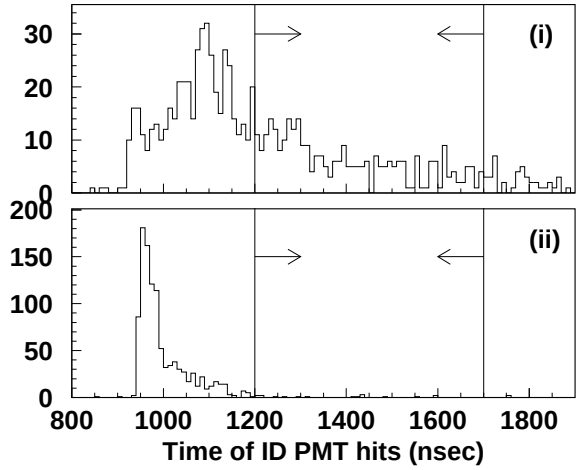

Figure 4.12: The timing distribution of (i) a typical flashing PMT event and (ii) a typical FC neutrino event. The arrows show the time window for counting NMIN_{100}.

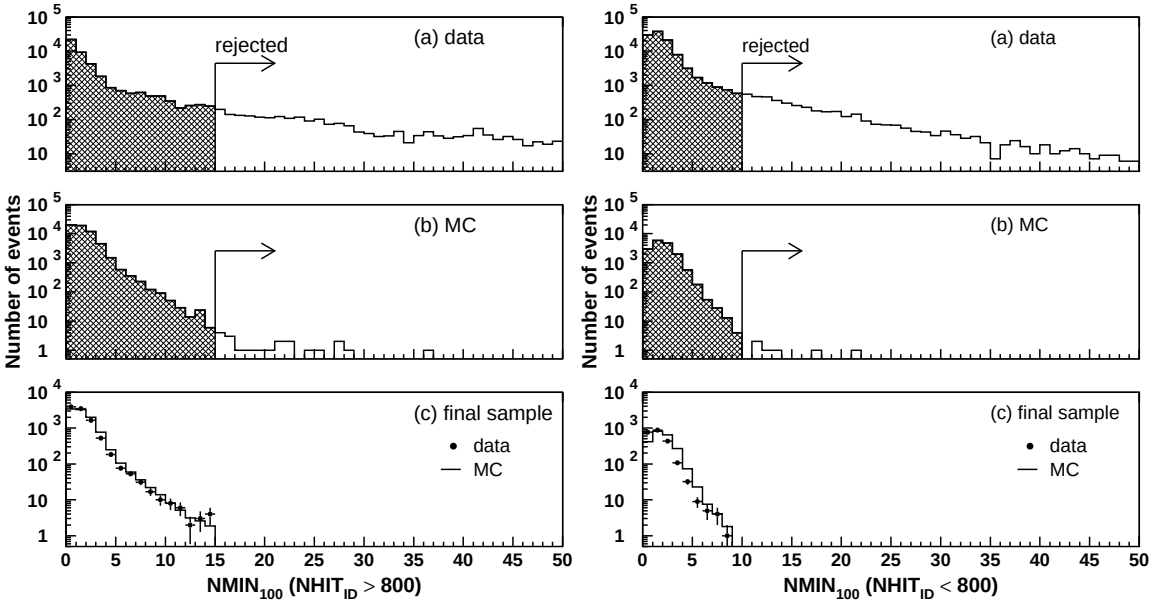

Figure 4.13: $NMIN_{100}$ distributions (left) for the events with more than 800 hit PMTs in the ID and (right) less than 800 hit PMTs for SK-I. Three figures show (a) the data after FC 2nd reduction, (b) fully contained atmospheric neutrino Monte Carlo events and (c) final samples, respectively. The number of the Monte Carlo events in (c) is normalized to that of the data. The selection criteria are shown by arrows.

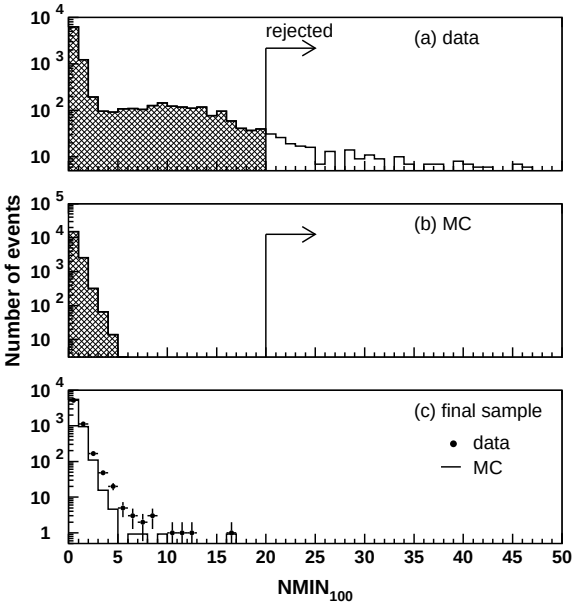

Figure 4.14: $NMIN_{100}$ distributions for SK-II. Three figures show (a) the data after FC 2nd reduction, (b) fully contained atmospheric neutrino Monte Carlo events and (c) final samples, respectively. The number of the Monte Carlo events in (c) is normalized to that of the data. The selection criteria are shown by arrows.

Accidental coincidence events cut

The accidental coincidence occurs when a low energy event forms the trigger and a cosmic ray muon event follows in a single trigger gate. These events are not rejected in the former reduction because of the absence of the OD activities on the trigger timing and the large number of total p.e.s in the ID due to the muons. The accidental coincidence events are removed by the following cuts :

(1) $NHITA_{off} \geq 20$
$NHITA_{off}$ is the number of hit OD PMTs in a fixed 500 nsec off-timing window from +400 nsec to +900 nsec after the trigger timing.

and

(2) $PE_{off} > 5000$ p.e.s (2500 for SK-II)
PE_{off} is the number of p.e.s observed by ID PMTs in a fixed 500 nsec off-timing window from +400 nsec to +900 nsec.

Low energy events cut

The remaining low energy events are from the decay of radio isotopes and the electrical noise. Events satisfying the following criteria are removed as low energy background events :

(1) $NHIT_{50} < 50$ (25 for SK-II)
$NHIT_{50}$ is the number of hit ID PMTs in a sliding 50 nsec time window.

where NHIT_{50} is counted after subtracting the time of flight (TOF) of each observed photon assuming all photons are generated at a point. The vertex is determined as the position at which the timing residual distribution is peaked. NHIT_{50}=50 corresponds to visible energy of 9 MeV and is low enough not to lose efficiency for contained neutrino events with $\mathrm{E}_{\mathrm{vis}}$ >30 MeV.

After the FC third reduction, the event rate is 45 (21) events/day for SK-I (SK-II).

4.2.4 Fourth Reduction

In the fourth reduction, an intelligent pattern matching algorithm is used to further remove the remaining flasher events. Flasher events usually repeat with similar hit patterns in the detector in the course of hours and days. These repeated events are not likely to be caused by neutrinos. Figure 4.15 shows the scatter plots of $\mathrm{N}_{\mathrm{match}}$ and the maximum value of the estimator r for the data after the FC 3rd reduction and atmospheric neutrino Monte Carlo events. For the Monte Carlo events, the data which were removed as flasher events in this reduction stage are mixed, and the estimator r is calculated. The cut criteria are also shown in Figure 4.15.

The algorithm of the pattern matching is as follows :

(1) Divide the ID wall into 1450 patches of 2 m×2 m square.

(2) Compute the correlation factor r by comparing the total charge in each patch of two events, A and B. The correlation is defined as :

$$r = \frac{1}{N}\sum_i \frac{\left(Q_i^A - \langle Q^A\rangle\right)\times\left(Q_i^B - \langle Q^B\rangle\right)}{\sigma_A \times \sigma_B} \tag{4.2}$$

where N is the number of the patches, and $\langle Q^{A(B)}\rangle$ and $\sigma_{A(B)}$ are the averaged charge and its standard deviation for event A and B, respectively.

(3) Calculate the distance ($\mathrm{DIST}_{\mathrm{max}}$)between the PMTs with the maximum pulse heights in the two compared events

(4) If $\mathrm{DIST}_{\mathrm{max}} < 75$ cm, an offset value is added to r :r=r+0.15.

(5) If r exceeds the threshold(r_{th}), events A and B are recognized as matched events. r_{th} is defined as :

$$r > r_{th} = 0.168 \times \log_{10}((\mathrm{PE}^A_{\mathrm{tot}} + \mathrm{PE}^B_{\mathrm{tot}})/2.) + 0.130, \tag{4.3}$$

where $\mathrm{PE}_{\mathrm{tot}}$ is the total number of p.e.s observed in the ID.

(6) Repeat the above calculation over 10,000 events around the target event and count the number of matched events.

(7) Remove the events with large correlation factor r, or large number of matched events.

The event rate after the fourth reduction is 18 events/day for both SK-I and SK-II.

4.2.5 Fifth Reduction

The remaining background events are removed by several criteria specialized for each kind of background events.

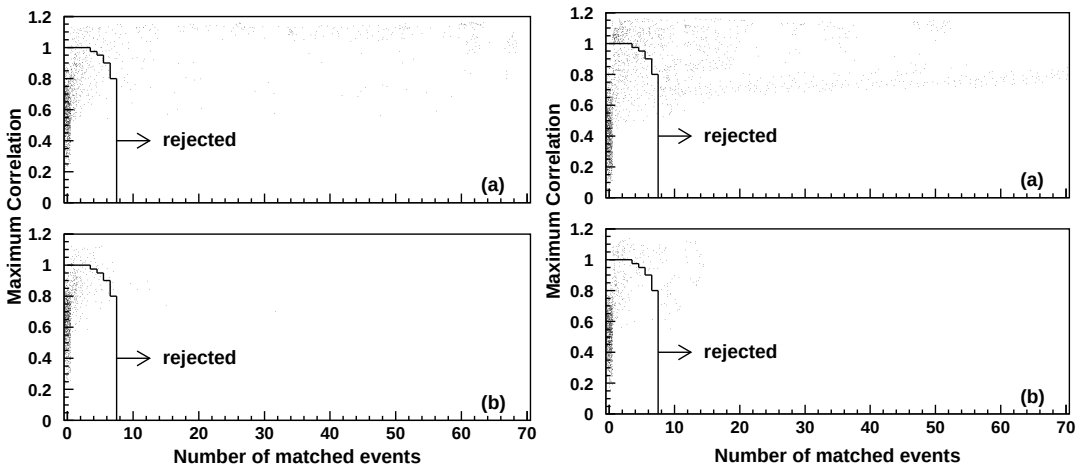

Figure 4.15: Scatter plots of N_{match} and the maximum value of the estimator r for (a) the data after the FC 3rd reduction and (b) atmospheric neutrino Monte Carlo events for SK-I (left) and SK-II (right). The cut criteria are shown by arrows.

Stopping muon cut

The remaining stopping muons are rejected by tighter criteria than those in the third reduction stage. Events satisfying the following criteria are rejected :

(1) $NHITA_{in} \geq 5$
$NHITA_{in}$ is the number of hit OD PMTs located within 8 m from the entrance point in a sliding 200 nsec time window from -400 nsec to $+400$ nsec.

The entrance position in the OD is estimated by a backward extrapolation from the reconstructed vertex determined by TDC-fit (see Section 5.2.1). Figure 4.16 shows $NHITA_{in}$ distributions for the data after the 4th reduction, the FC atmospheric neutrino Monte Carlo events and the FC final events.

Invisible muon cut

Invisible muon events are caused by cosmic ray muons with momenta less than the Cherenkov threshold and the subsequent decay electrons being observed. These events are characterized by a low energy signal from decay electron and a signal in the OD before the trigger timing. Events which satisfy the following cut criteria are rejected as invisible muons :

(1) $PE_{tot} < 1000$ p.e.s (500 for SK-II)
PE_{tot} is the total number of p.e.s observed in the ID.

and

(2) $NHITAC_{early} > 4$
$NHITAC_{early}$ is the maximum number of hit PMTs in the OD hit cluster in a sliding 200 nsec time window from -8800 nsec to -100 nsec.

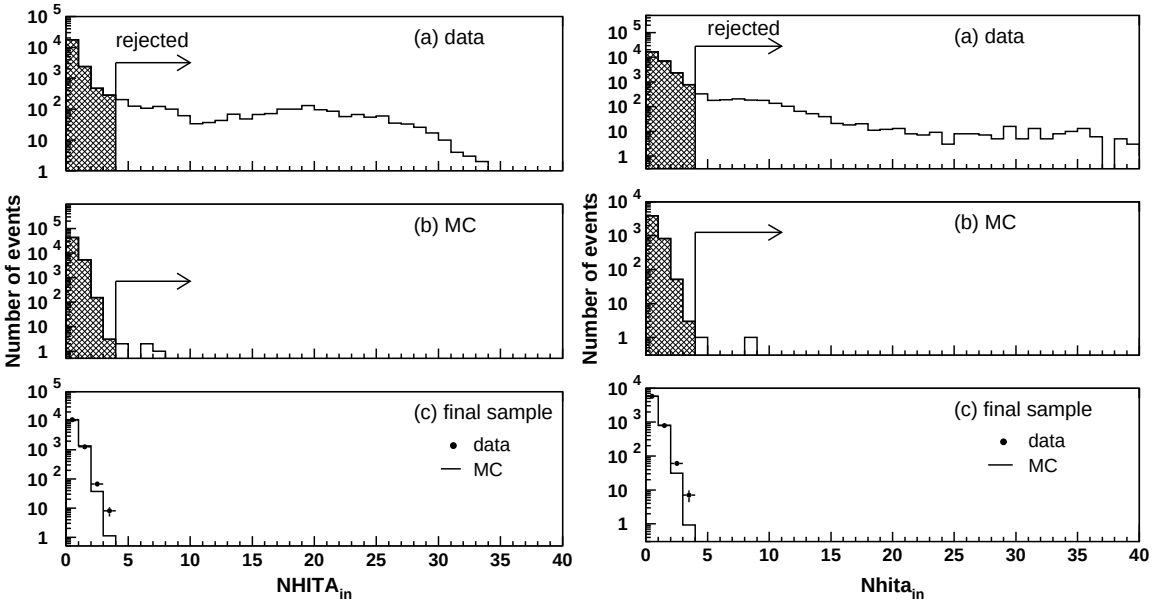

Figure 4.16: $\mathrm{NHITA_{in}}$ distribution for (a) the data after FC 4th reduction and (b) fully contained atmospheric neutrino Monte Carlo events, and (c) final samples. The number of the Monte Carlo events in (c) is normalized to that of the data for SK-I (left) and SK-II (right). The selection criteria are shown by arrows.

and

(3) $\mathrm{NHITAC_{early}} + \mathrm{NHITAC_{500}} > 9$ if $\mathrm{DIST_{clust}} < 500\,\mathrm{cm}$
$\mathrm{NHITAC_{early}} > 9$ otherwise

$\mathrm{NHITAC_{500}}$ is the number of hit PMTs in the OD hit cluster in a fixed 500 nsec time window from -100 nsec to $+400$ nsec.
$\mathrm{DIST_{clust}}$ is a distance between two OD hit clusters, which are used for the $\mathrm{NHITAC_{early}}$ and the $\mathrm{NHITAC_{500}}$.

Figure 4.17 shows the $\mathrm{NHITAC_{early}}$ distribution for the data after the FC 4th reduction, fully contained atmospheric neutrino Monte Carlo events and final samples, satisfying criterion (1) and $\mathrm{DIST_{clust}} > 500\,\mathrm{cm}$. Although the number of hit PMTs in off-timing window for data is larger than that for the Monte Carlo simulation, the cut is safe for FC sample.

Coincidence muon cut

The remaining accidental coincidence muon events are removed by :

(1) $\mathrm{PE_{500}} < 300$ p.e.s (150 for SK-II)
$\mathrm{PE_{500}}$ is the total number of p.e.s observed in the ID in a fixed 500 nsec time window from -100 nsec to $+400$ nsec.

and

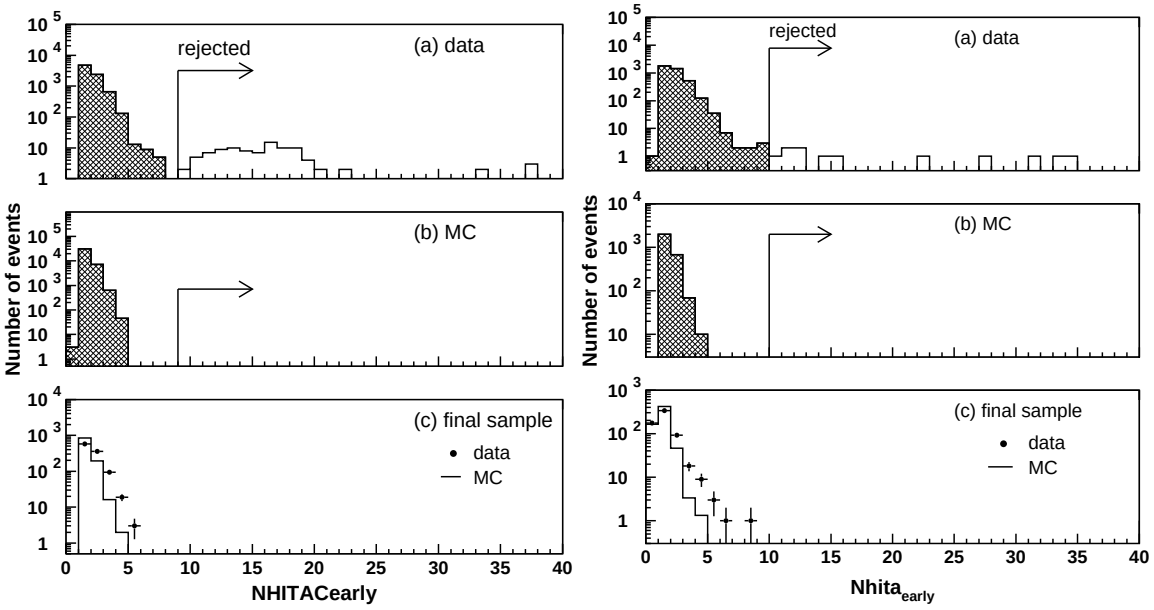

Figure 4.17: $\mathrm{NHITAC_{early}}$ distribution for (a) the data after FC 4th reduction and (b) fully contained atmospheric neutrino Monte Carlo events, and (c) final samples, satisfying criterion (1) and $\mathrm{DIST_{clust}} > 500\,\mathrm{cm}$ for SK-I (left) and SK-II (right). The number of the Monte Carlo events in (c) is normalized to that of the data. The selection criteria are shown by arrows.

(2) $\mathrm{PE_{late}} \geq 20\,\mathrm{p.e.s}$
$\mathrm{PE_{late}}$ is the maximum number of hit OD PMTs in a 200 nsec sliding time window from +400 nsec to +1600 nsec.

Figure 4.18 shows the $\mathrm{PE_{late}}$ distribution for the data after the FC 4th reduction, fully contained atmospheric neutrino Monte Carlo events and final samples, satisfying the criterion (1). The cut is safe for FC sample.

Long-tail flasher cut

This is a stricter version of flasher cut in the FC 3rd reduction stage. Events satisfying the following criterion are removed as flasher events :

(1) $\mathrm{NMIN_{100}} > 5$ if the goodness of point fit < 0.4
$\mathrm{NMIN_{100}}$ is the minimum number of the hit ID PMTs in a sliding 100 nsec time window from +300 nsec to +800 nsec.

For SK-II, in addition to the criteria above, the extra cuts are applied :

(3) Goodness of point fit < 0.3

and

(4) $\mathrm{NHITMIN_{100}} < 6$

See Section 5.2.1 for the explanation of point fit.

After the fifth reduction, the FC event rate is 16 events/day for both SK-I and SK-II.

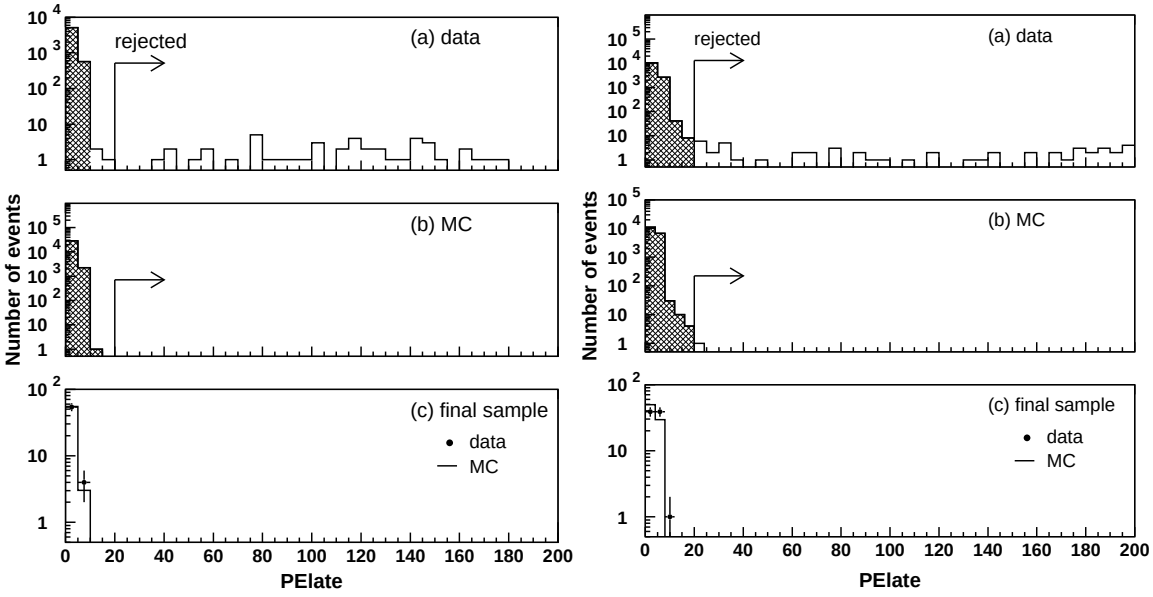

Figure 4.18: PE_{late} distribution for (a) the data after FC 4th reduction and (b) fully contained atmospheric neutrino Monte Carlo events, and (c) final samples, satisfying criterion (1) for SK-I (left) and SK-II (right). The number of the Monte Carlo events in (c) is normalized to that of the data. The selection criteria are shown by arrows.

4.2.6 FC Reduction Summary

Finally, the fully contained neutrino events are selected by applying the FC event cuts :

- Vertex of neutrino interactions should be inside the fiducial volume (2 m from the ID PMT surface).
- The number of hit PMTs in the highest charge OD cluster (NHITAC) should be less than 10 (16 for SK-II).
- Visible energy (E_{vis}) should be greater than 30 MeV.

The detection efficiencies in each reduction step are estimated by the atmospheric neutrino events as shown in Table 4.1. The detection efficiency for final events is estimated to be 97.6 % and 99.2 % for SK-I and SK-II, respectively. The systematic uncertainty of FC reduction is estimated to be 0.2 % for both SK-I and SK-II. The event rate of FC events for real data is shown in Figure 4.34 and is 8.18±0.07 (8.26±0.10) events/day for SK-I (SK-II).

The main sources of the background for FC events are cosmic ray muons, flasher events and neutrons from the rock around the detector. These background events are largely rejected by requiring fiducial volume cut. The contaminations of the backgrounds are estimated as shown in Table 4.2.

Reduction step	SK-I (%)	SK-II (%)
1st reduction	99.95	99.92
2nd reduction	99.94	99.89
3rd reduction	99.85	99.71
4th reduction	99.17	99.39
5th reduction	99.15	99.32
Final cut	97.59	99.17

Table 4.1: The detection efficiency in the each reduction step for SK-I and SK-II for events whose true vertices are in the fiducial volume, NHITAC less than 10 (16 for SK-II) and E_{vis} larger than 30 MeV. In the last line, the fitted vertex is used.

SK-I	Sub-GeV		Multi-GeV	
	($E_{vis} < 1330 MeV/c$)		($E_{vis} \geq 1330 MeV/c$)	
	e-like(%)	μ-like(%)	e-like(%)	μ-like(%)
Cosmic ray μ	—	0.07	—	0.09
Flashing PMT	0.42	—	0.16	—
Neutron event	0.1	—	0.1	—
SK-II	Sub-GeV		Multi-GeV	
	e-like(%)	μ-like(%)	e-like(%)	μ-like(%)
Cosmic ray μ	—	0.01	—	0.07
Flashing PMT	0.27	—	0.65	—
Neutron event	0.1	—	0.1	—

Table 4.2: Summary of the estimated upper limit of the contamination of each background.

4.3 Reduction for Partially Contained Sample

Since PC events have the OD activities by its definition, the reduction scheme is different from that that of FC events and it is rather difficult to eliminate cosmic ray muon backgrounds. There are five steps in PC reduction process.

4.3.1 First Reduction

The aim of the 1st reduction is to reject the through-going cosmic ray muons and low energy events. The selection criteria of the PC 1st reduction are as follows :

(1) PE_{tot} should be ≥ 1000 p.e.s (500 for SK-II).
PE_{tot} is the number of p.e.s observed in the ID.

and

(2) TWIDA should be ≤ 260 nsec (170 nsec for SK-II).
TWIDA is the width of the hit timing distribution in the OD PMTs.

and

(3) NCLSTA should be ≤ 1 (only for SK-I).
NCLSTA is the number of the hit clusters in the OD.

Exiting particles in the PC sample, mostly muons, must have at least 2 m track length in the ID, which corresponds to the momentum loss of 500 MeV/c for muons. In criterion (1), PE_{tot} should be larger than 1000 p.e.s (500 for SK-II), which corresponds to 310 MeV/c for muons. The second criteria rejects the through-going muons. The through-going muon events have a broad hit timing distribution and two hit clusters around the entrance and exit point in the OD. Figure 4.19 shows the TWIDA distribution for the raw data, partially contained atmospheric neutrino Monte Carlo events and final samples. Since the reflected photon in the OD is increased and the quantum efficiency of OD PMTs is increased in SK-II, the hit timing becomes broad. Therefore TWIDA is redefined by the counted hit OD PMTs with the threshold of 2 p.e.s in SK-II (it was 0 p.e. in SK-I) and the cut criterion for TWIDA is tuned. The hit cluster means the spatial cluster of neighboring hit PMTs. A hit cluster is formed around the PMT which detects more than 8 p.e.s and the clusters within 8 m are merged.

The event rate after the PC 1st reduction is 14000 (36000) events/day for SK-I (SK-II).

4.3.2 Second Reduction

In the second reduction, another clustering algorithm of OD hit is used to reject the remaining through-going muons and the stopping muons. The OD (ID) walls are divided into 11×11 (21×21) patches and the charge observed in each patch is counted. The clusters are formed by looking for the charge gradient to the neighboring patches. The algorithm is illustrated in Figure 4.20. Events satisfying the following criteria remain after the PC 2nd reduction for SK-I :

(1) NCLSTA2 should be ≤ 1
NCLSTA2 is the number of the OD hit clusters including more than 6 hit PMTs.

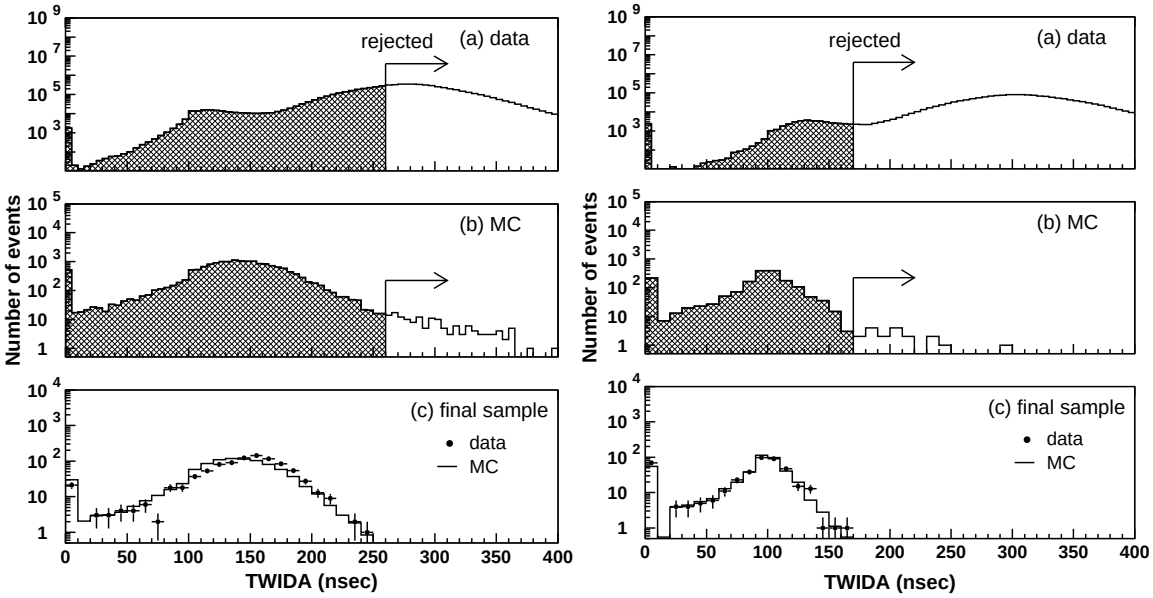

Figure 4.19: TWIDA distributions for (a) the raw data, (b) partially contained atmospheric neutrino Monte Carlo events whose vertex position is more than 2 m away from the ID wall and (c) final samples of the data and the Monte Carlo events for SK-I (left) and SK-II (right). The number of the Monte Carlo events in (c) is normalized to that of the data. The selection criteria are shown by arrows.

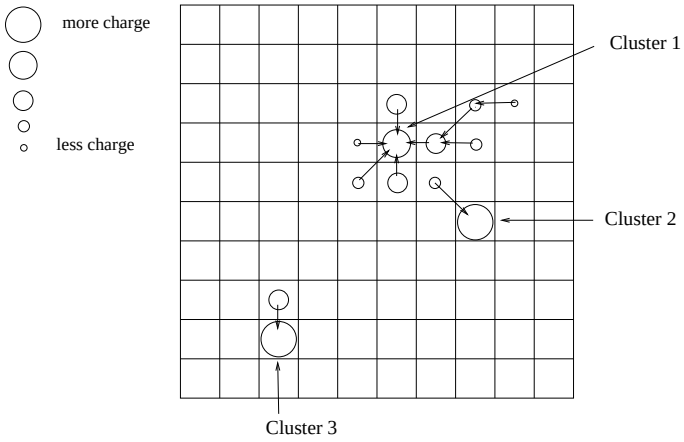

Figure 4.20: A schematic view of the algorithm to find hit clusters in the PC 2nd reduction. The circles represent the charge observed in each patch. The size of the circle is proportional to the number of p.e.s . The arrows represent the vector charge gradient, which point to the highest charge among the neighboring patches.

and

(2) $NHITAC_{min}$ should be < 7
$NHITAC_{min}$ is the minimum number of hit PMTs among top (or bottom) and side regions in the OD hit cluster.

and

(3) PE_{200} should be > 1000 p.e.s if NCLSTA2 $= 1$
PE_{200} is the number of the observed p.e.s within 200 cm from the highest charge PMT in the ID hit cluster closest to the OD hit cluster.

For SK-II, the criteria are tuned to keep the reduction efficiency.

(1) NCLSTA2(2) should be ≤ 1
NCLSTA2(2) is the number of the 2nd OD hit clusters including more than 10 hit PMTs.

and

(2) $NHITA_{endcap} < 20$ or $NHITA_{endcap} < MAX(NHITA_{side})$
$MAX(NHITA_{side})$ is defined as :
$MAX(NHITA_{side} = \exp(5.8\text{-}0.023\times\ NHITA_{side})$ if $NHITA_{side} < 75$
$MAX(NHITA_{side} = \exp(4.675\text{-}0.008\times\ NHITA_{side})$ if $NHITA_{side} \geq 75$
$NHITA_{endcap}$ is the number of OD hit PMTs in the top and bottom region.
$NHITA_{side}$ is the number of hit OD PMTs in the side region.

(3) $NHITAC2 < 12 + 0.085 \times PE_{200}$
NHITAC2 is the number of the OD hit PMTs in the 2nd cluster.

Criteria (2) for both SK-I and SK-II reject corner clipping muons, which left the hit PMTs in both top (or bottom) and side regions in the OD. Figure 4.21 shows the $NHITAC_{min}$ distributions for the data, atmospheric neutrino Monte Carlo events after the PC 1st reduction and final samples for SK-I. Figure 4.22 shows the scatter plots of the $NHITA_{endcap}$ and the $NHITA_{side}$ for the same samples. In criteria (3) for SK-I and SK-II, the number of p.e.s in the ID hit cluster located behind the OD hit cluster is used to reject the stopping muons. Figure 4.23 shows the scatter plots of the NCLSTA2 and the PE_{200} for the data, atmospheric neutrino Monte Carlo events after the PC 1st reduction and final samples for SK-I. Figure 4.24 shows the scatter plots of the NHITAC2 and the PE_{200} for the data, atmospheric neutrino Monte Carlo events after the PC 1st reduction and final samples for SK-II.

The event rate after the PC 2nd reduction is 2000 (5500) events/day for SK-I (SK-II).

4.3.3 Third Reduction

In the third reduction flasher events and cosmic ray stopping muons are rejected. The flasher events are rejected by the same way as that in the FC 3rd reduction, in which the broad timing distribution of the flasher events is used for cut. Events which satisfy the following criteria are rejected as flasher events for both SK-I and SK-II :

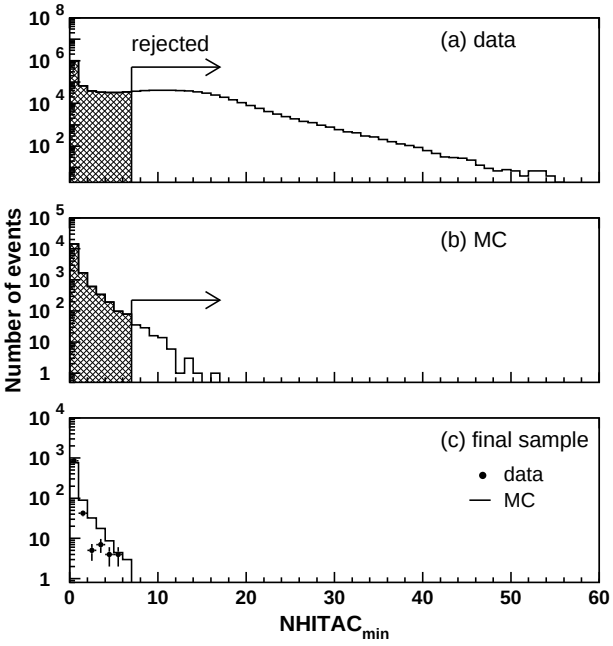

Figure 4.21: NHITAC$_{\rm min}$ distributions for (a) the data, (b) partially contained atmospheric neutrino Monte Carlo events after the PC 1st reduction and (c) final sample of the data and the Monte Carlo events for SK-I. The selection criteria are shown by arrows.

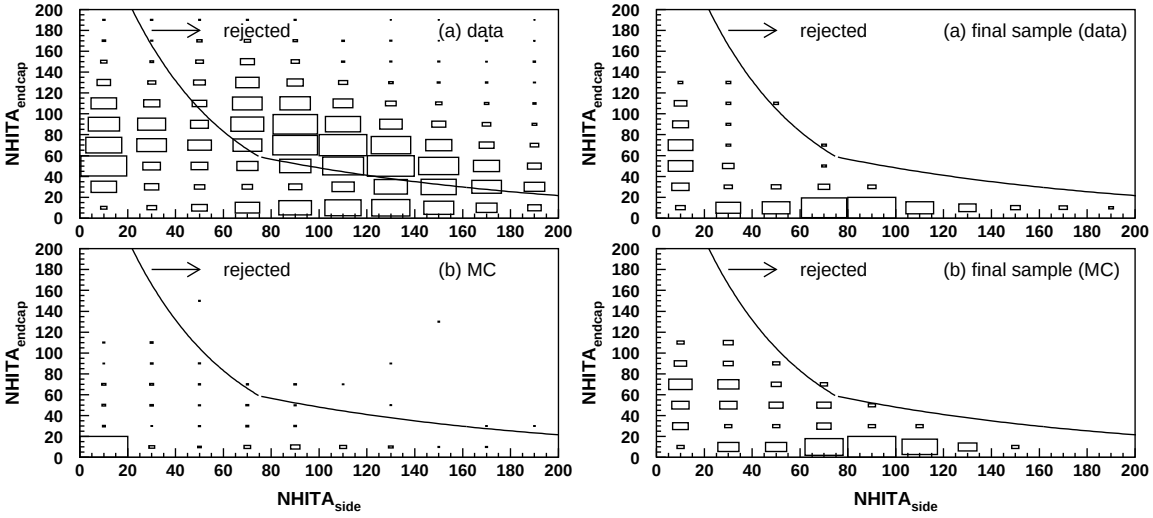

Figure 4.22: Scatter plots of NHITA$_{\rm endcap}$ and NHITA$_{\rm side}$ for (a) the data and (b) partially contained atmospheric neutrino Monte Carlo events after the PC 1st reduction and (c) final samples of the data and (d) the Monte Carlo events for SK-II. The size of the boxes shows the number of the events in each bin. The cut criteria are shown by the lines and arrows.

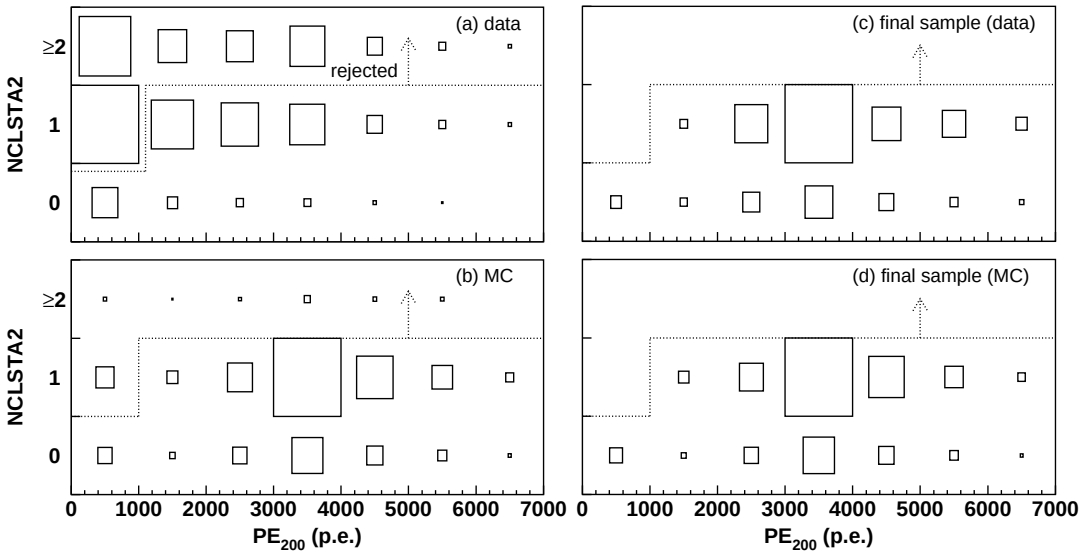

Figure 4.23: Scatter plots of NCLSTA2 and PE_{200} for (a) the data and (b) partially contained atmospheric neutrino Monte Carlo events after the PC 1st reduction and (c) final samples of the data and (d) the Monte Carlo events for SK-I. The size of the boxes shows the number of the events in each bin. The cut criteria are shown by the dashed lines and arrows.

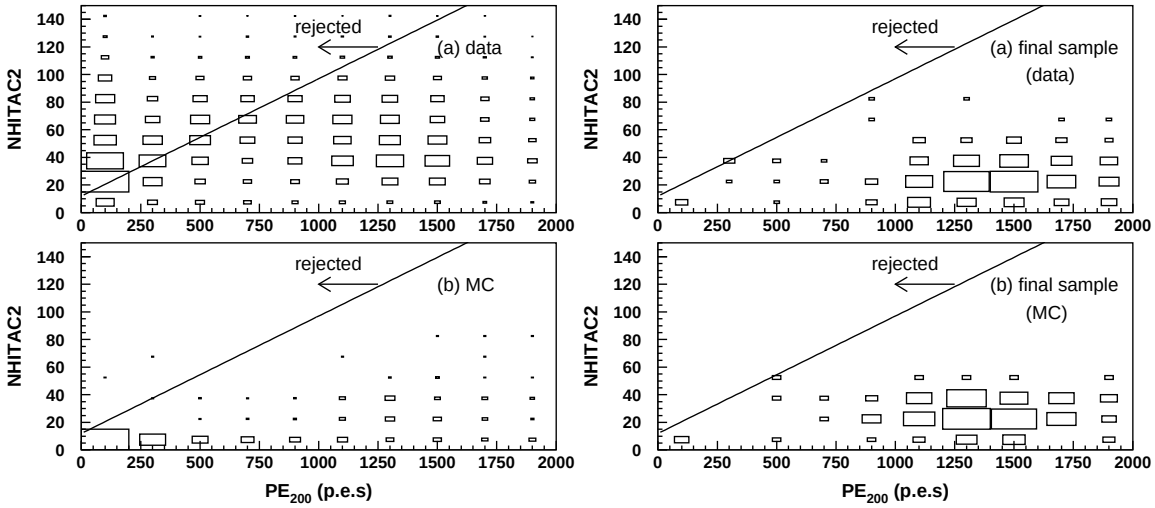

Figure 4.24: Scatter plots of NHITAC2 and PE_{200} for (a) the data and (b) partially contained atmospheric neutrino Monte Carlo events after the PC 1st reduction and (c) final samples of the data and (d) the Monte Carlo events for SK-II. The size of the boxes shows the number of the events in each bin. The cut criteria are shown by the lines and arrows.

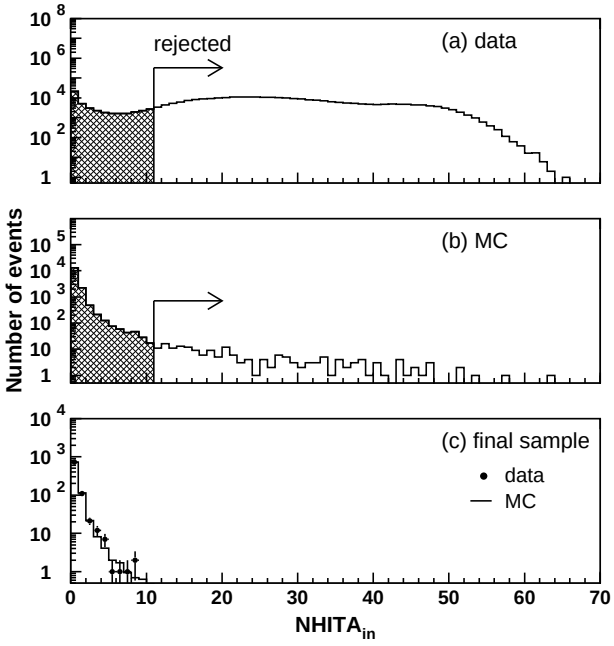

Figure 4.25: NHITA$_{in}$ distributions for (a) the data and (b) atmospheric neutrino Monte Carlo events after the PC 2nd reduction and (c) final samples. The number of the Monte Carlo events in (c) is normalized to that of the data for SK-I. The selection criteria are shown by arrows.

(1) NMIN$_{100} > 14$
or
NMIN$_{100} > 9$ if the number of hit ID PMTs < 800 (400 for SK-II)
NMIN$_{100}$ is the minimum number of hit ID PMTs in a sliding 100 nsec time window from +300 nsec to +800 nsec.

The stopping muon events are removed by the number of the hit OD PMTs near the entrance position. Simple vertex and direction fitter called point fit is applied. The vertex position is determined by point fit as the point where the timing residual distribution of hit PMTs has the sharpest peak assuming the photons are emitted from a point source (see Section 5.2.1). The direction of the ring is determined by summing up the charge weighted vector for all PMTs, and the entrance position is estimated by a backward extrapolation from the reconstructed vertex. Events satisfying the following criteria are rejected as stopping muons for both SK-I and SK-II :

(2) NHITA$_{in} > 10$
NHITA$_{in}$ is the number of hit OD PMTs located within 8 m from the entrance point in a fixed 500 nsec time window.

The NHITA$_{in}$ distributions for the data and atmospheric neutrino Monte Carlo events for SK-I after the PC 2nd reduction, and final samples are shown in Figure 4.25.

The event rate after the PC 3rd reduction is 100 (200) events/day for SK-I (SK-II).

4.3.4 Fourth Reduction

The PC 4th reduction rejects further cosmic ray muons, which pass through the PC 3rd reduction due to the relatively small OD activities. The two types of event reconstruction tools are used in this reduction stage, that is a point fit and a though going muon fit. The through

going muon fit determines the entrance point as the position of the earliest hit cluster in the ID. For the PC events, the entrance point can not be correctly determined by the through-going muon fit because they are generated inside the ID, and the goodness tends to be worse compared with the through-going muon events. On the other hand, the vertex position and the direction can be reasonably well estimated by the point fit for both the PC events and the cosmic ray muons. The selection criteria in the PC 4th reduction are as follows for SK-I and SK-II :

(1) $\vec{d}_{\rm pfit} \cdot \vec{d}_{\rm PMT}$ should be > -0.8
$\vec{d}_{\rm pfit}$ is the reconstructed direction by point fit, and $\vec{d}_{\rm PMT}$ is the direction from the reconstructed vertex to the earliest saturated PMT.

and

(2) DCORN should be $> 150\,$cm
DCORN is the distance from the reconstructed vertex by the point fit to the nearest fringe of the ID.

and

(3) TLMU should be $> 30\,$m if goodness of through-going muon fit > 0.85
TLMU is the track length of a muon estimated from the entrance and the exit points by the through going muon fit.

The criterion (1) rejects the cosmic ray stopping muons which have the entrance point in opposite direction to the reconstructed direction by point fit. The second criterion aims to reject corner clipping muons. The distribution for SK-I of the $\vec{d}_{\rm pfit} \cdot \vec{d}_{\rm PMT}$ and the DCORN are shown in Figure 4.26 and Figure 4.27, respectively. Through-going muons which have long track length are rejected by the third cut. Figure 4.28 shows the scatter plots of the TLMU and the goodness of the through-going muon fit for the data and atmospheric neutrino Monte Carlo events after the PC 3rd reduction, and final samples for SK-I. The events in the upper-right box region are rejected as through-going muons.

The event rate after the PC 4th reduction is 20 events/day for both SK-I and SK-II.

4.3.5 Fifth Reduction

The aim of the 5th reduction stage is the final rejection of the remaining background events for the PC sample. This is done by some elaborate criteria specialized for each background source. The event rate after the PC 5th reduction is 1 events/day for both SK-I and SK-II.

Low energy event cut

Events satisfying the following criteria are removed as the remaining low energy background events :

(1) $\rm PE_{tot} < 3000\,$p.e.s (1500 for SK-II)
$\rm PE_{tot}$ is the total number of p.e.s observed in the ID.

The requirement of total photoelectrons $> 3000\,$p.e.s, which corresponds to muon momentum of $500\,{\rm MeV}/c$, is safe for PC events because the exiting muons must have at least momentum of $700\,{\rm MeV}/c$ to reach the OD.

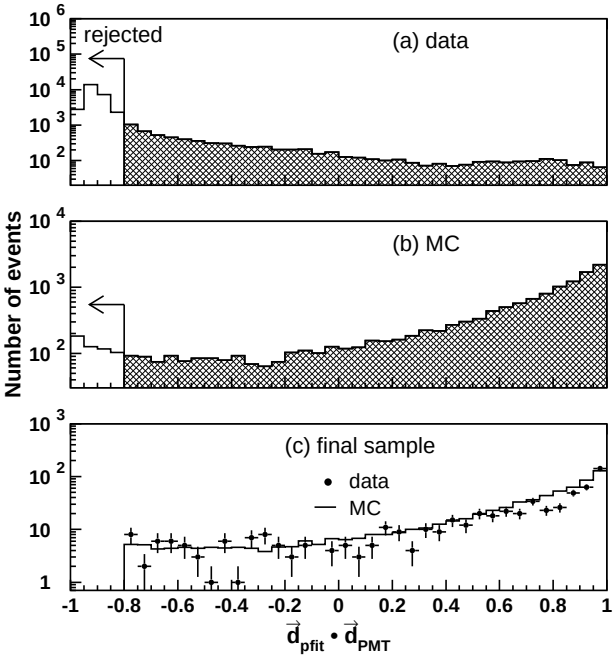

Figure 4.26: $\vec{d}_{\rm pfit} \cdot \vec{d}_{\rm PMT}$ distributions for (a) the data and (b) partially contained atmospheric neutrino Monte Carlo events after the PC 3rd reduction and (c) final samples. The number of the Monte Carlo events in (c) is normalized to that of the data for SK-I. The selection criteria are shown by arrows.

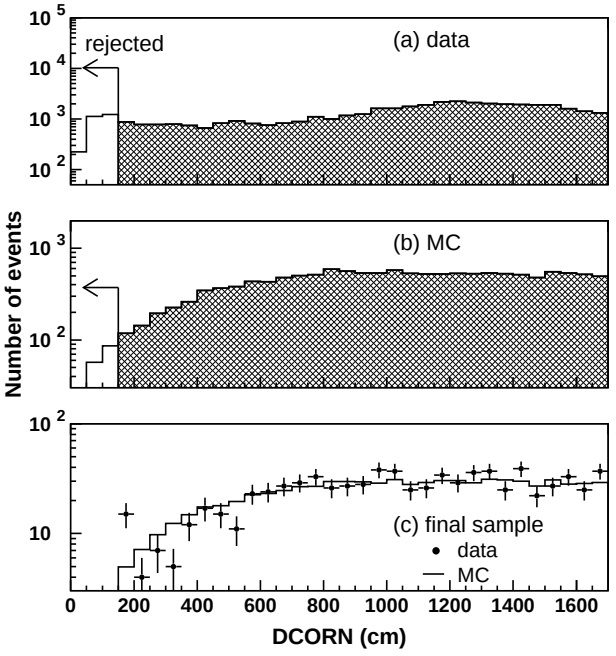

Figure 4.27: DCORN distributions for for (a) the data and (b) partially contained atmospheric neutrino Monte Carlo events after the PC 3rd reduction and (c) final samples. The number of the Monte Carlo events in (c) is normalized to that of the data for SK-I. The selection criteria are shown by arrows.

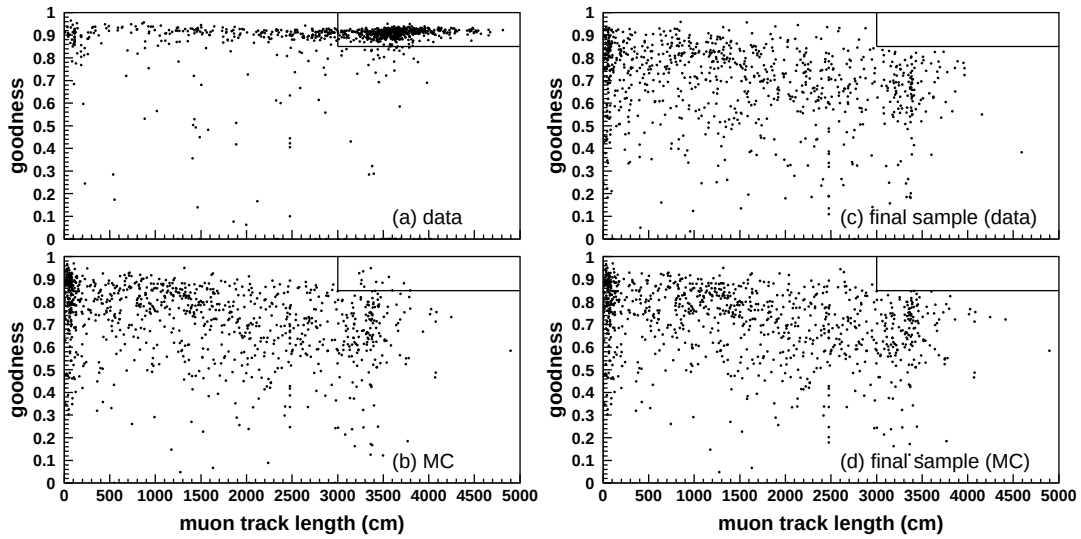

Figure 4.28: Scatter plots of muon track length and goodness of through-going muon fit for (a) the data and (b) partially contained atmospheric neutrino Monte Carlo events after the PC 3rd reduction, and (c) final samples of the data and (d) the Monte Carlo for SK-I. The events in the upper-right box region are rejected as through-going muons.

Through-going muon cut

The remaining through-going muons are removed by investigating the existence of two OD hit clusters and the existence of hit OD PMTs near the entrance and the exit points. The first cut uses the OD hit cluster information obtained by the algorithm in the PC 2nd reduction. Events satisfying the following criteria are removed as through-going muons :

(1) $\mathrm{DIST_{clust}} > 20\,\mathrm{m}$
$\mathrm{DIST_{clust}}$ is the distance between the highest charge OD hit cluster and the second highest one.

and

(2) $\mathrm{PEAC_{2nd}} \geq 10\,\mathrm{p.e.s}$
$\mathrm{PEAC_{2nd}}$ is the number of p.e.s detected in the second highest charge OD hit cluster.

and

(3) $\mathrm{NCLSTA5} \geq 2$
NCLST5 is the number of OD hit clusters which contain more than 9 hit PMTs.

In criterion (3), the same clustering algorithm as that in the PC 2nd reduction with different parameters is used. The OD wall is divided into 6×6 instead of 11×11 in the PC 5th reduction to avoid the boundary effect of the patches.

Some cosmic ray muons enters from the edge on top, passes along the ID wall and exits from the edge of the bottom. These through-going muon events tend to pass through the former reduction criteria because the light collection efficiency around the edge of the OD is not good and the event reconstruction is not so accurate for these events. To reject these events, the number of hit OD PMTs and the observed p.e.s in 8 m radius spheres centered at the top and the bottom edges or fringes are used. Events satisfying the following criteria are rejected as through-going muons :

(1) $\mathrm{NHITA_{top}} \geq 7$ and $\mathrm{NHITA_{bottom}} \geq 7$
$\mathrm{NHITA_{top}}$ ($\mathrm{NHITA_{bottom}}$) is the maximum number of hit OD PMTs in a 8 m radius sphere centered at the top (bottom) edge.

and

(2) $\mathrm{PEA_{top}} \geq 10$ p.e.s and $\mathrm{PEA_{bottom}} \geq 10$ p.e.s
$\mathrm{PEA_{top}}$ ($\mathrm{PEA_{bottom}}$) is the number of p.e.s in OD detected in the same sphere as that for the $\mathrm{NHITA_{top}}$ ($\mathrm{NHITA_{bottom}}$)

and

(3) $0.75 < \mathrm{TDIFFA} \times c/40\,\mathrm{m} < 1.5$
TDIFFA is a time interval between the averaged hit timing in the top and the bottom spheres.

The remaining through-going muons are removed by the number of hit OD PMTs near the entrance and the exit points. The vertex position and the ring direction are reconstructed by a precise fit (MS-fit) using the Cherenkov ring pattern (see Section 5.5). The entrance and the exit points on the detector wall are estimated by an extrapolation. The cut criteria for both SK-I and SK-II are as follows :

(1) $\mathrm{NHITA_{in}} \geq 5$ and $\mathrm{NHITA_{out}} \geq 5$
$\mathrm{NHITA_{in}}$ ($\mathrm{NHITA_{out}}$) is the number of hit OD PMTs within 8 m from the entrance (exit) point.

and

(2) $0.75 < \mathrm{TDIFFA} \times c/\mathrm{TRACK} < 1.5$
TRACK is distance between the entrance and exit point estimated using the vertex position and the ring direction reconstructed by MS-fit.

Stopping muon cut

Three types of stopping muon cuts are applied. In the first cut, the number of hit OD PMTs near the entrance position is counted. The entrance position of the stopping muons are estimated by reconstructing the vertex position and direction using MS-fit and back extrapolating to the wall. Events satisfying the following criteria are rejected as stopping muons :

(1) $\mathrm{NHITA_{in}} \geq 10$
$\mathrm{NHITA_{in}}$ is the number of OD hit PMTs within 8 m from the reconstructed entrance.

In the second stopping muon cut, the opening angles between the OD hit cluster and the ring estimated by two different fitters, TDC-fit and MS-fit are compared. In case of the stopping muon event, the opening angle is expected to be large, while it is small for th PC event. The cut criterion is the following :

(1) $\Theta_{\text{TDC-fit}} > 90^\circ$ or $\Theta_{\text{MS-fit}} > 90^\circ$

$\Theta_{\text{TDC-fit}}$ ($\Theta_{\text{MS-fit}}$) is the opening angle between the direction to the OD hit cluster and the ring direction reconstructed by TDC-fit (MS-fit).

In the third stopping muon cut, the charge inside a 42° cone in the ID is used. The vertex and direction are determined by stopping muon fit, which estimate the entrance as the position of the earliest hit cluster in the ID. The entrance position can not be reconstructed correctly for the PC events since the vertex of the PC events are not on the wall. Events satisfying the following criteria are rejected as stopping muons :

(1) goodness of stopping muon fit > 0

and

(2) $\text{PE}_{\text{cone}}/\text{PE}_{\text{tot}} \geq 0.6$
PE_{cone} is the number of p.e.s observed by ID PMTs located inside a 42° cone.
PE_{tot} is the total number of p.e.s observed in the ID.

and

(3) $\text{NHITA}_{\text{in}} > 6$
NHITA_{in} is the number of hit OD PMTs within 8 m from the entrance position.

These cut criteria are common for SK-I and SK-II.

Cable hole muon cut

The veto scintillation counters are placed over the four cable holes on top of the detector. Unlike the FC event selection, simple condition that only requiring veto counter hit is inapplicable for the PC event selection. Cut criteria rejecting for cable hole muons are as follows and common for SK-I and SK-II :

(1) One veto counter hit.

and

(2) $\vec{d}_{\text{ring}} \cdot \vec{d}_{\text{veto-vertex}} > -0.8$
$\vec{d}_{\text{ring}}$ is the reconstructed ring direction by TDC-fit, and $\vec{d}_{\text{vertex-veto}}$ is the direction from the hit veto counter to the reconstructed vertex.

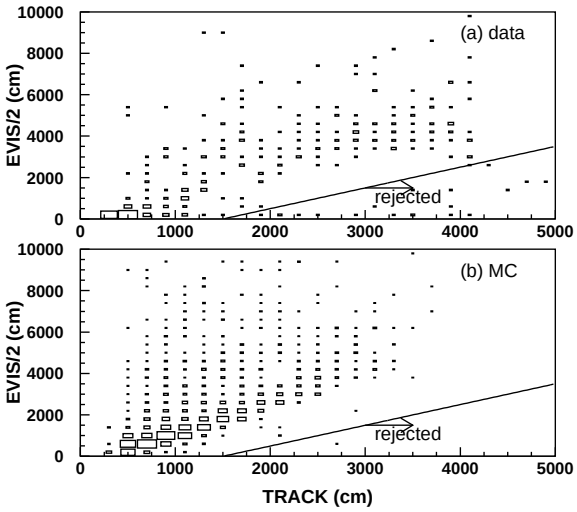

Figure 4.29: Scatter plots of $E_{vis}/2$ and TRACK for (a) the data and (b) atmospheric neutrino Monte Carlo events after the PC 4th reduction for SK-II. The selection criteria are shown by arrows.

Corner clipping muon cut

The corner clipping muon events are rejected in the PC 2nd and 3rd reduction steps. In this reduction step, the remaining corner clipping muon events. The corner clipping muon events have a small hit cluter in the ID, then the vertices are occasionally mis-reconstructed inside the ID. As a result, the track length from the vertex to the exit point reconstructed by MS-fit is large, while the track length which is estimated by the visible energy using the energy loss of muons $\sim$2 MeV/cm is small. This cut is applied in SK-II and the cut criterion for rejecting corner clipping events is the following :

(1) $E_{vis}/2\,(\mathrm{MeV/cm}) < \mathrm{TRACK} - 1500$ if TRACK > 15 m
$E_{vis}/2$ is the estimated track length by the visible energy and TRACK is the track length from the vertex to the exit point estimated from the vertex point and the direction by MS-fit.

Figure 4.29 shows the scatter plots of $E_{vis}/2$ and TRACK.

4.3.6 PC Reduction Summary

Finally, the fully contained neutrino events are selected by applying the PC event cuts :

- Vertex of neutrino interactions should be inside the fiducial volume (2 m from the ID PMT surface).
- The number of hit PMTs in the highest charge OD cluster (NHITAC) should be larger than 9 (15 for SK-II).
- Visible energy (E_{vis}) should be greater than 350 MeV.

The detection efficiency in each reduction step is estimated by the atmospheric neutrino Monte Carlo events as shown in Table 4.3. The systematic uncertainty of PC reduction is estimated to be 2.6 % and 4.0 % for SK-I and SK-II, respectively.

Reduction step	SK-I (%)	SK-II (%)
1st reduction	99.0	98.7
2nd reduction	94.2	94.2
3rd reduction	93.1	93.1
4th reduction	87.9	85.8
5th reduction	85.8	83.2

Table 4.3: The detection efficiencies in the each reduction step for SK-I and SK-II for events whose true vertices are in the fiducial volume, NHITAC larger than 9 (15 for SK-II) and E_{vis} larger than 350 MeV. In the last line, the fitted vertex is used.

The remaining background for PC sample is cosmic ray muons. After all reduction process, the remaining events are scanned by physicists and the contamination of background is estimated to be 0.2 % and 0.7 % for SK-I and SK-II, respectively. The event rate of PC events for real data is shown in Figure 4.34 and is 0.61±0.02 (0.53±0.03) events/day for SK-I (SK-II) as shown in Figure 4.34.

4.4 Reduction for Upward-Going Muon Sample

The upward going muon events are classified into two categories : (i) upward stopping muon events with only an entrance point in the OD and (ii) upward through-going muon events with an entrance point and exit point in the OD. In order to separate the upward stopping muon events and the upward through-going muon events, the number of hit OD PMTs within 8 m from the exit position (NHITEX) is used. Figure 4.30 shows the NHITEX distributions for upward stopping and upward through-going muon final samples. The events with NHITEX less than 10 (16 for SK-II) are regarded as stopping muons and the rest of events are categorized to through-going muons. In SK-II, the cut criterion is shifted larger due to the change for the OD responses. The systematic uncertainty for the stopping/through-going separation is estimated to be 0.4 % and 0.3 % for SK-I and SK-II, respectively, by comparing the NHITEX distributions for the observed data and the Monte Carlo events. Low energy events and downward-going muon events are rejected by the automated reduction process and the remaining background after automated process, mainly mis-reconstructed horizontal-going cosmic ray muons are rejected by physicists with eye-scanning.

Although the oscillation analysis uses upward-going muons, the solar term effect, which is the topic of this thesis, is only relevant to Sub-GeV neutrinos. Hence, the reduction for upward-going muons will be described only briefly.

4.4.1 Charge cut

In the first reduction, the low energy events and extremely high energy events are rejected :

(1) PE_{tot} should be > 8000 p.e.s (3000 for SK-II)

and

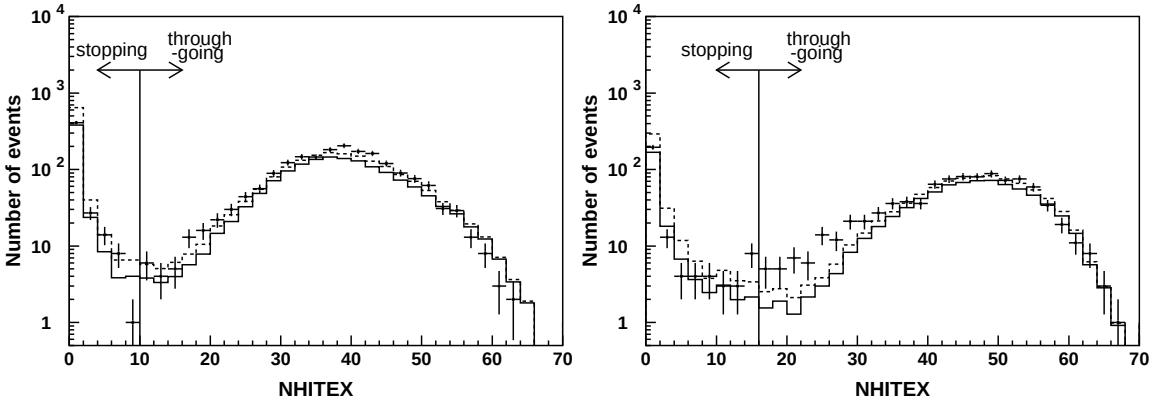

Figure 4.30: NHITEX distributions for upward stopping and through-going muon final samples for SK-I (left) and SK-II (right). The points show the observed data, and histograms show the atmospheric neutrino Monte Carlo events assuming no oscillation (dashed lines) and $\nu_\mu \leftrightarrow \nu_\tau$ 2-flavor oscillation with $(\sin^2 2\theta,\ \Delta m^2) = (1.00,\ 2.5 \times 10^{-3}\,\mathrm{eV}^2)$ (solid lines).

(2) $\mathrm{PE_{tot}}$ should be $< 1{,}750{,}000$ p.e.s (800,000 for SK-II) $\mathrm{PE_{tot}}$ is the total number of p.e.s observed in the ID.

$\mathrm{PE_{tot}}$=8000 p.e.s corresponds to muon momentum of 1 GeV/c and to track length of 3.5 m. The requirement for final sample is track length longer than 7 m and the criterion is safe. At very high ID charge corresponding to $\sim$ 1,750,000 p.e.s, the ID electronics is saturated and the muon fitters cannot work.

4.4.2 Zenith angle cut

In order to reject the downward-going muon cosmic ray muons, seven different fitters specialized to fit stopping muons, through-going muon events and muon events with Bremsstrahlung are used. The algorithm of the zenith angle cut is as following :

(1) Apply a muon fitter.

(2) If the event is classified as upward and the goodness of fit is above the threshold, the event is saved.

(3) If the event is classified as downward and the goodness of fit is above the threshold, the event is rejected.

(4) If the event is classified as horizontal with the goodness of fit above the threshold, or if the goodness of fit is below the threshold, the judgment is suspended.

(5) Go to (1) and apply the next muon fitter.

This sequence continues until the event has passed through all the fitters or has been classified. If no fitter gives a goodness above the threshold, the event is rejected, while if at least one fitter classifies the event as horizontal, the event is saved. Detailed description about the seven muon fitters and the definition of the goodness can be found in [118].

All events from the output of the upward-going muon reduction are passed through the precise fitter which is described in 5.10. The direction reconstructed by the precise fitter is used to select upward-going events by the criterion for cosΘ <0.

4.4.3 Scanning

In order to eliminate the background events such as horizontal-going, corner clipping or bremsstrahlung cosmic ray muons and noise events, the selected events as upward are scanned by physicists using a visual display and upward-going muon events are selected one by one. All events are checked by two independent scanners not to miss neutrino events. The possibility to miss a upward-going event is at most 1 % by a scanner. Therefore, the efficiency of scanning is estimated to be almost 100 %. About a half of the events remaining after all the automated reduction steps are rejected by this final scan. We note that the scanners only check that the reconstructed vertex and direction is not largely wrong. The reconstruction results in the previous stage are used in the final physics analysis.

4.4.4 Efficiency and Background for Upward-Going Muon Sample

The final samples of the upward going muons are required the following conditions :

- The reconstructed particle direction is upward.
- The reconstructed track length should be greater than 7 m.

The second criterion is to keep the quality of the event reconstruction. The systematic error for the track length cut is estimated to be 1.1 % for both SK-I and SK-II.

The reduction efficiency of the upward stopping and through-going muon events are estimated by the upward-going muon Monte Carlo events to be 102 % (101 %) for stopping muons and 96 % (94 %) for through-going muon events for SK-I (SK-II). Efficiency higher than 100 % for upward stopping muons is due to a slight bias in the separation of stopping and through-going muons, causing a small fraction of the more numerous through-going muons to be misidentified as stopping muons. The systematic uncertainty in the data reduction process for upward-going sample is estimated by comparing the distribution of each cut variable of the data with that of the Monte Carlo events. The estimated errors are 1.3 % (1.9 %) for upward stopping muons and 0.5 % (0.9 %) for upward through-going muons for SK-I (SK-II).

The final samples of upward-going muons contain cosmic ray muon background in the most horizontal bin ($-0.1 < \cos\Theta < 0$). Some of the down-going cosmic ray muons are fitted to be upward-going because of the fitter resolution and multiple Coulomb scattering of muons in the neaby rock. Figure 4.31 shows the zenith versus azimuth directions for the upward going muon sample. Clusters of cosmic ray downward muons are seen in the regions zenith angle cos$\Theta > 0$ (downward) and azimuth angle around $\phi = 120^\circ$, 180° and 270° because the rock of the mountain covered over the detector is thin for these directions. In order to estimate the contamination of the background events, the upward going muon samples are divided into two azimuth angle regions. Figure 4.32 shows the azimuth angle distributions for upward going muon samples, in which region (2) shows the thinner mountain direction, which is defined as $60^\circ < \phi < 310^\circ$ for stopping muons and $60^\circ < \phi < 240^\circ$ for through-going muons and region (1) shows the thicker mountain direction.

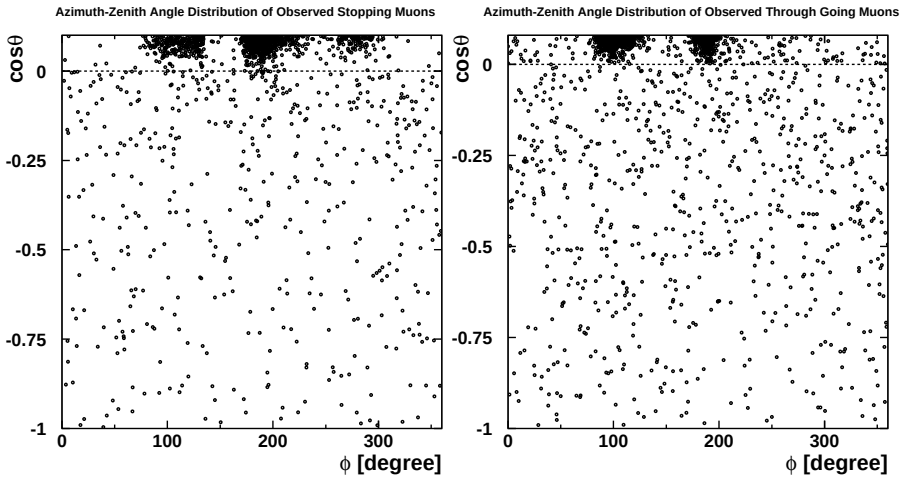

Figure 4.31: Scatter plots of the zenith angle and the azimuth angle of the muon directions for stopping (left) and through-going muon data (right) for SK-I. Vertical axis shows the cosine of zenith angle and horizontal axis shows the azimuth angle of the muon direction.

Figure 4.33 shows the zenith angle distributions for upward-going muon samples, in which region (1) and (2) are normalized by the coverage of the azimuth angle. While the zenith angle distributions are almost flat for upward going events (cosΘ <0), the number of events in the region (2) exponentially increase with the cosine of zenith angle for downward-going (cosΘ >0). The contaminations of the cosmic ray muons into the upward-going direction are estimated by an extrapolation from the upward direction in the region (2) with (*exponential + constant*) function. The numbers of background events in the range of $-0.1 < \cos\Theta < 0$ are estimated to be 40.3±13.7 for upward stopping muon and 14.4±7.2 for upward through-going muon for SK-I, respectively. For SK-II, 19.4±6.3 events for upward stopping muons and 9.0±5.2 events for through-going muons are estimated. The errors represent the statistical uncertainties of the fitting. The event rate of upward going muon events before background subtraction is shown in Figure 4.34. The event rate after background subtractio is 0.25±0.01 (0.25±0.02) events/day for stopping muon events and 1.12±0.03 (1.06±0.04) events/day for through-going muon events for SK-I (SK-II).

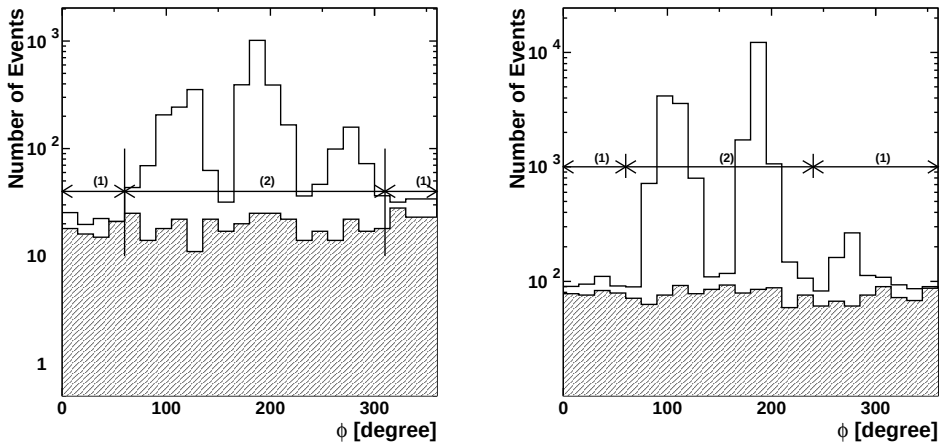

Figure 4.32: Azimuth angle distributions for stopping (left) and through-going muons (right) for SK-I. Region (2) shows the thinner-mountain direction and region (1) shows the thicker-mountain direction. White histograms show the distributions of downward-going muons ($0 < \cos\Theta < 0.1$) and the hatched histograms show the upward-going muons ($\cos\Theta < 0$). Peaks due to the contamination from cosmic ray muons are seen in region (2) for downward-going muons.

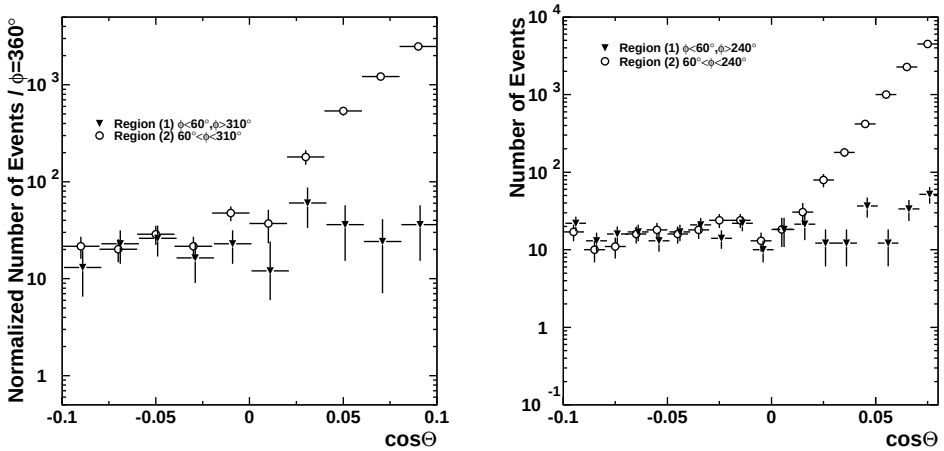

Figure 4.33: Zenith angle distributions for stopping muons (left) and through-going muons (right) for SK-I. Reverse triangles show those for region (1) (thicker-mountain direction) and open circles show those for region (2) (thinner-mountain region).

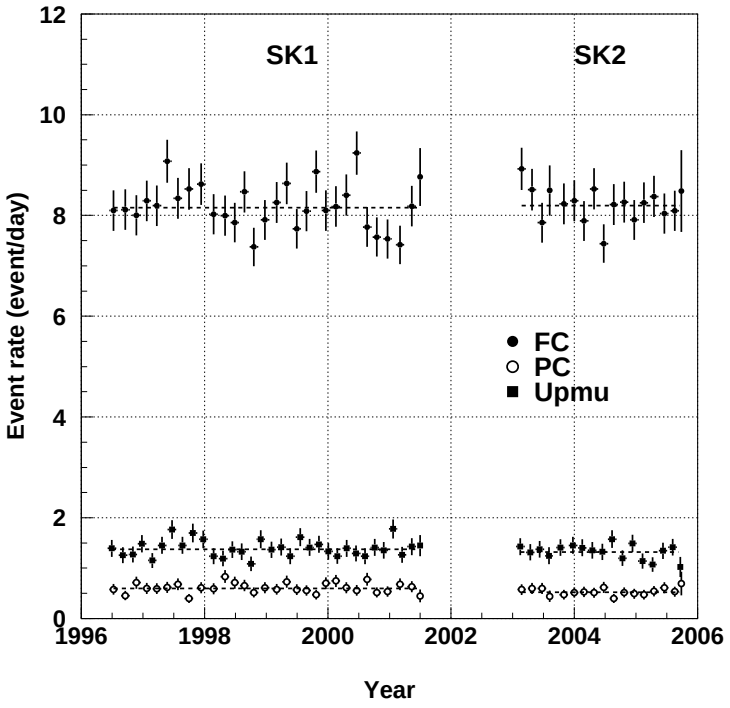

Figure 4.34: The event rate for FC, PC and upward-going muon events as a function of the elapse days from 1996. The dashed line shows the averaged event rate for each sample.

Chapter 5

Event Reconstruction

5.1 Overview

Event reconstruction process is applied to the atmospheric neutrino events which pass through the data reduction. The same programs are used for both the observed data and the atmospheric neutrino Monte Carlo events. The event reconstruction process is fully automated. The detailed explanations of the procedures are described in this chapter.

The outline of the reconstruction process for FC and PC events is the following :

(1) Vertex Fitting

The vertex position is determined as the point at which the timing residual distribution of hit PMTs has the sharpest peak. The direction and the outer edge of the dominant ring is estimated.

(2) Ring Counting

The other possible rings are searched using the vertex position and the direction of the dominant ring. The ring candidates are tested whether the ring is true or not by a likelihood method, and the number of rings is determined.

(3) Particle Identification

Each ring is classified into two types, a showering type ($e^{\pm}, \gamma$) and non-showering type ($\mu^{\pm}, \pi^{\pm}$), by the ring pattern and the opening angle. The showering type and non-showering type are commonly called e-like and μ-like, respectively.

(4) Precise Vertex Fitting (only for single-ring event)

The precise vertex position is obtained using the Cherenkov ring pattern assuming the particle type, a non-showering type or a showering type. This precise vertex fitter is called MS-fit.

(5) Momentum Determination

The momentum of each ring is determined from the charge detected inside a Cherenkov cone. The conversion from the charge to the momentum is determined based on a Monte Carlo simulation and the detector calibration.

(6) Ring Number Correction

Rings which have the low momentum and overlapped with the other energetic rings are discarded as fitting mistakes.

(7) Decay Electron finding

Decay electrons following the primary events are searched.

(8) π^0 Fitting

The other ring candidate of π^0 events is searched among the events which are recognized as single-ring e-like by the above reconstruction processes.

5.2 Vertex Fitting

The event reconstruction process starts from the vertex fitting. The vertex position is reconstructed using the timing information of hit PMTs in three steps.

5.2.1 Point-Fit

Vertex position is roughly estimated in the first step assuming all of the photons are emitted at the same time from a point source. The time of flight of photon is subtracted from the hit timing for each PMT. The vertex is estimated as the point where the timing residual distribution is peaked. This vertex reconstruction algorithm is called point-fit, and the goodness of the fit is defined as follows :

$$G_p = \frac{1}{N} \sum_i \exp\left(- \frac{(t_i - t_0)^2}{2\,(1.5 \times \sigma)^2} \right) \tag{5.1}$$

where N is the number of hit PMTs, t_i is the time residual of the i-th PMT, t_0 is a free parameter chosen to maximize G_p and takes a value near the mean value of t_i, and σ is the PMT timing resolution taken to be 2.5 nsec. The numerical factor 1.5 is chosen to optimize the fitter performance. The fitter searches for the vertex point which gives the maximum value of G_p.

The particle direction is also roughly estimated by summing up the charge weighted vector over all PMTs :

$$\vec{d_0} = \sum_i q_i \times \frac{\vec{P_i} - \vec{O_0}}{|\vec{P_i} - \vec{O_0}|} \tag{5.2}$$

where $\vec{d_0}$ is the particle direction, $\vec{O_0}$ is the vertex position obtained by point fit, $\vec{P_i}$ is the position and q_i is the detected charge of the i-th PMT.

5.2.2 Ring Edge Search

The direction and the outer edge of the dominant ring is measured in the second step. To determine the direction of the ring, the estimator $Q(\theta_{\rm edge})$ is defined as follows :

$$Q(\theta_{\rm edge}) = \frac{\int_0^{\theta_{\rm edge}} {\rm PE}(\theta) d\theta}{\sin\theta_{\rm edge}} \times \left(\left. \frac{d{\rm PE}(\theta)}{d\theta} \right|_{\theta=\theta_{\rm edge}} \right)^2 \times \exp\left(- \frac{(\theta_{\rm edge} - \theta_{\rm exp})^2}{2\sigma_\theta^2} \right) \tag{5.3}$$

where $\theta_{\rm exp}$ and σ_θ are the Cherenkov opening angle expected from the charge within the cone and its resolution, respectively. ${\rm PE}(\theta)$ is the angular distribution of the observed charge as a function of the opening angle θ from the particle direction. The observed charge is corrected for the effect from a water transparency and a PMT acceptance. The ring edge position $\theta_{\rm edge}$ is determined to satisfy the following two conditions :

(1) $\theta_{\rm edge} > \theta_{\rm peak}$

(2) $\left. \dfrac{d^2{\rm PE}(\theta)}{d^2\theta} \right|_{\theta_{\rm edge}} = 0$

where $\theta_{\rm peak}$ is the opening angle where ${\rm PE}(\theta)$ takes maximum. ${\rm PE}(\theta)$ distribution and the second derivative of ${\rm PE}(\theta)$ for a typical event are shown in Figure 5.1.

The estimator $Q(\theta_{\rm edge})$ is calculated changing the particle direction around $\vec{d_o}$ which is estimated by point fit. The direction of the ring and the ring edge position are determined to maximize the estimator $Q(\theta_{\rm edge})$.

5.2.3 TDC-Fit

Finally the vertex position is more precisely determined by TDC-fit. Instead of assuming a point-like, the track length of the charged particle and the scattered Cherenkov photons are taken into account in the TDC-fit.

The time residual of the i-th PMT is calculated by :

$$t_i = \begin{cases} t_i^0 - \dfrac{1}{c} \times |\vec{X}_i - \vec{O}| - \dfrac{n}{c} \times |\vec{P}_i - \vec{X}_i| & \text{for PMTs inside the Cherenkov ring} \\ t_i^0 - \dfrac{n}{c} \times |\vec{P}_i - \vec{O}| & \text{for PMTs outside the Cherenkov ring} \end{cases} \tag{5.4}$$

where $\vec{O}$ is the vertex position, $\vec{X}_i$ is the position at which Cherenkov photons are emitted toward the i-th PMT, n is the refractive index of water, $\vec{P}_i$ is the position and t_i^0 is the hit timing of the i-th PMT.

The estimator of the TDC-fit consists of three parts which are calculated by the different way based on the position of the PMT. For the hit PMTs inside the Cherenkov ring, the fitting estimator G_I is defined by :

$$G_I = \sum_i \frac{1}{\sigma_i^2} \exp\left(- \frac{(t_i - t_0)^2}{2\,(1.5 \times \sigma)^2} \right) \tag{5.5}$$

where σ_i is the timing resolution of the i-th PMT depending on the detected p.e.s, σ is the timing resolution for the average p.e.s of all hit PMTs and t_i is the time residual of the i-th PMT calculated by Equation (5.4). The definition for t_0 is same as that in Equation (5.1).

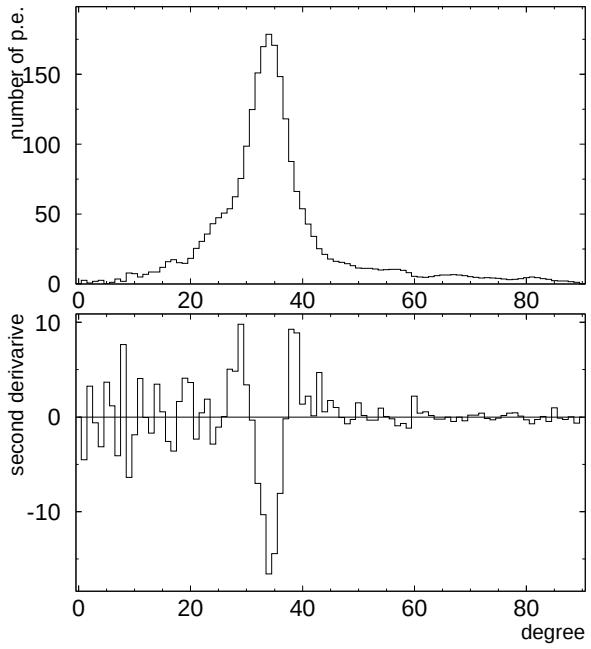

Figure 5.1: The typical PE(θ) distribution (upper) and its second derivative (bottom) as a function of Cherenkov opening angle.

For the hit PMTs outside the Cherenkov ring, the definition of the estimator changes with the time residual. If the hit timing is later than t_0, the contribution from the scattered photons are considered. The definitions of the estimator for hit PMTs outside the Cherenkov ring are as follows :

$$G_{O1} = \sum_i \frac{1}{\sigma_i^2}\left(\exp\left(-\frac{(t_i-t_0)^2}{2\,(1.5\times\sigma)^2}\right)\times 2-1\right) \qquad (\text{ for } t_i \le t_0\ ) \tag{5.6}$$

$$G_{O2} = \sum_i \frac{1}{\sigma_i^2}\left(\max\left[\exp\left(-\frac{(t_i-t_0)^2}{2\,(1.5\times\sigma)^2}\right)\ ,\ G_{\rm scatt}(t_i,t_0)\right]\times 2-1\right) \qquad (\text{ for } t_i > t_0\ ) \tag{5.7}$$

where

$$G_{\rm scatt}(t_i,t_0) = \frac{R_q}{1.5^2}\times\exp\left(-\frac{(t_i-t_0)^2}{2\,(1.5\times\sigma)^2}\right)+\left(1-\frac{R_q}{1.5^2}\right)\times\exp\left(-\frac{t_i-t_0}{60\text{nsec}}\right) \tag{5.8}$$

R_q is the fraction of the charge detected inside the Cherenkov ring. The numerical factors in the equations are chosen to optimize the fitter performance.

Then total estimator of TDC fit is obtained by :

$$G_T = \frac{G_I + (G_{O1}\text{ or }G_{O2})}{\sum_i \frac{1}{{\sigma_i}^2}} \tag{5.9}$$

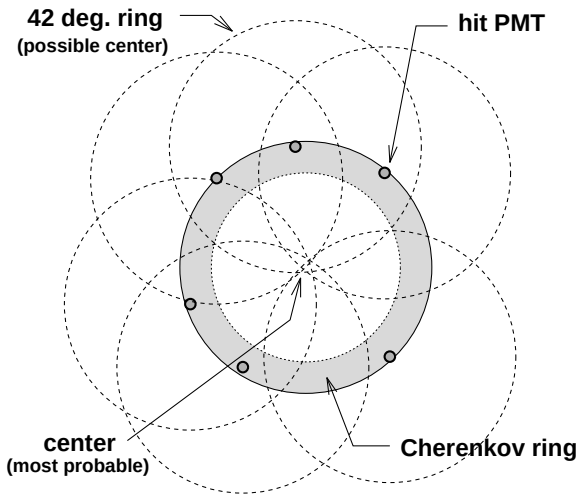

Figure 5.2: A basic idea of finding ring candidates is shown. By drawing rings around the hit PMT with Cherenkov opening angle of 42 ° from the vertex, the center of the actual Cherenkov ring can be identified.

The vertex position and the ring direction are determined to maximize the G_T.

The resolutions of the TDC-fit are estimated to be 57 cm (55 cm) and 60 cm (60 cm) for FC single-ring Sub-GeV e-like and μ-like events, 103 cm (87 cm) and 76 cm (83 cm) for FC single-ring Multi-GeV e-like and μ-like events, 62 cm (85 cm) for FC multi-ring μ-like events and 90 cm (109 cm) for PC events for SK-I (SK-II). For single-ring events, the vertex positions are more precisely estimated later by MS-fit using the ring pattern.

5.3 Ring Counting

Once the event vertex and the first Cherenkov ring is found, a ring counting algorithm is applied to search for any other Cherenkov rings in the event.

5.3.1 Ring Candidate Search

Cherenkov ring candidates are searched by an algorithm using a Hough transformation [119]. Figure 5.2 illustrates the basic concept to find other possible rings, in which a spherical coordinate centered on the vertex position is considered. The shaded circle in this figure represents the Cherenkov ring image projected to a plane perpendicular to the ring direction. Hit PMTs are picked up and virtual circles (dashed line) centered on the position of the hit PMT are drawn with 42 ° half angle. As a result of this procedure, the direction of a Cherenkov ring is identified as a intersection point of these circles. In practice, instead of drawing virtual circles, expected charge distribution function $f(\theta)$ with the weight of the observed charge is mapped on a (Θ, Φ) plane for each hit PMT. As a result of this Hough transformation method, ring center candidates are visible as the peaks of charge on the map. A typical charge map is shown in Figure 5.3. The two peaks correspond to the directions of Cherenkov rings.

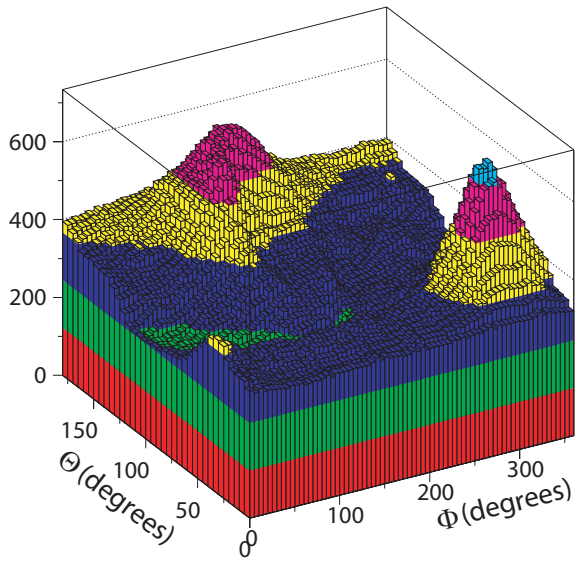

Figure 5.3: A charge map from Hough transformation algorithm for a typical two ring events. The peaks are the direction of the Cherenkov rings.

5.3.2 Ring Candidate Test

The ring candidates are tested by a likelihood method. When N rings are already found in the event, the test whether the (N+1)-th ring candidate is true or not by the likelihood function. The likelihood function for the assumption of N+1 rings is defined as :

$$L_{N+1} = \sum_i \log\left(prob\left(q_i^{\rm obs}\,,\,\textstyle\sum_{n=1}^{N+1}\alpha_n\cdot q_{i,n}^{\rm exp}\right)\right) \tag{5.10}$$

where hit PMTs inside N+1 Cherenkov rings is summed up. $q_i^{\rm obs}$ is the observed p.e.s in the i-th PMT and $\alpha_n \cdot q_{i,n}^{\rm exp}$ is the expected p.e.s in the i-th PMT from the n-th ring. The L^{N+1} is maximized by changing the scale factors α_n (n=1 , $\cdots$, N+1) with a constraint of lower momentum limit. The probability function in Equation (5.10) is defined by :

$$prob\,(q_i^{\rm obs}\,,\,q_i^{\rm exp}) = \begin{cases} \dfrac{1}{\sqrt{2\pi}\,\sigma}\exp\left(-\dfrac{(q_i^{\rm obs}-q_i^{\rm exp})^2}{2\,\sigma^2}\right) & (\text{for } q_i^{\rm exp} > 20 \text{ p.e.}) \\ \text{Probability obtained by the probability density distribution} \\ \text{function based on the convolution of a single p.e. distribution} \\ \text{and a Poisson distribution (for } q_i^{\rm exp} < 20 \text{ p.e.)} \end{cases} \tag{5.11}$$

where σ is the resolution for $q_{\rm exp}$. If no candidate satisfies $L^{N+1} \geq L^N$, the number of rings is determined to be N and the ring counting procedure is finalized. For the ring candidates satisfying $L^{N+1} \geq L^N$, following four evaluation functions are calculated :

F_1 : The difference $L(N+1) - L(N)$ corrected for the total p.e.s. When the difference is larger, the candidate is more likely to be true.

F_2 : The average of the expected p.e.s near the edge of the Cherenkov ring from the $(N+1)$-th ring, $Q_{\rm edge}$. The charge from the other rings is not included in the calculation. When the $Q_{\rm edge}$ is larger, the candidate is more likely to be true.

F_3 : The average of the expected p.e.s outside the $(N+1)$-th ring, $Q_{\rm out}$. The charge from the other rings is not included in the calculation. When the $Q_{\rm edge}$-$Q_{\rm out}$ is larger, the candidate is more likely to be true.

F_4 : The residual p.e.s from the expectaion with N rings are calculated. Then the residual-charge weighted vector from all PMTs are calculated. When the absolute value of the vector sum is large, the candidate is more likely to be true.

For SK-I, the final evaluation function is defined to be a linear combination of four evaluation functions with optimized weights (α_i) :

$$F_{\rm SK-I} = \sum_{i=1}^{4} [\alpha_i F_i] \tag{5.12}$$

If $F_{\rm SK-I}$ is positive, the $N+1$-th ring is determined to be true. In SK-II, other two evaluation functions are added :

F_5 : The difference in p.e's between the peak of a candidate ring and the average of inside and outside the ring. The larger F_5 is, the more probable the candidate is to be a true ring.

F_6 : The azimuthal symmetry of a ring with respect to the direction of the ring. A single-ring event is more symmetric than a multi-ring event. F_6 is only used to separated single and multi ring events.

In SK-II, the ring counting is modified to use a true log likelihood method. Using MC samples of single-ring and multi-ring events, the probability density functions (PDFs) for each evaluation function are determined, and the likelihood is calculated as :

$$F_{\rm SK-II} = \sum_{i}^{6} log\,[(\mathcal{P}_i)] \tag{5.13}$$

$$= \sum_{i}^{6} \{log\,[(\mathcal{P}_i)_{N+1}] - log\,[(\mathcal{P}_i)_N]\} \tag{5.14}$$

where $\mathcal{P}_i$ is the probability density function for i-th evaluation function, and $\mathcal{P}_{N+1}$ and $\mathcal{P}_N$ are the probability for $(N+1)$-ring and N-ring events. Figure 5.4 shows $F_{\rm SK-I}$ and $F_{\rm SK-II}$ distributions.

The efficiency for identifying Sub-GeV CCQE ν_e (ν_μ) events as single-ring is 93.2 % (96.0 %) for SK-I. The efficiency for identifying Multi-GeV CCQE ν_e (ν_μ) events as single-ring is 84.4 % (93.3 %) for SK-I. The efficiency for identifying Sub-GeV CCQE ν_e (ν_μ) events as single-ring is 93.2 % (96.6 %) for SK-II. The efficiency for identifying Multi-GeV CCQE ν_e (ν_μ) events as single-ring is 92.9 % (96.3 %) for SK-II.

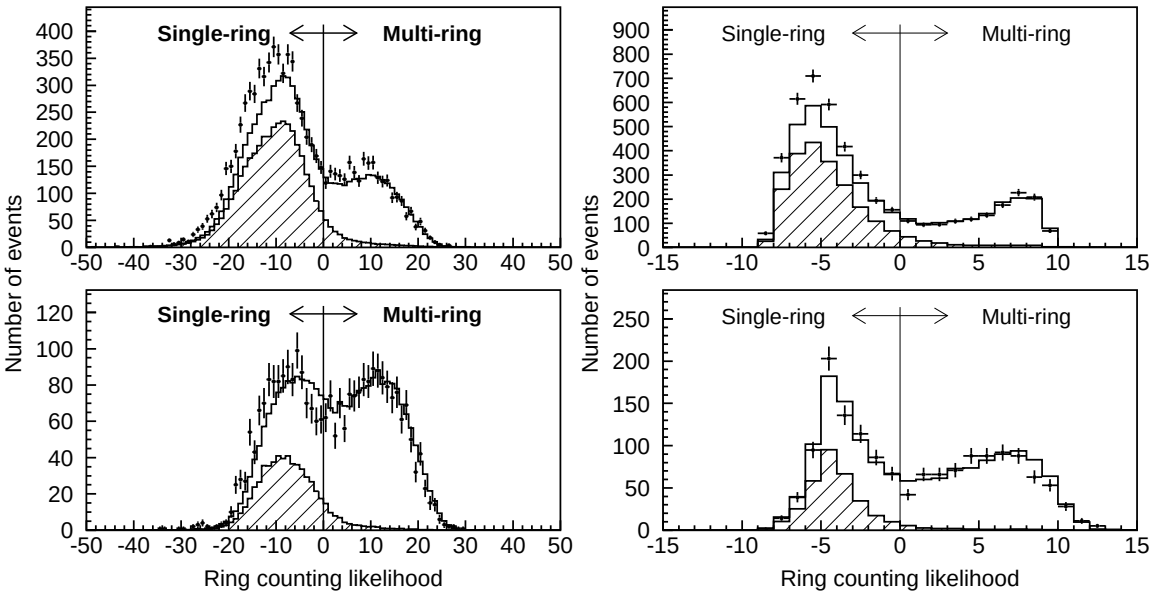

Figure 5.4: The ring-counting likelihood distributions for FC Sub-GeV events (top) and Multi-GeV events (bottom) of data (dot) and the Monte Carlo events (solid line) assuming 2-flavor $\nu_\mu \leftrightarrow \nu_\tau$ oscillation assumed with $(\sin^2 2\theta,\, \Delta m^2) = (1.00,\, 2.5 \times 10^{-3}\,\mathrm{eV}^2)$ for SK-I (left two panels) and SK-II (right two panels). The hatched histograms show the CCQE interactions.

5.4 Particle Identification

A particle identification (PID) program is applied to classify the Cherenkov rings into two types:showering (e-like) or non-showering (μ-like). Due to the electromagnetic shower and multiple scattering, electrons or gamma-rays produce e-like rings, which give diffused ring patterns. Non-showering (μ-like) rings are produced by muons or charged pions and have sharper ring edges. Figure 5.5 shows the event display of electron and muon neutrino MC events with a momentum of 1 GeV. In addition, the Cherenkov rings from electrons and gamma-rays have the Cherenkov opening angle of 42 °, but the Cherenkov rings from muons or charged pions can have smaller angles if they are not highly relativistic ($\beta = v/c < 1$) and when they lose energy. The PID algorithm exploits these differences in the patterns and the opening angles of the Cherenkov rings. The details of PID are described below.

5.4.1 Expected Charge Distributions

The first step of PID is to calculate the expected p.e.s in each PMT from an electron or muon. The expected p.e.s in the i-th PMT from an electron is calculated as follows :

$$q_i^{\mathrm{exp}}(e) = \alpha_e \times Q^{\mathrm{exp}}(p_e, \theta_i) \times \left(\frac{R}{r_i}\right)^{1.5} \times \frac{1}{\exp(r_i/L)} \times f(\Theta_i) + q_i^{\mathrm{scatt}} \tag{5.15}$$

where

α_e : normalization factor

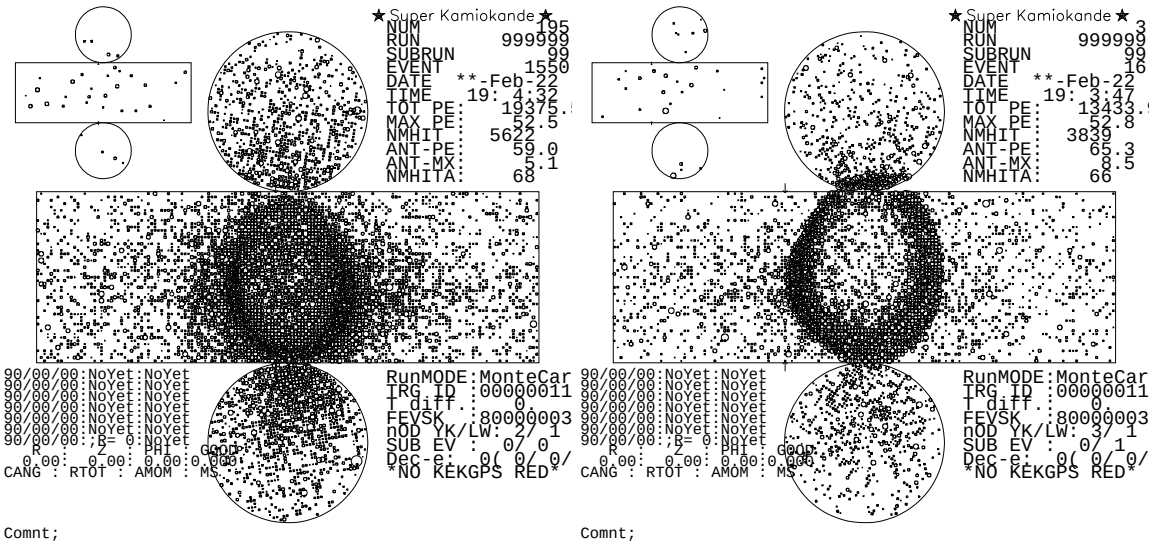

Figure 5.5: Event display of single-ring electron (left) and single-ring muon (right) neutrino MC event. Each small circle on the figure represents a hit ID PMT, and the size of a circle corresponds to the number of photoelectrons detected. An electron event gives diffused ring pattern, and a muon event has a sharp ring edge.

r_i : distance from the vertex to the i-th PMT

θ_i : opening angle between the i-th PMT direction and the ring direction

L : light attenuation length in water

$f(\Theta_i)$: correction for the PMT acceptance as a function of the photon incidence angle Θ_i

R : radius of the virtual sphere (16.9 m)

$Q^{\exp}(p_e, \theta_i)$: expected p.e. distribution from an electron as a function of the opening angle and the electron momentum

q_i^{scatt} : expected p.e.s for the i-th PMT from scattered photons

The expected p.e. $Q^{\exp}(p_e, \theta_i)$ as a function of the opening angle of the i_{th} PMT and the electron momentum is obtained by a Monte Carlo simulation. The distance dependence of the light intensity is corrected by a factor $(R/l_i)^{1.5}$. In addition to the direct photons, the expectation from scattered photons are also considered.

In the case of muon, the expected p.e.s in i-th PMT is analytically calculated as follows :

$$q_i^{\exp}(\mu) = \left(\alpha_\mu \times \frac{\sin^2 \theta_{x_i}}{r_i \left(\sin \theta_{x_i} + r_i \cdot \frac{d\theta}{dx}\big|_{x=x_i} \right)} + q_i^{\text{knock}} \right) \times \frac{1}{\exp(r_i/L)} \times f(\Theta_i) + q_i^{\text{scatt}} \qquad (5.16)$$

where

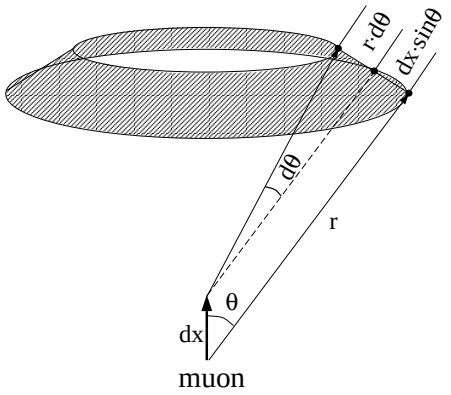

Figure 5.6: A schematic view of Cherenkov radiation from a muon. Cherenkov photons are emitted to the area of $2\pi r \sin\theta(dx \sin\theta + rd\theta)$ while a muon travels the distance of dx.

α_μ	:	normalization factor
x	:	track length of the muon
x_i	:	track length of the muon at which Cherenkov photons are emitted toward the i-th PMT
θ	:	Cherenkov opening angle of the muon traveling at x
θ_{x_i}	:	Cherenkov opening angle of the muon traveling at x_i
$q_i^{\rm knock}$	:	expected p.e.s. for the i-th PMT from knock-on electrons

$\sin^2\theta$ comes from the Cherenkov angle dependence of the Cherenkov light intensity. The term $r(\sin\theta + r(d\theta/dx))$ comes from the area where Cherenkov photons are emitted to. The Cherenkov angle shows a decrease of $d\theta$ while a muon travels a distance of dx, and Cherenkov photons are emitted to the area of $2\pi r \sin\theta(dx\sin\theta + rd\theta)$ as shown in Figure 5.6. The contribution from knock-on electrons $q_i^{\rm knock}$ is estimated by a Monte Carlo simulation.

5.4.2 Estimation of Particle Types

The definition of likelihood for the n-th ring is expressed by :

$$L_n(e \text{ or } \mu) = \prod_{\theta_i < (1.5\times\theta_c)} prob\left(q_i^{\rm obs} \ , \ q_{i,n}^{\rm exp}(e \text{ or } \mu) + \sum_{n' \neq n} q_{i,n'}^{\rm exp} \right) \tag{5.17}$$

where the product is made over the PMTs inside the n-th ring. $q_i^{\rm obs}$ is the observed p.e.s in the i-th PMT, $q_{i,n}^{\rm exp}(e \text{ or } \mu)$ is the expected p.e.s from the n-th ring assuming an electron or a muon (Equation (5.15), (5.16)) and $q_{i,n'}^{\rm exp}$ are the expected p.e.s from the n'-th ring without any assumption of the particle type. The function *prob* gives the probability to detect $q_i^{\rm obs}$ in the i-th PMT when $q_i^{\rm exp}$ is expected (Equation (5.11)). The $q_{i,n}^{\rm exp}(e)$ and $q_{i,n}^{\rm exp}(\mu)$ is optimized by

changing the direction and the opening angle of the n-th ring to give the maximum likelihood value.

In order to combine with another estimator which uses the Cherenkov opening angle, the likelihood for the ring pattern is translated into a χ^2 parameter :

$$\chi^2_n(e \text{ or } \mu) = -2 \log L_n(e \text{ or } \mu) + \text{constant} \tag{5.18}$$

The probability from the ring pattern is given by :

$$P_n^{\text{pattern}}(e \text{ or } \mu) = \exp\left(- \frac{\left(\chi^2_n(e \text{ or } \mu) - \min\left[\chi^2_n(e)\,,\, \chi^2_n(\mu)\right] \right)^2}{2\,\sigma^2_{\chi^2_n}} \right) \tag{5.19}$$

The resolution of the χ^2 distribution is approximated by $\sigma_{\chi^2_n} = \sqrt{2N}$, where N is the number of PMTs used in the calculation.

The probability from the Cherenkov opening angle is given by :

$$P_n^{\text{angle}}(e \text{ or } \mu) = \exp\left(- \frac{\left(\theta_n^{\text{obs}} - \theta_n^{\text{exp}}(e \text{ or } \mu) \right)^2}{2\,(\delta\theta_n)^2} \right) \tag{5.20}$$

where θ_n^{obs} and $\delta\theta_n$ are the reconstructed opening angle of the n-th ring and the fitting error, respectively. $\theta_n^{\text{exp}}(e \text{ or } \mu)$ is the expected opening angle of the n-th ring, which is estimated from the reconstructed momentum assuming an electron or a muon.

The probability functions of the PID for single-ring events and multi-ring events are defined as :

$$P_{single}(e,\mu) = P^{\text{pattern}}_{single}(e,\mu) \times P^{\text{angle}}_{single}(e,\mu) \quad \text{(Single-ring event)} \tag{5.21}$$

$$P_{multi}(e,\mu) = P^{\text{pattern}}_{multi}(e,\mu) \quad \text{(Multi-ring event)} \tag{5.22}$$

For a single-ring event, the final probability is defined as the product of the probabilities from the ring pattern and the opening angle. On the other hand, for multi-ring events, only $P^{\text{pattern}}_{multi}(e \text{ or } \mu)$ is used since the opening angle and its error is not estimated precisely. This algorithm was tested by a beam test experiment at KEK [120]. The distributions of PID likelihood, $P_{PID} \equiv \sqrt{-\log P(\mu)} - \sqrt{-\log P(e)}$, for single-ring events and multi-ring events are shown in Figure 5.7 and Figure 5.8. $P_{PID} < 0$ is e-like and $P_{PID} \geq 0$ is μ-like. Also, Figure 5.8 shows the PID likelihood distributions for SK-II. The misidentification probabilities are estimated to be 0.8 % (0.7 %) and 0.7 % (1.0 %) for FC Sub-GeV single-ring ν_e and ν_μ using CCQE events for SK-I (SK-II).

5.5 Precise Vertex Fitting

For single-ring events, the vertex resolution in the longitudinal directions fitted by vertex fitting algorithm described in Section 5.2 is not optimized since it only uses the timing information. This can be improved by re-fitting the vertex position using the ring pattern. The MS-fit modifies the vertex position and the particle direction by using the PID likelihood, and the vertex position is adjusted parallel to the particle direction using the first vertex fitter with

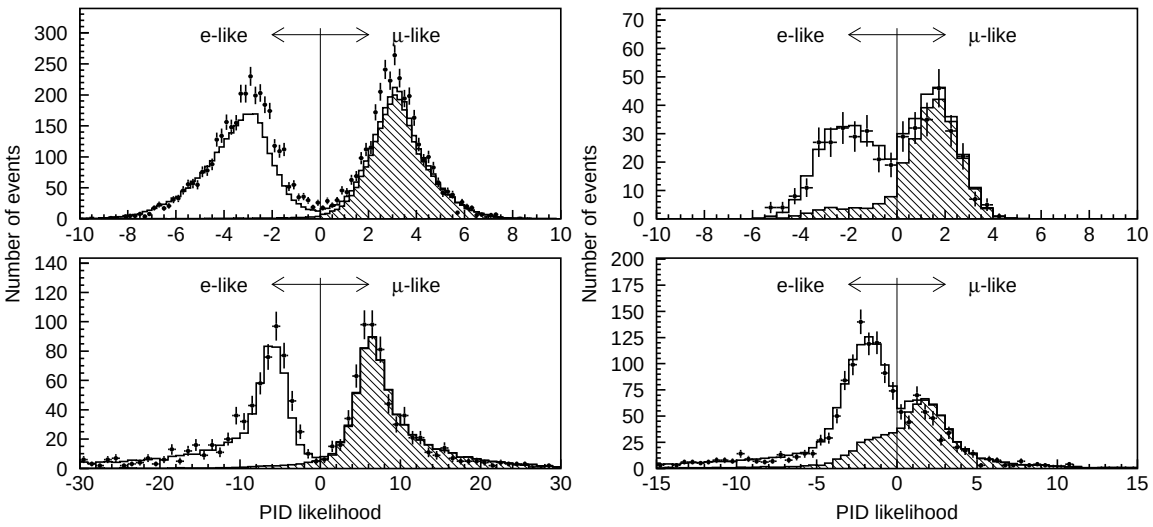

Figure 5.7: The PID likelihood distributions for FC Sub-GeV single-ring (left top), Multi-GeV single-ring (left bottom), Sub-GeV multi-ring (right top) and Multi-GeV multi-ring events (right bottom) of data (dot) and the Monte Carlo events (solid line) assuming 2-flavor $\nu_\mu \leftrightarrow \nu_\tau$ oscillation with $(\sin^2 2\theta,\, \Delta m^2) = (1.00,\, 2.5 \times 10^{-3}\,\mathrm{eV}^2)$ for SK-I. The hatched histograms show the ν_μ CC interactions.

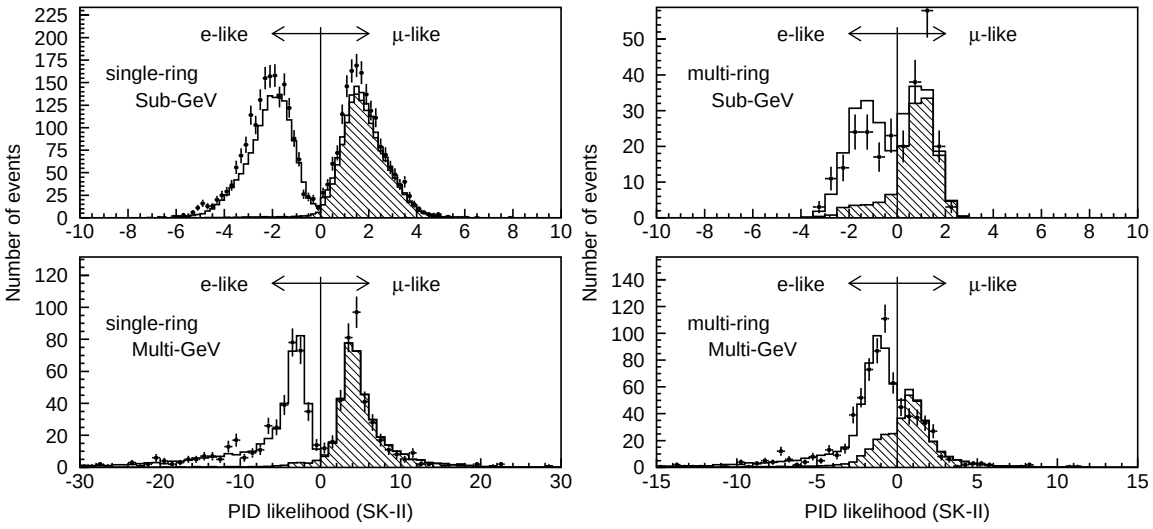

Figure 5.8: The PID likelihood distributions for FC Sub-GeV single-ring (left top), Multi-GeV single-ring (left bottom), Sub-GeV multi-ring (right top) and Multi-GeV multi-ring events (right bottom) of data (dot) and the Monte Carlo events (solid line) assuming 2-flavor $\nu_\mu \leftrightarrow \nu_\tau$ oscillation with $(\sin^2 2\theta,\, \Delta m^2) = (1.00,\, 2.5 \times 10^{-3}\,\mathrm{eV}^2)$ (solid lines) for SK-II. The hatched histograms show the ν_μ CC interactions.

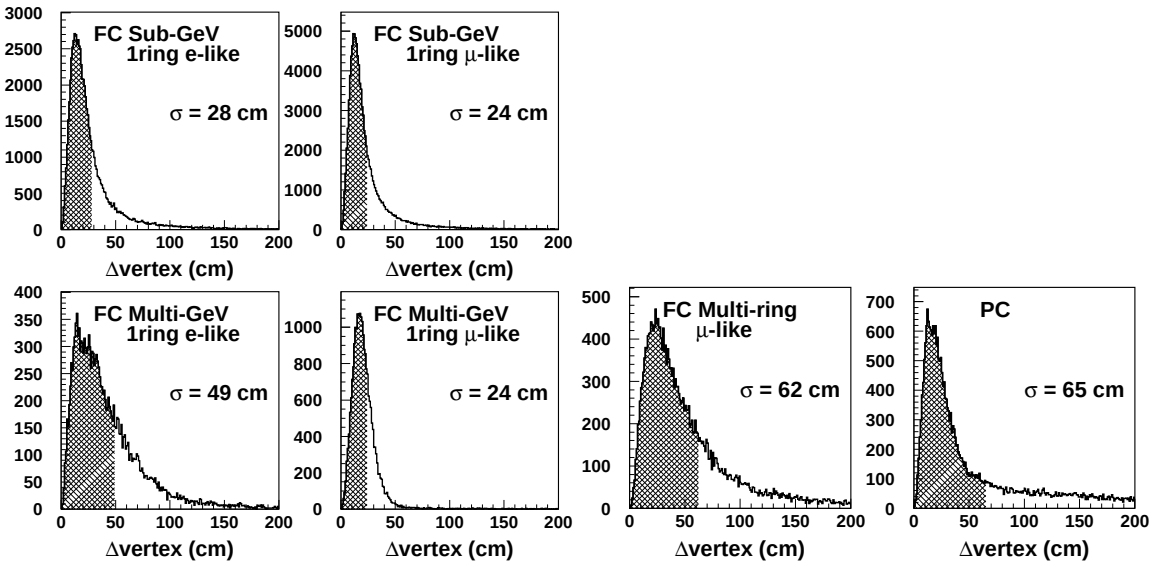

Figure 5.9: Distance between the true vertex and the reconstructed vertex for FC single-ring events, FC multi-ring μ-like events and PC events in the atmospheric neutrino Monte Carlo sample for SK-I.

the timing information. This process is iterated until the changes in the vertex position and the particle direction is less than 5 cm and 0.5 degrees. The vertex resolution for single-ring events is approximately 30 cm.

The performance of the fitting algorithm, TDC-fit or MS-fit, is examined by applying it to the atmospheric neutrino Monte Carlo sample. Figure 5.9 and 5.10 show the distance between the true vertex and the reconstructed vertex for FC single-ring events, FC multi-ring μ-like events and PC events for SK-I and SK-II. The vertex resolutions are estimated to be 28 cm (32 cm) and 24 cm (31 cm) for single-ring Sub-GeV e-like and μ-like events, 49 cm (47 cm) and 24 cm (26 cm) for single-ring Multi-GeV e-like and μ-like events, 62 cm (85 cm) for multi-ring μ-like events and 65 cm (68 cm) for PC events for SK-I (SK-II). Figure 5.11 shows the angular differences between the true electron or muon direction and the reconstructed direction for CC quasi-elastic scattering events in the atmospheric neutrino Monte Carlo sample. The angular resolutions are estimated to be 3.3° (3.5°) and 2.0° (2.2°) for Sub-GeV e-like events and μ-like events, 1.7° (1.6°) and 0.8° (1.0°) for Multi-GeV e-like events and μ-like events for SK-I (SK-II). The resolution is defined as the width where 68 % of the events are included.

5.6 Momentum Determination

The momentum of each particle is estimated by the observed p.e.s inside a cone with half opening angle of 70°. In order to determine the momentum for individual rings, the observed p.e.s in hit PMTs are separated to the contribution from each ring. The separation of the observed p.e.s is carried out based on the expected p.e. distribution from each ring as a function of the opening angle θ and uniform in azimuthal angle ϕ. The observed p.e.s in the i-th PMT

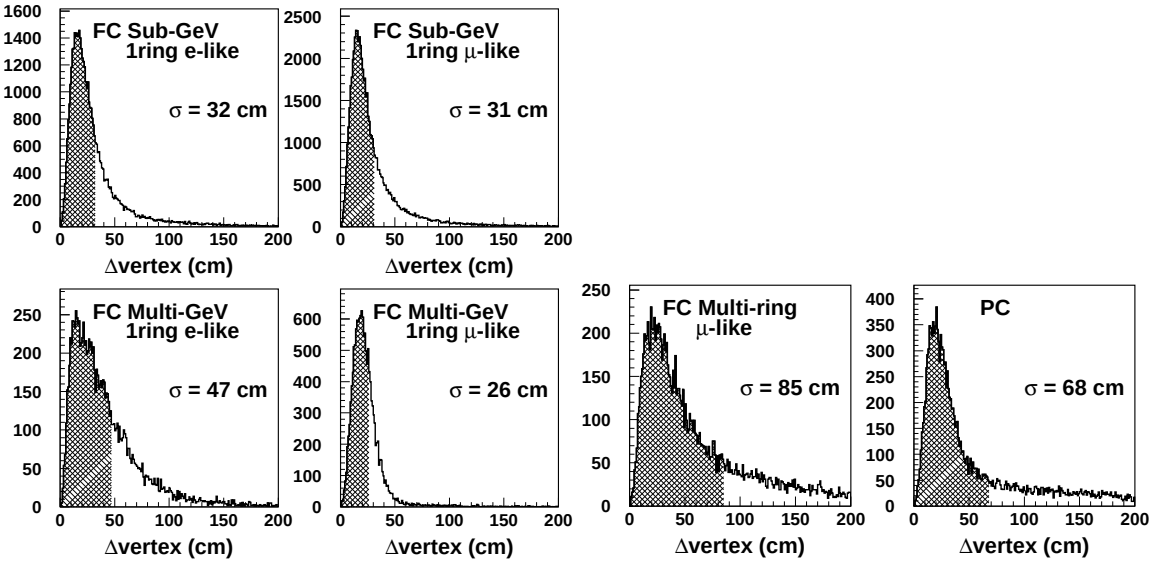

Figure 5.10: Distance between the true vertex and the reconstructed vertex for FC single-ring events, FC multi-ring μ-like events and PC events in the atmospheric neutrino Monte Carlo sample for SK-II.

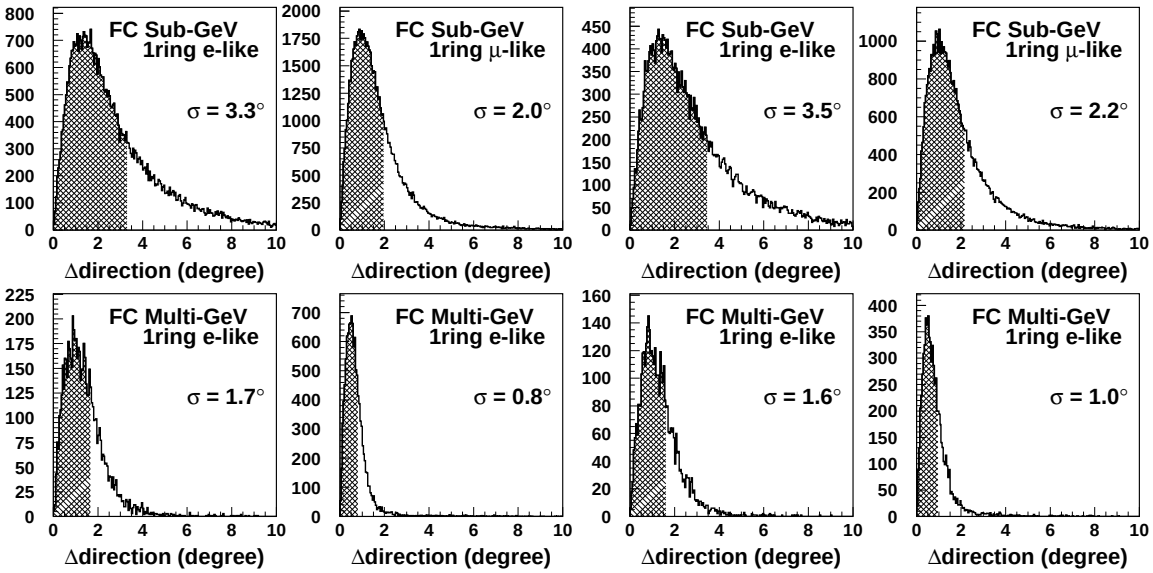

Figure 5.11: Angular difference between the true electron or muon direction and the reconstructed direction for CC quasi-elastic scattering events in the atmospheric neutrino Monte Carlo events. The left four panels show for SK-I and the right four show for SK-II.

from the n-th ring are estimated as :

$$q_{i,n}^{\rm obs} = q_i^{\rm obs} \times \frac{q_{i,n}^{\rm exp}}{\sum_{n'} q_{i,n'}^{\rm exp}} \tag{5.23}$$

where $q_{i,n}^{\rm obs}$ is the fractional p.e.s from the n-th ring in the i-th PMT, $q_i^{\rm obs}$ is the observed p.e.s in the i-th PMT and $q_{i,n}^{\rm exp}$ is the expected p.e.s .

To calculate the total number of p.e.s inside the 70° cone, the number of p.e.s in each PMT is corrected for the light attenuation in water and the acceptance of the PMT as follows :

$$RTOT_n = \frac{G_{\rm MC}}{G_{\rm data}} \left[\alpha \times \sum_{\substack{\theta_{i,n}<70^\circ \\ -50{\rm nsec}<t_i<250{\rm nsec}}} \left(q_{i,n}^{\rm obs} \times \exp\left(\frac{r_i}{L}\right) \times \frac{\cos\Theta_i}{f(\Theta_i)} \right) - \sum_{\theta_{i,n}<70^\circ} S_i \right] \tag{5.24}$$

where

α	:	normalization factor
$G_{\rm data}$, $G_{\rm MC}$	:	relative PMT gain parameter for the data and the Monte Carlo simulation
$\theta_{i,n}$	:	opening angle between the n-th ring direction and the i-th PMT direction
t_i	:	TOF subtracted hit timing of the i-th PMT position
L	:	light attenuation length in water
r_i	:	distance from the vertex position to the i-th PMT
$f(\Theta_i)$	:	correction function for the PMT acceptance as a function of the photon incidence angle Θ_i
S_i	:	expected p.e.s for the i-th PMT from scattered photons

The summation is restricted inside the time window from -50 nsec to +250 nsec around the peak of the TOF subtracted hit timing distribution to reject the effect from muon decay electrons. For the attenuation length in water L, the continuous measurement using cosmic ray through-going muons (Section 2.6.4) is used to correct the time variation for the observed data. Figure 5.12 shows the momentum resolution for electrons and muons estimated from the Monte Carlo simulation as a function of the true momentum. The resolution is defined as 1 σ width of the Gaussian fit.

The absolute energy scale is calibrated using the four independent calibration sources as described in Section 2.6.5. The uncertainty of the energy scale is estimated to be less than 2.5 % for the momentum range from a few ten MeV/c to about 10 GeV/c.

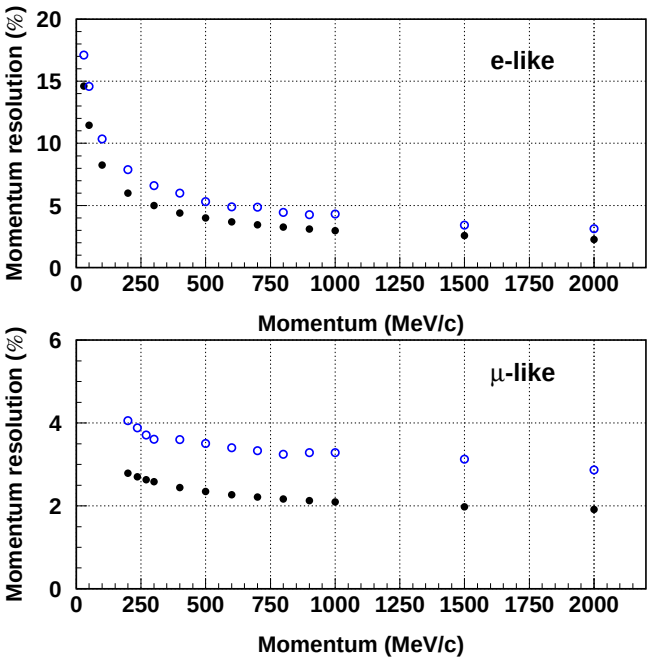

Figure 5.12: Momentum resolutions for electron (top) and muon (bottom) estimated by the Monte Carlo simulation as a function of the true momentum. The closed circles show those for SK-I and the open circles show those for SK-II.

5.7 Ring Number Correction

Next, if the number of rings are larger than 2, the number of rings is corrected using the energy and angle information obtained for each ring, and mis-fit rings are removed. The criteria for the correction to remove the i-th ring are :

(1-1) $p_i < p_j$; i $\neq$ j
p_i is the momentum of i-th ring.

and

(1-2) $\theta_{ij} < 30^\circ$
θ_{ij} is opening angle between the i-th and j-th rings.

and

(1-3) $p_i \cos\theta_{ij} < 60\,\mathrm{MeV/c}$
$p_i \cos\theta_{ij}$ is the momentum of i-th ring projected perpendicularly to j-th ring.

or

(2-1) $p_i < 40\,\mathrm{MeV/c}$

and

(2-2) $p_i/p_{\rm tot} < 0.05$
$p_{\rm tot}$ is the total momentum for all rings.

In SK-I, the momentum for the ring correction is determined without using the PID information, but in SK-II, the momentum is calculated using the PID information.

5.8 Decay Electron Finding

In this section, the detection method of electrons from muon decays following the primary events is described. There are three types of observed decay electrons :

- sub-event type
  Decay electrons observed as a separate event (sub-event) as shown in Figure 5.13.
- primary-event type
  Decay electrons observed in the same event as primary event.
- split type
  Decay electrons occurred around the end of event timing window. The event is recorded separately in the primary event and the sub-event.

For sub-event type events, the following criteria are required :

(1) The time interval from a primary event(Δt) is $< 30\,\mu$sec.

and

(2) The total number of hit PMTs is greater than 50 (25 for SK-II).

and

(3) The goodness of vertex fit is greater than 0.5.

and

(4) The number of hit PMTs in a 50 nsec time window is greater than 30 (15 for SK-II).

and

(5) The total number of photoelectrons is less than 2000 (1000 for SK-II).

and

(6) The number of hit PMTs in a 50 nsec time window (N_{50}) is greater than 60 (30 for SK-II).

For primary-event type decays, another peak after the primary event is searched with requirenment more than 20 hits in 30 nsec window above the background level. Additional conditions for decay electrons are as follows :

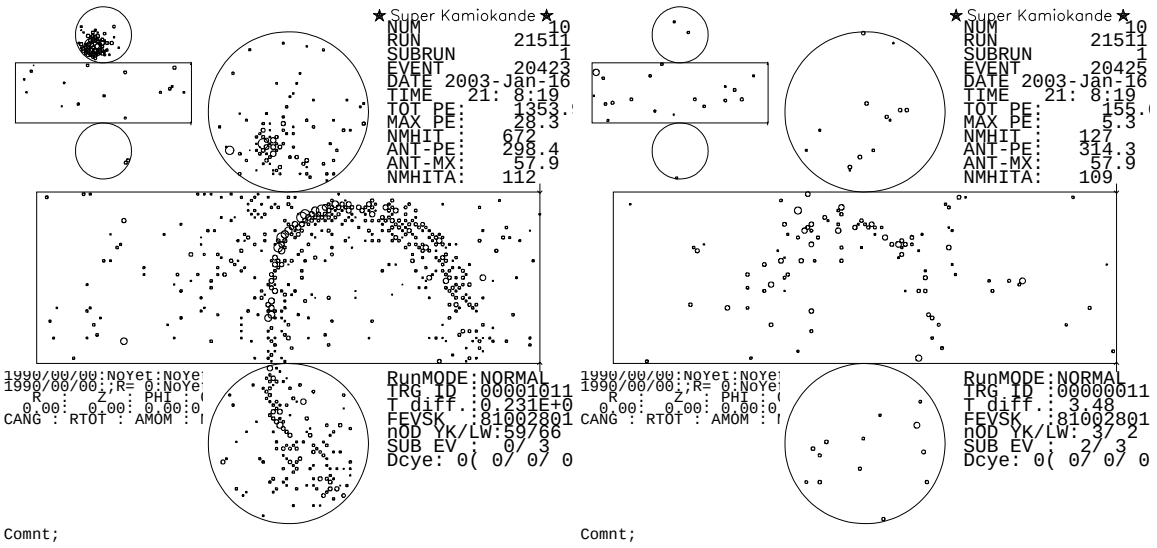

Figure 5.13: An event display of a sub-event type decay electron. The left figure shows the primary event (cosmic ray stopping muon) and the right figure shows the following decay electron event. The time difference between two events is about 3.5 μsec.

(7) The number of hit PMT in a 30 nsec time window is greater than 40 (20 for SK-II). (for primary-event type and split type)

and

(8) $0.1\,\mu\text{sec} < \Delta t < 0.8\,\mu\text{sec}$ or $1.2\,\mu\text{sec} < \Delta t < 30\,\mu\text{sec}$ (for all types)

N_{50}=60 (30 for SK-II) corresponds to about 11 MeV of electron energy. Criterion (1) rejects the gamma emission from μ^- captured on ^{16}O nuclei. Criterion (8) rejects the decays in the inefficient time interval around 1 μsec. The efficiency of detecting these electrons are 80 % and 63 % for μ^+ and μ^-, respectively.

5.9 Event reconstruction for single-ring π^0 sample

Figure 5.14 shows the momentum distribution of FC Sub-GeV single-ring e-like events in the Monte Carlo events with each interaction mode. The 9 % of NC events is mostly originated from a NC single π^0 production (NC1π^0) and is a background to ν_e-induced CCQE events. A π^0 immedeately decays into two γ's and can be identified as a π^0 event by the reconstruction algorism described in Section 2.6.5. However, one γ is sometimes missed by the standard reconstruction algorism and then such events are classified as single-ring e-like events. A γ ray from π^0 decay could not identified by the following reasons :

1. The energies of two γ's are highly asymmetric and the energy of the second γ ($E_{\gamma 2}$) is too small to be reconstructed as a ring.

2. The two rings of γ's are overlapped and reconstructed as one ring when the opening angle between two γ's is small.

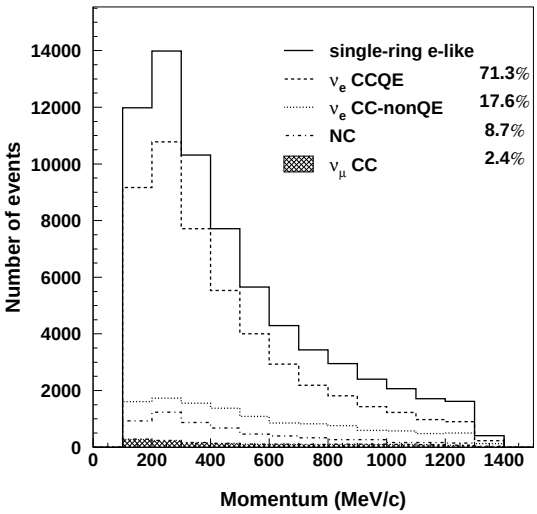

Figure 5.14: The momentum distributions of FC Sub-GeV single-ring e-like events in the atmospheric neutrino events. The dashed line shows ν_e-induced CCQE events, the dotted line shows ν_e-induced CC non-QE events (such as single- or multi- meson production), the dashed and dotted line shows NC events and the hatched region shows ν_μ-induced CCQE events. The values are the fraction of each interaction mode in FC single-ring e-like events.

Figure 5.15(a) shows the scatter plot between the energy of the second γ and the opening angle between two γ's for NC1π^0 events in the atmospheric Monte Carlo events. To separate these π^0 events from the CCQE events, π^0 fitter is introduced. Figure 5.15(b) shows the momentum distribution for NC1π^0 events in the atmospheric Monte Carlo events and the hatched region shows the events identified as single-ing e-like. About 33 % of NC1π^0 events are identified as single-ring e-like in our standard reconstruction procedure.

5.9.1 Reconstruction algorism for π^0 fitter

The π^0 fitter reconstructs the second gamma-ray on the assumption of the existence of two Cherenkov rings, comparing the observed charge distribution on the PMTs with the expected charge distribution of two gamma-rays. The two gamma-rays are supposed to be emitted at one point and the direction of the more energetic gamma-ray is set to the direction derived from the vertex fitter (Section 5.5). Varying the direction of the second gamma-ray and the fraction of energy shared among the two gamma-rays, the combination of two gamma-rays which matches best with the observed charge distribution is determined.

The expected charge distribution for the i-th PMT is calculated as follows :

$$q_i^{\rm exp} = \alpha_e \times Q^{\rm exp}(\theta_i, p_\gamma, r_i) \times \left(1 - \frac{r_i}{\sqrt{r_i^2 + R_{PMT}^2}}\right) \times \frac{1}{\exp(r_i/L)} \times f(\Theta_i) + q_i^{\rm scatt} \qquad (5.25)$$

where

α_e : normalization factor

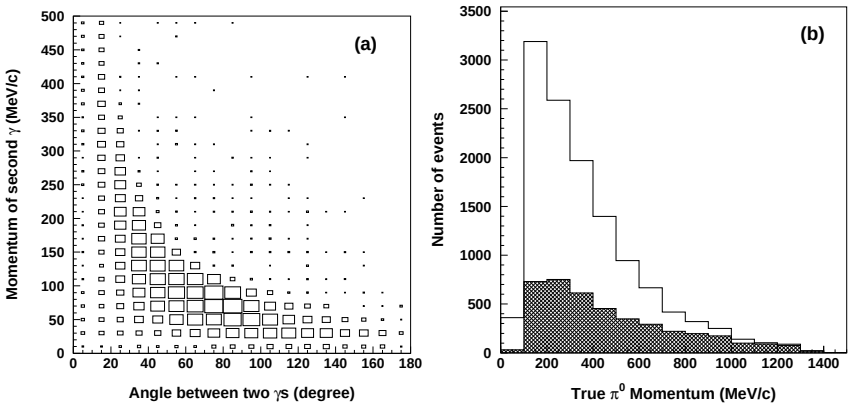

Figure 5.15: (a) The scatter plot between the true momentum of the second gamma and the true opening angle between two gammas for NC1π^0 events in the atmospheric Monte Carlo events. (b) The distribution of the true π^0 momentum for NC1π^0 events in the atmospheric Monte Carlo events. The hatched region shows the NC1π^0 identified as single-ring e-like events.

$Q^{\rm exp}$	:	expected photon distribution from a gamma-ray as a function of θ_i, p_γ and r_i
θ_i	:	opening angle between the i-th PMT direction and the ring direction
p_γ	:	initial gamma-ray momentum
r_i	:	distance from the vertex to the i-th PMT
R_PMT	:	PMT radius of 25 cm
L	:	light attenuation length in water
$f(\Theta_i)$	:	correction for the PMT acceptance as a function of the photon incidence angle Θ_i
$q_i^{\rm scatt}$	:	expected p.e.s for the i-th PMT from scattered photons

The factors of $\left(1 - r_i/\sqrt{r_i^2 + R_{PMT}^2}\right)$ and exp(-r_i/L) represent the corrections of solid angle and light attenuation, respectively. $Q^{\rm exp}$ is the expected photon flux which is estimated as a function of the photon incident angle Θ_i, the initial gamma-ray momentum p_γ and the distance from the vertex to the i-th PMT r_i in the Monte Carlo simulation.

5.9.2 Best-fit Ring Configuration

To determine the best-fit configuration of two gamma-rays, a log likelihood method is used. Using the same probability function as Equation (5.11), the likelihood is defined as :

$$L = \sum_{i=1} log\left(prob\left(q_i^{\rm obs}, q_i^{\rm exp}\right)\right) \tag{5.26}$$

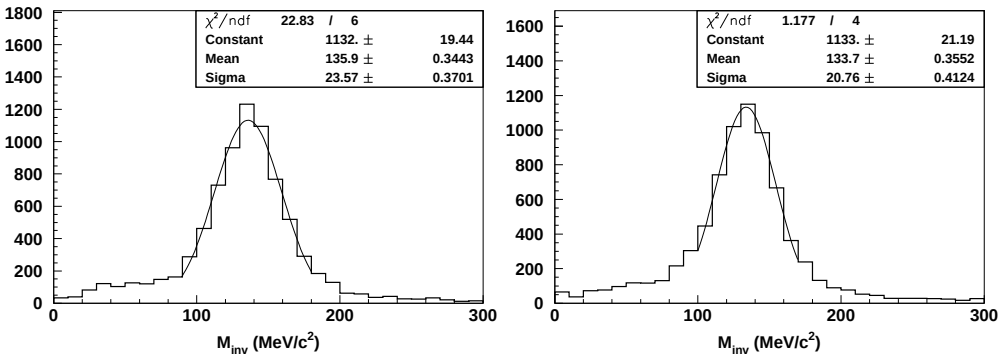

Figure 5.16: The invariant mass distributions for NC1π^0 events with the line of the Gaussian fit for SK-I (left) and SK-II (right).

The $q_i^{\rm exp}$ is optimized by changing the direction of the second gamma and the momentum fraction for the second gamma to give the minimum likelihood value, using the simplex method [121, 122]. In the procedure, any kinematical constraint of π^0 decay is not required. The π^0 events such as two rings are almost overlapped have a narrow L distribution in the direction of the first ring. To improve the fitting performance for such events, the second fit is performed with the finer stepping size to look for the second gamma-ray near the first gamma-ray ring. The smaller L between the first wide fit and the second narrow fit is chosen as a fitting result.

Figure 5.16 shows the distribution of the invariant mass (M_{inv}) reconstructed from two gamma-rays of NC1π^0 events found by the π^0 fitter. M_{inv} is defined as :

$$M_{inv} = \sqrt{2E_{\gamma 1}E_{\gamma 2}(1-\cos\theta_{\gamma\gamma})}. \tag{5.27}$$

The mean value of the reconstructed invariant mass is 135.9 MeV/c^2 and 133.7 MeV/c^2 and the resolution of the invariant mass is 23.6 MeV/c^2 and 20.8 MeV/c^2 for SK-I and SK-II, respectively. Figure 5.17 shows the invariant mass distributions for ν_e CCQE events and NC events among the FC single-ring e-like events. The invariant mass for CCQE events is reconstructed smaller than π^0 mass, while that for NC is reconstructed close to π^0 mass. Therefore 100 MeV/c^2 cut can separate between CCQE events and NC events among FC single-ring e-like events. For ν_eCCQE events, there is no real second ring and the fitter could reconstruct the second fake ring with hits around the first energetic ring. Since the electromagnetic shower defuses the edge of the first ring and hits around the first ring, the fitter recognizes these hits as a ring of gamma-ray. Then, the opening angle between the first ring and the fake second ring is small and the energies of the first ring and the fake second ring are expected to be small after sharing the initial visible energy of electron as shown in Figure 5.18. The left plot on Figure 5.18 shows the opening angle between two gammas found by π^0 fitter for ν_e CCQE events and NC events among the FC single-ring e-like events and the right plot on Figure 5.18 shows the distribution of the energy fraction of the second gamma $E_2/(E_1+E_2)$ for the same events. The separation of the single-ring π^0 events among the FC single-ring e-like events will be described in Section 6.1.1.

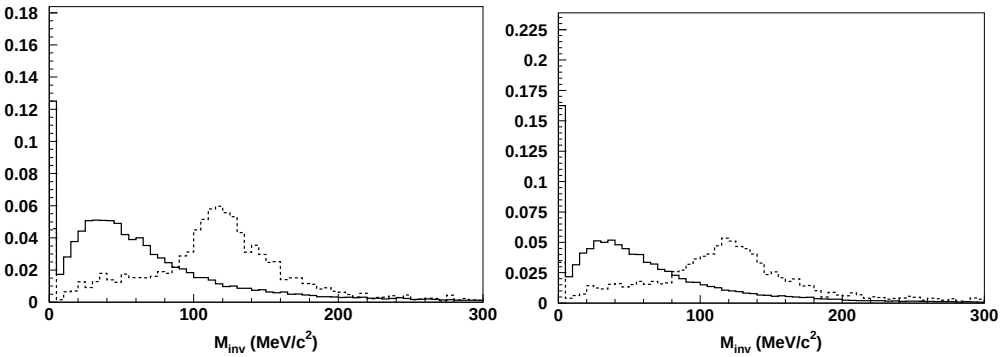

Figure 5.17: The invariant mass distribution for ν_eCCQE (solid line) and NC (dashed line) among the FC single-ring e-like events for SK-I (left) and SK-II (right). Each distribution is normalized to 1.

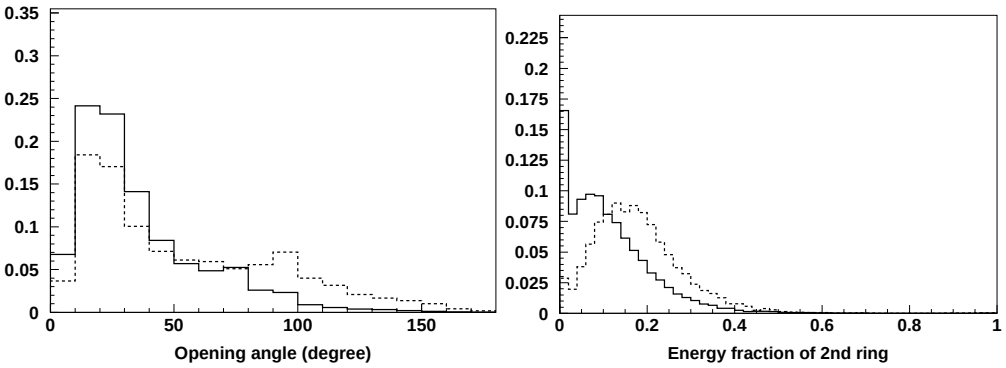

Figure 5.18: The reconstructed opening angle between two gammas (left) and the energy fraction of the second gamma $E_2/(E_1+E_2)$ (right) for ν_eCCQE (solid line) and NC (dashed line) among the FC single-ring e-like events. Each distribution is normalized to 1.

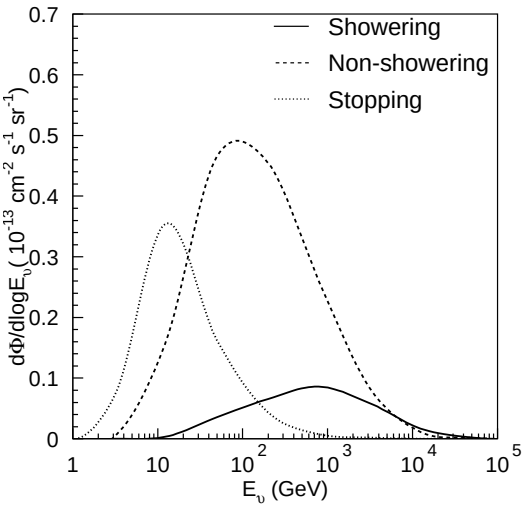

Figure 5.19: The energy spectrum of primary neutrino for upward stopping (dotted line), non-showeing (dashed line) and showering (solid line) muon events.

5.10 Event Reconstruction for Upward-Going Muon Sample

Among the upward through-going muon events, some of them are accompanied with an electromagnetic shower. The typical energy of these muons are higher than that for non-showering upward through-going muons. Figure 5.19 shows the primary neutrino energy distributions for these events.

Therefore, the upward through going muons are separated to non-showering and showering events. Details of the criteria to separate them can be found in [123]. The event reconstruction algorithm for upward-going muons is different from that for FC and PC events. The same program is used for both observed data and atmospheric neutrino Monte Carlo events which pass through the data reduction process. The reconstruction is based on MS-fit (see Section 5.5) with the assumption that the particle is a muon and the vertex is at the inner detector surface. However, when the muon produces an electromagnetic shower, almost all the ID PMTs are hit or the Cherenkov ring cannot observed. For these events, the information of OD hit is used to determine the particle direction. The angular resolution is 2.0° (2.3°) for stopping muon events for SK-I (SK-II), 1.3° (1.6°) for non-showering muon events for SK-I (SK-II) and 1.5° (2.7°) for showering muon events for SK-I (SK-II) as shown in Figure 5.20.

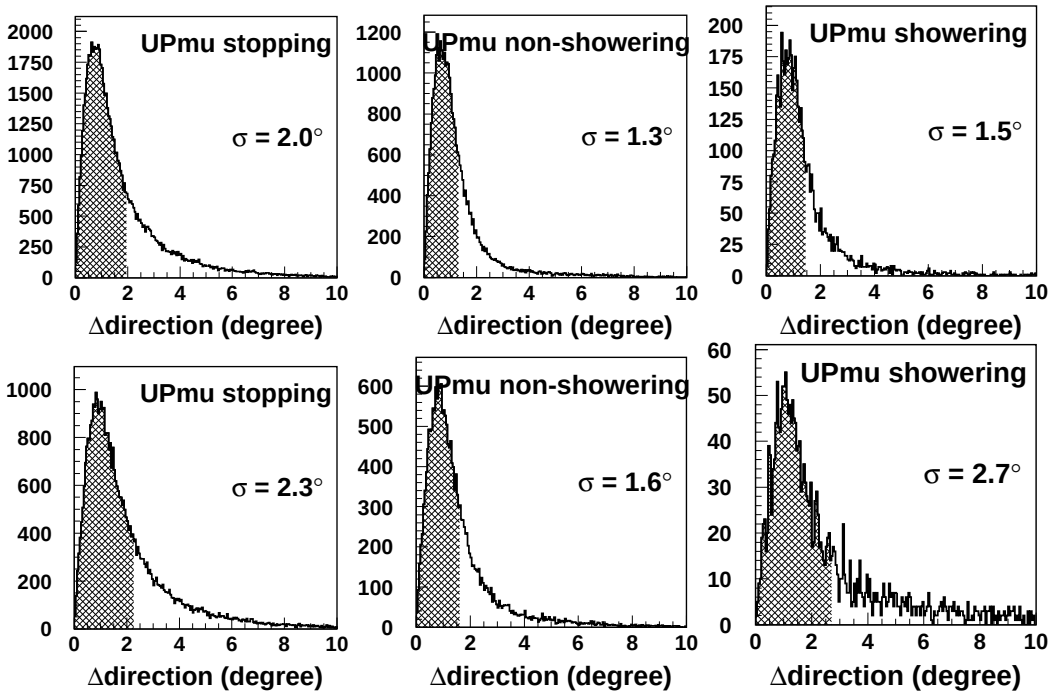

Figure 5.20: Angular difference between the true direction and the reconstructed direction for upmu stopping event, upmu non-showering events and upmu showering events in the atmospheric neutrino Monte Carlo sample. The upper three panels are for SK-I and the bottom three are for SK-II.

Chapter 6

Data set

In this analysis, FC, PC and UPMU data during the SK-I period (1489.2 days exposure for FC and PC, 1645.9 days for UPMU) and the SK-II period (798.6 days for FC and PC, 827.7 days for UPMU) are used. Since the reconstruction of long path length muon is less sensitive to the detector condition, the live time of the UPMU data is larger than that of FC and PC data. The amount of simulated the atmospheric neutrino events are equivalent to an exposure of 100 years for SK-I and 60 years for SK-II.

Final samples of FC and PC events are selected by requiring the following criteria after data reduction and event reconstruction processes :

- FC samples

  (1) Number of hit PMTs in the OD hit cluster (NHITAC) < 10 (16 for SK-II)

  (2) Distance from event vertex to the nearest ID wall (D_{wall}) $> 200\,\mathrm{cm}$

  (3) Visible energy assuming electrons (E_{vis}) $> 30\,\mathrm{MeV}$

  – FC single-ring μ-like samples

    (4) $p_\mu > 200\,\mathrm{MeV}/c$

  – FC single-ring e-like samples

    (5) $p_e > 100\,\mathrm{MeV}/c$

  – FC multi-ring μ-like sample

    (6) The most energetic ring is identified as μ-like and the momentum $p_\mu > 600\,\mathrm{MeV}/c$ and $E_{vis} > 600\,\mathrm{MeV}$

  – FC multi-ring e-like sample

    (7) The most energetic ring is identified as e-like and $E_{vis} > 1330\,\mathrm{MeV}$

- PC samples

  (1) NHITAC ≥ 10 (16 for SK-II)

  (2) $D_{wall} > 200\,\mathrm{cm}$

  (3) $E_{vis} > 350\,\mathrm{MeV}$

  – PC OD stopping sample

(4) The maximum number of p.e.s observed in the OD in a sliding 500 nsec time window from −400 nsec to +600 nsec (PE_{anti}) is less than $PE_{exp}/1.5$, where PE_{exp} is the expected number of p.e.s in the OD from the potential track length in the OD

(5) The most energetic ring or the second one should be identified as μ-like

– PC OD through-going sample

(6) $PE_{anti} > PE_{exp}/1.5$

FC and PC samples are separated by the number of hit PMTs in the OD hit cluster (NHITAC, see Chapter 4). The fiducial volume for the FC and PC samples defined by D_{wall} >200 cm corresponds to 22.5 kton. The visible energy (E_{vis}) is defined as the sum of the energy of each ring assuming all rings are produced by electrons. The criterion (3) for the FC sample, $E_{vis} > 30$ MeV, is required to reject remaining low energy background events. FC samples are divided into "Sub-GeV sample" whose visible energy is below 1.33 GeV and "Multi-GeV sample" whose visible energy is above 1.33 GeV. The FC samples are classified into single-ring and multi-ring samples according to the number of Cherenkov rings. The FC single-ring sample is classified into μ-like and e-like samples by the results of particle identification. To increase the purity of the interaction mode in each sample, the FC Sub-GeV single-ring events are separated into more finer samples as described in Section 6.1. For multi-ring sample, the most energetic ring is used to identify the particle type. For PC events, the requirement of $E_{vis} >$ 350 MeV, which corresponds to muon momentum of 530 MeV/c, is safe for PC events because the exiting muons must have at least momentum of 700 MeV/c to reach the OD. PC events are separated into two categories, "OD stopping sample" and "OD through-going sample" using the observed p.e.s in the OD and the expected charge derived from the track length. Muons in the "OD stopping sample" are assumed to stop in the OD, while more energetic muons in the "OD through-going sample" are assumed to pass through the OD.

The upward stopping and through-going muon samples are selected by requiring the following criteria after data reduction and event reconstruction processes :

- Upward stopping muon sample

  (1) Number of hit OD PMTs within 8 m from the exit point (NHITEX) < 10 (16 for SK-II)

  (2) Fitted direction is upward (zenith angle cosΘ ≤ 0)

  (3) $p_\mu \geq 1.6$ GeV/c (equivalent to track length of 7 m for muon)

- Upward through-going muon sample

  (1) NHITEX ≥ 10 (16 for SK-II)

  (2) Fitted direction is upward (zenith angle cosΘ ≤ 0)

  (3) Distance from the entrance point to the exit point ≥ 7 m

Upward stopping and through going muon samples are separated by the number of hit OD PMTs near the exit point (NHITEX, see Chapter 4). The third criterion is required to keep the performance of the event reconstruction. The track length is determined by the distance between the entrance and exit points for upward through-going muons. The upward through-going muon

sample is further separated into showering muon sample and non-showering muon sample. The showering muon events consist of the high energy muons which lose energy through radiative processes such as bremsstrahlung, e^+e^- pair production and photo-nuclear interactions and the energy of the parent neutrino is approximately 1 TeV. The momentum of upward stopping muon is determined from the observed charge by the same way as that for FC and PC events (see Section 5.6).

The number of events for the atmospheric neutrino data in each final sample is shown in Table 6.1 together with the Monte Carlo predictions.

6.1 Event Samples for FC Sub-GeV

As mentioned in Section 1.3, the excess of ν_e in the low energy region is expected by the sub-dominant oscillation effect due to the solar neutrino parameters. In order to enhance the purity of CCQE interactions and to improve the sensitivity for the solar term effect, FC Sub-GeV events are further separated to sub-samples using the information such as the number of decay electrons.

6.1.1 FC Sub-GeV single-ring e-like events

The FC Sub-GeV single-ring e-like sample contains about 10 % of NC events which are mainly π^0 events from $\nu N \rightarrow \nu N \pi^0$ interactions and can be background for the observation of the excess of ν_e events. Therefore these π^0 events are separated from ν_e-enriched samples using the likelihood analysis with the information of π^0 fitter (Section 5.9.1). Figure 6.1 and Figure 6.2 show the invariant mass distributions from the π^0 fitter for $\nu_e + \overline{\nu}_e$ charged current (CCQE) and neutral current (NC) events among FC Sub-GeV single-ring e-like Monte Carlo events in the each energy region. In the figure, the area of each distribution is normalized to 1. For e-like events with the electron momentum below 250 MeV/c, π^0 mass $> 100\,\mathrm{MeV/c^2}$ cut well separates between CCQE and NC. For e-like events with the electron momentum above 250 MeV/c, since the π^0 mass > 100 cut is not efficient enough to separate the two samples, the likelihood selection using π^0mass, energy fraction of the second ring and Δ-likelihood from π^0 fitter is applied. Δ-likelihood is defined as $L(wide) - L(narrow)$ using Equation 5.26 with wide fitting and narrow fitting. Figure 6.3 and Figure 6.4 show the distributions of these valuables used in the likelihood. CCQE events and NC events are separately shown and normalized by area. The likelihood distributions are shown in Figure 6.5 together with the criteria values shown by arrows. To keep the statistics of CCQE events, the different cut criteria in each energy region are applied.

After the likelihood selection of π^0-like sample, the rest of e-like events are separated to two categories according to the number of decay electrons, 0μedecay sample which has no decay electron or 1μedecay sample which has one or more decay electrons. Figure 6.6 show the distributions of number of decay electrons of FC Sub-GeV single-ring e-like events π^0-like events are subtracted for data and Monte Carlo events assuming no oscillation and 2-flavor $\nu_\mu \leftrightarrow \nu_\tau$ oscillation with $(\sin^2 2\theta_{23},\, \Delta m^2_{23}) = (1.00,\, 2.5 \times 10^{-3}\,\mathrm{eV^2})$. The live time of the Monte Carlo events is normalized to that of the observed data. As shown in Table 6.2, the CCQE fraction of FC Sub-GeV single-ring e-like 0μedecay sample compared with that of FC Sub-GeV single-ring e-like sample is improved to 80.4 % from 71.3 % and the fraction of NC is decreased to 4.9 % from 8.7 %. The momentum distributions of the separated three e-like samples are shown in

	SK-I		SK-II	
	Data	Monte Carlo	Data	Monte Carlo
FC Sub-GeV				
single-ring				
e-like	3353	2789.2	1842	1494.8
0μedecay	2930	2434.8	1607	1302.1
1μedecay	259	179.1	147	103.4
π^0-like	164	175.2	91	89.3
μ-like	3227	4132.7	1718	2155.3
0μedecay	1028	1338.6	576	727.5
1μedecay	2049	2644.4	1059	1347.9
2μedecay	150	149.7	83	79.8
2-ring π^0-like	506	379.3	266	203.2
FC Multi-GeV				
single-ring				
e-like	746	667.7	417	415.7
μ-like	651	881.3	379	496.2
multi-ring				
μ-like	647	1017.4	349	504.6
PC	911	1143.8	427	588.4
Upward-going muon				
stopping	417.7	721.4	208.6	338.3
non-showering	1544.8	1429.1	771.2	741.9
showering	296.5	251.0	105.4	89.9

Table 6.1: Summary of atmospheric neutrino events for data and Monte Carlo events of FC, PC and upward-going muon samples for SK-I and SK-II. The live time of FC and PC is 1489.2 days for SK-I and 798.6 days for SK-II and the live time of upward-going muon samples is 1645.9 days for SK-I and 827.7 days for SK-II. The number of the Monte Carlo events is normalized by the live time of the data.

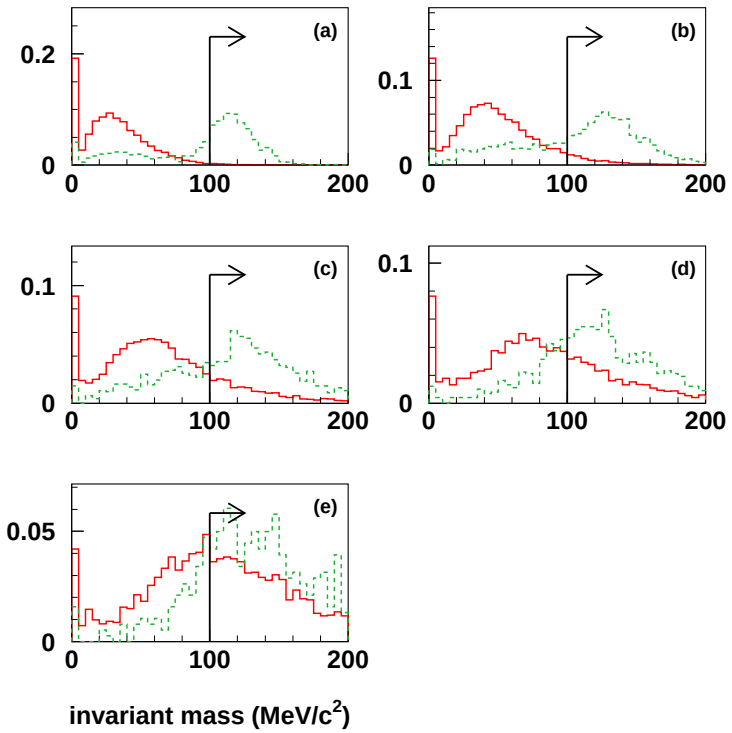

Figure 6.1: The invariant mass distributions for $\nu_e+\overline{\nu}_e$ charged current (solid line) and neutral current (dashed line) events for FC Sub-GeV single-ring e-like Monte Carol events in (a) $P_e < 250\,\mathrm{MeV/c}$, (b) $250\,\mathrm{MeV/c} \leq P_e < 400\,\mathrm{MeV/c}$, (c) $400\,\mathrm{MeV/c} \leq P_e < 630\,\mathrm{MeV/c}$, (d) $630\,\mathrm{MeV/c} \leq P_e < 1000\,\mathrm{MeV/c}$, (e) $1000\,\mathrm{MeV/c} \leq P_e$ for SK-I. Each distribution is normalized to 1.

Figure 6.7 for data and Monte Carlo events. The distributions for data and the oscillated Monte Carlo events are consistent, if the uncertainty in the absolute normalization of the Monte Carlo (which is about 20 %) is taken into account. The systematic errors in the event separation will be described in Section 7.3.3.

6.1.2 FC Sub-GeV single-ring μ-like events

The FC Sub-GeV single-ring μ-like events are separated to three samples according to the number of decay electrons. They are 0μedecay, 1μedecay and 2μedecay samples which have no decay electron, one decay electron and two or more decay electrons, respectively. Figure 6.8 shows the distribution of the number of decay electrons for FC Sub-GeV single-ring μ-like events. The fraction of each interaction mode in three samples is summarized in Table 6.2. The number of 0μedecay events is about 30 % of the total FC Sub-GeV single-ring μ-like events. The fraction of CCQE events is about 73 % in which decay electrons are not detected and the fraction of NC events is about 11 %, most of which are $\nu\mathrm{N}\rightarrow\nu\mathrm{N}'\pi^{\pm}$. The number of 1$\mu$edecay events is about 64 % of the total FC Sub-GeV single-ring μ-like events. The fraction of CCQE events is about 80 %, which is improved from 74.4 % in FC Sub-GeV single-ring μ-like events. The momentum distributions for the separated three μ-like samples are shown in Figure 6.9 for data and Monte

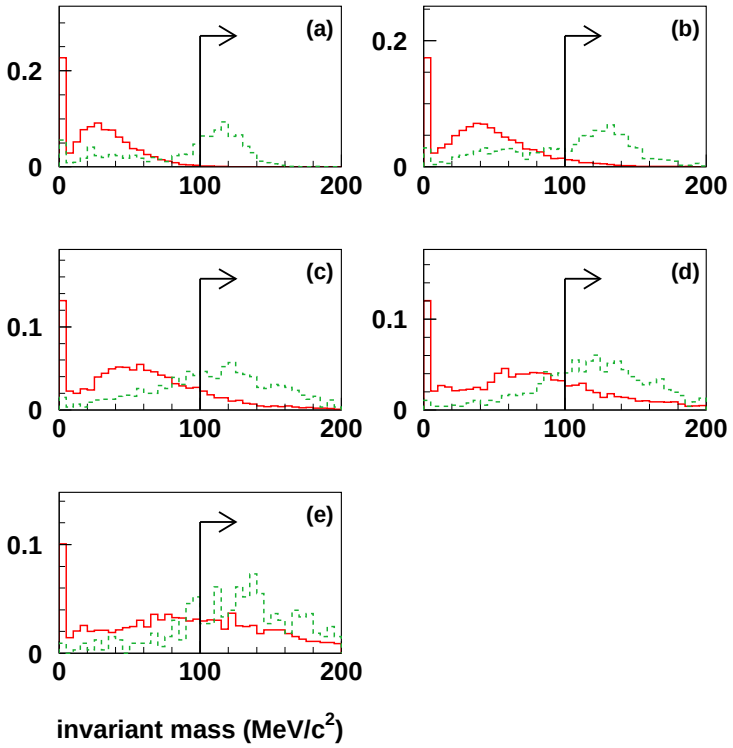

Figure 6.2: The invariant mass distributions for ν_e+$\overline{\nu}_e$ charged current (solid line) and neutral current (dashed line) events for FC Sub-GeV single-ring e-like Monte Carol events in (a) $P_e < 250\,\mathrm{MeV/c}$, (b) $250\,\mathrm{MeV/c} \leq P_e < 400\,\mathrm{MeV/c}$, (c) $400\,\mathrm{MeV/c} \leq P_e < 630\,\mathrm{MeV/c}$, (d) $630\,\mathrm{MeV/c} \leq P_e < 1000\,\mathrm{MeV/c}$, (e) $1000\,\mathrm{MeV/c} \leq P_e$ for SK-II. Each distribution is normalized to 1.

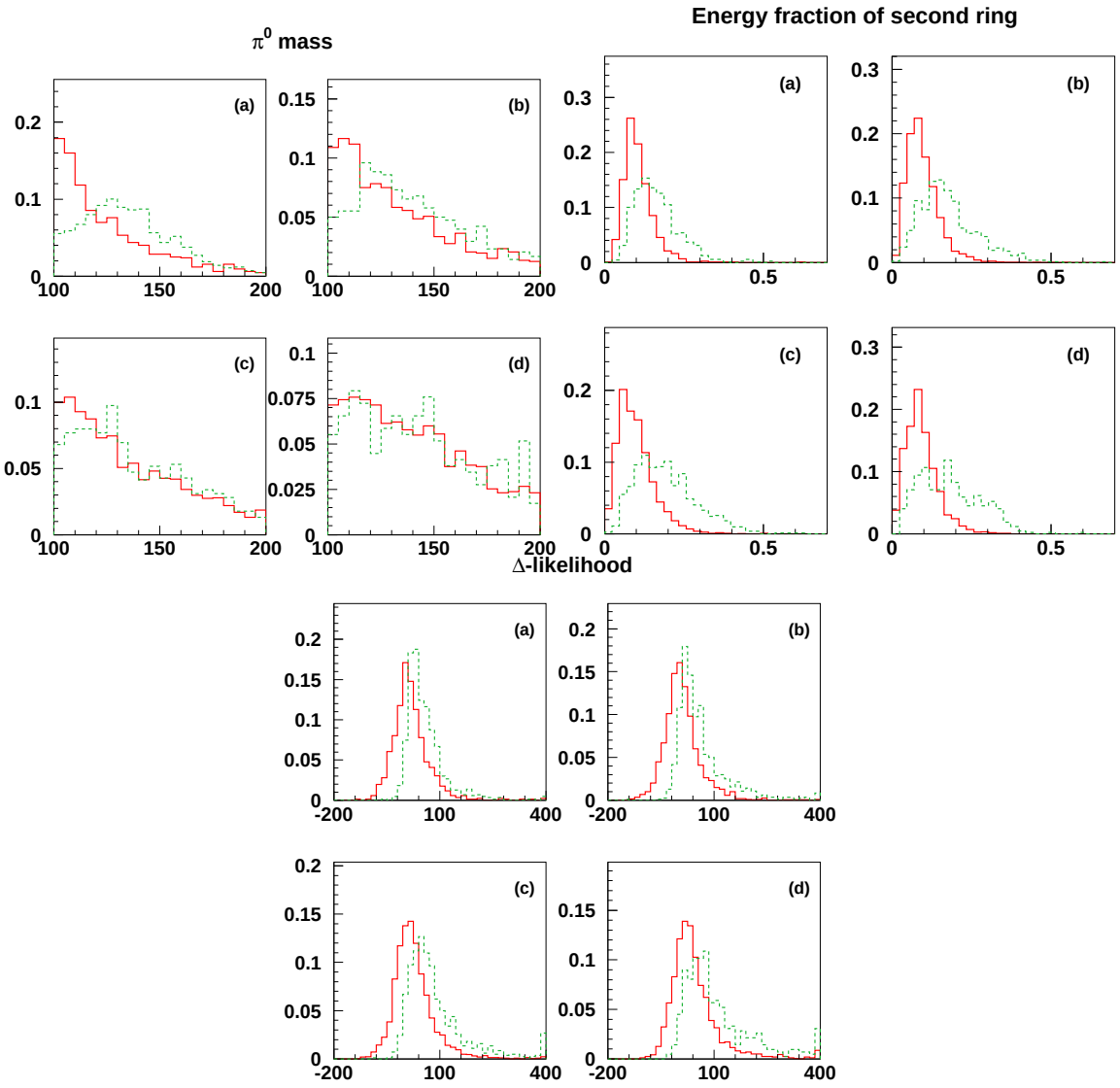

Figure 6.3: The distributions of valuables used in the likelihood analysis of the π^0-like sample selection likelihood for CCQE (solid line) and NC (dashed line) among FC Sub-GeV single-ring e-like Monte Carlo events in (a) $250\,\mathrm{MeV/c} \leq P_e < 400\,\mathrm{MeV/c}$, (b) $400\,\mathrm{MeV/c} \leq P_e < 630\,\mathrm{MeV/c}$, (c) $630\,\mathrm{MeV/c} \leq P_e < 1000\,\mathrm{MeV/c}$, (d) $1000\,\mathrm{MeV/c} \leq P_e$ for SK-I. Each distribution is normalized to 1. The upper left four panels show π^0 mass distributions above $100\,\mathrm{MeV/c^2}$, the upper right four panels show the energy fraction of the second ring which is found by the π^0 fitter and the bottom four panels show the Δ-likelihood.

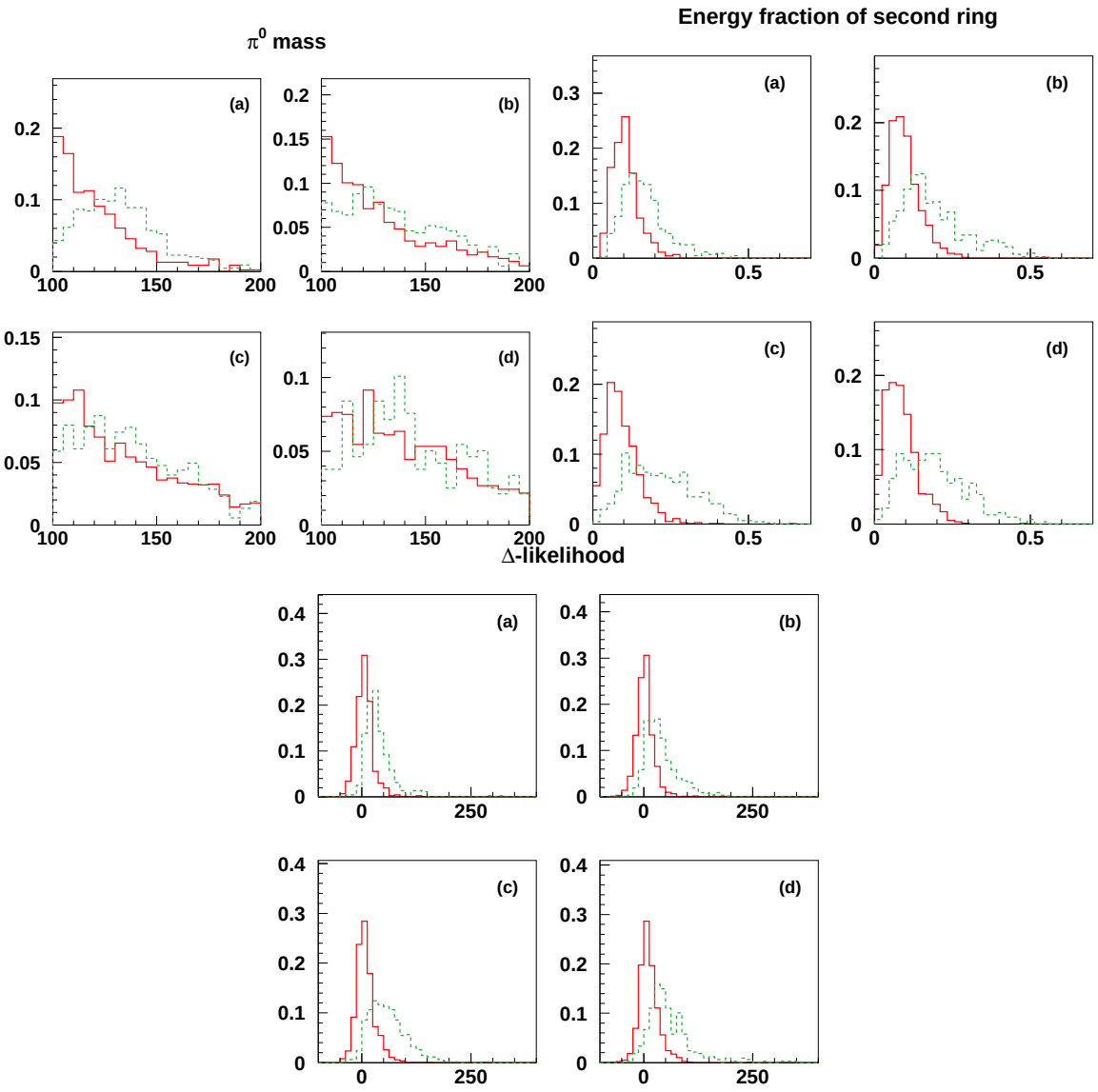

Figure 6.4: The distributions of valuables used in the likelihood analysis of the π^0-like sample selection likelihood for CCQE (solid line) and NC (dashed line) among FC Sub-GeV single-ring e-like Monte Carlo events in (a) $250\,\mathrm{MeV/c} \leq P_e < 400\,\mathrm{MeV/c}$, (b) $400\,\mathrm{MeV/c} \leq P_e < 630\,\mathrm{MeV/c}$, (c) $630\,\mathrm{MeV/c} \leq P_e < 1000\,\mathrm{MeV/c}$, (d) $1000\,\mathrm{MeV/c} \leq P_e$ for SK-II. Each distribution is normalized to 1. The upper left four panels show π^0 mass distributions above $100\,\mathrm{MeV/c^2}$, the upper right four panels show the energy fraction of the second ring which is found by the π^0 fitter and the bottom four panels show the Δ-likelihood.

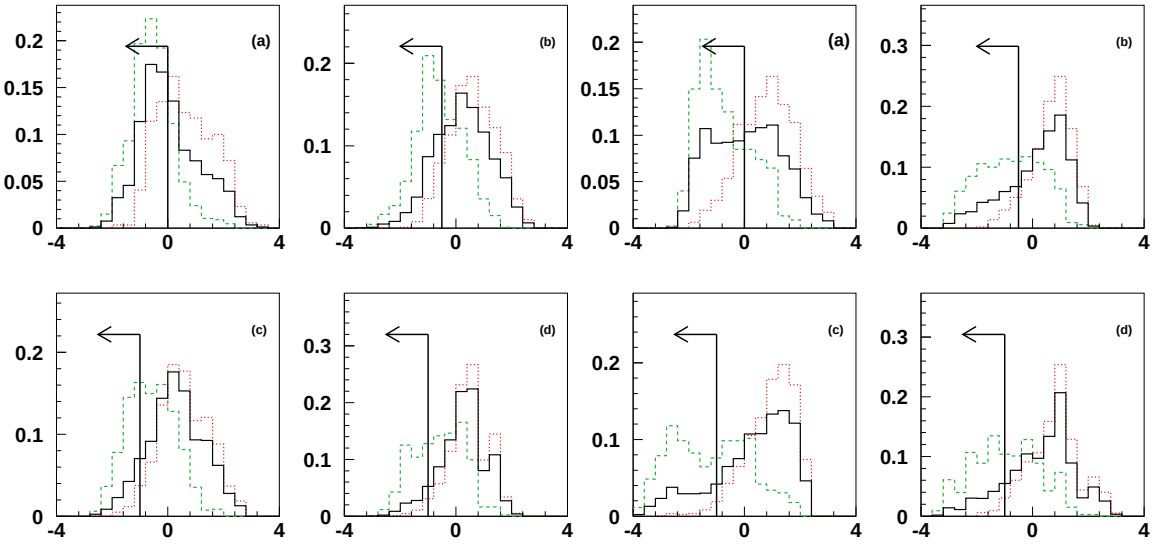

Figure 6.5: The distributions of the likelihood of the π^0-like selection for CC (dotted line) and NC (dashed line) events among FC Sub-GeV single-ring e-like events (solid line) in (a) 250 MeV/c $\leq P_e <$ 400 MeV/c, (b) 400 MeV/c $\leq P_e <$ 630 MeV/c, (c) 630 MeV/c $\leq P_e <$ 1000 MeV/c, (d) 1000 MeV/c $\leq P_e$. The left four panels show for SK-I and the right four panels show for SK-II. The selection criteria for single-ring π^0-like events are shown with arrows.

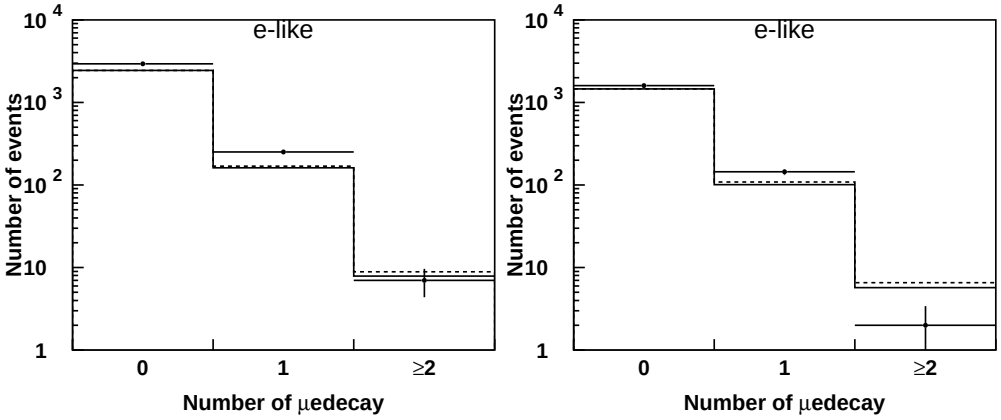

Figure 6.6: The distributions of number of decay electrons for FC Sub-GeV single-ring e-like events for data (dot) and Monte Carlo events assuming no oscillation (dashed line) and 2-flavor $\nu_\mu \leftrightarrow \nu_\tau$ oscillation assumed with $(\sin^2 2\theta,\ \Delta m^2) = (1.00,\ 2.5 \times 10^{-3}\,\mathrm{eV}^2)$ (solid line). The left plot is SK-I and the right is SK-II. Single-ring π^0-like events are subtracted.

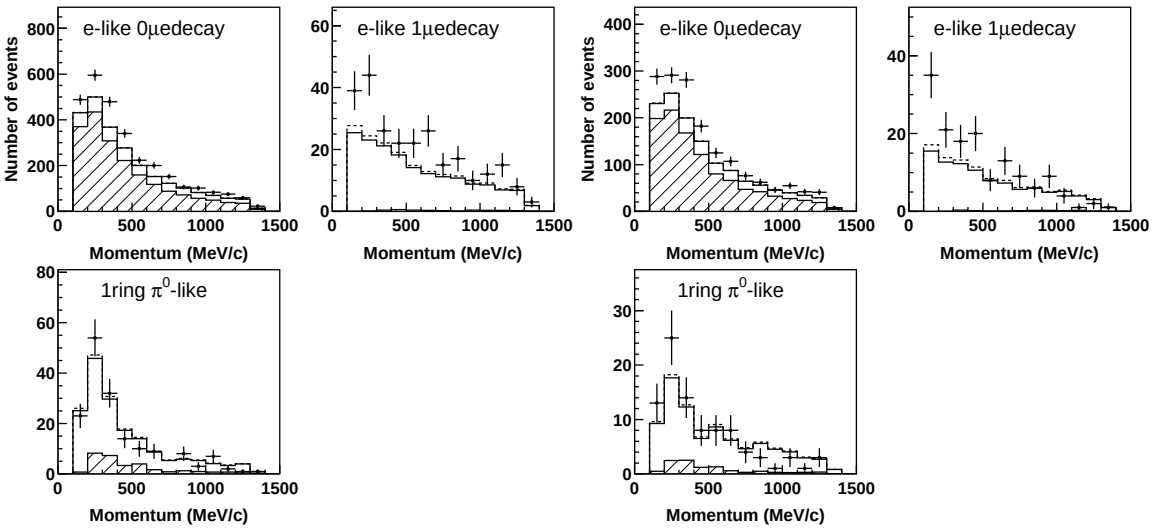

Figure 6.7: The momentum distributions for FC Sub-GeV single-ring e-like events for data (dot) and Monte Carlo events assuming no oscillation (dashed line) and 2-flavor $\nu_\mu \leftrightarrow \nu_\tau$ oscillation with $(\sin^2 2\theta,\ \Delta m^2) = (1.00,\ 2.5 \times 10^{-3}\,\mathrm{eV}^2)$ (solid line). The hatched regions show ν_e CCQE events in the oscillated events. The left three plots are for SK-I and the right are for SK-II.

Carlo events. The distributions for data and the oscillated Monte Carlo events are consistent. The systematic errors in the event separation will be described in Section 7.3.3.

6.1.3 FC Sub-GeV two-ring π^0-like events

To constrain the contamination from the neutral current events, the two-ring π^0-like sample is categorized. The selection criteria are the same as Section 2.6.5. The momentum distributions of FC Sub-GeV two-ring π^0-like samples are shown in Figure 6.10 for data and Monte Carlo events.

6.2 Vertex Distributions

Figure 6.11 and Figure 6.12 show the reconstructed vertex distributions for the FC and PC samples projected to $R^2 = (X^2+Y^2)$ and Z axes. Points show the observed data and histograms show the atmospheric neutrino Monte Carlo events assuming no oscillation and 2-flavor $\nu_\mu \leftrightarrow \nu_\tau$ oscillation with $(\sin^2 2\theta,\ \Delta m^2) = (1.00,\ 2.5\times10^{-3}\,\mathrm{eV}^2)$. The live time of the Monte Carlo events is normalized to that of the observed data. The vertex distributions of the data and the Monte Carlo events with neutrino oscillation agree well in the fiducial volume, which are shown with arrows. For Multi-GeV single-ring μ-like events, the excess due to the cosmic ray muons at Z = 1810 cm, the upper edge of the inner detector is seen in Z distribution for both SK-I and SK-II, but they are rejected by the fiducial volume cut.

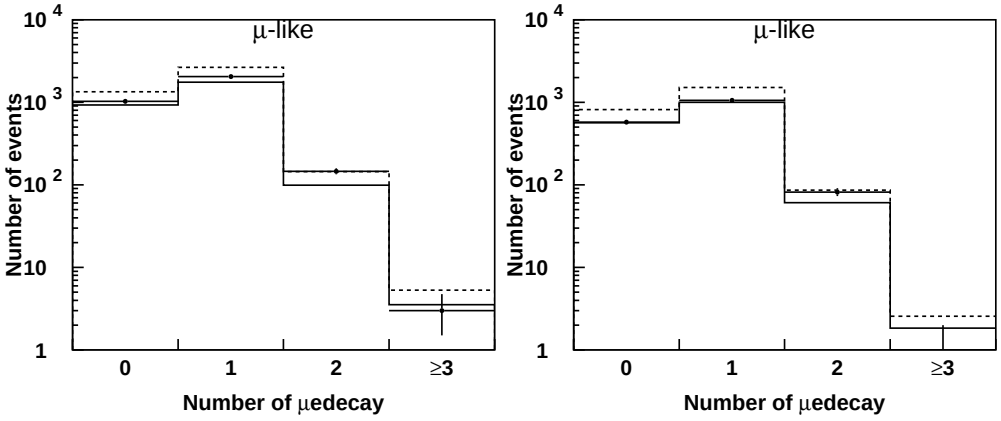

Figure 6.8: The distributions of the number of decay electrons for FC Sub-GeV single-ring μ-like events for data (dot) and Monte Carlo events assuming no oscillation (dashed line) and 2-flavor $\nu_\mu \leftrightarrow \nu_\tau$ oscillation assumed with $(\sin^2 2\theta,\ \Delta m^2) = (1.00,\ 2.5 \times 10^{-3}\,\mathrm{eV}^2)$ (solid line). The left plot is for SK-I and the right is for SK-II.

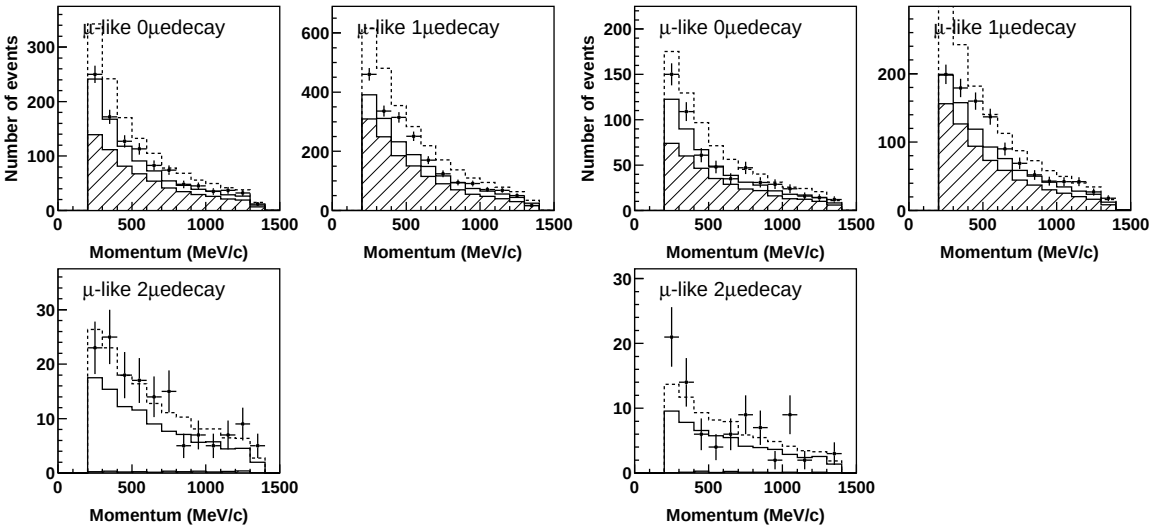

Figure 6.9: The momentum distributions for FC Sub-GeV single-ring μ-like events for data (dot) and Monte Carlo events assuming no oscillation (dashed line) and 2-flavor $\nu_\mu \leftrightarrow \nu_\tau$ oscillation with $(\sin^2 2\theta,\ \Delta m^2) = (1.00,\ 2.5 \times 10^{-3}\,\mathrm{eV}^2)$ (solid line). The hatched regions show ν_μ CCQE events in the oscillated events. The left three plots are SK-I and the right are SK-II.

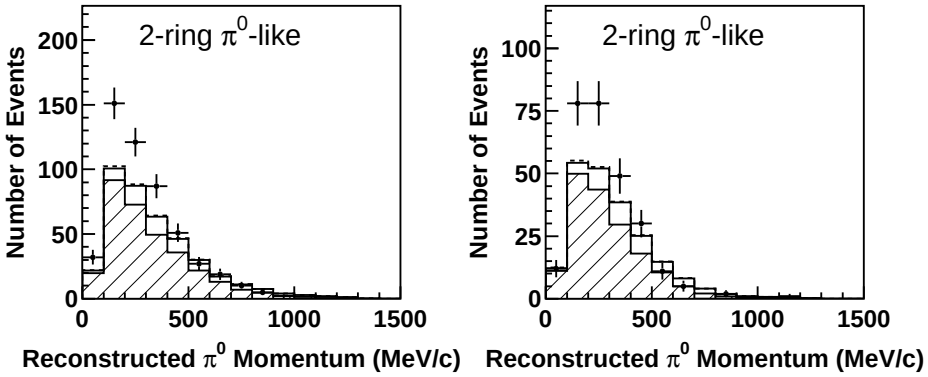

Figure 6.10: The reconstructed π^0 momentum for data (dot) and Monte Carlo events assuming no oscillation (dashed line) and 2-flavor $\nu_\mu \leftrightarrow \nu_\tau$ oscillation with $(\sin^2 2\theta,\ \Delta m^2) = (1.00,\ 2.5 \times 10^{-3}\,\mathrm{eV}^2)$ (solid line) for Sub-GeV two-ring π^0-like events. The hatched regions show NC events in the oscillated events. The left figure shows SK-I and the right shows SK-II.

		FC Sub-GeV single-ring e-like				FC Sub-GeV
		0μedecay	1μedecay	π^0-like	all	2-ring π^0-like
	Q.E.	80.4 %	2.2 %	17.2 %	71.3 %	0.07 %
CC	single meson	12.2 %	56.1 %	9.1 %	14.9 %	3.0 %
$\nu_e + \overline{\nu}_e$	multi π	1.5 %	14.6 %	3.3 %	2.5 %	1.0 %
	coherent π	0.1 %	0.7 %	0.07 %	0.2 %	0.01 %
CC $\nu_\mu + \overline{\nu}_\mu$		0.7 %	17.7 %	10.0 %	2.4 %	16.7 %
NC		4.9 %	8.9 %	59.9 %	8.7 %	79.2 %

		FC Sub-GeV single-ring μ-like			
		0μedecay	1μedecay	2μedecay	all
	Q.E.	72.9 %	79.3 %	2.9 %	74.4 %
CC	single meson	13.0 %	15.9 %	71.5 %	17.0 %
$\nu_\mu + \overline{\nu}_\mu$	multi π	1.4 %	2.1 %	21.1 %	2.6 %
	coherent π	0.1 %	0.2 %	0.7 %	0.2 %
CC $\nu_e + \overline{\nu}_e$		1.5 %	0.07 %	0.05 %	0.5 %
NC		10.9 %	2.3 %	2.2 %	5.1 %

Table 6.2: Fraction of each neutrino interaction mode in FC Sub-GeV atmospheric neutrino Monte Carlo events.

		FC Multi-GeV 1-ring e-like
CC $\nu_e + \overline{\nu}_e$	Q.E.	38.2 %
	single meson	24.9 %
	multi π	18.8 %
	coherent π	0.8 %
CC $\nu_\mu + \overline{\nu}_\mu$		7.1 %
NC		10.1 %

Table 6.3: Fraction of each neutrino interaction mode in FC Multi-GeV atmospheric neutrino Monte Carlo events.

		FC multi-ring μ-like	FC Multi-GeV 1-ring μ-like	PC	UPμ stop	UPμ through
CC $\nu_\mu + \overline{\nu}_\mu$	Q.E.	5.7 %	51.8 %	18.8 %	13.9 %	3.4 %
	single meson	35.8 %	30.7 %	22.1 %	20.2 %	6.6 %
	multi π	51.7 %	16.0 %	54.7 %	64.3 %	89.8 %
	coherent π	0.5 %	0.9 %	1.8 %	0.3 %	0.0 %
CC $\nu_e + \overline{\nu}_e$		2.7 %	0.4 %	1.8 %	0.9 %	0.1 %
NC		3.7 %	0.2 %	0.9 %	0.4 %	0.1 %

Table 6.4: Fraction of each neutrino interaction mode in FC Multi-GeV, PC and UPMU atmospheric neutrino Monte Carlo events.

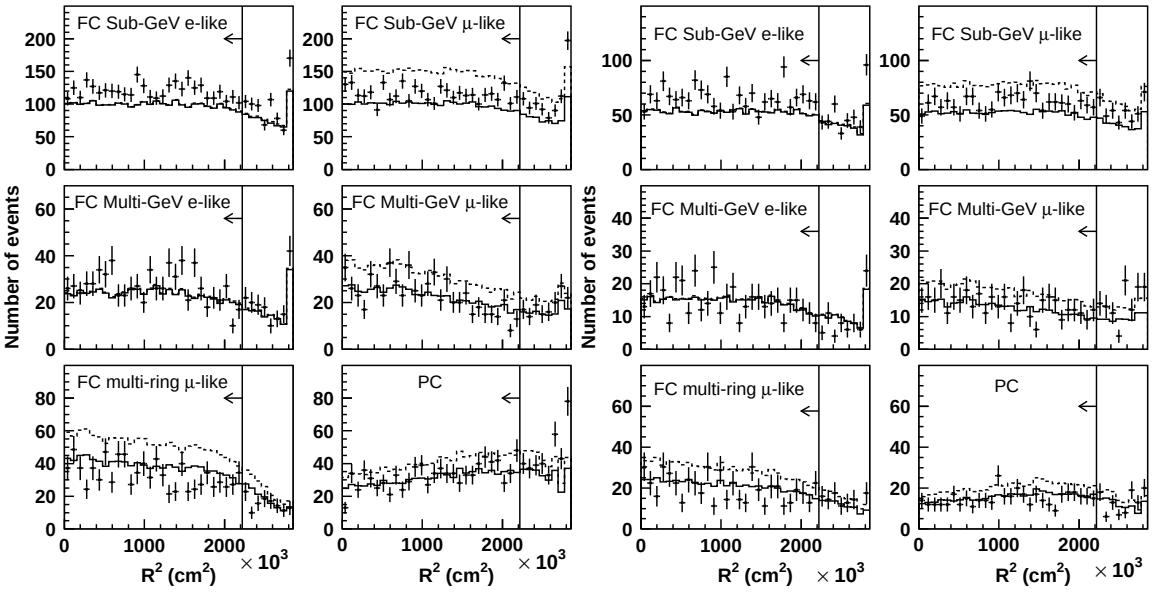

Figure 6.11: The vertex distributions projected on R^2 axis for data (dot) and Monte Carlo events assuming no oscillation (dashed line) and 2-flavor $\nu_\mu \leftrightarrow \nu_\tau$ oscillation with $(\sin^2 2\theta, \Delta m^2) = (1.00, 2.5 \times 10^{-3}\,\mathrm{eV}^2)$ (solid line). The left six panels show those for SK-I and the right panels show those for SK-II.

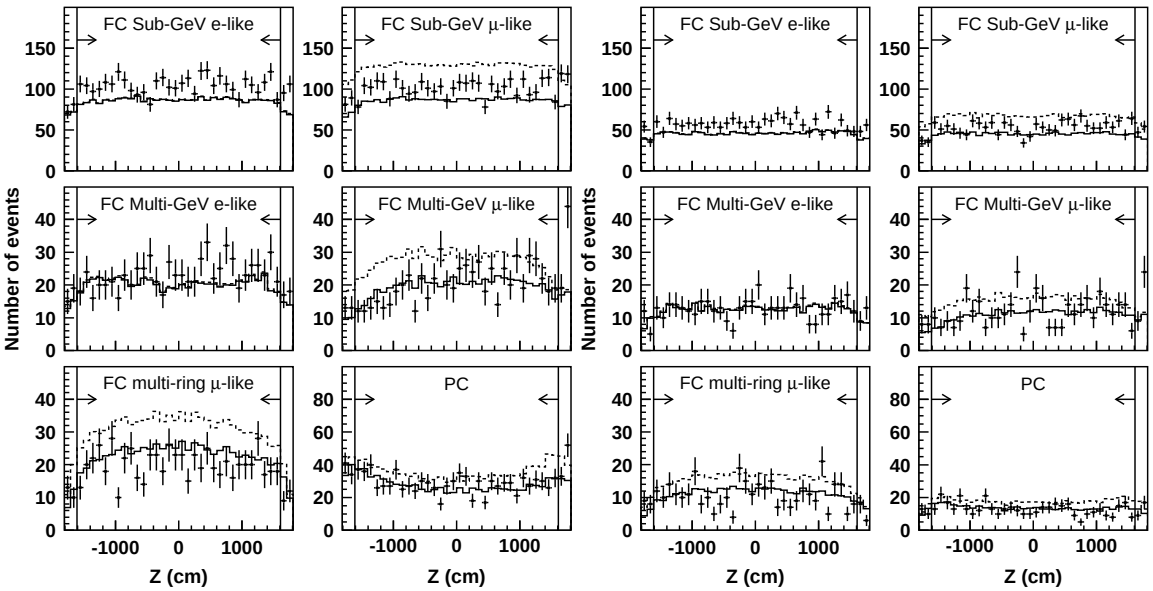

Figure 6.12: The vertex distributions projected on Z axis for data (dot) and Monte Carlo events assuming no oscillation (dashed line) and 2-flavor $\nu_\mu \leftrightarrow \nu_\tau$ oscillation with $(\sin^2 2\theta, \Delta m^2) = (1.00, 2.5 \times 10^{-3}\,\mathrm{eV}^2)$ (solid line). The left six panels show those for SK-I and the right panels show those for SK-II.

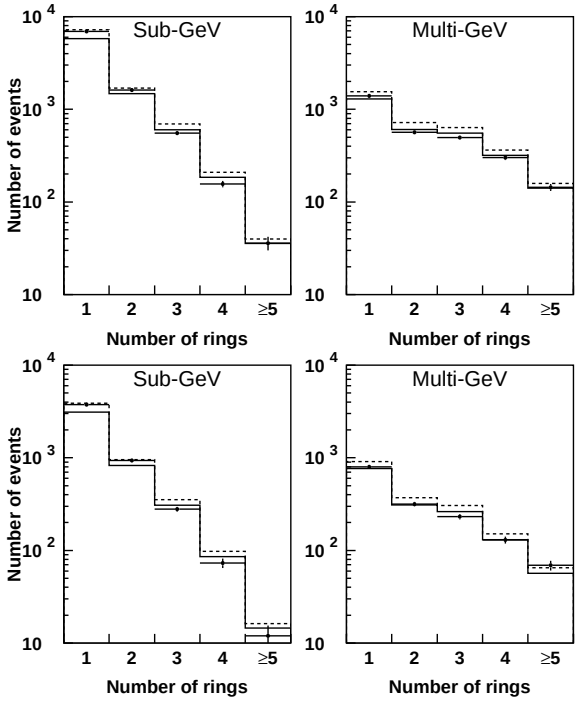

Figure 6.13: The number of rings for data (dot) and Monte Carlo events assuming no oscillation (dashed line) and 2-flavor $\nu_\mu \leftrightarrow \nu_\tau$ oscillation with $(\sin^2 2\theta, \Delta m^2) = (1.00, 2.5 \times 10^{-3}\,\mathrm{eV}^2)$ (solid line) for Sub-GeV events (left) and Multi-GeV events (right). The upper two panels show those for SK-I and the bottom panels show those for SK-II.

6.3 Number of Rings and Momentum Distributions

Figure 6.13 shows the distribution of the number of rings for data and Monte Carlo events. Figure 6.14 shows the distribution of the momentum for data and Monte Carlo for FC Multi-GeV single-ring events. The distributions for data and the oscillated Monte Carlo events are consistent.

6.4 Flavor Ratio

The flavor ratio of the atmospheric neutrino, $\nu_\mu + \overline{\nu}_\mu / \nu_e + \overline{\nu}_e$ is predicted with the 3 % of the uncertainty described in Section 3.2. As shown in Table 6.2-6.4, the results of the reconstructed particle identification in single-ring events can be used to estimate the flavor of the parent neutrino well, and the ratio of the number of e-like events and μ-like events can be used to estimate the flavor ratio of the atmospheric neutrino flux. The double ratio of the μ/e ratios is defined by :

$$R(\mu/e) \equiv (N_\mu/N_e)_{Data}/(N_\mu/N_e)_{MC} \tag{6.1}$$

where N_e and N_μ are the number of e-like and μ-like events, respectively. If the ratio of data agrees with that of the expected result, the double ratio should be 1.

The measured double ratios for Sub-GeV and Multi-GeV for SK-I are as follows :

$$R(\mu/e) = \begin{cases} 0.650\ ^{+0.016}_{-0.016}(stat) \pm 0.035(syst) & \text{(Sub-GeV)} \\ \\ 0.695\ ^{+0.032}_{-0.030}(stat) \pm 0.100(syst) & \text{(Multi-GeV + PC)} \end{cases} \tag{6.2}$$

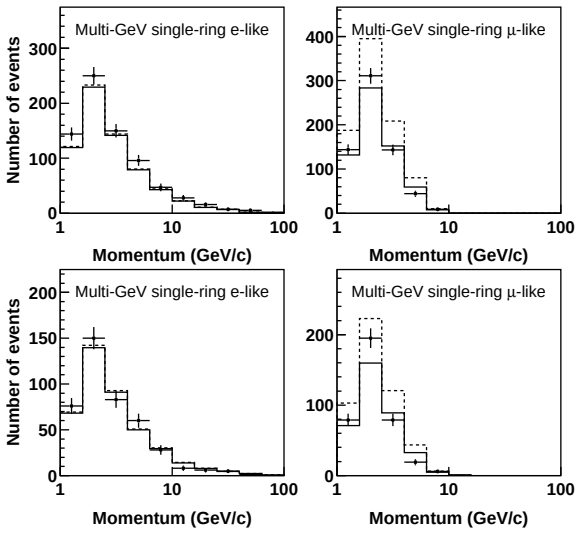

Figure 6.14: The momentum distributions for data (dot) and Monte Carlo events assuming no oscillation (dashed line) and 2-flavor $\nu_\mu \leftrightarrow \nu_\tau$ oscillation with $(\sin^2 2\theta, \Delta m^2) = (1.00, 2.5 \times 10^{-3}\,\mathrm{eV}^2)$ (solid line) for Multi-GeV single-ring e-like events (left) and μ-like events (right). The upper two panels show those for SK-I and the bottom panels show those for SK-II.

and for SK-II are as follows :

$$R(\mu/e) = \begin{cases} 0.647\ ^{+0.022}_{-0.021}(stat) \pm 0.033(syst) & \text{(Sub-GeV)} \\ \\ 0.741\ ^{+0.046}_{-0.043}(stat) \pm 0.055(syst) & \text{(Multi-GeV + PC)} \end{cases} \tag{6.3}$$

where PC events are treated as the Multi-GeV μ-like sample because of the high fraction of ν_μCC interactions. The systematic errors of the double ratio are estimated to be 5.3 % for SK-I Sub-GeV and 14.4 % for SK-I Multi-GeV. For SK-II, since the systematic error on the ring number estimation is smaller, the systematic errors of the double ratio are smaller than those of SK-I and estimated to be 5.0 % for Sub-GeV and 7.4 % for Multi-GeV. The sources of these systematic of the double ratio are listed in Table 6.5. The explanation of each source is described in Section 7.3. For Sub-GeV and Multi-GeV sample, the double ratios are significantly smaller than 1 and the double ratios are consistent for SK-I and SK-II.

6.5 Zenith angle Distributions

Figure 6.15 shows the zenith angle distributions for data and the Monte Carlo expectations for FC Sub-GeV single-ring samples, FC Multi-GeV samples, FC Multi-GeV μ-like + PC samples and upward-going muon samples. Zenith angle cosΘ=-1(+1) indicates upward-going (downward-going) direction. FC Sub-GeV single-ring events are divided into two by the reconstructed lepton momentum of 400 MeV/c. Since the angular correlation between the neutrino direction and the charged lepton direction is weak below 400 MeV/c, the zenith angle distributions are almost flat even though the prediction of the atmospheric neutrino flux has the zenith angle dependence as shown in Figure 3.5. Figure 6.16 shows the angular resolution of the neutrino directions as a function of the momentum. The angular resolution is defined as the angular difference between the parent neutrinos and the reconstructed direction of outgoing leptons in which 68 % of the events are included. For Multi-GeV samples, the excess in the horizontal direction is explained by the excess of the atmospheric neutrino flux due to the high decay probability of

	Sub-GeV(%)	Multi-GeV + PC(%)
Prediction of ν_μ/ν_e ratio	2.7 (2.7)	2.2 (2.2)
Prediction of $\nu/\overline{\nu}$ ratio	1.6 (1.6)	0.8 (0.7)
K/π ratio	0.6 (0.6)	1.9 (1.8)
E_ν spectral index	0.6 (0.5)	2.3 (2.0)
Sample-by-sample	– (–)	2.9 (2.7)
ν interaction		
quasi-elastic scattering	1.4 (1.4)	1.0 (0.8)
single-meson production	<0.1 (<0.1)	0.3 (0.1)
deep-inelastic scattering	0.2 (0.3)	0.5 (0.5)
coherent-pion production	0.4 (0.4)	0.2 (0.4)
NC/CC ratio	0.5 (0.6)	2.0 (2.1)
nuclear effects	1.3 (1.2)	0.8 (1.0)
Hadron simulation	0.7 (0.7)	<0.1 (<0.1)
FC reduction	0.1 (<0.1)	0.1 (0.1)
PC reduction	– (–)	1.5 (2.2)
Non-ν background	0.5 (0.3)	0.3 (1.1)
μ/e separation	1.3 (1.7)	0.6 (0.3)
Single-ring/multi-ring separation	3.2 (2.6)	13.2 (4.4)
Energy calibration	0.6 (0.6)	1.2 (1.4)
MC statistics	0.5 (0.6)	0.9 (1.1)
Total	5.3 (5.0)	14.4 (7.4)

Table 6.5: Sources of the systematic errors on double ratio R for the Sub-GeV and Multi-GeV+PC samples for SK-I (SK-II).

high energy muon in the atmosphere. Comparing data with Monte Carlo expectations assuming no oscillation, the clear deficit for higher energy μ-like upward-going events is observed. The data are consistent with the Monte Carlo expectations assuming two-flavor $\nu_\mu \leftrightarrow \nu_\tau$ oscillation with $(\sin^2 2\theta,\, \Delta m^2) = (1.00,\, 2.5 \times 10^{-3}\,\mathrm{eV}^2)$, while data and the no-oscillation Monte Carlo expectations for e-like events are consistent.

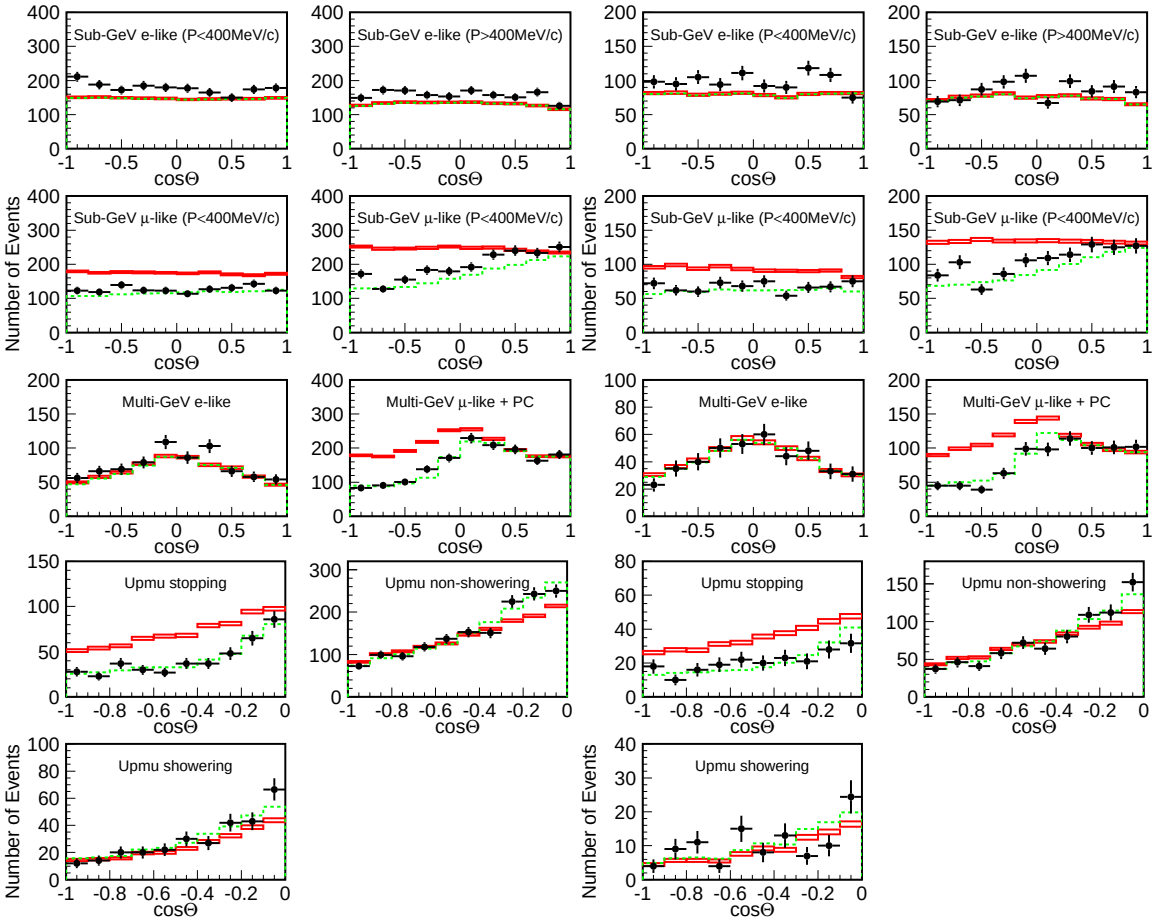

Figure 6.15: Zenith angle distributions for data (dot) and Monte Carlo events assuming no oscillation (box) and two-flavor $\nu_\mu \leftrightarrow \nu_\tau$ oscillation with $(\sin^2 2\theta,\ \Delta m^2) = (1.00,\ 2.5 \times 10^{-3}\,\mathrm{eV}^2)$ (dotted lines) for FC Sub-GeV single-ring e-like events, FC Sub-GeV single-ring μ-like events, FC Multi-GeV e-like events, FC Multi-GeV μ-like + PC events and upward-going muon events. FC Sub-GeV single-ring events are divided by the reconstructed lepton momentum of 400 MeV/c. The left nine figures show those for SK-I and the right figures show those for SK-II. Zenith angle cosΘ=-1(+1) indicates upward-going (downward-going) direction.

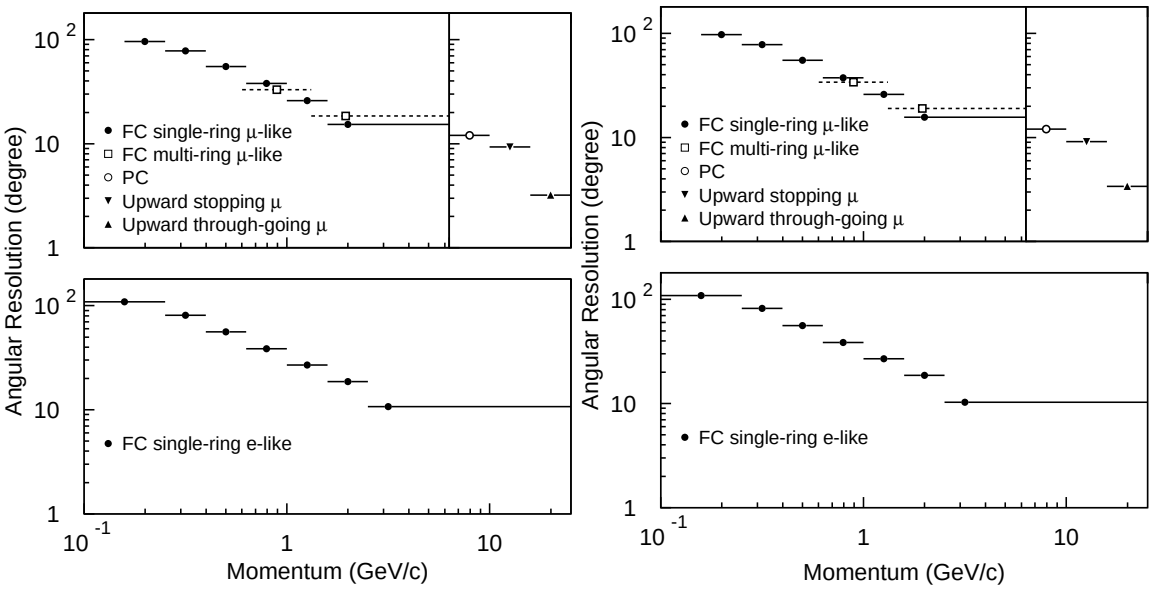

Figure 6.16: Angular resolution of the neutrino direction as a function of the outgoing charged lepton momentum for SK-I (left) and SK-II (right).

Chapter 7

Oscillation analysis with solar terms

As described in Chapter 1, the atmospheric neutrino data are well explained by the $\nu_\mu \leftrightarrow \nu_\tau$ two-flavor mixing framework. The 2-3 neutrino oscillation parameters are constrained to be

$$1.9 \times 10^{-3} < \Delta m^2_{23} < 3.1 \times 10^{-3} eV^2, \quad \sin^2 2\theta_{23} > 0.92, \tag{7.1}$$

at 90 % C.L. [25]. On the other hand, the 1-2 oscillation parameters are precisely measured by combining the solar neutrino data and the KamLAND reactor neutrino data as follows [13]:

$$7.3 \times 10^{-5} < \Delta m^2_{12} < 8.1 \times 10^{-5} eV^2, \quad 0.28 < \sin^2 \theta_{12} < 0.37 \quad (1\sigma). \tag{7.2}$$

If these LMA-MSW oscillation parameters are taken into consideration, the oscillation of atmospheric ν_e in the Sub-GeV energy region is expected to appear regardless of the θ_{13} value. The effect of this sub-dominant oscillation depends on the size of the deviation of $\sin^2 2\theta_{23}$ from the maximal mixing and on the octant of θ_{23}.

In this chapter, an analysis to observe the sub-dominant oscillation by the 1-2 parameters and determine the octant of θ_{23} is described.

7.1 Overview

As discussed in Section 1.3, the oscillation effect on the atmospheric ν_e flux driven by the solar neutrino parameters can be written from Equation (1.25) as follows [28, 29]:

$$\frac{F_e^{osc}}{F_e^0} - 1 = P_2(r \cos^2 \theta_{23} - 1), \tag{7.3}$$

where F_e^{osc} and F_e^0 are the atmospheric ν_e flux with and without oscillations and r is the ratio of the original muon and electron neutrino fluxes F_μ^0/F_e^0. P_2 is the neutrino transition probability ($\nu_e \to \nu_x$, $x = \mu$ or τ) in matter driven by the 1-2 parameters as shown in Figure 1.2.

The factor in parentheses in Equation (7.3) is called the 'screening' factor. Since the flavor ratio r is approximately 2 in the Sub-GeV neutrino energy region as described in Section 3.2, the screening factor is ~ 0 in the case of the maximal 2-3 mixing (i.e. $\theta_{23} = 45°$). According to the screening factor, the appearance of the sub-dominant oscillation effect depends largely on the deviation of θ_{23} from the maximal mixing. If $\theta_{23} < 45°$, the screening factor is positive and an excess of the Sub-GeV e-like sample is expected. If $\theta_{23} > 45°$, the screening factor is negative

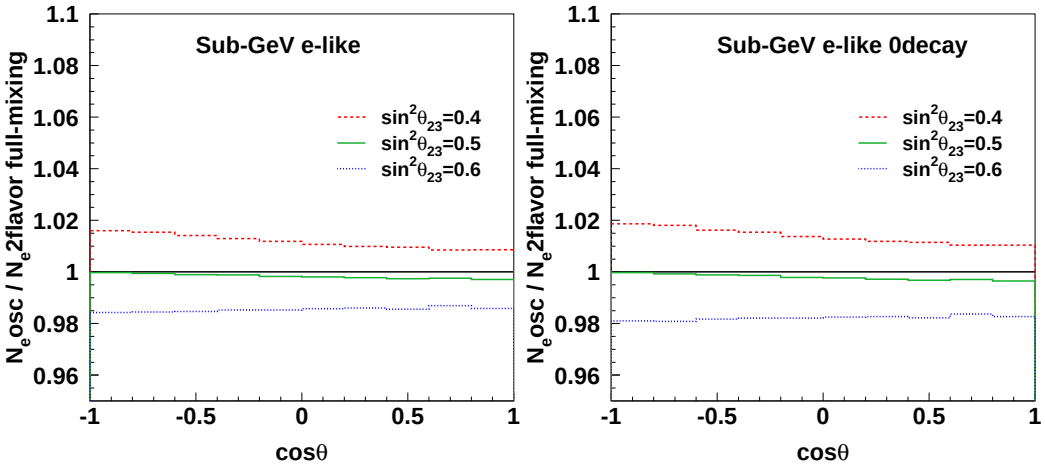

Figure 7.1: Zenith angle dependence of the ratio of the number of FC Sub-GeV single-ring e-like events (left) and e-like 0μedecay events (right) including sub-dominant oscillations due to the 1-2 oscillations (N_e^{osc}) and with pure $\nu_\mu \leftrightarrow \nu_\tau$ two-flavor full-mixing oscillations ($N_e^{2flavorfull-mixing}$). For calculation of N_e^{osc}, $\Delta m^2_{12} = 7.9 \times 10^{-5} eV^2$, $\sin^2\theta_{12} = 0.31$, $\Delta m^2_{23} = 2.5 \times 10^{-3} eV^2$ and three different values of $\sin^2\theta_{23}$, $\sin^2\theta_{23} = 0.4$ (dashed line), 0.5 (solid line) and 0.6 (dotted line), are assumed. For calculation of $N_e^{2flavorfull-mixing}$, $\Delta m^2_{23} = 2.5 \times 10^{-3} eV^2$ and $\sin^2\theta_{23} = 0.5$ are assumed.

and the Sub-GeV e-like sample is expected to be reduced. Figure 7.1 shows the zenith angle dependence of relative effect due to 1-2 oscillations on the number of FC Sub-GeV single-ring e-like events (left) and e-like 0μedecay events (right) for different values of $\sin^2\theta_{23}$. The 1-2 oscillation parameters are assumed as $\Delta m^2_{12} = 7.9 \times 10^{-5} eV^2$ and $\sin^2\theta_{12} = 0.31$. In the figures, the number of e-like events with sub-dominant 1-2 oscillations (N_e^{osc}) is normalized by the number of e-like events with pure $\nu_\mu \leftrightarrow \nu_\tau$ two-flavor full-mixing oscillations ($N_e^{2flavorfull-mixing}$). Although ν_e does not oscillate at all in the pure $\nu_\mu \leftrightarrow \nu_\tau$ two-flavor full-mixing oscillation scenario, $N_e^{2flavorfull-mixing}$ differs from N_e^0 (the number of e-like events without oscillations) because the FC Sub-GeV single-ring e-like sample contains $\sim 1\,\%$ contamination of ν_μCC interactions. The sub-dominant oscillation effect is negligible for $\sin^2\theta_{23}$=0.5. For $\sin^2\theta_{23}$=0.4 and 0.6, the sub-dominant oscillation effect appears as a $\sim$2 % excess and deficit of Sub-GeV e-like events, respectively. The size of the sub-dominant oscillation effect for e-like 0μedecay events is larger than that of e-like events by $\sim$0.5 % due to the enrichment of CCQE interactions in the 0μedecay sample. When the right plot of Figure 7.1 is divided by the reconstructed electron momentum as shown in Figure 7.2, the sub-dominant oscillation effect is expected larger in the lower energy region. In the higher energy region, the size of the effect is smaller but its zenith angle dependence is stronger. This is because the direction of a higher momentum lepton has a stronger correlation to the parent neutrino direction (see Figure 6.16).

The sub-dominant oscillation effect due to the solar neutrino parameters also appears on the Sub-GeV single-ring μ-like events as shown in Figure 7.3. The relative effect is found to be very small for $\sin^2\theta_{23}$=0.5. Since the number of FC Sub-GeV single-ring μ-like events is modified largely by the dominant oscillation channel $\nu_\mu \leftrightarrow \nu_\tau$, the relative effect of sub-dominant oscillations for $\sin^2\theta_{23}$=0.4 and $\sin^2\theta_{23}$=0.6 can be extracted by comparing with the

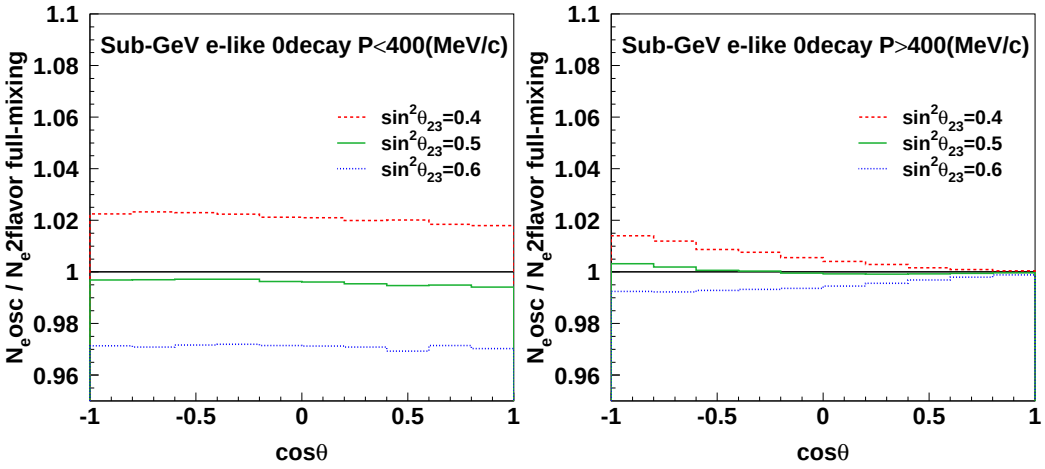

Figure 7.2: Zenith angle dependence of $N_e^{osc}/N_e^{2flavor full-mixing}$ with electron momentum below 400 MeV/c and above 400 MeV/c. The line definitions are same as Figure 7.1.

case of pure $\nu_\mu \leftrightarrow \nu_\tau$ two-flavor oscillations with the corresponding $\sin^2 2\theta_{23}$=0.96. In Figure 7.3, the effect of sub-dominant oscillation on the FC Sub-GeV single-ring μlike sample appears on the opposite side of that on the e-like sample. The size of the sub-dominant oscillation effect for μ-like 1μedecay events is larger than that of μ-like events by $\sim$0.1 % due to the enrichment of CCQE interactions in the sample. The discrimination between $\sin^2\theta_{23}$=0.4 and $\sin^2\theta_{23}$=0.6 is expected to be larger by taking the μ/e ratio. Figure 7.4 shows the zenith angle dependence of the sub-dominant oscillation effect on the ratio between the number of FC Sub-GeV single-ring μ-like events and the number of FC Sub-GeV single-ring e-like events, and the ratio between the number of FC Sub-GeV single-ring μ-like 1μedecay events and the number of FC Sub-GeV single-ring e-like 0μedecay events. For upward-going events, the difference on the μ/e ratio between the $\sin^2\theta_{23}$=0.4 and $\sin^2\theta_{23}$=0.6 cases reaches about 5 %, which is comparable to the size of the estimated systematic error on the μ/e ratio measurement and it is enhanced by $\sim$1 % for the sub-samples separated by the number of decay electrons compared with that for the Sub-GeV single-ring samples without decay-e cuts.

Figure 7.5 compares the sensitivity of the analysis for the determination of $\sin^2\theta_{23}$ based on the event samples without decay-e cuts and with decay-e cuts. It is found that the event samples with decay-e cuts improve the sensitivity and give a more stringent arrowed region for $\sin^2\theta_{23}$.

The oscillation analysis of the Sub-GeV samples taking into account the sub-dominant 1-2 oscillation has the possibility to determine the octant of θ_{23} for the non-maximal $\sin^2 2\theta_{23}$. Since the value of $\sin^2 2\theta_{23}$ affects the distribution for the other samples, a combined analysis of all the samples is needed.

7.2 Analysis Method

In the analysis, the FC, PC and UPMU samples of the SK-I and SK-II atmospheric neutrino data are used. The SK-I samples are divided into 400 bins and the SK-II samples are divided into 350 bins by the reconstructed event types, momenta and zenith angles : 310 bins for the SK-I FC samples, 60 bins for the SK-I PC samples, 30 bins for the SK-I upward-going muon

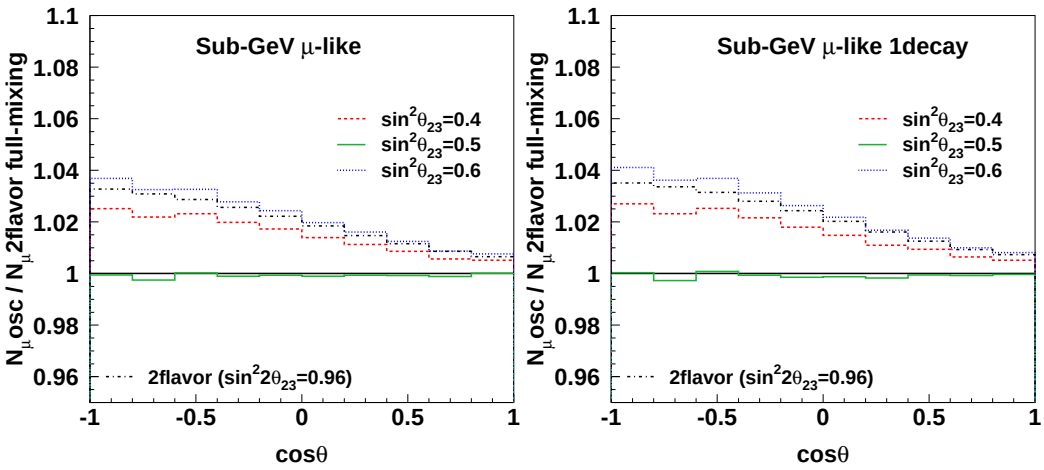

Figure 7.3: Zenith angle dependence of the ratio of the number of FC Sub-GeV single-ring μ-like events (left) and μ-like 1μedecay events (right) including sub-dominant oscillations due to the 1-2 oscillations (N_μ^{osc}) and the number of FC Sub-GeV single-ring μ-like 1μedecay events with pure $\nu_\mu \leftrightarrow \nu_\tau$ two-flavor full-mixing oscillations ($N_\mu^{2flavor\,full-mixing}$). For the dash-dotted line, the numerator is the number of μ-like events in the case of pure $\nu_\mu \leftrightarrow \nu_\tau$ two-flavor oscillations with $\sin^2 2\theta_{23} = 0.96$, which corresponds to $\sin^2\theta_{23} = 0.4$ or $\sin^2\theta_{23} = 0.6$. The other line definitions are same as Figure 7.1.

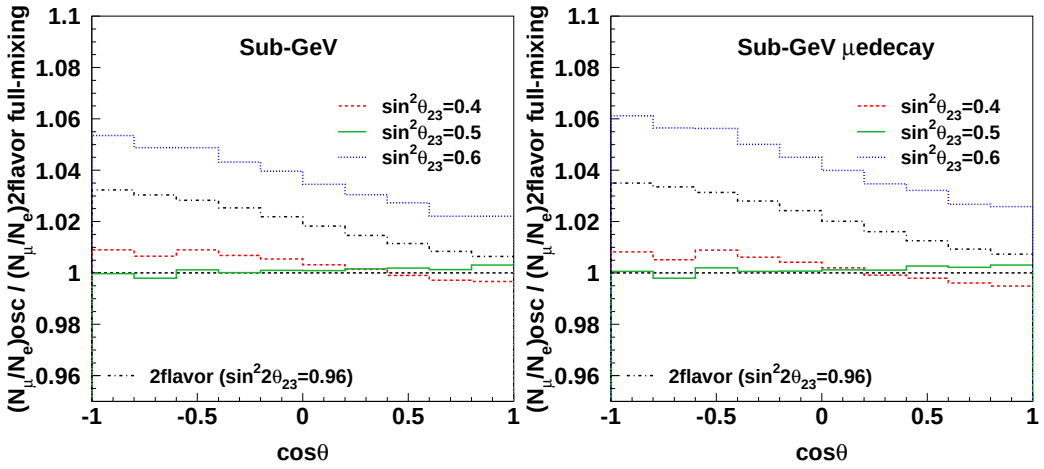

Figure 7.4: Zenith angle dependence of the N_μ/N_e ratio including sub-dominant oscillations due to the 1-2 oscillations normalized by the N_μ/N_e with pure $\nu_\mu \leftrightarrow \nu_\tau$ two-flavor full-mixing oscillations. The line definitions are same as Figure 7.3. The left figure shows the N_μ/N_e ratio of FC Sub-GeV single-ring events and the right figure shows the N_μ/N_e ratio between FC Sub-GeV single-ring μ-like 1μedecay events and e-like 0μedecay events.

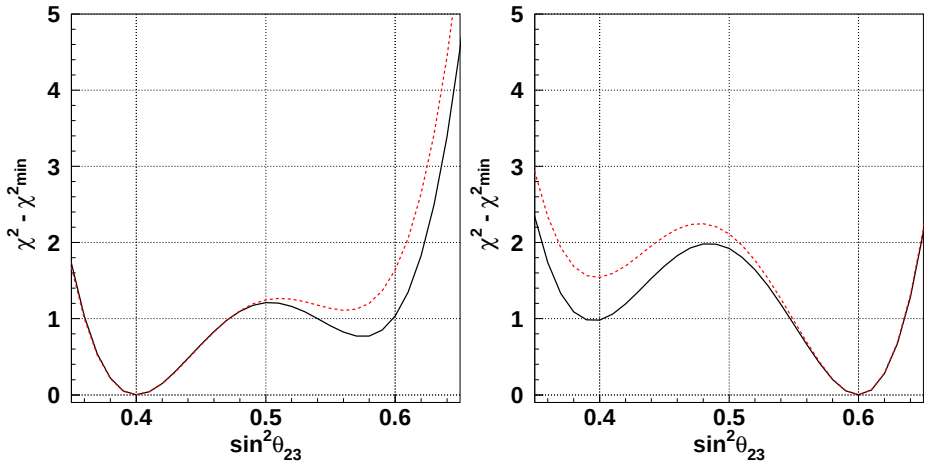

Figure 7.5: χ^2-χ^2_{min} distribution as a function of $\sin^2\theta_{23}$ using the oscillated Monte Carlo events of a 6 year exposure with the true oscillation parameters of $\theta_{13} = 0$, $\sin^2\theta_{12} = 0.32$, $\Delta m^2_{12} = 7.8\times10^{-5}$ eV^2, $\Delta m^2_{23} = 2.5\times10^{-3}$ eV^2 and $\sin^2\theta_{23} = 0.4$ (left), 0.6 (right). Details of the definition of χ^2 will be described in the next section. The solid line shows the sensitivity based on the standard event samples without decay-e cuts and the dotted line shows on the event samples with decay-e cuts.

samples, 280 bins for the SK-II FC samples, 40 bins for the SK-II PC samples and 30 bins for the SK-II upward-going muon samples as shown in Figure 7.6 and Figure 7.7. The number of bins are different between SK-I and SK-II to avoid the binning effect on fitting results. The small number of expected events (typically less than 5 events) in a bin gives a large reduced-χ^2 statistically. Since the expected number of events for SK-II is smaller than that for SK-I, the binning is different especially in higher energy regions which have less statistics.

The FC samples are divided into 'single-ring e-like', 'single-ring μ-like', 'multi-ring e-like' and 'multi-ring μ-like' events by the number of Cherenkov rings and the particle type. The single-ring events are separated into 'Sub-GeV' and 'Multi-GeV' events at 1.33 GeV of the visible energy. Additionally the FC Sub-GeV single-ring samples are separated according to the number of μedecays. 'Single-ring π^0-like' events and '2-ring π^0-like' events are selected as described in Chapter 6. PC events are separated into 'PC stop' and 'PC through' events according to the amount of charge deposit in the outer detector. The FC and PC samples except for the FC single-ring e-like 1μedecay sample, the FC single-ring μ-like 2μedecay sample and the π^0-like samples are divided into 10 bins equally spaced between $\cos\Theta = -1$ and $\cos\Theta = +1$, where $\cos\Theta$ is cosine of zenith angle of particle direction. The FC single-ring e-like 1μedecay sample, the FC single-ring μ-like 2μedecay sample and π^0-like samples are divided only by the momentum, not by the zenith angle because of small statistics and poor angular correlation for NC events. The SK-I and SK-II data are separately considered due to the difference of the detector response. A total of 750 bins are considered in the calculation of χ^2 with their associated sets of the observations and the Monte Carlo predictions.

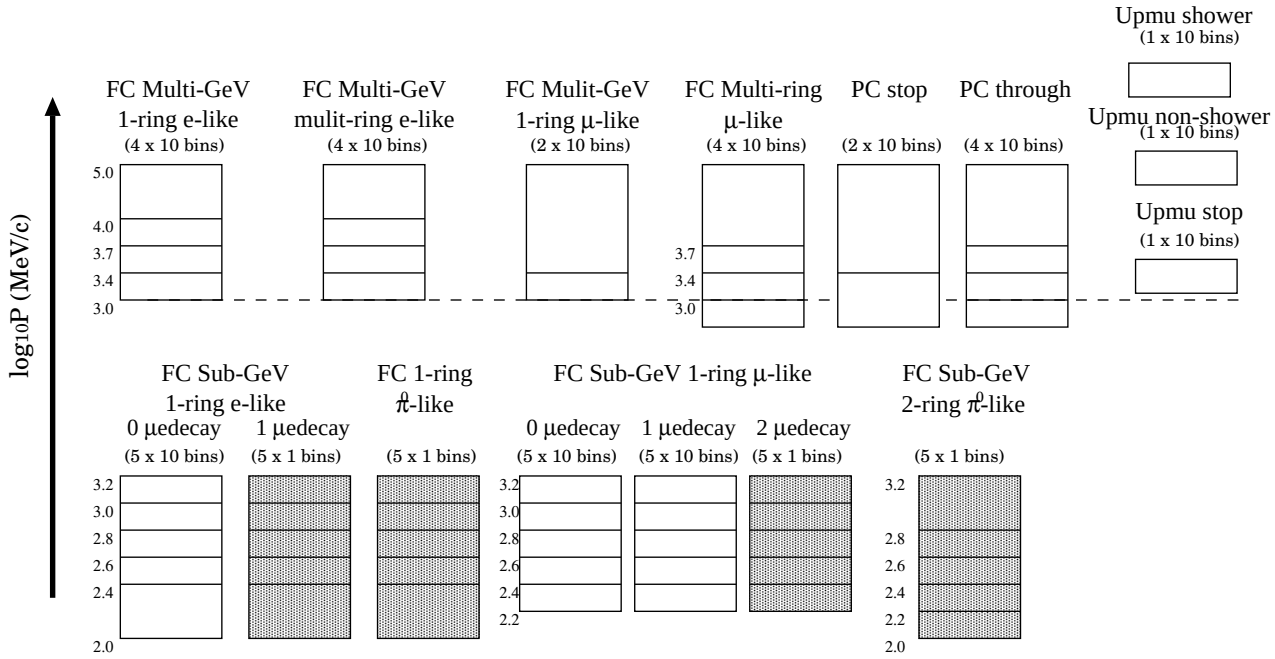

Figure 7.6: The definition of the binning for the SK-I data for the neutrino oscillation analysis : 310 bins for the FC samples, 60 for the PC samples, 30 for the upward-going muon samples. The momentum bins shown in white boxes are divided into 10 bins equally spaced between $\cos\Theta = -1$ and $\cos\Theta = +1$. The FC single-ring e-like 1μedecay sample, the μ-like 0μedecay sample and the π^0 samples are not divided by the zenith angle bins.

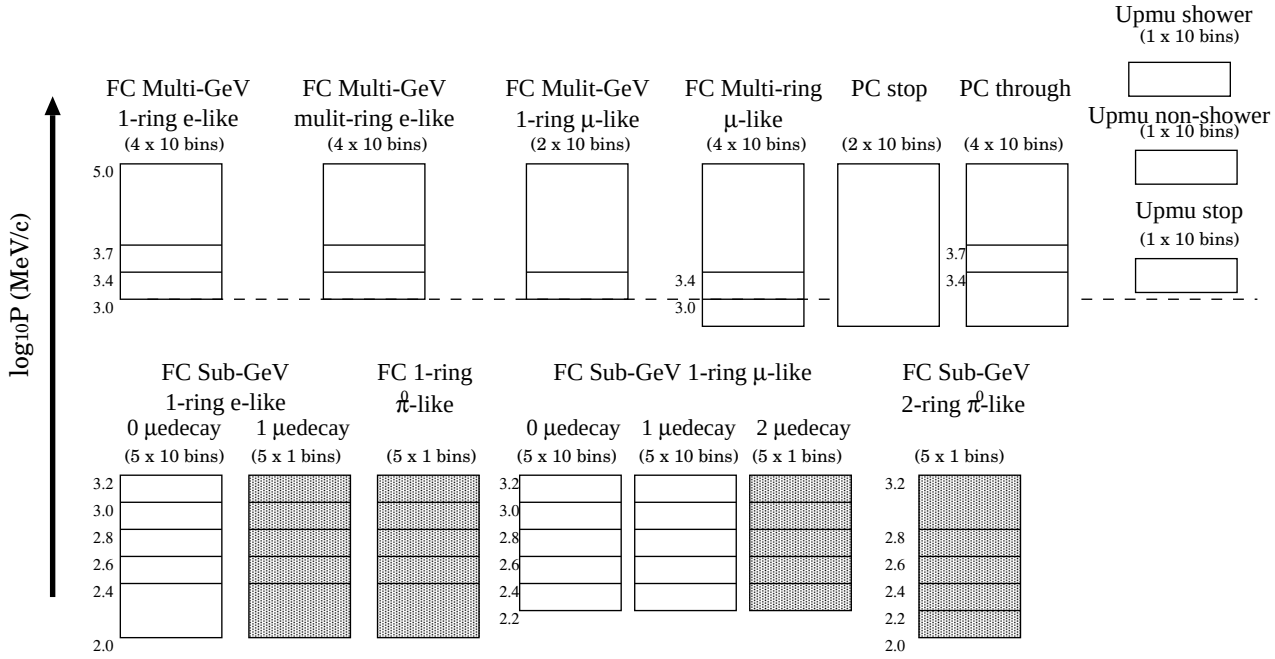

Figure 7.7: The definition of the binning for the SK-II data for the neutrino oscillation analysis : 280 bins for the FC samples, 40 for the PC samples and 30 for the upward-going muon samples.

A χ^2 value is defined according to the Poisson probability distribution as follows [131]:

$$\chi^2 \equiv \sum_{i=1}^{750} \left(2 \left(N_i^{\rm exp}(1 + \sum_{j=1}^{80} f_j^i \cdot \epsilon_j) - N_i^{\rm obs} \right) + 2N_i^{\rm obs} \ln \left(\frac{N_i^{\rm obs}}{N_i^{\rm exp}(1 + \sum_{j=1}^{80} f_j^i \cdot \epsilon_j)} \right) \right) + \sum_{j=1}^{77} \left(\frac{\epsilon_j}{\sigma_j^{sys}} \right)^2 + \Delta\chi^2_{solar}, \quad (7.4)$$

where $N_i^{\rm obs}$ is the number of observed events in the i-th bin and $N_i^{\rm exp}$ is the expected number of events in the i-th bin from the Monte Carlo simulation. During the fit, the values of $N_i^{\rm exp}$ is recalculated to account for neutrino oscillations and 80 systematic errors which come from uncertainties in the neutrino flux model, neutrino cross-section model and detector response. The details of the systematic errors are described in the next section. The systematic uncertainties are represented by 80 parameters ϵ_j. These 80 ϵ_j are varied to minimize χ^2 for each choice of oscillation parameters. The second sum in the χ^2 definition represents the contributions from the systematic errors. Among 80 errors, only 77 errors contribute to the χ^2 since the three errors related to the sample normalization are allowed to be free (the systematic uncertainties on the absolute normalization and sample normalization of multi-ring e-like events for SK-I and SK-II). σ_j^{sys} is an estimated 1-sigma value of the j-th systematic uncertainty. The factor f_j^i represents the fractional change in the predicted event rate in the i-th bin due to a variation of the parameter ϵ_j.

At the minimum χ^2 location for each choice of oscillation parameters, $\partial\chi^2/\partial\epsilon_j = 0$ is realized for each of the parameters ϵ_j. As a result, the minimization of χ^2 in Equation (7.4) is equivalent to solving the following $k = 1, 80$ equations [130]:

$$\sum_{j=1}^{80} \left(\frac{1}{(\sigma_j^{sys})^2} \delta_{jk} + \sum_{i=1}^{750} N_i^{\rm obs} f_j^i f_k^i \right) \epsilon_j = \sum_{i=1}^{750} \left(\left(1 + (\sum_{j=1}^{80} f_j^i \epsilon_j)^2 - ... \right) N_i^{\rm obs} - N_i^{\rm exp} \right) f_k^i. \quad (7.5)$$

Since these equations have nonlinear terms of ϵ_j, an approximate solution by an iteration method is obtained.

A value of χ^2 is calculated at each grid point in the four-dimensional oscillation parameter space of $\Delta{\rm m}^2_{12}$, $\Delta{\rm m}^2_{23}$, $\sin^2\theta_{12}$ and $\sin^2\theta_{23}$, because $\theta_{13} = 0$ is assumed in this analysis. To compare the solar term effect, two scenarios are examined. In one scenario with the solar neutrino parameters turned on, the solar neutrino parameters are chosen around the allowed region obtained by a combined analysis of the solar neutrino data and KamLAND data [13] as shown in Figure 7.8. To constrain the solar neutrino parameter, a $\Delta\chi^2$ value by the solar+KamLAND combined analysis is added to χ^2 from the atmospheric neutrino data ($\Delta\chi^2_{solar}$ in Equation (7.4)). The other scenario is an ordinary "one mass scale dominance" approximation with $\Delta m^2_{12} = 0$, that is, the pure $\nu_\mu \leftrightarrow \nu_\tau$ two-flavor oscillation scenario.

7.3 Systematic Uncertainties

In this section, the 80 systematic uncertainties are described. Though the systematic errors related to the event selection and the detector response are different between SK-I and SK-II, other parameters are identical for SK-I and SK-II. Among 80 systematic errors, 14 are for the

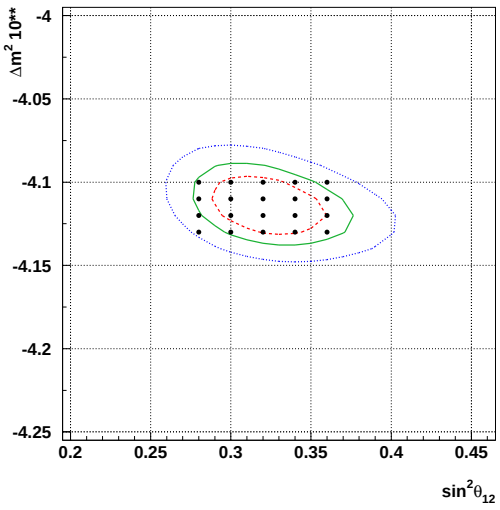

Figure 7.8: The arrowed 1-2 parameters obtained from the results of the solar neutrino and KamLAND data [13]. The 20 points show the scanned points and the $\Delta\chi^2_{solar}$ from the solar plus KamLAND data at the each point is added to the χ^2 from the atmospheric neutrino data. Three contours correspond to the 68 % (dashed line), 90 % (solid line) and 99 % (dotted line).

neutrino flux model, 16 for the interaction, 25 for the SK-I detector response and 25 for the SK-II detector response. All systematic errors are considered to be uncorrelated.

7.3.1 Systematic Uncertainties in Atmospheric Neutrino Flux

The details of the atmospheric neutrino flux are described in Section 3.2. Systematic uncertainties in the prediction of the atmospheric neutrino flux are estimated by comparing the Honda flux [14] with the other calculations, the Fluka flux [41] and the Bartol flux [42]. The systematic errors in the atmospheric neutrino flux are listed in Table 7.1 and 7.2.

- Absolute normalization
  The absolute normalization uncertainty in the atmospheric neutrino flux calculation is estimated to be about 20 % for $E_\nu < 100\,\mathrm{GeV}$ 30 % for $E_\nu > 100\,\mathrm{GeV}$, which comes from the uncertainty in the primary cosmic ray flux and the hadronic interaction models used in the calculation. The absolute normalization parameter is treated as a free parameter in this analysis because of the large uncertainty.

- Flavor ratio
  The flavor ratio $(\nu_\mu + \overline{\nu}_\mu)/(\nu_e + \overline{\nu}_e)$ of the atmospheric neutrino flux is estimated within approximately 3 % by the different models. The systematic error is 3 % for $E_\nu < 5\,\mathrm{GeV}$. For $E_\nu > 5\,\mathrm{GeV}$, the error increases almost linearly with $\log E_\nu$ from 3 % (5 GeV) to 10 % (100 GeV). In the low energy range, the uncertainty mainly comes from the pion spectrum in the primary hadronic interactions. In the high energy range, the uncertainty mainly comes from the K/π production ratio. A positive number means the number of MC $\nu_\mu + \overline{\nu}_\mu$ events is increased.

			uncertainty (%)	best-fit (%)
(A1) Systematic uncertainties in neutrino flux				
Absolute normalization			free	25.6
$(\nu_\mu + \overline{\nu}_\mu)/(\nu_e + \overline{\nu}_e)$	$E_\nu < 5\,\mathrm{GeV}$		3.0	-2.8
	$E_\nu > 5\,\mathrm{GeV}$		3.0[a]	2.1
$\nu_e/\overline{\nu}_e$	$E_\nu < 10\,\mathrm{GeV}$		5.0	2.7
	$E_\nu > 10\,\mathrm{GeV}$		5.0[b]	-0.2
$\nu_\mu/\overline{\nu}_\mu$	$E_\nu < 10\,\mathrm{GeV}$		5.0	-1.3
	$E_\nu > 10\,\mathrm{GeV}$		5.0[c]	3.4
Up/down	$< 400\,\mathrm{MeV}$	e-like 0μedecay	0.4	-0.03
		μ-like 0μedecay	1.1	-0.08
		μ-like 1μedecay	0.7	-0.05
	$> 400\,\mathrm{MeV}$	e-like 0μedecay	2.1	-0.1
		μ-like 0μedecay	1.7	-0.1
		μ-like 1μedecay	1.9	-0.1
	Multi-GeV	e-like	1.5	-0.10
		μ-like	0.8	-0.06
	PC		0.4	-0.03
	Sub-GeV multi-ring μ		0.8	-0.06
	Multi-GeV multi-ring μ		0.7	-0.05
Horizontal/vertical	$< 400\,\mathrm{MeV}$	e-like 0μedecay	0.4	0.05
		μ-like 0μedecay	0.3	0.03
		μ-like 1μedecay	0.3	0.03
	$> 400\,\mathrm{MeV}$	e-like 0μedecay	1.1	0.1
		μ-like 0μedecay	1.4	0.2
	Multi-GeV	e-like	2.8	0.3
		μ-like	1.9	0.2
	PC		1.4	0.2
	Sub-GeV multi-ring μ		1.5	0.2
	Multi-GeV multi-ring μ		1.3	0.1

Table 7.1: Summary of systematic uncertainties in the prediction of the atmospheric neutrino flux. Estimated uncertainty and the best-fit value is listed for each error.

[a] Error linearly increases with $\log E_\nu$ from 3 % (5 GeV) to 10 %(100 GeV).
[b] Error linearly increases with $\log E_\nu$ from 5 %(10 GeV) to 10 %(100 GeV).
[c] Error linearly increases with $\log E_\nu$ from 5 %(10 GeV) to 25 %(100 GeV).

		uncertainty (%)	best-fit (%)
(A2) Systematic uncertainties in neutrino flux			
K/π ratio		20.0	-8.6
L_ν (production height)		10.0	0.03
Energy spectrum	$E_k < 100\,\mathrm{GeV}$	0.03	0.010
	$E_k > 100\,\mathrm{GeV}$	0.05	0.017
Sample-by-sample	FC Multi-GeV	5.0	-4.5
	PC + upward stopping μ	5.0	-9.1
Solar activity	SK-I	0.2	0.01
	SK-II	0.5	0.43

Table 7.2: Summary of systematic uncertainties in the prediction of the atmospheric neutrino flux. Estimated uncertainty and the best-fit value is listed for each error.

- Anti-neutrino/neutrino ratio
  The systematic uncertainty of anti-neutrino to neutrino ratio comes from π^+/π^- ratio in hadronic interaction in the flux calculation. The uncertainties of $\overline{\nu}_e/\nu_e$ and $\overline{\nu}_\mu/\nu_\mu$ are estimated to be 5 % for $E_\nu < 10\,\mathrm{GeV}$. For $E_{\nu_e} > 10\dot{\mathrm{G}}\mathrm{eV}$, the errors increase linearly with $\log E_\nu$ from 5 % (10 GeV) to 10 % (100 GeV). For $E_{\nu_\mu} > 10\dot{\mathrm{G}}\mathrm{eV}$, the error increases linearly with $\log E_\nu$ from 5 % (10 GeV) to 25 % (100 GeV). A positive number means the number of MC ν_e (ν_μ) events is increased.

- Up/down ratio
  As described in Section 3.2, the neutrino flux below a few GeV has up/down asymmetry because of the rigidity cutoff by the geomagnetic field, while flux above a few GeV is up/down symmetric. The systematic uncertainty in the up/down ratio of atmospheric neutrino flux is derived from the treatment of the geomagnetic field in the calculation. Since the up/down asymmetry in low energy neutrino flux is largely canceled due to the poor angular correlation in neutrino interactions, the uncertainty of flux calculation does not directly affect the zenith angle distributions observed in Super-Kamiokande. The systematic uncertainties of up/down ratio are estimated by comparing the predictions of zenith angle distributions in Super-Kamiokande from independent flux calculations. The magnitude of the uncertainty in the up/down ratio is a function of energy, but is assumed to be fully correlated. A positive number means the number of MC upward events is increased.

- Horizontal/vertical ratio
  The systematic uncertainty of horizontal/vertical ratio is due to the difference in the 3-dimensional calculation method for each model for neutrino energy below 3 GeV. For higher energy neutrinos, the uncertainties comes from the predicted K/π ratio in hadronic interactions in the atmosphere. The magnitude of the uncertainty in the horizontal/vertical ratio is a function of energy, but is assumed to be fully correlated. A positive number means the number of MC horizontally-going events is increased.

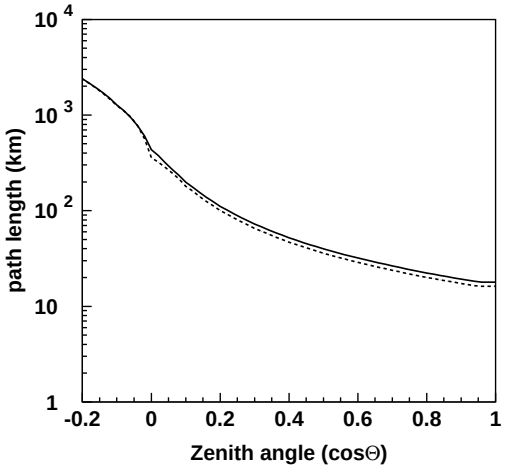

Figure 7.9: Neutrino flight length as a function of zenith angle. Solid line shows the flight length used in our analysis and dashed line shows that for the compressed density structure of atmosphere by 10 %.

- K/π ratio
  The uncertainty of K/π production ratio in cosmic ray interactions in the atmosphere is estimated to be 20 %. A positive number means that the fraction of K is increased.

- Neutrino flight length
  The uncertainty of neutrino flight length affects on the oscillation probabilities of neutrinos. The systematic uncertainty is negligible for upward-going neutrinos which pass through the Earth because the flight length for those neutrino can be easily calculated from the geometry. For downward-going and horizontally-going neutrinos, the production height of the neutrinos must be considered to calculate the flight length. The uncertainty of the neutrino production height is related to the structure of the atmosphere. To estimate the systematic uncertainty in the production height and neutrino flight length, the calculation is carried out by changing the density structure of atmosphere by 10 %. Figure 7.9 shows the comparison of the flight length used in the analysis with that for the case of different structure of atmosphere (compressed by 10 %). The effect of this difference is considered as the systematic error. A positive number means a more compressed atmospheric density structure.

- Energy spectrum
  The energy spectrum of primary cosmic rays is proportional to E^{γ} with the spectral index for the primary proton flux, γ = -2.74. 0.03 and 0.05 uncertannies in the spectral index of the primary cosmic rays below and above 100 GeV. Spectral index unertanties below and above 100 GeV are assumed to be correlated. A positive number means that the spectrum is harder.

- Sample-by-sample normalization
  Different flux calculations predict different energy dependence that cannot be explained by a simple spectral index uncertainty as shown in Figure 7.10. From a comparison of the

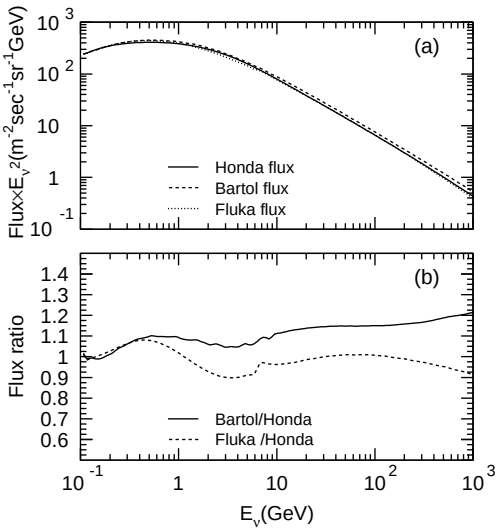

Figure 7.10: (a)The direction averaged atmospheric neutrino energy spectrum for $\nu_\mu + \overline{\nu}_\mu$ calculated by Honda [14], Bartol [42] and Fluka [41]. (b) The ratio of the calculated neutrino flux. The fluxes calculated in Bartol (solid line) and Fluka (dashed line) are normalized by the flux in Honda.

predicted number of events based on different flux models, 5 % is assigned as the relative normalization uncertanty for these samples.

- Solar activity
  The primary cosmic ray flux is affected by the solar activity changing in every 11 year period and the atmospheric neutrino flux calculations considers the solar activity. ± 1 year of uncertainty is assigned to the modulation of solar activity, which corresponds to 20 % for 5 years in SK-I period and 50 % for 2 years in SK-II period.

7.3.2 Systematic Uncertainties in Neutrino Interaction

The neutrino cross-section and kinematics are calculated theoretically and measured by several experiments as described in Section 3.3. The systematic errors in the neutrino interactions are listed in Table 7.3.

- Quasi-elastic scattering and single-meson production (M_A)
  The cross-section and kinematics in quasi-interaction scattering and single-meson production have a dependence on the axial vector mass M_A, which is set to be 1.11 in our simulation based on experimental data. The uncertainty of M_A, which affects the cross-section and the angular correlations between incident neutrinos and outgoing leptons, is estimated to be 10 % as described in Section 3.3.1.

- Quasi-elastic scattering for bound nucleon (Total cross-section)
  The CCQE cross-section for the bound nucleon is based on the model of Smith and Monitz. The systematic uncertainty in the CCQE cross-section is estimated from the difference between the model of Nieves *et al.* [125] and our MC and is set to be 1σ. In the Nieves'

	uncertainty (%)	best-fit (%)
(B) Systematic uncertainties in neutrino interaction		
Quasi-elastic scattering and single-meson production (M_A)	10.0	-0.8
Quasi-elastic scattering for bound nucleon (total cross-section)	1.0[a]	0.7
Quasi-elastic scattering for bound nucleon ($\overline{\nu}/\nu$ ratio)	1.0[b]	0.9
Quasi-elastic scattering for bound nucleon (ν_μ/ν_e ratio)	1.0[c]	0.5
Single-meson production (total cross-section)	20.0	3.2
1 π^+ production (model dependence)	20.0	25.5
1 π^0 production (model dependence)	20.0	4.4
1 π^- production (model dependence)	20.0	-11.3
Multi-pion production (a few GeV region)	1.0[d]	1.75
Multi-pion production (total cross-section)	5.0	-0.7
Coherent pion production (total cross-section)	100.0	-97.1
NC/CC ratio	20.0	-8.6
Nuclear Effect in ^{16}O nucleus	30.0	-17.9
Nuclear Effect in pion spectrum	1.0[e]	1.7
CC ν_τ interaction cross-section	30.0	-19.2
Hadron simulation	10.0	2.0

Table 7.3: Summary of systematic uncertainties in neutrino interactions. Estimated uncertainty and the best-fit value are listed for each error.

[a] Difference from the Nieves model is set to 1.0
[b] Difference from the Nieves model is set to 1.0
[c] Difference from the Nieves model is set to 1.0
[d] Difference from the Bodek model is set to 1.0
[e] Difference between NEUT [62] and NUANCE [124] is set to 1.0

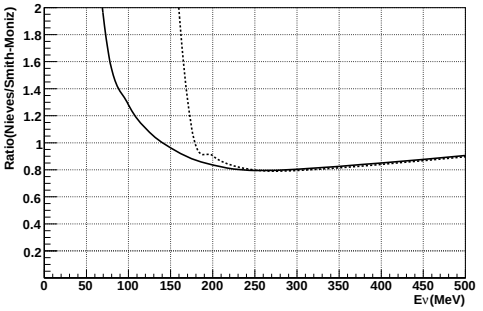

Figure 7.11: The ratio of the calculated CCQE cross-sections for $\nu_e + \overline{\nu}_e$ (solid line) and $\nu_\mu + \overline{\nu}_\mu$ (dashed line) of Nieves' calculation to the calculation of Smith and Monitz.

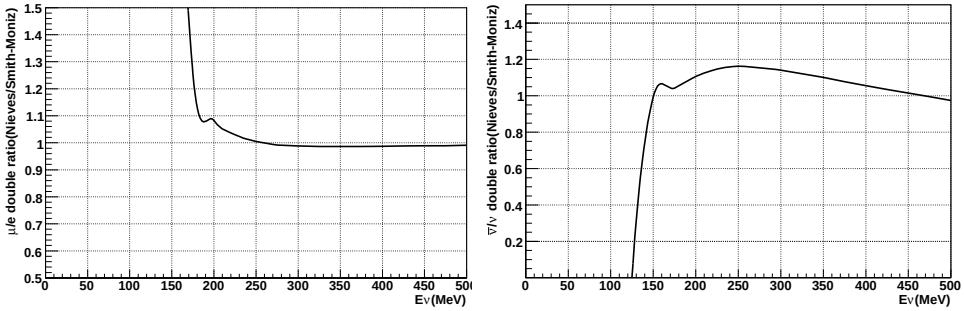

Figure 7.12: The ratio of the calculated CCQE cross-section of Nieves' calculation to the calculation of Smith and Monitz for $\overline{\nu}/\nu$ ratio (left) and ν_μ/ν_e ratio (right).

model the effect of in target nucleous in the target nucleon is taken into account. Figure 7.11 shows the calculated CCQE cross-section in Nieves' model normalized by that in the model of Smith and Monitz as a function of neutrino energy.

- Quasi-elastic scattering for bound nucleon ($\overline{\nu}/\nu$ ratio)
  The uncertainty in the CCQE cross-section of $\overline{\nu}/\nu$ ratio is estimeted from the difference between the model of Nieves *et al.* and our MC. The left plot on Figure 7.12 shows the calculated CCQE cross-section of $\overline{\nu}/\nu$ ratio in Nieves' model normalized by that in the model of Smith and Monitz as a function of neutrino energy.

- Quasi-elastic scattering for bound nucleon (ν_μ/ν_e)
  The uncertainty in the CCQE cross-section of ν_μ/ν_e ratio is estimeted from the difference between the model of Nieves *et al.* and our MC. The right plot on Figure 7.12 shows the calculated CCQE cross-section of ν_μ/ν_e ratio in Nieves' model normalized by that in the model of Smith and Monitz as a function of neutrino energy.

- Single pion production (Total cross-section)
  The uncertainty in the single-meson production cross-section is estimated to be 20 %. Details of the single pion production are described in Section 3.3.2.

- Single pion production (Model dependence)
  The uncertainty in the single-meson production cross-section for each π^+, π^0 and π^- production is estimated by taking the difference between the FKR model [77] and the model calculation based on [78] to be 20 %.

			uncertainty (%)	best-fit (%)
(C) Systematic uncertainties in event selection for SK-I				
Reduction for FC event			0.2	-0.003
Reduction for PC event			2.6	0.4
FC/PC separation			0.9	-0.3
Non-ν background	Sub-GeV	e-like 0μedecay	0.5	0.02
		μ-like 0μedecay	<0.1	-0.001
		μ-like 0μedecay	<0.1	0.0
	Multi-GeV	e-like	0.2	0.03
		μ-like	0.1	-0.01
	PC		0.2	-0.03
Reduction for upward going muon	stopping μ		1.3	-0.1
	through-going μ		0.5	-0.04
Separation of upward stopping/through-going muon			0.4	-0.05

Table 7.4: Summary of systematic uncertainties in event selection for SK-I. Estimated uncertainty and the best-fit value are listed for each error.

- NC/CC ratio
  The systematic uncertainty in the NC/CC ratio is estimated to be 20 %. A positive number means more NC events in the Monte Carlo.

- Nuclear Effect in ^{16}O nucleus
  The systematic uncertainty in the mean free path of hadrons produced via neutrino interactions in the ^{16}O nucleus is estimated to be 30 %. A positive number means stronger nuclear effect in ^{16}O.

- Nuclear Effect in pion spectrum
  The difference in the predicted pion energy spectrum by NEUT [62] and NUANCE [124] interaction models is taken to be a systematic error.

- Charged-current ν_τ interaction
  The systematic uncertainty in the ν_τ cross-sections for CC interactions is estimated to be 30 % by comparing two models of NEUT [62] and Hagiwara *et al.* [128].

7.3.3 Systematic Uncertainties in Event Selection

- FC and PC reduction
  Details of FC and PC reduction are described in Section 4.2 and **??**. The uncertainty of the FC and PC reduction efficiencies are estimated by comparing the distributions of the each cut valuables of data and MC. The uncertainty is estimated to be 0.2 % (0.2 %) and 2.6 % (4.0 %) for FC and PC reduction of SK-I (SK-II), respectively.

			uncertainty (%)	best-fit (%)
(D) Systematic uncertainties in event selection for SK-II				
Reduction for FC event			0.2	0.007
Reduction for PC event			4.0	-3.8
FC/PC separation			0.5	0.07
Non-ν background	Sub-GeV	e-like 0μedecay	0.3	0.006
		μ-like 0μedecay	0.1	-0.001
		μ-like 0μedecay	<0.1	0.0
	Multi-GeV	e-like	0.7	0.01
		μ-like	0.1	-0.001
	PC		0.7	-0.006
Reduction for upward going muon	stopping μ		1.9	-0.08
	through-going μ		0.9	-0.04
Separation of upward stopping/through-going muon			0.4	0.003

Table 7.5: Summary of systematic uncertainties in event selection for SK-II. Estimated uncertainty and the best-fit value are listed for each error.

- FC/PC separation
  The FC and PC events are separated by the number of hit PMTs in the OD hit PMT cluster (NHITAC). The systematic uncertainty in the FC/PC separation is estimated to be 0.9 % (SK-I) and 0.5 % (SK-II) from the difference between data and MC NHITAC distributions. A positive number means that the number of MC FC events is increased.

- Non-ν background
  The possible sources of background in FC and PC samples are cosmic ray muons for μ-like samples and flasher PMTs and neutron from the rock for e-like samples. The contamination of the background is estimated to be 0.5 % (0.3 %) for FC Sub-GeV e-like events, 0.2 % (0.7 %) for FC Multi-GeV e-like events, <0.1 % (<0.1 %) for FC Sub-GeV μ-like events, 0.1 % (0.1 %) for FC Multi-GeV μ-like event and 0.2 % (0.7 %) for PC events.

- Upward going muon reduction
  The methods of the reduction for upward going muon events are described in Section 4.4. The systematic uncertainty in the data reduction process for upward-going sample is estimated by comparing the distribution of each cut variable of the data with that of the Monte Carlo events. The estimated errors are 1.3 % (1.9 %) for upward stopping muons and 0.5 % (0.9 %) for upward through-going muons for SK-I (SK-II). Uncertainties for upward stopping μ and upward through-going μ are assumed to be correlated.

- Upward stopping/through-going muon separation
  The upward stopping muon events and the upward through-going muon events are separated by the number of hit OD PMTs within 8 m from the exit position (NHITEX). The systematic uncertainty for the stopping/through-going separation is estimated to be 0.4 %

and 0.3 % for SK-I and SK-II, respectively, by comparing the NHITEX distributions for the observed data and the Monte Carlo events. A positive number means that the number of MC stopping muons is increased.

7.3.4 Systematic Uncertainties in Event Reconstruction

- Ring separation
  The ring-counting algorithm is described in Section 5.3. The systematic error in single-ring and multi-ring separation is due to several uncertainties such as water transparency and detector calibration. The uncertainties are estimated by comparing the ring counting likelihood distributions for the observed data with that for the Monte Carlo events.

- Particle Identification
  The systematic errors in the particle identification are estimated by taking the difference in the PID likelihood distributions between data and MC (see Section 5.4).

- Energy calibration
  The absolute energy scale is calibrated using several sources as described in Section 2.6.5 and the systematic uncertainty is estimated to be 2.0 % for SK-I and 2.5 % for SK-II.

- Up/down symmetry of energy calibration
  The difference in the energy scale for upward-going and downward-going events is measured by using decay electrons from cosmic ray stopping muons (see Figure 2.33). The up/down asymmetry of the energy scale is estimated to be 0.6 % for SK-I and SK-II.

- Single ring π^0-like sample selection
  The FC Sub-GeV single-ring π^0-like event sample is separated from the FC Sub-GeV single-ring e-like events as described in Section 6.1.1. The uncertainty of the single-ring π^0-like sample selection is derived from the difference between data and MC of the invariant mass distribution and total likelihood distributions. Figure 7.13 shows the invariant mass distributions for FC Sub-GeV single-ring e-like events from the π^0 fitter (see Section 5.9.1). In the separation of π^0-like sample, the π^0 mass is required to be larger than $100\,\mathrm{MeV}/c^2$. The uncertainty of the π^0 mass cut is estimated to be 9.6 % (5.1 %) by comparing the π^0 mass distributions for the observed data and the Monte Carlo events for SK-I (SK-II). The distributions of the total likelihood for 1-ring π^0 like sample selection of data and MC are shown in Figure 7.14. The uncertainties in the selection efficiency from the likelihood distributions are estimated to be 6.2, 21.3, 16.9, 8.7 % (6.1, 16.6, 8.5, 9.6 %) from the low to high momentum bins for SK-I (SK-II). Since the selection criteria have energy dependent, the uncertainty in the absolute enregy scale is also a source of the π^0 selection uncertainty. The uncertainties from the energy scale uncertainty of 2.0 % (2.5 %) are 5.7, 1.3, 0.6, 0.6, 1.3 % (5.5, 4.0, 2.3, 4.0, 2.0 %) for SK-I (SK-II). Combining these uncertainties, the systematic errors on the 1-ring π^0-like sample selection are estimated to be 11.2, 11.5, 23.4, 19.1, 13.0 % (7.5, 8.9, 17.5, 10.7, 11.1 %) in the each momentum binsfor SK-I (SK-II). Exactly the same methods are sed to evaluate the systematic uncertainties for SK-II, which are summarized in Table 7.7.

- Two ring π^0-like sample selection
  The FC Sub-GeV two-ring π^0-like sample is separated as described in Section 6.1.3. The

			uncertainty (%)	best-fit (%)
(E) Systematic uncertainties in event reconstruction for SK-I				
Single-ring/multi-ring separation	$< 400\,\mathrm{MeV}$	e-like	6.3	2.6
		μ-like	2.4	1.0
	$> 400\,\mathrm{MeV}$	e-like	3.4	1.4
		μ-like	1.3	0.5
	Multi-GeV	e-like	15.9	6.7
		μ-like	6.2	2.6
	Sub-GeV	multi-ring μ	3.7	-1.5
	Multi-GeV	multi-ring μ	7.2	-3.0
Particle identification	Sub-GeV	e-like	-0.6	0.06
		μ-like	0.6	-0.06
	Multi-GeV	e-like	-0.4	0.04
		μ-like	0.4	-0.04
	Sub-GeV	multi-ring μ	3.4	-0.7
	Multi-GeV	multi-ring μ	4.7	-0.9
Energy calibration for FC event			2.0	-1.8
Up/down symmetry of energy calibration			0.6	0.1
FC Sub-GeV single-ring	$100< P_e <250\,\mathrm{MeV/c}$		11.2	-10.2
π^0-like sample selection	$250< P_e <400\,\mathrm{MeV/c}$		11.5	-10.5
	$400< P_e <630\,\mathrm{MeV/c}$		23.4	-21.3
	$630< P_e <1000\,\mathrm{MeV/c}$		19.1	-17.4
	$1000< P_e <1330\,\mathrm{MeV/c}$		13.0	-11.9
FC Sub-GeV two-ring π^0-like sample selection			8.4	1.9
Decay electron tagging		e-like 0μedecay	0.2$\sim$0.5	-0.2$\sim$-0.4
for FC Sub-GeV single-ring sample		e-like 1μedecay	-4.4$\sim$-4.2	2.9$\sim$3.0
		μ-like 0μedecay	1.6$\sim$1.7	-1.1$\sim$-1.2
		μ-like 1μedecay	-1.4$\sim$-1.1	0.7$\sim$0.9
		μ-like 2μedecay	-6.4$\sim$-5.9	4.0$\sim$4.3

Table 7.6: Summary of systematic uncertainties in event reconstruction for SK-I. Estimated uncertainty and the best-fit value are listed for each error.

			uncertainty (%)	best-fit (%)
(F) Systematic uncertainties in event reconstruction for SK-II				
Single-ring/multi-ring separation	$< 400\,\mathrm{MeV}$	e-like	1.3	0.01
		μ-like	0.7	0.07
	$> 400\,\mathrm{MeV}$	e-like	2.8	0.03
		μ-like	0.5	0.05
	Multi-GeV	e-like	3.7	0.03
		μ-like	1.5	0.01
	Sub-GeV	multi-ring μ	-0.8	-0.007
	Multi-GeV	multi-ring μ	-2.2	-0.02
Particle identification	Sub-GeV	e-like	-0.8	0.1
		μ-like	0.9	-0.2
	Multi-GeV	e-like	-0.2	0.04
		μ-like	0.2	-0.04
	Sub-GeV	multi-ring μ	13.9	4.1
	Multi-GeV	multi-ring μ	9.1	2.7
Energy calibration for FC event			2.5	-3.1
Up/down symmetry of energy calibration			0.6	-0.3
FC Sub-GeV single-ring	$100< P_e <250\,\mathrm{MeV/c}$		7.5	-4.7
π^0-like sample selection	$250< P_e <400\,\mathrm{MeV/c}$		8.9	-5.6
	$400< P_e <630\,\mathrm{MeV/c}$		17.5	-11.0
	$630< P_e <1000\,\mathrm{MeV/c}$		10.7	-6.7
	$1000< P_e <1330\,\mathrm{MeV/c}$		11.1	-7.0
FC Sub-GeV two-ring π^0-like sample selection			6.9	-0.7
Decay electron tagging		e-like 0μedecay	0.2$\sim$0.5	-0.1$\sim$-0.3
for FC Sub-GeV single-ring sample		e-like 1μedecay	-4.2$\sim$-4.4	2.4$\sim$2.5
		μ-like 0μedecay	1.6$\sim$1.7	-0.9$\sim$-1.0
		μ-like 1μedecay	-1.4$\sim$-1.1	0.6$\sim$0.8
		μ-like 2μedecay	-6.4$\sim$-5.9	3.4$\sim$3.6

Table 7.7: Summary of systematic uncertainties in event reconstruction for SK-II. Estimated uncertainty and the best-fit value are listed for each error.

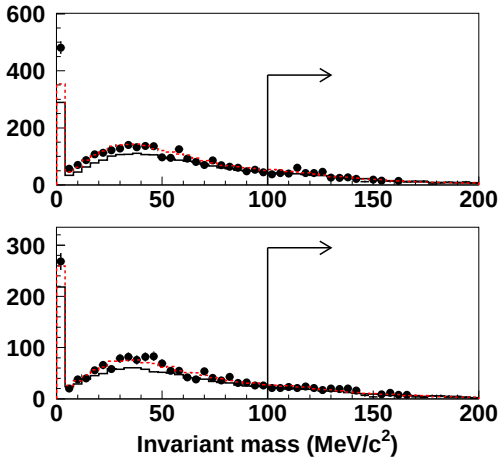

Figure 7.13: The π^0 mass distributions from the π^0 fitter for data (dot) and Monte Carlo events (solid line) of FC Sub-GeV single-ring e-like for SK-I (top) and SK-II (bottom) together with the shifted distribution (dotted line) by the fitted results.

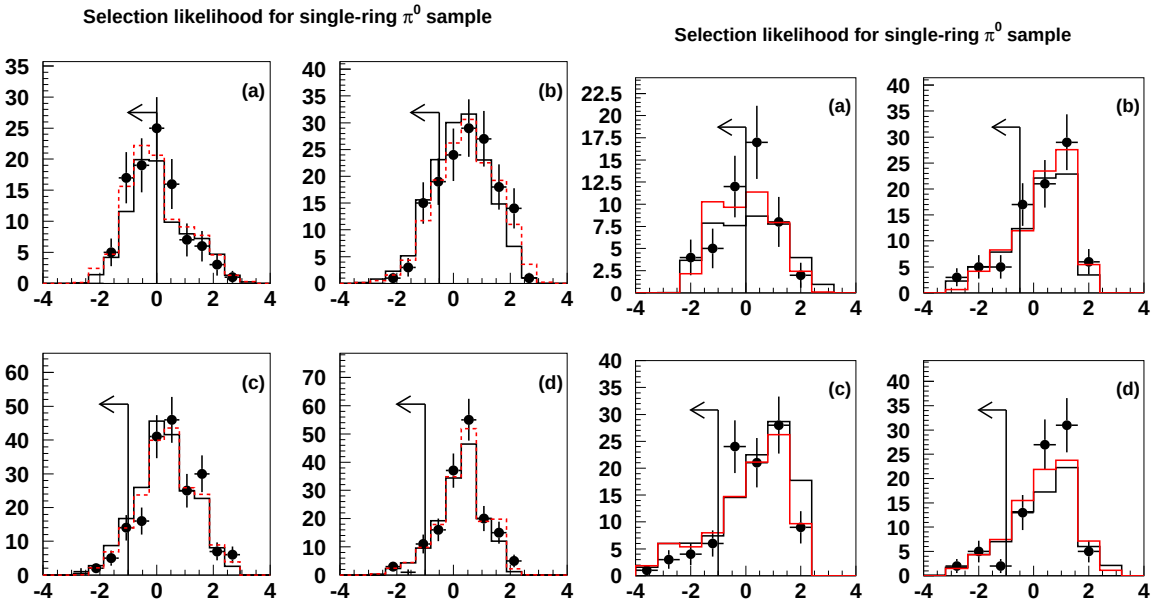

Figure 7.14: The π^0-like sample selection likelihood distributions for data (dot) and Monte Carlo events (solid line) of FC Sub-GeV single-ring e-like for SK-I (left) and SK-II (right) together with the shifted distribution (dotted line) by the fitted results in (a)$P_e < 250\,\mathrm{MeV/c}$, (b) $250\,\mathrm{MeV/c} \leq P_e < 400\,\mathrm{MeV/c}$, (c) $400\,\mathrm{MeV/c} \leq P_e < 630\,\mathrm{MeV/c}$, (d) $630\,\mathrm{MeV/c} \leq P_e < 1000\,\mathrm{MeV/c}$, (e) $1000\,\mathrm{MeV/c} \leq P_e$.

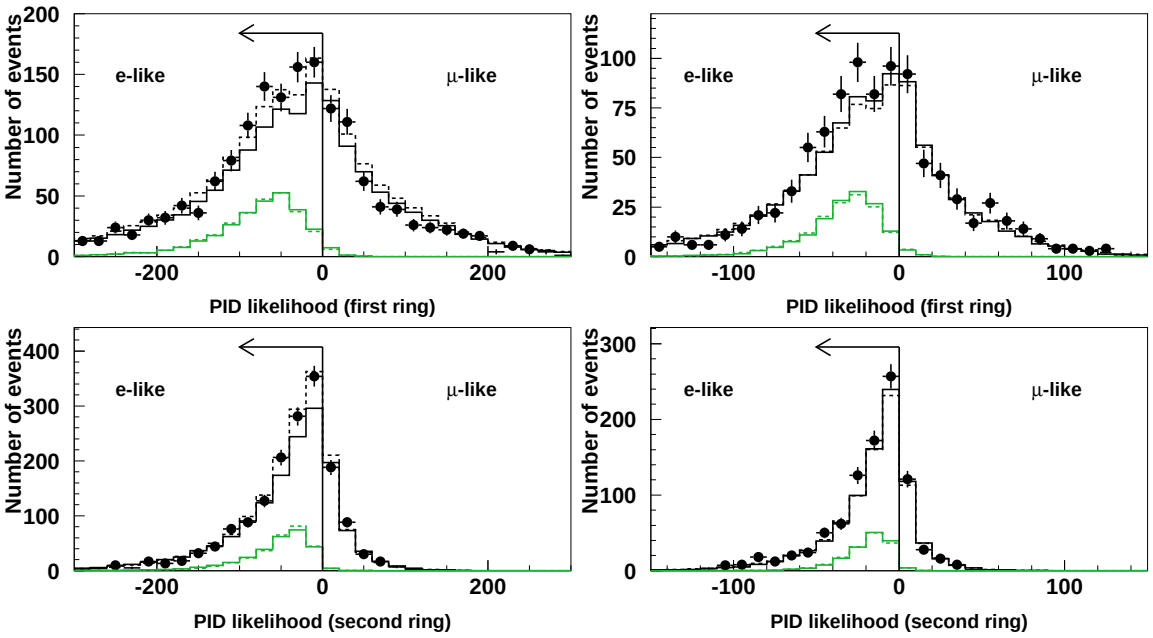

Figure 7.15: The PID likelihood distributions of data (dot) and Monte Carlo events (solid line) for FC Sub-GeV two-ring events with the shifted distribution (dotted line) by the fitted results. The distributions shown by green histgrams are from the Monte Carlo π^0 events. The left two panels show for SK-I and the right two show for SK-II.

uncertainty in two-ring π^0-like sample selection comes from the ring-counting and PID. Figure 7.15 shows the PID parameter distributions of FC Sub-GeV two-ring events for the data and MC. In order to estimate the uncertainty due to PID, the Monte Carlo likelihood distributions are renormalized (vertical) and scaled (horizontal) to get the best-fit to the data. The differences in the number of events which identified to be e-like before and after shifted are 0.6 % and 0.2 % for the first ring and the second ring, respectively. Figure 7.16 shows the ring-counting distributions of FC Sub-GeV events for data and MC with the most energetic ring being identified to be e-like. By fitting data and MC by the same as method for PID, the differences of the number of the events which are identified to be two ring before and after the shift are 6.7 % and 5.0 % for the separation from a single ring to more rings and the separation from two rings to more rings, respectively. Combined the uncertainties from ring-counting and PID, the uncertainty of the two ring π^0-like sample selection is calculated to be 8.4 % for SK-I. For SK-II, the same methods are used to evaluate the systematic uncertainties. The uncertainties due to PID are estimated to be 0.4 % and 0.2 % for the first ring and the second ring, respectively. The uncertainties due to ring-counting are estimated to be 0.04 % and 6.9 % for the separation from a single ring to more rings and the separation from two rings to more rings, respectively. Combined the uncertainties from ring-counting and PID, the uncertainty of the two ring π^0-like sample selection is calculated to be 6.9 % for SK-II.

- Decay electron tagging
  The uncertainty in the decay electron tagging comes from that of muon decay and also π^+

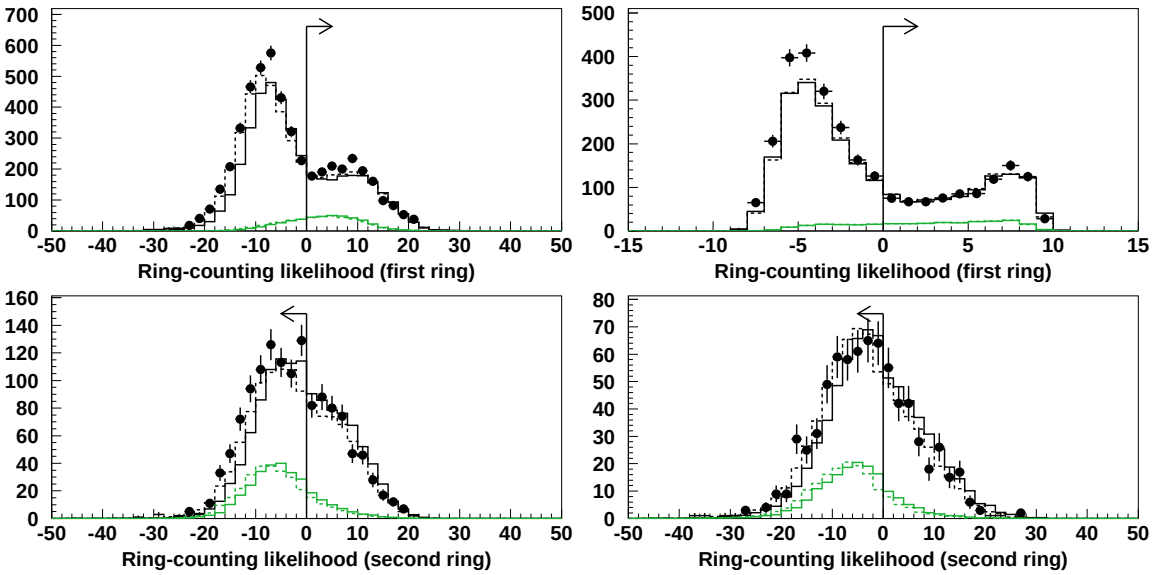

Figure 7.16: The ring-counting likelihood distributions of FC Sub-GeV events for data (dot) and Monte Carlo events (solid line) which the most energetic ring is identified to be e-like with the shifted distribution (dotted line) by the fitted results. The distributions shown by green histgrams are from the Monte Carlo π^0 events. The left two panels show for SK-I and the right two show for SK-II.

decay probability. The uncertainty in tagging efficiency of an electron from a muon decay has been estimated to be 1.5 % using cosmic ray muons [129]. The uncertainty on π^+ interaction in water is mainly considered to come from the energy dependent uncertainties on the cross-section of π^+-^{16}O interaction. Figure 3.13 shows the cross-section for π^+-^{16}O as a function of π^+ momentum. The uncertainties are estimated from the difference between experimental data and the theoretical calculation used in our Monte Carlo to be 20$\sim$60 % depending on the pion energy. The uncertainty of π^+ decay probability is estimated by the π^+ MC generated with increased or decreased mean free path by the uncertainties of π^+-^{16}O interaction. Figure 7.17 shows the π^+ decay probabilities when the mean free path of $\pi+$ in water is increased and decreased. The differences of the probability are 3$\sim$13 % depending on the π^+ momentum and affect the uncertainty of decay electron tagging by 0.3$\sim$0.6 % for FC single-ring Sub-GeV e-like 0μedecay sample, 3.5$\sim$4.2 % for FC single-ring Sub-GeV e-like 1μedecay sample, 0.5$\sim$0.9 % for FC single-ring Sub-GeV μ-like 0μedecay sample, 0.1$\sim$0.3 % for FC single-ring Sub-GeV μ-like 1μedecay sample and 5.0$\sim$5.7 % for FC single-ring Sub-GeV μ-like 2μedecay sample. Combining the uncertainties from π^+ decay and tagging efficiency of an electron from a muon decay, the systematic uncertainties on decay electron tagging are obtained as Table 7.6. Uncertainties for 0μedecay and 1μedecay (2μedecay) are asuumed to be correlated. The unceratainty in the decay electron tagging for SK-II is asuumed to be identical to SK-I.

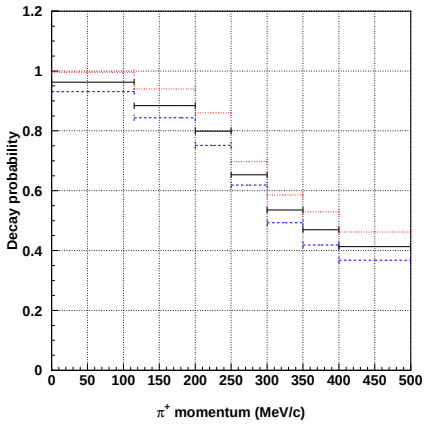

Figure 7.17: The probabilities of π^+ decay when the mean free path of π^+ in water is increased (dashed line) and decreased (dotted line). The solid line shows the π^+ decay probability in our Monte Carlo simulation.

7.4 Results

Since θ_{13}=0 is assumed in the analysis, χ^2 is calculated in the four dimensional oscillation parameter space of Δm^2_{12}, Δm^2_{23}, $\sin^2\theta_{12}$ and $\sin^2\theta_{23}$. For the solar neutrino parameters, two scenarios are examined. In one scenario with the solar neutrino parameters turned on, the scanning points of solar parameters are chosen around the allowed region obtained by a combined analysis of the solar neutrino data and KamLAND data [13]. To take into account the constraint on the solar neutrino parameters, the $\Delta\chi^2_{solar}$ values from the combined analysis of the solar neutrino and KamLAND data is added to χ^2 from the atmospheric neutrino data for each (Δm^2_{12}, $\sin^2\theta_{12}$) point as shown in Equation (7.4). The other scenario is the ordinary "one mass scale dominance" approximation with Δm^2_{12} =0, that is, the pure $\nu_\mu \leftrightarrow \nu_\tau$ oscillation analysis case.

Figure 7.18 shows the χ^2-χ^2_{min} distributions with and without the 1-2 parameters as a function of $\sin^2\theta_{23}$, where Δm^2_{12}, Δm^2_{23} and $\sin^2\theta_{12}$ are chosen so that χ^2 is minimized. The best-fit point without the 1-2 parameters is located at $\sin^2\theta_{23}$=0.50, on the other hand, the best-fit point with the 1-2 parameters is 0.53. The minimum χ^2 value is 828.1/743 d.o.f. in case with the 1-2 parameters at $(\sin^2\theta_{23}, \Delta m^2_{23}, \sin^2\theta_{12}, \Delta m^2_{12}) = (0.53, 2.5\times10^{-3}\,\mathrm{eV}^2, 0.32, 7.8\times10^{-5}\,\mathrm{eV}^2)$. There is no significant discrepancy of $\sin^2\theta_{23}$ from 45°, but the asymmetric shape due to the effect of the solar terms is seen in the χ^2 distribution. The stringent constraint on $\sin^2\theta_{23}$ has been observed in the analysis with the solar terms. The 1σ arrowed region for $\sin^2\theta_{23}$, which is defined to be $\Delta\chi^2$ =1.0 is $0.43 < \sin^2\theta_{23} < 0.58$, which is equivalent to $\sin^2 2\theta_{23} > 0.973$ as shown in Figure 7.19. This is a more stringent constraint on θ_{23} compared with the published result; $\sin^2 2\theta_{23} > 0.95$ corresponding to $0.39 < \sin^2\theta_{23} < 0.61$ [25].

The gray scale in Figure 7.20 shows the χ^2-χ^2_{min} distribution at each solar parameter point. Since the difference of χ^2-χ^2_{min} in a 1-2 parameter plane is small (≤ 0.14), the global χ^2 distribution has weak dependence on the details for the 1-2 parameters.

Constraint on Δm^2_{23} is expected not to be affected by the solar terms as shown in Figure 7.21. Compared with the published result [25] on χ^2 as a function of Δm^2_{23}, the χ^2 distribution is less smooth. This is because the averaged oscillation probability technique can not be used in the analysis involving the solar terms, and therefore the oscillated Monte Carlo prediction is less smooth.

Zenith angle dependence of the ratio between the number of FC Sub-GeV single-ring μ-like

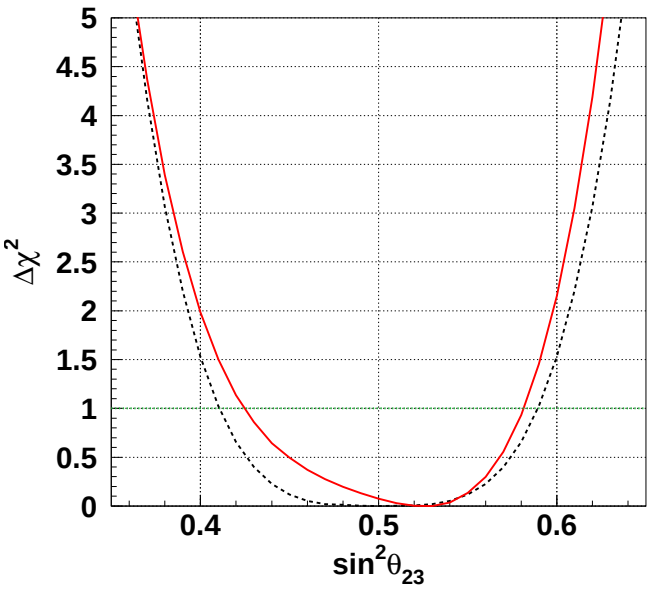

Figure 7.18: χ^2-χ^2_{min} distribution as a function of $\sin^2\theta_{23}$ for oscillations without the 1-2 parameters (dotted line) and with the 1-2 parameters (solid line). For each $\sin^2\theta_{23}$ point, Δm^2_{23} is chosen so that χ^2 is minimized. The green line corresponds to the 68 % confidence level which is located at $\chi^2_{min} + 1.0$.

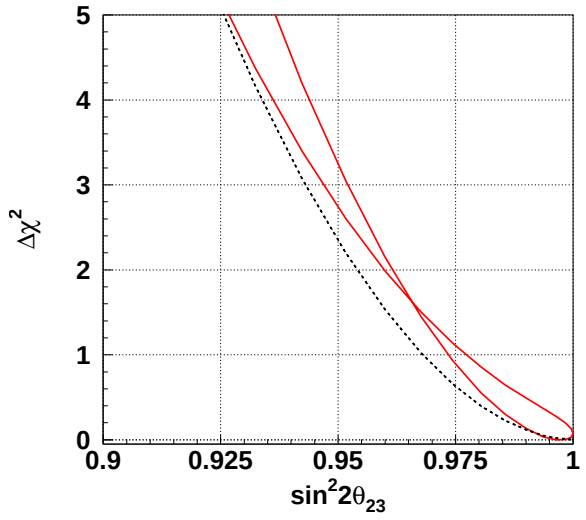

Figure 7.19: χ^2-χ^2_{min} distribution as a function of $\sin^2 2\theta_{23}$ for oscillations without the 1-2 parameters (dashed line) and with the 1-2 parameters (solid line). There are 2 solid lines due to the different χ^2 curve below and above $\sin^2\theta_{23} = 0.5$ as seen in Figure 7.18.

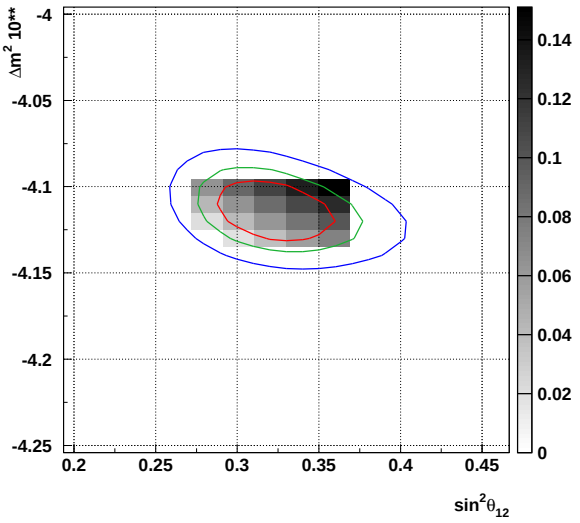

Figure 7.20: The gray scale shows χ^2-χ^2_{min} at each solar parameter point. The lines show the arrowed region from the result of the solar neutrino and KamLAND data [13], correspondng to the 68 % (dashed line), 90 % (solid line) and 99 % (dotted line).

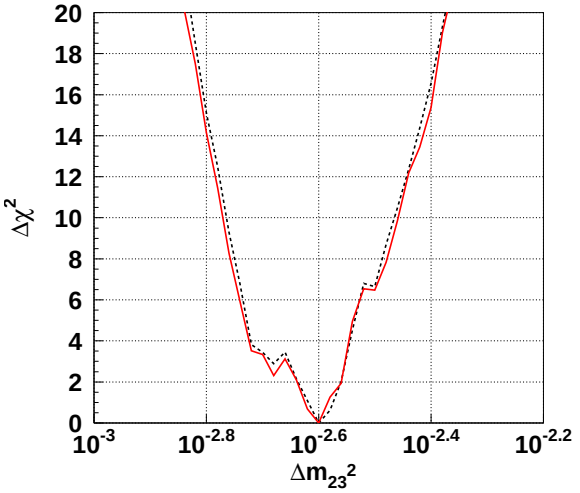

Figure 7.21: χ^2-χ^2_{min} distribution as a function of Δm^2_{23} for oscillations without the 1-2 parameters (dashed line) and with the 1-2 parameters (solid line).

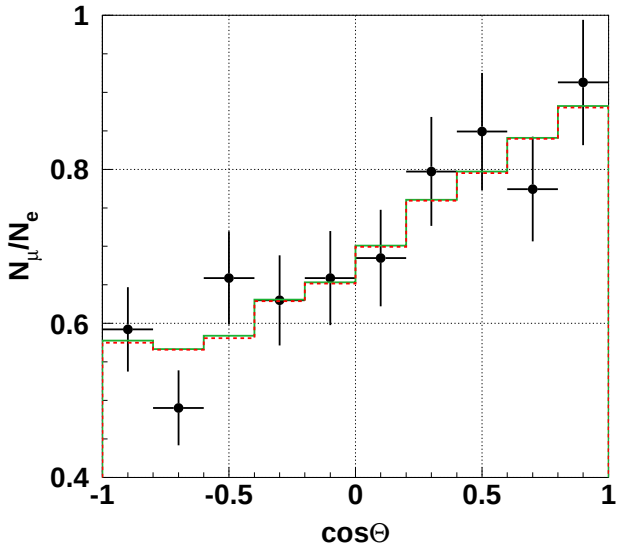

Figure 7.22: Zenith angle dependence of (N_μ/N_e) for the data (dot), the best-fit results with solar terms (solid line) and the best-fit results without solar terms (dotted line). $N_\mu(N_e)$ is the number of events for FC Sub-GeV single-ring μ-like 1μedecay sample (e-like 0μedecay sample).

1μedecay events and FC Sub-GeV e-like 0μedecay events (N_μ/N_e) for the data and the best-fit results with and without the solar terms are shown in Figure 7.22. The two fitting results equally explain the data and the effect of the solar terms on the (N_μ/N_e) ratio has not been observed.

Figure 7.23, 7.24, 7.25 and 7.26 show the zenith angle distributions for FC Sub-GeV event samples, FC Multi-GeV or multi-ring event samples, PC event samples and Upward going-muon event samples for SK-I divided by each momentum bin. Figure 7.27, 7.28, 7.29 and 7.30 show the zenith angle distributions for FC Sub-GeV event samples, FC Multi-GeV or multi-ring event samples, PC event samples and Upward going-muon event samples for SK-II divided by each momentum bin. The data are also consistent with the best-fit results with solar parameters for both SK-I and SK-II.

The probability for $\chi^2_{min} = 828.1/743$ d.o.f. or larger is calculated by "toy Monte Carlo" events. Assuming the fitted number of events (N_{fit}) in each bin is true, the expected number of events (N_{rnd}) is determined based on the Poisson distribution. χ^2 for the toy Monte Carlo is calculated as :

$$\chi^2 = 2(N_{fit} - N_{rnd}) + 2N_{rnd} \log\left(\frac{N_{rnd}}{N_{fit}}\right). \tag{7.6}$$

The χ^2 distribution shown in Figure 7.31 is obtained by 100000 calculations. The probability for $\chi^2_{min} = 828.1/743$ d.o.f. is estimated to be 11.7 %.

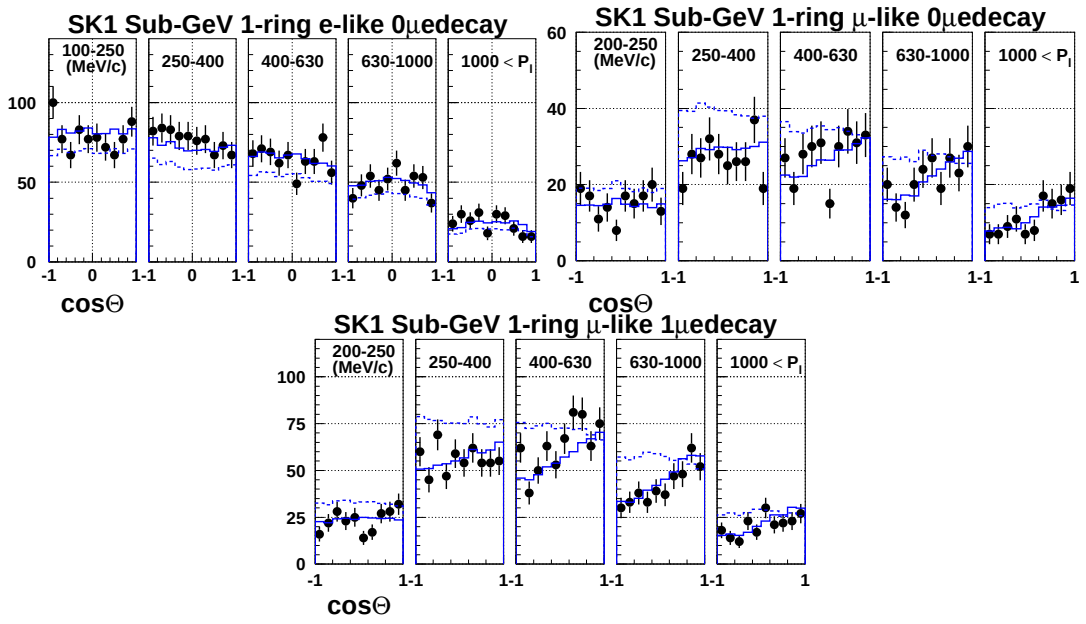

Figure 7.23: Zenith angle distributions for all event bins for data (dot) and Monte Carlo events assuming no oscillation (dotted line) and the best-fit results (solid line) for SK-I FC Sub-GeV single-ring event samples. Each panel shows the distributions of each momentum bin.

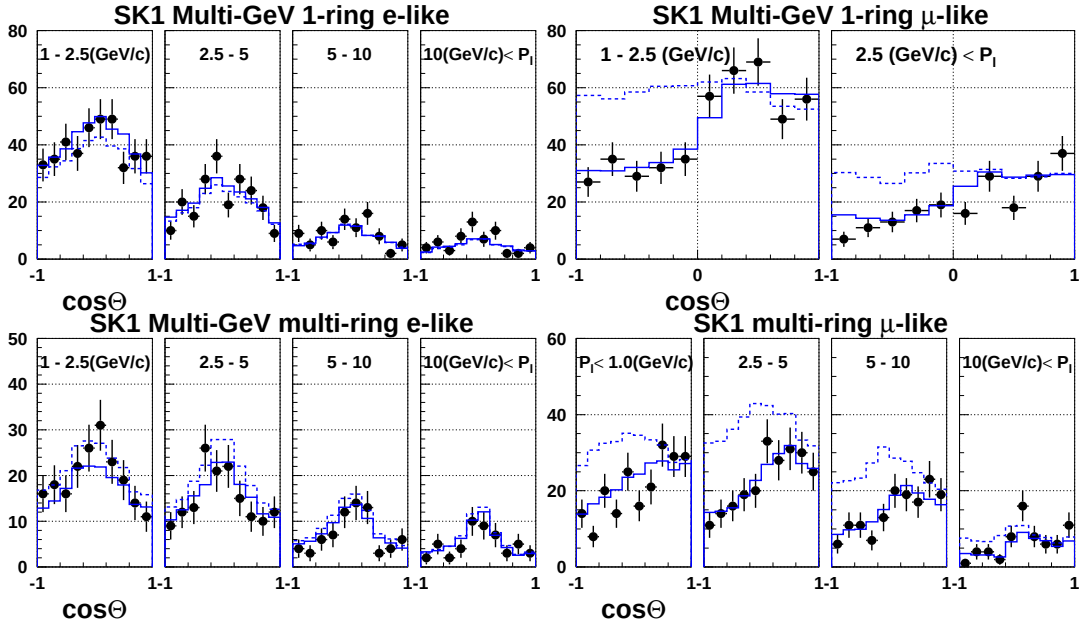

Figure 7.24: Zenith angle distributions for all event bins for data (dot) and Monte Carlo events assuming no oscillation (dotted line) and the best-fit results (solid line) for SK-I FC Multi-GeV or multi-ring event samples. Each panel shows the distributions of each momentum bin.

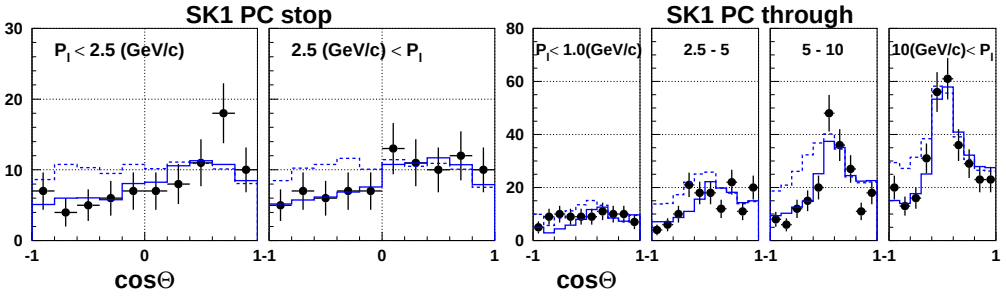

Figure 7.25: Zenith angle distributions for all event bins for data (dot) and Monte Carlo events assuming no oscillation (dotted line) and the best-fit results (solid line) for SK-I PC event samples. Each panel shows the distributions of each momentum bin.

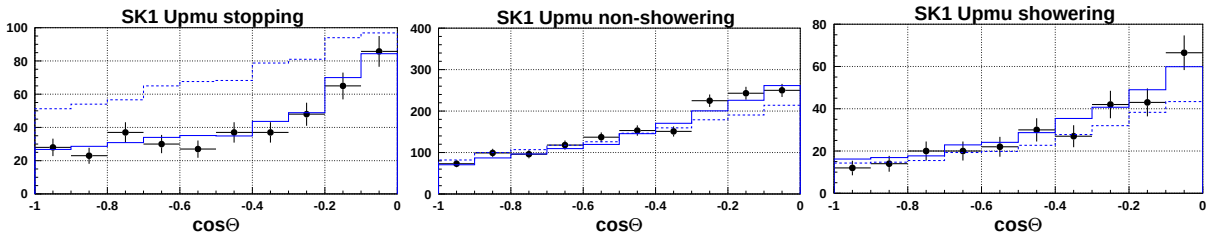

Figure 7.26: Zenith angle distributions for all event bins for data (dot) and Monte Carlo events assuming no oscillation (dotted line) and the best-fit results (solid line) for SK-I upward-going muon event samples.

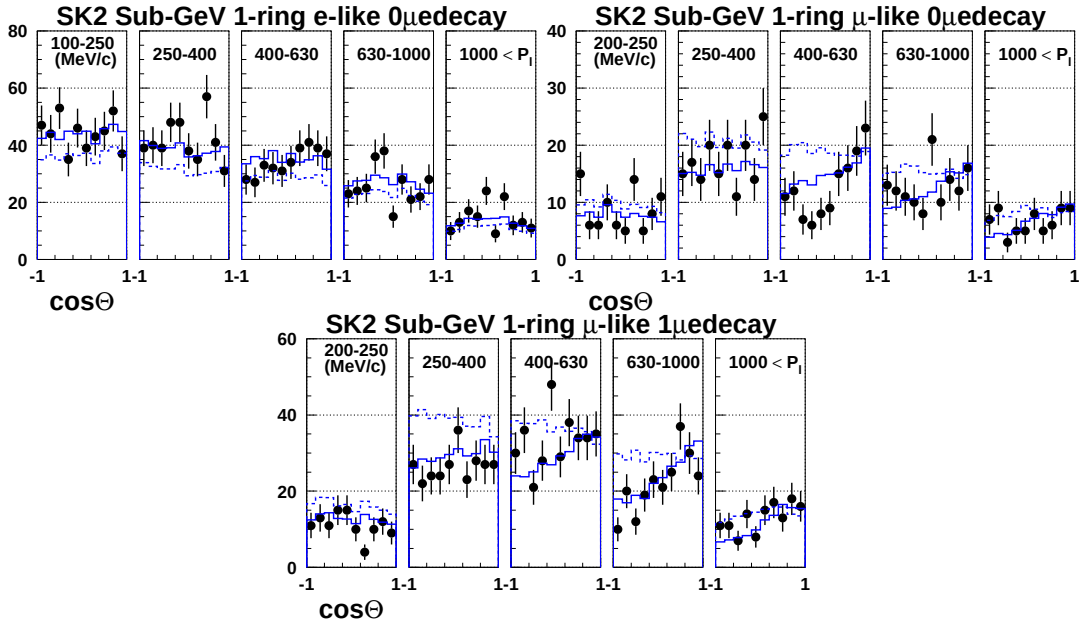

Figure 7.27: Zenith angle distributions for all event bins for data (dot) and Monte Carlo events assuming no oscillation (dotted line) and the best-fit results (solid line) for SK-II FC Sub-GeV single-ring event samples. Each panel shows the distributions of each momentum bin.

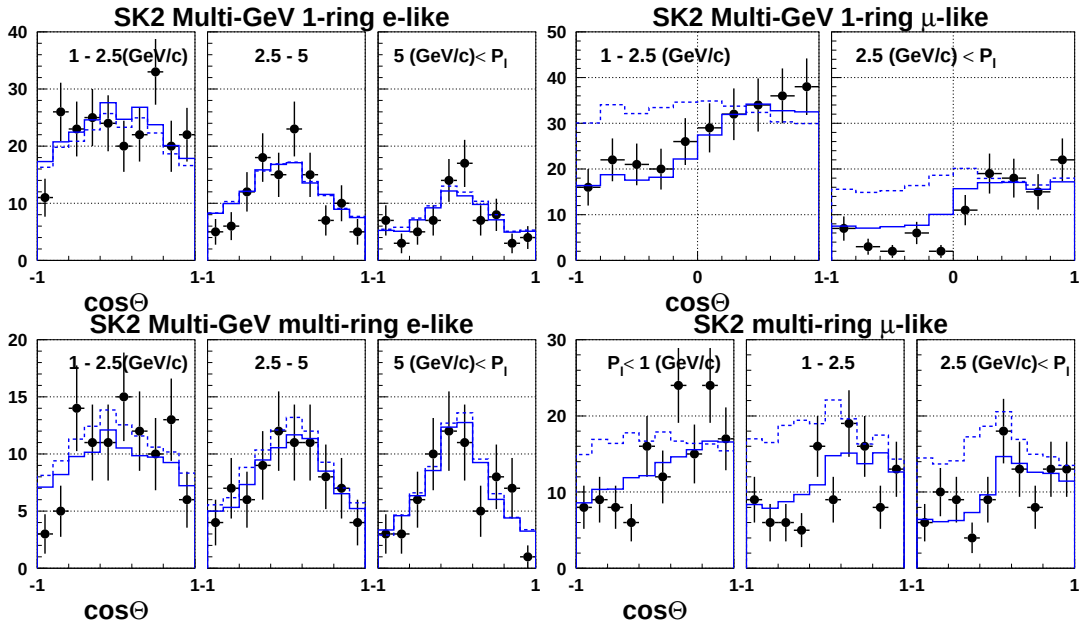

Figure 7.28: Zenith angle distributions for all event bins for data (dot) and Monte Carlo events assuming no oscillation (dotted line) and the best-fit results (solid line) for SK-II FC Multi-GeV or multi-ring event samples. Each panel shows the distributions of each momentum bin.

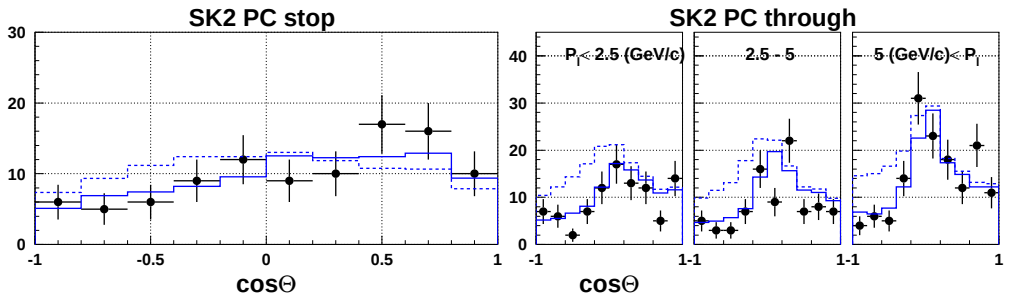

Figure 7.29: Zenith angle distributions for all event bins for data (dot) and Monte Carlo events assuming no oscillation (dotted line) and the best-fit results (solid line) for SK-II PC event samples. Each panel shows the distributions of each momentum bin.

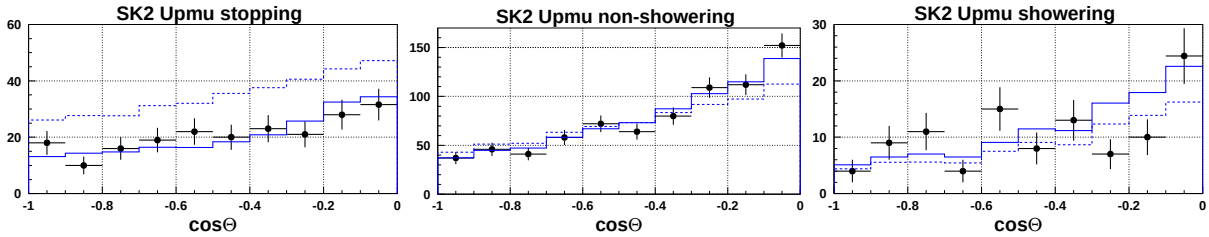

Figure 7.30: Zenith angle distributions for all event bins for data (dot) and Monte Carlo events assuming no oscillation (dotted line) and the best-fit results (solid line) for SK-II upward-going muon event samples.

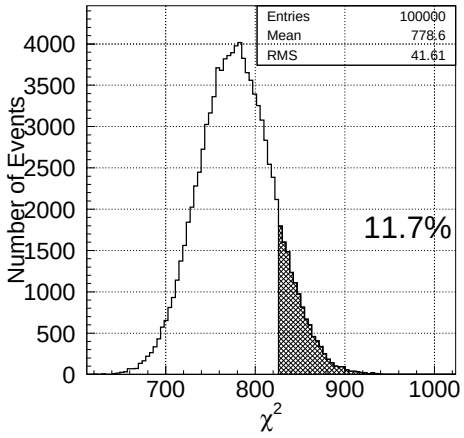

Figure 7.31: χ^2 distribution of toy Monte Carlo events.

Chapter 8

Future Sensitivity on the θ_{23} Determination

The future sensitivity on the θ_{23} determination is studied by simulating the signal according to the expectation from some specific choice of the true parameters. The oscillated Monte Carlo sample renormalized to a 20 year exposure, which corresponds to about 3 times the whole SK-I and SK-II data, is replaced to the observed data. As the true $\sin^2\theta_{23}$, three different values, 0.40, 0.50 and 0.60 are selected. For the other parameters, θ_{13} =0, $\sin^2\theta_{12}$ =0.32, $\Delta m^2_{12} = 7.8\times10^{-5}$ eV^2 and $\Delta m^2_{23} = 2.5\times10^{-3}$ eV^2 are assumed both for making fake signal and for the expectation to calculate χ^2. Therefore, only $\sin^2\theta_{23}$ is scanned for the χ^2 minimum. The 80 systematic errors, which are related to the sample normalizations, neutrino flux calculations, neutrino interaction models and detector responses, are considered in the oscillation analysis as described in Section 7.3. In this study, in order to research which systematic errors should be reduced for obtaining a better sensitivity, the size of specific systematic errors is reduced down to 1/4 of the current estimation and then χ^2 are compared.

Figure 8.1 shows the $\chi^2 - \chi^2_{min}$ as a function of $\sin^2\theta_{23}$ for each true $\sin^2\theta_{23}$. The thin solid line (black) and middle-thick solid line (green) show the case with all systematic errors unchanged for a 6 year exposure and a 20 year exposure, respectively. While the best-fit point is located at the true $\sin^2\theta_{23}$ value, $\Delta\chi^2$ distribution has the second local minimum around the false solution $1-\sin^2\theta_{23}$. It seems to be difficult to measure $\sin^2\theta_{23}$ precisely in this statistics in the case that the deviation of $\sin^2\theta_{23}$ from the maximal is small. The other lines in Figure 8.1 show the cases of reducing the systematic errors in neutrino flux, neutrino interactions, detector responses and all systematic errors by a factor of 0.25. It is found that reducing the systematic uncertainties on neutrino interactions is most effective to distinguish the true $\sin^2\theta_{23}$ from false one.

To explore which systematic errors are dominant, χ^2 distributions are compared by reducing each systematic error one by one. As a result, the dominant systematic errors to be reduced for the future determination of $\sin^2\theta_{23}$ are as follows :

- neutrino flux : $(\nu_\mu + \overline{\nu}_\mu)/(\nu_e + \overline{\nu}_e)$ for $E_\nu < 5$ GeV
- neutrino flux : $\nu_e/\overline{\nu}_e$ for $E_\nu < 10$ GeV
- neutrino flux : $\nu_\mu/\overline{\nu}_\mu$ for $E_\nu < 10$ GeV

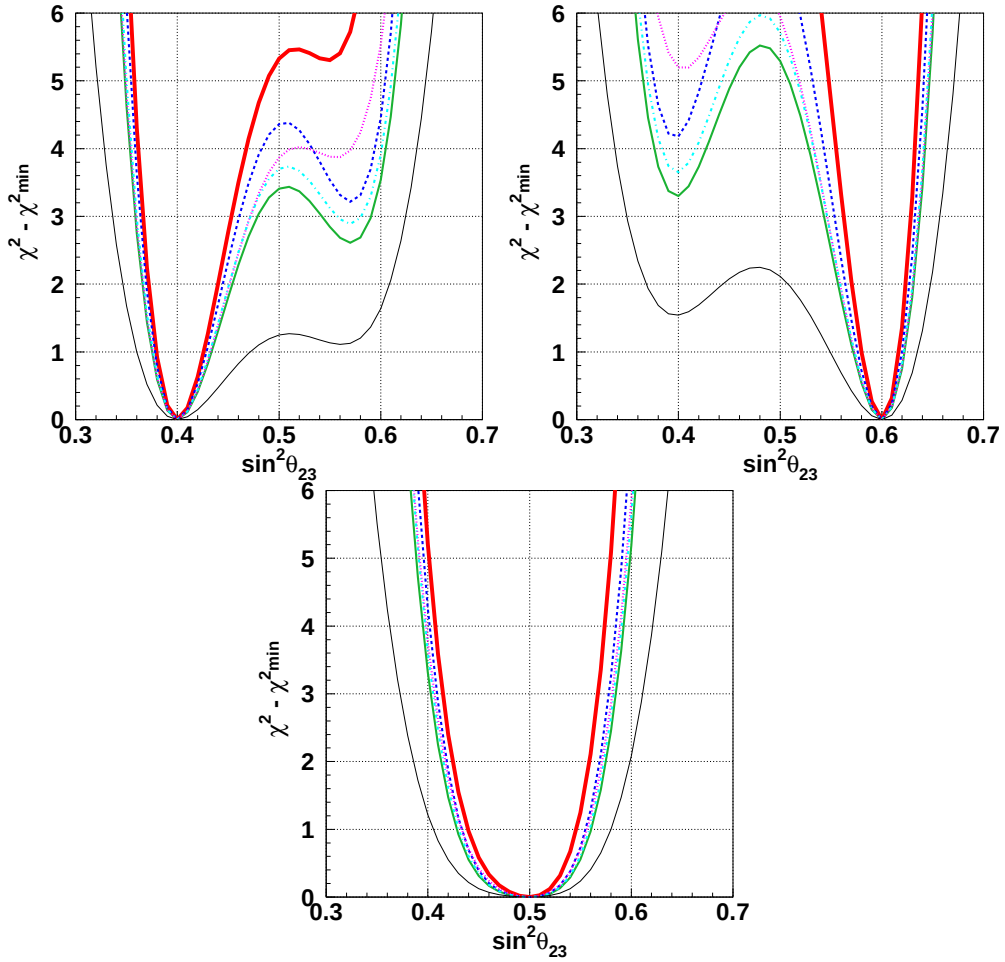

Figure 8.1: χ^2-χ^2_{min} distribution as a function of $\sin^2\theta_{23}$ using the oscillated Monte Carlo events of a 20 year exposure with the true oscillation parameters of $\theta_{13} = 0$, $\sin^2\theta_{12} = 0.32$, $\Delta m^2_{12} = 7.8\times10^{-5}$ eV^2, $\Delta m^2_{23} = 2.5\times10^{-3}$ eV^2 and $\sin^2\theta_{23} = 0.4$ (top left), 0.5 (bottom) and 0.6 (top right). The thin solid (black) line and middle-thick solid (green) line show the case with all systematic errors unchanged for a 6 year exposure, which is equivalent to the period for SK-I and SK-II, and a 20 year exposure, respectively. All the other lines are for 20 year exposure. The dashed (blue) line shows for the case of reducing the systematic errors on neutrino flux by a factor of 0.25. The dotted (pink) line on neutrino interactions and the dashed-dotted (light-blue) line on the detector responses. The thick solid (red) line shows for the case of reducing all the systematic errors.

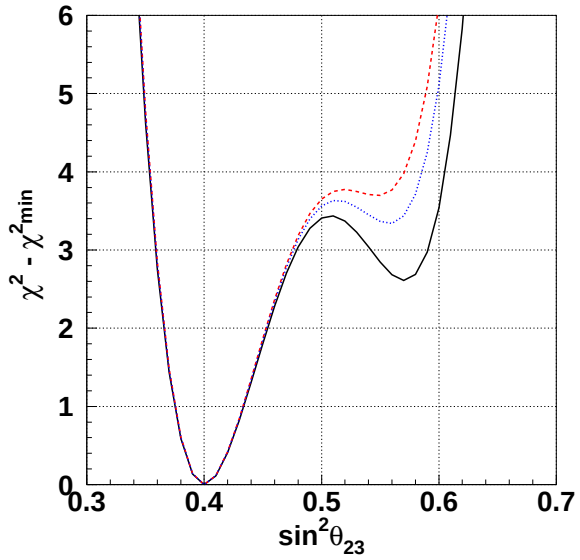

Figure 8.2: χ^2-χ^2_{min} distribution as a function of $\sin^2\theta_{23}$ using the oscillated Monte Carlo events of a 20 year exposure with the true $\sin^2\theta_{23} = 0.4$. The size of the 7 dominant systematic errors is assumed as 1/2 (dotted line) and 1/4 (dashed line).

- neutrino interaction : M_A in quasi-elastic scattering and single-meson production
- neutrino interaction : $\overline{\nu}/\nu$ ratio on CCQE cross-section
- neutrino interaction : NC/CC cross-section ratio
- detector response : decay electron tagging

Figure 8.2 shows the χ^2-χ^2_{min} distribution as a function of $\sin^2\theta_{23}$ for the true $\sin^2\theta_{23} = 0.4$ with the 7 dominant systematic errors reduced down to 1/2 and 1/4 of the current estimates. It is concluded that future higher statistics atmospheric neutrino experiments could improve our knowledge on θ_{23}.

Chapter 9

Conclusion

The effect of the sub-dominant oscillation derived by the 1-2 parameters on the low energy atmospheric neutrinos strongly depends on the deviation of $\sin^2\theta_{23}$ from 0.5.

The oscillation analysis including the 1-2 oscillation parameters are performed using the atmospheric neutrino data during Super-Kamiokande-I (1489.2 days exposure for FC and PC, 1645.9 days for UPMU) period and Super-Kamiokande-II (798.6 days for FC and PC, 827.7 days for UPMU) period. This is the first experimental results that involves two Δm^2s (Δm^2_{12} and Δm^2_{23}).

In order to improve the sensitivity to observe the sub-dominant oscillation effect induced by the 1-2 parameters, sub-GeV e-like events and sub-GeV μ-like events are separated to CCQE-enriched sample and others.

The result of the oscillation analysis without the solar terms gives the best-fit value on $\sin^2\theta_{23}$ at 0.50. On the other hand, the best-fit value on $\sin^2\theta_{23}$ is 0.53 by the analysis with solar terms. No significant deviation of θ_{23} from 45° is observed, but the asymmetric shape due to the effect of the solar terms is seen in the χ^2 distribution. The stronger constraint on $\sin^2\theta_{23}$ is observed in the analysis with the solar terms. The 1σ arrowed region for $\sin^2\theta_{23}$ is $0.43 < \sin^2\theta_{23} < 0.58$, which is equivalent to $\sin^2 2\theta_{23} > 0.973$. This is the more stringent constraint on θ_{23} compared with the published result.

Bibliography

[1] S.L. Glashow, Nucl. Phys. **22**, 579 (1961).

[2] S. Weinberg, Phys. Rev. Lett. **19**, 1264 (1967).

[3] A. Salam, In *Proceedings of the 8th Nobel Symposium on Elementary particle theory, relativistic groups and analyticity*, edited by N. Svartholm (1969).

[4] Z. Maki, M. Nakagawa, and S. Sakata, Prog. Theo. Phys. **28**, 870 (1962).

[5] R. Davis Jr., D.S. Harmer, and K.C. Hoffman, Phys. Rev. Lett. **20**, 1205 (1968).

[6] K.S. Hirata *et al.*, Phys. Rev. Lett. **63**, 16 (1989);
K.S. Hirata *et al.*, Phys. Rev. D **44**, 2241 (1991), Erratum-ibid. **D45**, 2170 (1992).

[7] A.I. Abazov *et al.*, Phys. Rev. Lett. **67**, 3332 (1991);
J.N. Abdurashitov *et al.*, JETP **95**, 181 (2002).

[8] P. Anselmann *et al.*, Phys. Lett. B **285**, 376 (1992);
W. Hampel *et al.*, Phys. Lett. B **447**, 127 (1999).

[9] S. Fukuda *et al.*, Phys. Lett. B **539**, 179 (2002);
M.B. Smy *et al.*, Phys. Rev. D **69**, 011104 (2004).

[10] Q.R. Ahmad *et al.*, Phys. Rev. Lett. **87**, 071301 (2001);
Q.R. Ahmad *et al.*, Phys. Rev. Lett. **89**, 011301 (2002);
S.N. Ahmed *et al.*, Phys. Rev. Lett. **92**, 181301 (2002).

[11] J.N. Bahcall and M.H. Pinsonneault, Rev. Mod. Phys. **64**, 885 (1992).

[12] J. Hosaka *et al.*, Phys. Rev. D **73**, 112001 (2006).

[13] M. Maltoni *et al.*, hep-ph/0405172v6, (2007).

[14] M. Honda *et al.*, Phys. Rev. D **70**, 043008 (2004).

[15] K.S. Hirata *et al.*, Phys. Lett. B **205**, 416 (1988).

[16] K.S. Hirata *et al.*, Phys. Lett. B **280**, 146 (1992).

[17] D. Casper *et al.*, Phys. Rev. Lett. **66**, 2561 (1991).

[18] R. Becker-Szendy *et al.*, Phys. Rev. D **46**, 3720 (1992).

[19] M. C. Sanchez *et al.*, Phys. Rev. D **68**, 113004 (2003).

[20] Y. Fukuda *et al.*, Phys. Lett. **81**, 1562 (1998).

[21] The MACRO collaboration, Phys. Lett. B **434**, 451 (1998).

[22] Y.Fukuda *et al.*, Phys. Rev. Lett. **82** 2644 (1999).

[23] E. Aliu *et al.*, Phys. Rev. Lett. **94** 081802 (2005).

[24] D. G. Michael *et al.*, Phys. Rev. Lett. **97** 191801 (2006).

[25] Y. Ashie *et al.*, Phys. Rev. D **71**, 112005 (2005).

[26] Y. Ashie *et al.*, Phys. Rev. Lett. **93** 101801 (2004).

[27] M. Apollonio *et al.*, Eur. Phys. J. C **27** 331 (2003).

[28] O. L. G. Peres and A. Y. Smirnov, Phys. Rev. Lett. B **456** 204 (1999).

[29] O. L. G. Peres and A. Y. Smirnov, Nucl. Phys. B **680** 479 (2004).

[30] I. Frank and I.Tamm, C. R. Acad. Sci. USSR **14**, 109 (1937).

[31] H. Kume *et al.*, Nucl. Inst. and Meth. **205**, 443 (1983).

[32] A. Suzuki *et al.*, Nucl. Inst. and Meth. A **329**, 299 (1993).

[33] R. Claus *et al.*, Nucl. Inst. and Meth. A **261**, 540 (1987).

[34] S. Fukuda *et al.*, Nucl. Inst. Meth. Phys. Res. Sect. A **501**, 418 (2003).

[35] Y. Takeuchi *et al.*, Phys. Lett. **452**, 418 (1999).

[36] H. Ikeda *et al.*, Nucl. Inst. and Meth. A **320**, 310 (1992).

[37] T. Tanimori *et al.*, IEEE Trans. Nucl. Sci. **NS-36**, 497 (1989).

[38] J. George, Ph.D. Thesis, University of Washington (1998).

[39] T. Shiabata, Master Thesis, Niigata University (2002).

[40] M. Yamada *et al.*, Phys. Rev. D **44** 617 (1991).

[41] G.Battistoni *et al.*, Astropart.Phys. **19** 269 (2003) [Erratum-ibid. **19** 291 (2003)]. (http://www.mi.infn.it/ battist/neutrino.html)

[42] G. Barr *et al.*, Phys. Rev. D **70**, 0423006 (2004).

[43] T. Sanuki *et al.*, Astrophys. J. **545** 1135 (2000).

[44] J.Alcarez *et al.*, Phys. Lett. B **490** 27 (2000).

[45] W.R. Webber, R.L. Golden and S.A. Stephens, In *Proceedings of the 20th International Cosmic Ray Conference* (1 987).

[46] E.S. Seo *et al.*, Astrophys. J. **378** 763 (1991).

[47] P. Pappini *et al.*, In *Proceedings of the 23rd International Cosmic Ray Conference* (1 993).

[48] M. Boezio *et al.*, Astrophys. J. **518** 457 (1999).

[49] W. Menn *et al.*, Astrophys. J. **533** 281 (2000).

[50] M.J. Ryan, J.F. Ormes and V.K. Balasubrahmanyan, Phys. Rev. Lett. **28** 985 (1972).

[51] K. Asakamori *et al.*, Astrophys. J. **502** 985 (1998).

[52] I.P. Ivanenko *et al.*, In *Proceedings of the 23rd International Cosmic Ray Conference* (1993).

[53] Y. Kawamura *et al.*, Phys. Rev. D **40** 729 (1989).

[54] A.V. Apanasenko *et al.*, Astropart. Phys. **16** 13 (2001).

[55] http://modelweb.gsfc.nasa.gov/atmos/usstandard.html.

[56] K. Hänssget and J. Ranft, Comput. Phys. **39** 37 (1986).

[57] S. Roesler, R. Engel, and J. Ranft, Phys. Rev. D **57** 2889 (1998).

[58] M.Motoki *et al.*, Astropart.Phys. **19** 113 (2003).

[59] P. Hansen *et al.*, Phys.Rev. D **68** 103001518 (2003).

[60] M.Honda *et al.*, In *Proceedings of the 27th International Cosmic Ray Conferences, H amburg, Germany*, (2001).

[61] G. Battistoni *et al.*, Astopart. Phys. **12**, 315 (2000).

[62] Y. Hayato, Nucl. Phys. Proc. Suppl. **112**, 171 (2002).

[63] C. H. Llewellyn Smith, Phys. Rep. **3**, 261 (1972).

[64] S. K. Singh and E. Oset, Phys. Rev. C **48**, 1246 (1993).

[65] M. H. Ahn *et al.*, Phys. Rev. Lett. **90**, 041801 (2003).

[66] F.Cavanna *et al.*, Nucl. Phys. Proc. Suppl. **139**, 1-328 (2005)

[67] R. A. Smith and E. J. Moniz, Nucl. Phys. B **43**, 605 (1972). [Erratum-ibid. B **101**, 547 (1975).]

[68] C.H. Albright *et al.*, Phys. Rev. D **14**, 1780 (1976).

[69] K. Abe *et al.*, Phys. Rev. Lett. **56**, 1107 (1986).

[70] S. Barish *et al.*, Phys. Rev. D **16**, 3103 (1977).

[71] S. Bonetti *et al.*, Nouvo Cimento **38**, 260 (1977).

[72] M. Pohl *et al.*, Nuovo Cimento **26**, 332 (1979);
N. Arimenise *et al.*, Nucl. Phys. B **152**, 365 (1979).

[73] A.S. Vovenko *et al.*, Yad. Fiz. **30**, 1014 (1979).

[74] S. Belikov *et al.*, Z. Phys. **320**, 625 (1985).

[75] J.Brunner *et al.*, Z. Phys. C **45**, 551 (1990).

[76] D. Rein and L.M. Sehgal, Ann. of Phys. **133**, 1780 (1981).

[77] R. Feynman *et al.*, Phys. Rev. D **3**, 2706 (1971).

[78] G.L. Fogli and G. Nardulli, Nucl. Phys. B **160**, 116 (1979).

[79] S.K. Singh, M.J. Vicente-Vacas and E.Oset, Phys. Lett. B **416**, 23 (1998).

[80] G. Radecky *et al.*, Phys. Rev. D **25**, 116 (1982).

[81] T. Kitagaki *et al.*, Phys. Rev. D **34**, 2554 (1986).

[82] P. Allen *et al.*, Nucl. Phys. B **264**, 221 (1986).

[83] P. Allen *et al.*, Nucl. Phys. B **176**, 269 (1980).

[84] W. Lerche *et al.*, Phys. Lett. **4**, 510 (1978).

[85] D. Allisia *et al.*, Z. Phys. C **24**, 119 (1984).

[86] S.J. Barish *et al.*, Phys. Lett. B **91**, 161 (1980).

[87] C.H. Albright and C. Jarlskog, Nucl Phys. B **84**, 467 (1975).

[88] M. Glück, E. Reya and A. Vogt, Z. Phys. D **57**, 433 (1995).

[89] P. Musset and J.P. Vialle, Phys. Rep. C **39**, 1 (1978).

[90] J.E. Kim *et al.*, Rev. Mod. Phys. **53**, 211 (1981).

[91] S.J. Barish *et al.*, Phys. Rev. **D17**, 1 (1978).

[92] S. Barlag *et al.*, Z. Phys. C **11**, 283 (1982).

[93] T. Sjöstrand *et al.*, CERN-TH-7112-93 (1994).

[94] D. Rein and L.M. Sehgal, Nucl. Phys. B **233**, 29 (1983).

[95] A. Kartavtsev, E. A. Paschos, and G. J. Gounaris, Phys. Rev. D **74**, 054007 (2006).

[96] M. Hasegawa *et al.*, Phys. Rev. Lett. **95**, 252301 (2005).

[97] F. Bergsma *et al.*, Phys. Lett. B **157**, 469 (1985).

[98] J. L. Raaf, Ph.D. thesis, University of Cincinnati (2005).

[99] H. Faissner *et al.*, Phys. Lett. B **125**, 230 (1983).

[100] E. Isiksal, D. Rein, and J. G. Morfin, Phys. Rev. Lett. **52**, 1096 (1984).

[101] R. Woods and D. Saxon, Phys. Rev. **95**, 577 (1954).

[102] L. Salcedo *et al.*, Nucl. Phys. A **484**, 557 (1988).

[103] G. Rowe *et al.*, Phys. Rev. C **18**, 584 (1978).

[104] D. Ashery *et al.*, Phys. Rev. C **23**, 2173 (1981).

[105] C. Ingram *et al.*, Phys. Rev. C **27**, 1578 (1983).

[106] B. R. Martin and M. K. Pidcock, Nuc. Phys. B **126**, 266 (1977).

[107] B. R. Martin and M. K. Pidcock, Nuc. Phys. B **126**, 285 (1977).

[108] J. S. Hyslop *et al.*, Phys. Rev. D **46**, 961 (1992).

[109] D. A. Sparrow, Proc. of the Conf. on the intersection between partivle and nuclear physics, 1019 (1984).

[110] H. W. Bertini *et al.*, Phys. Rev. C **6**, 631 (1972).

[111] S. J. Lindenbaum *et al.*, Phys. Rev. **105**, 1874 (1957).

[112] L.V. Volkova, Sov. J. Nucl. Phys. **31**, 784 (1980).

[113] GEANT, CERN Program Library Long Writeup W5013 (1994).

[114] C. Zeitnitz and T.A. Gabriel, Nucl. Inst. and Meth. A **349**, 106 (1994).

[115] M. Nakahata *et al.*, J. Phys. Soc. Jpn. **55**, 3786 (1986).

[116] E. Bracci *et al.*, CERN/HERA 72-1 (1972).

[117] A.S. Carrol *et al.*, Phys. Rev. C **14**, 635 (1976).

[118] S. Desai, Ph.D. Thesis, Boston University.

[119] E. R. Davies, *Machine Vision: Theory, Algorithms, Practicalities*, Academic Press, San Diego (1997).

[120] S. Kasuga *et al.*, Phys. Lett. B **374**, 238 (1996).

[121] T. Barszczak, Ph.D. Thesis, University of California, Irvine (2005).

[122] J. A. Nelder and R. Mead, Computer Journal **7**, 308 (1965).

[123] S. Desai *et al.*, Astopart. Phys. **29**, 42 (2008).

[124] D. Casper, Nucl. Phys. Proc. Suppl. **112**, 161 (2002).

[125] J. Nieves *et al.*, Phys. Rev. C **70**, 055503 (2004).

[126] C.H. Albright and C. Jarlskog, Nucl. Phys. B **84**, 467 (1975).

[127] A. Bodek and U. K. Yang, Nucl. Phys. Proc. Suppl. **112**, 70 (2002)

[128] K. Hagiwara *et al.*, Nucl. Phys. B **668**, 364 (2003).

[129] Y. Fukuda *et al.*, Phys. Lett. B **433**, 9 (1998).

[130] G.L. Fogli *et al.*, Phys. Rev. D **66**, 053010 (2002).

[131] S.Baker and R.D. Cousins, Nucl. Inst. and Meth. **221**, 437 (1984).